

**NRC HIGH-LEVEL RADIOACTIVE
WASTE RESEARCH AT CNWRA
JANUARY-JUNE 1995**

Prepared for

**Nuclear Regulatory Commission
Contract NRC-02-93-005**

Prepared by

**Center for Nuclear Waste Regulatory Analyses
San Antonio, Texas**

August 1995



**NRC HIGH-LEVEL RADIOACTIVE
WASTE RESEARCH AT CNWRA
JANUARY—JUNE 1995**

Prepared for

**Nuclear Regulatory Commission
Contract NRC-02-93-005**

Contributors

**R.G. Baca, A.C. Bagtzoglou, D. Balin, F.P. Bertetti,
C.B. Connor, F.M. Conway, D.A. Ferrill, C.J. Goulet, B.E. Hill,
M.S. Jarzempa, R.V. Klar, P. LaFemina, P.C. Lichtner,
A.P. Morris, W.M. Murphy, R.T. Pabalan, E.C. Percy,
D.A. Pickett, J.D. Prikryl, K.H. Spivey, J.A. Stamatakos,
S.A. Stothoff, D.R. Turner, G.W. Wittmeyer**

Edited by

Budhi Sagar

**Center for Nuclear Waste Regulatory Analyses
San Antonio, Texas**

August 1995

PREVIOUS REPORTS IN SERIES

Number	Name	Date Issued
CNWRA 90-01Q	First Quarterly Research Report for 1990 January 1–March 30	May 1990
CNWRA 90-02Q	Second Quarterly Research Report for 1990 April 1–June 30	August 1990
CNWRA 90-03Q	Third Quarterly Research Report for 1990 July 1–September 30	November 1990
NUREG/CR-5817 Volume 1 CNWRA 90-01A	Report on Research Activities for Calendar Year 1990	December 1991*
CNWRA 91-01Q	First Quarterly Research Report for 1991 January 1–March 30	May 1991
CNWRA 91-02Q	Second Quarterly Research Report for 1991 April 1–June 30	August 1991
CNWRA 91-03Q	Third Quarterly Research Report for 1991 July 1–September 30	November 1991
NUREG/CR-5817 Volume 2 CNWRA 91-01A	NRC High-Level Radioactive Waste Research at CNWRA Calendar Year 1991	May 1993
NUREG/CR-5817 Volume 3, No. 1 CNWRA 92-01S	NRC High-Level Radioactive Waste Research at CNWRA January–June 1992	May 1993
NUREG/CR-5817 Volume 3, No. 2 CNWRA 92-02S	NRC High-Level Radioactive Waste Research at CNWRA July–December 1992	July 1993
CNWRA 93-01S	NRC High-Level Radioactive Waste Research at CNWRA January–June 1993	August 1993
CNWRA 93-02S	NRC High-Level Radioactive Waste Research at CNWRA July–December 1993	February 1994

PREVIOUS REPORTS IN SERIES (Cont'd)

Number	Name	Date Issued
CNWRA 94-01S	NRC High-Level Radioactive Waste Research at CNWRA January-June 1994	September 1994
CNWRA 94-02S	NRC High-Level Radioactive Waste Research at CNWRA July-December 1994	February 1995

PREFACE

The Center for Nuclear Waste Regulatory Analyses (CNWRA), a Federally Funded Research and Development Center, conducts research on behalf of the Nuclear Regulatory Commission (NRC). The NRC-funded research at the CNWRA is focused on activities related to the NRC responsibilities defined under the Nuclear Waste Policy Act, as amended. Progress for the period of January 1, 1995 to June 30, 1995 on nine of eleven research projects that are currently active is described in this report. Those projects not reported here are the Integrated Waste Package Experiments (IWPE) and the Seismic Rock Mechanics (SRM) Projects. The work scope defined with the IWPE Project was essentially completed in early 1995 and a final report was prepared and submitted to five external peers for review. A new project plan titled "Engineered Barrier System Experimental Research" has been prepared in accordance with a statement of work provided by the NRC. A workshop which will be attended by the five external peer reviewers is planned in October 1995, to gather their comments on the final report and also on the new project plan. The majority of the work scope defined in the SRM Project was also completed and documented in a final report. A peer review of this project was also conducted in July 1995, through a workshop held at the CNWRA. An additional work scope has been defined in the updated "Rock Mechanics" Project Plan. Because the final reports for these projects were only recently submitted to the NRC and are planned to be published as NUREG/CR documents, chapters on these projects are not included in this report. An Executive Summary is provided to give a brief summary of the work performed on the other nine projects during the reporting period.

In addition to disseminating research results through publications in appropriate open literature (e.g., CNWRA topical reports, NRC documents, and journals) and at technical meetings, workshops, and symposia, the CNWRA produces these research reports twice yearly. A list of previous reports in this series is given on pages iii and iv.

Each chapter in this semi-annual report summarizes the progress made in a particular research project and is authored by the researchers contributing to that project. Since readers of this report may be interested only in a particular topic, each chapter is self-contained and can be read without reference to other chapters. Coverage in the semi-annual reports is limited to only the key aspects of progress made; greater detail is provided in topical reports that are produced during the course of the research or at its conclusion, as appropriate. The editor of this report ensures that each chapter is reviewed for its technical and programmatic content and that some uniformity as to the depth of descriptions is maintained across the various chapters.

The NRC evaluates its research needs continually as the research progresses. The research needs are based on user needs identified jointly by the NRC Offices of Nuclear Material Safety and Safeguards (NMSS) and Nuclear Regulatory Research. Generally, NMSS is the user in the sense that its staff applies the research results to strengthen reviews of the submittals by the U.S. Department of Energy, including the License Application for the first High-Level Nuclear Waste Repository. In their turn, the user needs are based on Key Technical Uncertainties (KTUs) identified during the process of developing strategies and methods for determining compliance with the applicable regulation—in this case, 10 CFR Part 60. Thus, the research is directed toward evaluation of the KTUs.

CONTENTS

Section	Page
FIGURES	xiii
TABLES	xix
ACKNOWLEDGMENTS	xxi
QUALITY OF DATA	xxi
1 EXECUTIVE SUMMARY	1-1
1.1 INTRODUCTION	1-1
1.2 GEOCHEMICAL ANALOG OF CONTAMINANT TRANSPORT IN UNSATURATED ROCK	1-2
1.3 SORPTION MODELING FOR HIGH-LEVEL WASTE PERFORMANCE ASSESSMENT	1-4
1.4 PERFORMANCE ASSESSMENT RESEARCH	1-5
1.5 VOLCANIC SYSTEMS OF THE BASIN AND RANGE	1-6
1.6 TECTONIC PROCESSES IN THE CENTRAL BASIN AND RANGE REGION	1-7
1.7 FIELD VOLCANISM	1-9
1.8 REGIONAL HYDROGEOLOGIC PROCESSES OF THE DEATH VALLEY REGION	1-10
1.9 SUBREGIONAL HYDROGEOLOGIC FLOW AND TRANSPORT PROCESSES	1-12
1.10 HIGH-LEVEL WASTE NEAR-FIELD PROCESSES AND VARIATIONS	1-13
1.11 REFERENCES	1-14
2 GEOCHEMICAL NATURAL ANALOG RESEARCH	2-1
2.1 TECHNICAL OBJECTIVES	2-1
2.2 SIGNIFICANT TECHNICAL ACCOMPLISHMENTS	2-2
2.2.1 Background	2-5
2.2.1.1 Fracture Description	2-5
2.2.1.2 Analytical Methods	2-5
2.2.2 Results	2-6
2.2.2.1 Mineralogic and Petrographic Characteristics	2-6
2.2.2.2 U and Th Concentrations of Bulk Fracture-Infilling	2-9
2.2.2.3 U and Th Isotopic Profiles	2-12
2.2.2.4 U and Trace Element Distribution	2-14
2.2.3 Discussion	2-16
2.2.4 Conclusions	2-21
2.3 ASSESSMENT OF PROGRESS TOWARD MEETING PROJECT OBJECTIVES ..	2-22
2.4 PLANS FOR NEXT REPORT PERIOD	2-23
2.5 REFERENCES	2-23

CONTENTS (Cont'd)

Section	Page	
3	SORPTION MODELING FOR HIGH-LEVEL WASTE PERFORMANCE ASSESSMENT	3-1
3.1	TECHNICAL OBJECTIVES	3-1
3.2	PLUTONIUM EXPERIMENTS	3-2
3.2.1	Plutonium Experimental Solutions	3-2
3.2.2	Plutonium Oxidation State Determination by Solvent Extraction	3-2
3.2.3	Preparation of "Pure" Oxidation State Plutonium Solutions	3-3
3.2.4	Container Sorption Experiments	3-4
3.2.5	Calculated Plutonium Oxidation States	3-4
3.3	NEPTUNIUM SORPTION EXPERIMENTS	3-4
3.3.1	Mineral Preparation	3-5
3.3.1.1	Quartz	3-5
3.3.1.2	Clinoptilolite	3-6
3.3.1.3	Montmorillonite	3-6
3.3.2	Neptunium Solutions	3-7
3.3.3	Experimental Procedure	3-7
3.3.4	Results and Discussion	3-10
3.3.4.1	Neptunium Sorption onto Quartz	3-10
3.3.4.2	Neptunium Sorption onto Clinoptilolite	3-12
3.3.4.3	Neptunium Sorption onto Montmorillonite	3-14
3.3.4.4	Neptunium Sorption onto Containers	3-15
3.3.5	Conclusions	3-17
3.4	ASSESSMENT OF PROGRESS TOWARD MEETING PROJECT OBJECTIVES	3-17
3.5	PLANS FOR NEXT REPORTING PERIOD	3-19
3.6	REFERENCES	3-19
4	PERFORMANCE ASSESSMENT RESEARCH	4-1
4.1	TECHNICAL OBJECTIVES	4-1
4.2	SIGNIFICANT TECHNICAL ACCOMPLISHMENTS	4-3
4.2.1	Methodology for Modeling Radionuclide Adsorption	4-3
4.2.1.1	Model Development for Totally Saturated Media	4-3
4.2.1.2	Data Extraction	4-6
4.2.1.3	Significance of the New Model	4-8
4.2.1.4	Interpretation of Results	4-10
4.2.2	Advanced Computational Methods	4-11
4.2.2.1	Mathematical Theory of New Transform-Based Approach	4-12
4.2.2.2	Example Application of New Computational Method	4-13
4.3	ASSESSMENT OF PROGRESS TOWARD MEETING PROJECT OBJECTIVES	4-15
4.4	PLANS FOR NEXT REPORTING PERIOD	4-17
4.5	REFERENCES	4-18

CONTENTS (Cont'd)

Section	Page
5	VOLCANIC SYSTEMS OF THE BASIN AND RANGE 5-1
5.1	OVERALL TECHNICAL OBJECTIVES 5-1
5.2	SIGNIFICANT TECHNICAL ACCOMPLISHMENTS 5-2
5.2.1	Recurrence Rates of Basaltic Volcanism 5-2
5.2.2	Defining Volcanic Events in the Springerville Volcanic Field 5-5
5.2.2.1	Mapping Volcanic Events 5-6
5.2.2.2	Dating Volcanic Events 5-7
5.2.3	Temporal Trends in Volcanism 5-9
5.2.4	Spatial Trends in Volcanism 5-11
5.2.5	Modeling Patterns of Basaltic Volcanism in the Springerville Volcanic Field 5-13
5.2.6	Recurrence Rate and Probability Maps 5-16
5.2.7	Discussion 5-23
5.2.7.1	Patterns of Volcanism in the Springerville Volcanic Field 5-23
5.2.7.2	Hazard Models 5-24
5.2.8	Conclusions 5-26
5.3	ASSESSMENT OF PROGRESS TOWARD MEETING PROJECT OBJECTIVES . . 5-26
5.4	PLANS FOR NEXT REPORTING PERIOD 5-27
5.5	REFERENCES 5-27
6	TECTONIC PROCESSES IN THE CENTRAL BASIN AND RANGE REGION 6-1
6.1	TECHNICAL OBJECTIVES 6-1
6.2	SIGNIFICANT TECHNICAL ACCOMPLISHMENTS 6-2
6.2.1	Tectonic Setting and Significance of Bare Mountain 6-3
6.2.2	Stratigraphy of Bare Mountain 6-6
6.2.3	Structure of Bare Mountain 6-9
6.2.4	Salient Points and Problems in the Tectonic History of Bare Mountain . . 6-11
6.2.5	Vertical Axis Rotation of Bare Mountain 6-14
6.2.5.1	Background 6-14
6.2.5.2	Uncertainties 6-15
6.2.5.3	Sampling and Experimental Methods 6-16
6.2.5.4	Paleomagnetic Results 6-17
6.3	ASSESSMENT OF PROGRESS TOWARD MEETING PROJECT OBJECTIVES . . 6-21
6.4	PLANS FOR NEXT REPORTING PERIOD 6-22
6.5	REFERENCES 6-23
7	FIELD VOLCANISM 7-1
7.1	OVERALL TECHNICAL OBJECTIVES 7-1
7.2	SIGNIFICANT TECHNICAL ACCOMPLISHMENTS 7-2

CONTENTS (Cont'd)

Section	Page
7.2.1	7-3
7.2.1.1	7-5
7.2.1.2	7-9
7.2.1.3	7-13
7.2.1.4	7-13
7.2.2	7-14
7.3	7-15
7.4	7-17
7.5	7-17
8	8-1
8.1	8-1
8.2	8-2
8.2.1	8-3
8.2.2	8-5
8.2.3	8-6
8.2.4	8-10
8.3	8-14
8.4	8-15
8.5	8-15
9	9-1
9.1	9-1
9.2	9-3
9.2.1	9-3
9.2.2	9-5
9.2.2.1	9-5
9.2.2.2	9-7
9.2.2.3	9-8
9.2.3	9-12
9.2.3.1	9-13
9.2.4	9-16
9.2.4.1	9-17
9.2.4.2	9-18
9.3	9-21
9.4	9-22
9.5	9-22

CONTENTS (Cont'd)

Section	Page
10 HIGH-LEVEL WASTE NEAR-FIELD PROCESSES AND VARIATIONS	10-1
10.1 TECHNICAL OBJECTIVES	10-1
10.2 SIGNIFICANT TECHNICAL ACCOMPLISHMENTS	10-2
10.2.1 Review of Literature on Thermodynamic Data for Uranyl Minerals	10-2
10.2.2 Temperature Dependence of Uranyl Mineral Solubility	10-3
10.2.3 Synthesis of Uranophane	10-6
10.3 ASSESSMENT OF PROGRESS TOWARD MEETING PROJECT OBJECTIVES ..	10-8
10.4 PLANS FOR NEXT REPORTING PERIOD	10-9
10.5 REFERENCES	10-9

FIGURES

Figure	Page
1-1	Relationship of the NRC HLW Research Program to licensing needs 1-2
2-1	Map showing the location of the 13.5 m N fracture set on the Level +10 surface of the Nopal I deposit. The fracture set crosscuts the western margin of the deposit 2-4
2-2	XRD patterns (2-theta vs counts) of bulk fracture-infilling minerals from the 13.5 m N fracture. The EW coordinate at which each sample was collected is displayed to the left of each pattern 2-7
2-3	Reflected light photomicrograph of fracture-infilling consisting of goethite (G), hematite (H), and amorphous Fe-oxyhydroxide intergrown with kaolinite (A). This sample was collected at 6.1 m E along the 13.5 m N fracture. 2-8
2-4	Reflected light photomicrograph of fracture-infilling collected from the 13.5 m N fracture at -10.1 m E. Hematite (H) forms a continuous colloform rim on goethite (G) and amorphous Fe-oxyhydroxides (A). Goethite shows zoning, which suggests replacement of precursor pyrite by two hydrous Fe-oxide phases. 2-8
2-5	Reflected light photomicrograph of fracture-infilling collected at -10.1 m E. Hematite (H) forms a continuous rim on earlier formed goethite (G) and amorphous Fe-oxyhydroxide (A). 2-9
2-6	Reflected light photomicrograph of fracture-infilling collected at 6.1 m E. Goethite (G) forms a meshwork of gossan. Jarosite (J) partially fills the open voids (V) left by dissolution of pyrite and tuff fragments. 2-9
2-7	U and Th concentrations in bulk fracture-infilling samples along the 13.5 m N fracture 2-11
2-8	U versus Th concentrations in bulk fracture-infilling samples from the 13.5 m N fracture 2-12
2-9	$^{234}\text{U}/^{238}\text{U}$ and $^{230}\text{Th}/^{234}\text{U}$ activity ratios of bulk fracture-infilling samples along the 13.5 m N fracture 2-13
2-10	Average concentrations of (A) U, (B) Pb, (C) As, and (D) S in goethite, hematite, and amorphous Fe-oxyhydroxide along the 13.5 m N fracture. Numbers above bars in the plot for U (A) represent the number of analyses on which the averages are based 2-15
2-11	Relative sequence of formation of minerals in the 13.5 m N fracture 2-17
3-1	Estimated percent abundances of Pu(V) and Pu(VI) in dissolved Pu in 0.1 M NaClO_4 at varying pH in equilibrium with atmosphere. Calculations performed using EQ3NR (Wolery, 1992). 3-5
3-2	Eh-pH diagram of neptunium (adapted from Lieser and Mühlenweg, 1988) 3-8
3-3	Sorption of Np(V) onto quartz as a function of pH, initial Np concentration, and solid-mass to solution-volume ratio (M/V). Error bars indicate calculated total uncertainties (2σ) for selected points. 3-11

FIGURES (Cont'd)

Figure		Page
3-4	Sorption of Np(V) onto quartz as a function of pH and CO ₂ (g) equilibrium. Solutions were allowed to equilibrate with atmospheric CO ₂ (filled circles) or capped immediately after pH adjustment, resulting in conditions undersaturated with respect to atmospheric CO ₂ (open circles).	3-11
3-5	Sorption of Np(V) onto quartz as a function of pH and surface area. Initial [Np]=1×10 ⁻⁶ M. Both experiments conducted with capped solution containers (low CO ₂)	3-13
3-6	Sorption of Np(V) onto quartz as a function of pH and surface area after normalizing data from Figure 3-5 for surface area of quartz used in each experiment	3-13
3-7	Comparison of surface-complexation model representations of Np(V) sorption onto quartz. Data from Righetto et al. (1991) collected with initial [Np]=1×10 ⁻¹⁴ M, no CO ₂ , and colloidal silica.	3-14
3-8	Sorption of Np(V) onto clinoptilolite as a function of pH and CO ₂ (g) equilibrium. Solutions were allowed to equilibrate with atmospheric CO ₂ (filled squares) or capped immediately after pH adjustment, resulting in conditions undersaturated with respect to atmospheric CO ₂ (open circles).	3-15
3-9	Sorption of Np(V) onto montmorillonite as a function of pH and CO ₂ (g) equilibrium. Solutions were allowed to equilibrate with atmospheric CO ₂ (open circles) or capped immediately after pH adjustment, resulting in conditions undersaturated with respect to atmospheric CO ₂ (filled triangles).	3-16
3-10	Sorption of Np(V) onto Na-montmorillonite over a large pH range. Filled triangles and open circles represent data from this study. Open squares are data from Kozai (1994). Sorption of Np(V) below about pH 7 is attributed to ion exchange	3-16
3-11	Speciation of Np(V) in solution in 0.1 m NaNO ₃ at equilibrium with atmospheric CO ₂ . [Np]=1×10 ⁻⁶ M	3-18
4-1	A comparison of groundwater Pu concentrations with the retardation factor method and the new method with n_r as a parameter	4-11
4-2	Comparison of computed and measured moisture content profiles for UZ-16	4-16
5-1	Physiographic provinces and distribution of late Cenozoic basaltic volcanic fields in Arizona and New Mexico (adapted from Luedke and Smith, 1978)	5-4
5-2	Outline of SVF with vent clusters and vent alignments identified by Connor et al. (1992) and faults and flexures mapped by Crumpler et al., (1994)	5-5
5-3	Timing of volcanic events in the SVF is constrained by mapped stratigraphic relationships, rock magnetic polarity, and radiometric ages	5-8
5-4	Cumulative number of vents in the SVF estimated at 0.2-Ma intervals. The center curve (solid circles) shows the frequency of vent formation using mean estimates of unit ages	5-10

FIGURES (Cont'd)

Figure		Page
5-5	Cumulative area covered by lava flows, a proxy for volume estimates, is remarkably steady in the field between 1.75 and 0.75 Ma	5-11
5-6	Cumulative percent of volcanic events by (a) petrologic type: TH—tholeiite, TR—transitional basalt, AOB + HAW—alkali-olivine basalt and hawaiite, MUG + BEN—mugearite and benmoreite, and (b) alkalinity index: plus sign—subalkaline ($AI < 0$), open triangle—mildly alkaline ($0 \leq AI < 1$), open square—alkaline ($1 < AI \leq 1.75$), solid square—highly alkaline ($1.7 \leq AI$)	5-12
5-7	Density of mapped volcanic events in the SVF: (a) 1.75–1.5 Ma, (b) 1.5–1.25 Ma, (c) 1.25–1.0 Ma, and (d) 1.0–0.75 Ma, based on mean estimated ages of vents and lava flows and using an Epanechnikov kernel ($h=5$ km)	5-14
5-8	Comparison of recurrence rate estimates based on $m=6, 7, 8,$ and 10 near-neighbor model (labeled lines) and the observed mean estimate of recurrence rate (heavy line with solid squares)	5-16
5-9	Volcanism has waned in the SVF since about 0.75 Ma	5-17
5-10	Areas of waxing and waning basaltic volcanism in the SVF are delineated through application of the recurrence rate model	5-18
5-11	Probability maps of volcanism in the SVF calculated using the near-neighbor model. $P[\text{volcanic event} \mid a=10 \text{ km}^2, t=50,000 \text{ yr}]$ is contoured using volcanoes formed	5-20
5-12	The relative success of the spatio-temporal model can be evaluated by comparing the recurrence rates estimated by the model at the locations of subsequent volcanic events	5-22
6-1	Digital elevation map of Bare Mountain, Nevada, and surrounding region. The line of the subregional cross section (Figure 6-3) is shown	6-4
6-2	Bare Mountain, Nevada, physiography and important features referred to in the text	6-5
6-3	Semi-restorable cross sections through Bare Mountain and YM from B to C (Figure 6-1) illustrating two alternative interpretations of the deep BMF-YM fault system	6-6
6-4	Geological map of Bare Mountain (after Monsen et al., 1992) showing the line of section B-B'	6-7
6-5	Stratigraphic section of Bare Mountain (after Monsen et al., 1992; Sawyer et al., 1994), with interpretations of weathering profile and compressional and extensional detachments	6-8
6-6	Plunge-perpendicular cross section of Bare Mountain along section line BB' (Figure 6-4, after Monsen et al., 1992)	6-10
6-7	Structural domain map of Bare Mountain based on data in Monsen et al., (1992)	6-12
6-8	Map of Bare Mountain showing the distribution of paleomagnetic sites. The sampled Oligocene dikes at the northwesternmost corner of BM are presently unmapped	6-17

FIGURES (Cont'd)

Figure		Page
6-9	Paleomagnetic results from the Oligocene dike in the northwest corner of Bare Mountain	6-19
6-10	Paleomagnetic results from the Antelope Valley Formation in the Meiklejohn Peak fold on northeastern Bare Mountain	6-20
7-1	Location map of Cerro Negro and adjacent volcanoes, Nicaragua. Volcanoes named in this report are highlighted, and location of the town of Malpaisillo is shown by circles. Dashed ellipses show the interpreted extent of 0.5- and 1 mm-thick ash deposits for June 2-5, 1995, activity	7-4
7-2	(A) Location and concentrations of soil-gas radon for March 1994 study. Radon values shown in pCi l ⁻¹ . Shaded inset shows stations on the northern crater wall of Cerro Negro, which also is shaded in the smaller scale map. (B) Population distributions for March and June 1994 and June 1995 radon surveys	7-7
7-3	(A) Location and concentrations of soil-gas radon for June 1994 study. Radon values in pCi l ⁻¹ . Shaded inset shows stations on the northern crater wall of Cerro Negro, which also is shaded in the smaller scale map. (B) Location and concentrations of soil-gas radon for June 1995 study. Note scale change	7-8
7-4	Cumulative percent radon concentration plotted by day during the June, 1995 eruption. Radon concentrations were significantly higher on June 2-3 (solid circles) compared with concentrations on June 3-4 (open circles), June 4-5 (open triangles), and June 5-6 (open squares)	7-10
7-5	(A) Timing of Cerro Negro eruptions for June 2-5, 1995. Eruptions show no obvious pattern, although periods of waxing and waning activity occur. (B) Column height for the June 1995 eruption shows no correlation with repose time	7-11
7-6	Schematic diagram of parameters used to calculate ejection velocities of large blocks during June 1995 activity at Cerro Negro	7-13
7-7	Location of pyroclastic fall samples from the Lathrop Wells volcano used in granulometry studies. Basalt outcrops in black from Faulds et al. (1994) and Swadley and Carr (1987), stars mark the location of aeromagnetic anomalies (Kane and Bracken, 1983; Langenheim et al., 1993)	7-15
7-8	Median diameter and simple sorting parameters for Lathrop Wells (Figure 7-7) and the 1975 Tolbachik eruption pyroclastic fall deposits. Both deposits plot in the field of typical strombolian eruptions (Walker and Croasdale, 1972)	7-16
8-1	Eleana Range-Las Vegas Range hydrostratigraphic cross section	8-7
8-2	Location of Eleana Range-Las Vegas Range cross section overlain on pre-Cenozoic surface hydrostratigraphy	8-8

FIGURES (Cont'd)

Figure		Page
8-3	Simplified geologic map of the NTS region showing mapped and inferred locations of Mesozoic thrusts and other major tectonic features. BRT=Belted Range Thrust (Caskey and Schweickert, 1992); FPAZ=French Peak accommodation zone; RVF=Rock Valley Fault; SRT=Spotted Range Thrust; YF=Yucca Fault; CPT=CP Thrust; CBF=Carpet Bag Fault; MPT=Meiklejohn Peak Thrust (from Cole et al., 1994).	8-11
8-4	Location of Eleana Range-Las Vegas Range cross section overlain on water level contour map from Wittmeyer et al., (1995)	8-12
8-5	Predicted steady-state hydraulic head and hydraulic head gradient between the northwest terminus and the bend in the Eleana Range-Las Vegas Range hydrostratigraphic section	8-14
9-1	Topopah Spring welded unit outcrop as predicted by the CNWRA GFMs, and comparison with geologic map of Frizzell and Shulters (1990)	9-4
9-2	Schematic for GIS-based infiltration evaluation methodology	9-7
9-3	Yucca Mountain mean daily solar radiation on February 1, of a typical year, as inferred from ARC/INFO calculations. Mean daily solar radiation is given in dimensionless units.	9-8
9-4	Relationship between average moisture content at 30 m depth and average flux through the column	9-10
9-5	Sensitivities of average flux to various meteorologic forcings. The horizontal line is the base case flux.	9-10
9-6	Major faults present in the YM site, as identified in the geologic map by Frizzell and Shulters (1990). Map coordinates are in Universal Transverse Mercator (UTM) units.	9-13
9-7	Cross section of a hypothetical fault-induced trap. Cross-hatched areas represent potential perched-water zones.	9-15
9-8	Depth versus $\delta^{18}\text{O}$ for secondary calcite (Data modified from Whelan and Stuckless, 1992)	9-15
9-9	Smectite content (as weight percent) shown as a function of depth (Data modified from Bish and Chipera, 1989)	9-16
9-10	Logarithm of the distribution coefficient for sorption of uranium and neptunium on goethite plotted as a function of pH with (dashed curve) and without (solid curve) CO_2 present. Total carbon (C_T) in moles/L H_2O	9-19
9-11	Logarithm of the concentration of selected (a) uranium- and (b) neptunium-bearing species plotted as a function of pH	9-20
10-1	Natural logarithm of the equilibrium constant for the dissolution of schoepite (reaction 10-3) as a function of inverse temperature in kelvins. Temperature in $^\circ\text{C}$ is given at the top of the figure	10-5

FIGURES (Cont'd)

Figure		Page
10-2	XRD pattern of uranophane synthesized in this study compared with the XRD pattern (PDF 39-1360) taken from the International Centre for Diffraction Data (1993) database, and diffraction data for synthetic uranophane reported by Nguyen et al. (1992) and uranophane collected at the Nopal I U deposit	10-7
10-3	Scanning electron photomicrograph of uranophane synthesized in this study	10-8

TABLES

Table		Page
2-1	U and Th concentration and isotopic data of bulk fracture-infilling samples from the 13.5 m N fracture. Uncertainties in U and Th concentrations are $\pm 5\%$. Uncertainties in $^{234}\text{U}/^{238}\text{U}$ and $^{230}\text{Th}/^{234}\text{U}$ activity ratios are from counting statistics and are at the 2 sigma level (or 95% confidence level)	2-10
3-1	Comparison of solvent extraction results at different Pu concentrations	3-3
3-2	Summary of Np(V) sorption experiments	3-9
4-1	Hydrostratigraphy and van Genuchten-Mualem parameters for UZ-16	4-14
9-1	Normalized cross correlation between the modeled and mapped Topopah Spring unit outcrop as a function of search window size (in pixels)	9-5
9-2	Porous medium parameters used in sensitivity analyses	9-9
9-3	Surface complexation reactions for sorption of uranium and neptunium on goethite	9-17
9-4	Diffuse-layer (MINTEQA2) model parameters used	9-18

ACKNOWLEDGMENTS

This report was prepared to document work performed by the Center for Nuclear Waste Regulatory Analyses (CNWRA) for the Nuclear Regulatory Commission (NRC) under Contract NRC-02-93-005. The activities reported herein were performed on behalf of the NRC Office of Nuclear Regulatory Research, Division of Regulatory Applications. The report is an independent product of the CNWRA and does not necessarily reflect the views or regulatory position of the NRC.

Active support from several people during the production of this report is thankfully acknowledged. First and foremost, this report is possible only because of the wholehearted cooperation from the principal investigators and researchers within each project who kept to the tight schedule of the editor. Technical reviewers—A.C. Bagtzoglou, D.A. Ferrill, B.E. Hill, P.C. Lichtner, P.C. Mackin, H.L. McKague, E.C. Percy, J.L. Russell, N. Sridhar, and G.W. Wittmeyer—provided substantive comments that materially improved the quality of the report. Programmatic reviews were performed by P.C. Mackin, W.C. Patrick, and the editor. Able secretarial support was provided by E.F. Cantu, C. Garcia, L.F. Gutierrez, M.A. Gruhlke, L.G. Hearon, A. Ramos, and R.A. Sanchez.

Southwest Research Institute (SwRI) Publications Services staff provided illustration, editorial, format adherence, printing, and binding support.

Finally, the valued interaction with NRC Project Officers R.E. Cady, L.A. Kovach, T.J. Nicholson, E. O'Donnell, J.D. Randall, and P.R. Reed is gratefully acknowledged.

QUALITY OF DATA

DATA: Sources of data are referenced in each chapter. CNWRA-generated laboratory and field data contained in this report meet quality assurance (QA) requirements described in the CNWRA Quality Assurance Manual. Data from other sources, however, are freely used. For data from non-CNWRA sources, their referenced sources should be consulted for determining their level of QA.

ANALYSES AND CODES: Scientific/engineering computer codes used in analyses contained in this report are: ARC/INFO Geographic Information System (GIS) (Chapters 5 through 9), GeoSec (Chapter 6), and BREATH and MINTEQA2 (Chapter 9). The computer code MINTEQA2 is presently controlled under the CNWRA Technical Operating Procedure, Development and Control of Scientific and Engineering Software, (TOP-018). ARC/INFO and GeoSec are commercial software, and only the object codes of these programs are available to the CNWRA.

1 EXECUTIVE SUMMARY

1.1 INTRODUCTION

Progress from January 1 to June 30, 1995, on nine of eleven research projects underway at the Center for Nuclear Waste Regulatory Analyses (CNWRA) is discussed in this report. Those projects not reported are Integrated Waste Package Experiments and the Seismic Rock Mechanics Projects. Final reports for both of these projects have been produced recently, and both projects are undergoing external peer review (Sridhar et al., 1995, Hsiung et al., 1995). At the completion of the peer review, these reports will be published as NUREG/CR documents.

All research projects at the CNWRA are sponsored by the Nuclear Regulatory Commission (NRC) to fulfill its mandate under the Nuclear Waste Policy Act, as amended. To understand the role of NRC-funded research, it is important to recognize that the NRC regulatory responsibilities are distinct from those of the U.S. Department of Energy (DOE), which is responsible for siting, constructing, and operating a repository for the permanent disposal of high-level waste (HLW). The DOE has undertaken the development and implementation of a broad range of techniques and methods to obtain information and to produce analyses necessary to determine site suitability, design the engineered portions of the repository, and complete a license application for review by the NRC. In fulfilling its responsibilities for assuring the radiological health and safety of the public, the NRC conducts confirmatory and exploratory (also referred to as anticipatory) research to:

- Develop the licensing tools and technical bases necessary to judge the adequacy of the DOE license application
- Ensure a sufficient independent understanding of the basic physical processes taking place at the proposed geologic repository site
- Maintain an independent, but limited, confirmatory research capability to be used in evaluating DOE preclicensing and license application submittals

Figure 1-1 depicts the basic relationship between the NRC research program and licensing needs. Regulations applicable to the licensing of a HLW repository (primarily 10 CFR Part 60) are translated into regulatory requirements, each of which must be met before the NRC staff can recommend the issuance of a license. Strategies and methods for determining if the DOE demonstration of compliance with the regulatory requirements is acceptable are currently being developed and documented in the NRC License Application Review Plan (LARP) (Nuclear Regulatory Commission, 1994). Key technical uncertainties (KTUs) are defined based on the risk to compliance determination and repository performance. Evaluation and reduction of those aspects of the KTUs that are the NRC responsibility are the primary objectives of the research undertaken by the NRC. Each chapter of this report outlines the specific KTUs being addressed by the research described in that chapter.

Each research project discussed herein has been conducted in accordance with approved research project plans, which were developed consistent with an associated NRC statement of work. These plans establish the project objectives, technical approach, justification, deliverables, and funding for each of

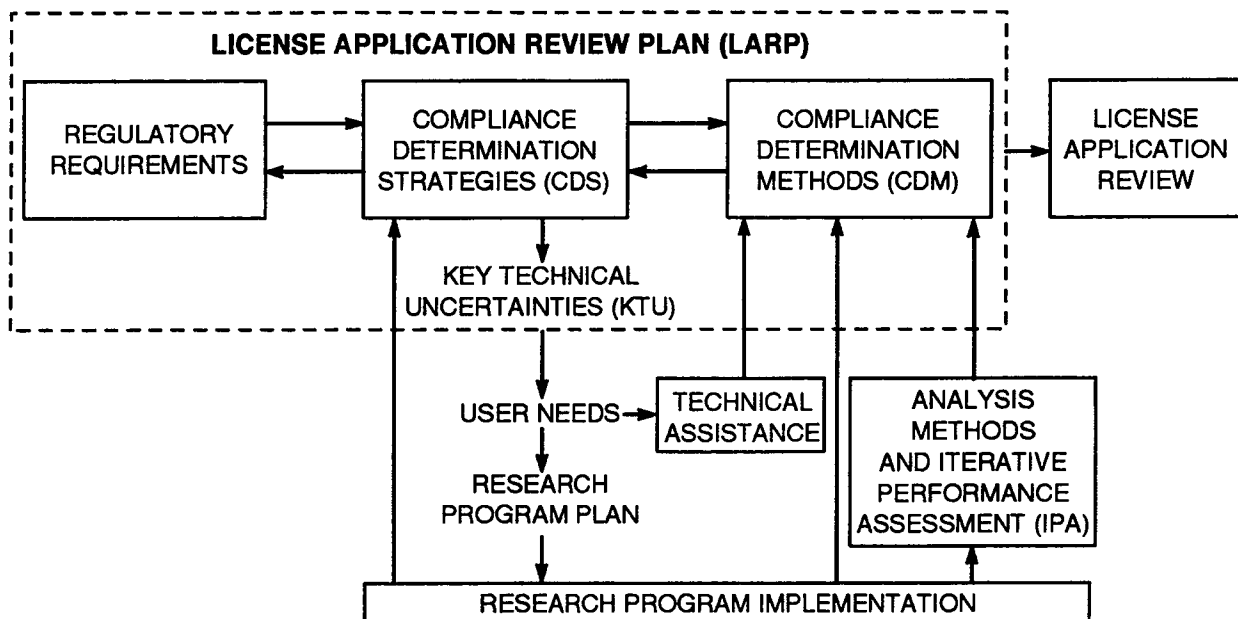


Figure 1-1. Relationship of the NRC HLW Research Program to licensing needs

the studies. They also describe the interrelationships among the various projects, which provide a sound basis for integrating research results across disciplines.

This executive summary covers, in capsule form, the progress of each research project over the past 6 mo. The executive summary is followed by Chapters 2 through 10, representing each of the nine currently active research projects (excluding two that are near completion, as noted above). Project objectives and a report of research activities and results to date, as appropriate, are given in each chapter. The progress toward fulfillment of identified research needs and the development of particular regulatory products are addressed in cases where such progress has been significant. In addition, commentary is provided on anticipated progress for each project in the ensuing 6-mo period.

1.2 GEOCHEMICAL ANALOG OF CONTAMINANT TRANSPORT IN UNSATURATED ROCK

The central objective of the Geochemical Natural Analog Research Project is to develop an understanding of the utility and limitations of natural analog studies used to support a license application for a HLW repository and to provide fundamental data on the long-term behavior of HLW within a repository environment. Natural systems that have existed for periods comparable to that required for HLW disposal (i.e., 10^3 – 10^4 yr and greater) provide an opportunity to obtain observational knowledge of the long-term behavior of HLW components. Such information is important for support of long-term predictive models of repository performance. This report describes recent results of analog research at the Nopal I uranium (U) deposit in the Peña Blanca district, Chihuahua, Mexico.

Migration of radionuclides along fluid-conducting fractures in the host rock of a geologic repository for HLW is one mechanism by which hazardous radionuclides can be transported to the accessible environment. Retention of radionuclides in or on minerals deposited in fractures is a potentially important retardation mechanism. At the Nopal I U deposit, an association has been noted between anomalous U in the surrounding, fractured host rock and secondary non-U mineral occurrences. On the Level +10 surface of Nopal I, a major fracture (hereafter referred to as the 13.5 m N fracture) that crosscuts the orebody contains fracture-infilling minerals. Outside the orebody, these minerals have much higher U concentrations than the surrounding rock. The processes by which secondary non-U minerals within this fracture retain U and, thus, retard its migration are the focus of this report. Infilling materials from this fracture were selected for detailed analyses including: (i) mineralogic and petrographic characterization; (ii) U, Th, and trace element distributions; and (iii) U-series isotopic measurements.

Pyrite and kaolinite in the 13.5 m N fracture are interpreted, based on textural evidence from petrographic examination, to be the primary mineralization. Oxidation of pyrite has led to the following relative sequence of formation of secondary minerals within the 13.5 m N fracture: goethite—amorphous Fe-oxyhydroxide—hematite—jarosite. Anomalous U concentrations (i.e., several hundred to several thousand ppm U) measured in goethite, hematite, and amorphous Fe-oxyhydroxide indicate that these secondary minerals are capable of retaining U. Very high *in situ* U contents within these Fe phases and the absence of U minerals within the fracture, even at the nanometer scale, suggest that U was coprecipitated in secondary minerals. U mobilization and transport away from the deposit is suggested by decreasing U concentrations measured in bulk fracture-infilling and in goethite and hematite with progressively greater distance from the deposit. U within the deposit was most likely mobilized and transported away from the deposit by episodic infiltration of meteoric water.

$^{234}\text{U}/^{238}\text{U}$ radioactive disequilibrium analyses of bulk fracture-infilling samples collected along the 13.5 m N fracture indicate U mobilization within the last 1 Ma. All fracture-infilling samples have greater than unity $^{234}\text{U}/^{238}\text{U}$ activity ratios, which is indicative of U uptake from fracture fluids that carried excess ^{234}U . Systematic decreases in $^{234}\text{U}/^{238}\text{U}$ activity ratios with distance from the deposit margin suggest a multistage U mobilization process. Two possible scenarios are offered to explain the $^{234}\text{U}/^{238}\text{U}$ trend: (i) remobilization of U from ^{234}U -enriched infill minerals and (ii) differential transport of U-bearing solutions containing excess ^{234}U away from the deposit. Like $^{234}\text{U}/^{238}\text{U}$, $^{230}\text{Th}/^{234}\text{U}$ activity ratios of bulk fracture-infilling samples are all greater than unity. The excess ^{230}Th may result from remobilization of U from infill minerals after ^{230}Th ingrowth or preferential sorption of ^{230}Th generated by dissolved ^{234}U .

The data reported here add to the understanding of a system in which radionuclides have been available for transport under conditions comparable to those anticipated for the candidate Yucca Mountain (YM) HLW repository. The NRC Iterative Performance Assessment (IPA) program has identified retardation associated with fracture flow as an important aspect; however, uncertainties remain as to the proper implementation of fracture transport and fracture retardation in transport models. Results reported here have identified specific mineral phases that have retained transported U under YM-comparable conditions. Likely processes by which U was mobilized, transported, and retained by secondary mineral assemblages at the Nopal I U deposit have been identified. These results will help reduce conceptual uncertainties regarding U transport in future versions of performance assessment models.

1.3 SORPTION MODELING FOR HIGH-LEVEL WASTE PERFORMANCE ASSESSMENT

The broad objective of this project is to develop sufficient understanding of radionuclide transport so that timely prelicensing guidance can be provided to the DOE and a sound basis is available for evaluating the DOE license application. To develop such an understanding of radionuclide sorption processes and the important physical and chemical parameters that affect sorption behavior in the YM environment, experiments are being conducted to investigate the sorption behavior of actinides on geologic media. Experiments were performed to determine the effects of pH, partial pressure of CO₂(g), and initial neptunium concentration on the sorption of neptunium(V) onto quartz, clinoptilolite, and montmorillonite, minerals representative of both matrix and fracture-lining minerals at YM. Experiments were also conducted to determine the extent to which plutonium oxidation states in solution could be characterized, given the present analytical capabilities at the CNWRA.

Because of its long half-life (2.14×10^6 yr), suspected high radiotoxicity, occurrence in HLW, and reportedly low sorption characteristics, ²³⁷Np is a particular concern to the safety suitability of YM as a repository. However, uncertainties remain with respect to the magnitude of neptunium sorption over the pH range of natural groundwaters (~6–9). Neptunium(V) sorption experiments were conducted over a pH range of 5–10.5 using ²³⁷Np as the radionuclide of interest. Experimental solutions were allowed to equilibrate with atmospheric CO₂ or, alternatively, were capped tightly to prevent exposure to atmospheric CO₂, resulting in low CO₂ conditions. The results show that, for all three minerals, neptunium(V) sorption is strongly influenced by solution pH. Little or no sorption is observed below pH about 7, but as pH increases so does neptunium(V) sorption. For solutions in equilibrium with atmospheric CO₂, neptunium sorption increases until about pH 8–8.5 where it reaches a maximum; as pH continues to increase, neptunium(V) sorption decreases to near zero by pH 9.5. For the capped solutions, which are undersaturated with respect to atmospheric CO₂, neptunium(V) sorption increases continuously as pH increases, with the maximum sorption observed at the maximum pH studied (~10.5). The difference in neptunium(V) sorption behavior caused by differences in the amount of CO₂ present is likely due to formation of neptunyl-carbonate complexes in solution. At higher pH, these complexes are calculated to become the dominant neptunyl species in solution about pH 8.5. In the case of montmorillonite, though sorption reached a minimum at the pH values described above, neptunium(V) sorption did not reach zero. It is postulated, through comparisons of results from previous studies, that ion exchange of NpO₂⁺ for Na⁺ occurs in the montmorillonite at pH below 7. Interestingly, although the minerals studied exhibit considerably different surface characteristics (e.g., pH of zero surface charge), the pH-dependent neptunium(V) sorption behavior described is similar for all three. This observation parallels those made during studies of uranium(VI) sorption onto mineral surfaces and suggests that solution chemistry may play the most important role in influencing the sorption behavior of actinides.

Largely due to its complex, multivalent redox chemistry, much uncertainty remains regarding the sorption behavior of plutonium in a repository environment. Available data are insufficient to estimate sorption coefficients with any degree of confidence. Moreover, data on plutonium sorption coefficients and their sensitivities to chemical conditions would be incomplete without information on the distribution of different plutonium species or, at a minimum, the different oxidation states, in minerals and solution. Consequently, it was decided that an attempt would be made to track plutonium oxidation states under conditions similar to those expected for plutonium sorption experiments. Solutions were prepared with ²³⁹Pu in different oxidation states following published chemical or electrochemical methods. Attempts were then made to analyze the solutions using established solvent extraction, spectrophotometric, and

liquid scintillation counting techniques. Results indicated that the solvent extraction techniques were unreliable for determination of plutonium oxidation states at the low concentrations of interest ($\sim 10^{-8}$ M, due to solubility constraints). As a result, access to or acquisition of other methodologies (e.g., photoacoustic spectroscopy) or further refinement of existing techniques must occur before experiments investigating the sorption behavior of plutonium can begin in earnest. Concurrent experiments investigating the sorption of plutonium onto proposed experimental container materials showed that polycarbonate was an acceptable medium to use in future experiments.

Results of the laboratory experiments and modeling activities provide the CNWRA with an understanding of the important parameters that control the sorption behavior of an actinide element. Because of the strong dependence on solution chemistry (including oxidation state and presence of CO_2) and surface site concentration, modeling of sorption processes will likely require that changes in groundwater chemistry and in rock/fluid ratio be properly accounted for in PA calculations if retardation by sorption processes is included. The success of surface-complexation models (SCMs) in describing and predicting actinide sorption onto minerals suggests that SCMs offer a scientifically defensible approach that may be useful for PA calculations.

The similarity in the pH-dependence of actinide sorption on different minerals is important. It may help to identify simplified approaches to modeling sorption and thus facilitate in the development of compliance determination methods relevant to KTUs identified in LARP Section 3.2 and in developing models related to the PA Research Project and IPA Phase 3. Moreover, by developing data on the expected magnitude of actinide sorption under relevant groundwater conditions, realistic bounding values for sorption may be input to future repository performance assessments.

1.4 PERFORMANCE ASSESSMENT RESEARCH

Three top-level objectives are being pursued in this research project. The first of these objectives is to provide essential modeling technology for use in the NRC IPA activity and in the application of the total-system Compliance Determination Methods. A second, and equally important, objective is to focus research on the KTUs identified in Chapter 6 of the LARP, which are also part of the NRC Vertical Slice Key Technical Issues. The third top-level objective is to provide the technical basis for formulating guidance to the DOE in the specific areas of PA modeling approaches with emphasis on aspects related to disruptive event scenarios and model validation.

Studies conducted under the PA Research Project are divided among three interrelated tasks: Task 1—Conceptual Model Development; Task 2—Computational Model Development; and Task 3—Model Evaluation. During this reporting period, research was conducted in all three major tasks. As part of Task 1, for example, hydraulic properties for tuff cores were used in model predictions for a proposed infiltration experiment at the Peña Blanca field site. A second study under Task 1 produced a new conceptual and mathematical approach for describing radionuclide adsorption in saturated porous media. Under Task 2, research was performed on advanced computational and computer methods. A new computational method was developed for solving the nonlinear equation for flow in unsaturated media, and a preliminary evaluation was conducted of the Parallel Virtual Machine technology. The advanced computational and computer methods are expected to enhance the IPA analysis capability. As part of Task 3, benchmark testing of DOE and NRC/CNWRA thermohydrologic codes was performed using a series of challenging test cases. Work was also performed on preparation of NUREG/CR reports and journal

articles on previously completed research activities. Two research activities, conducted as part of Tasks 1 and 2, are highlighted in this report. Summaries of these activities are given below.

Under Task 1, a new methodology for modeling radionuclide adsorption in saturated porous media was developed that represents an improvement over the classical retardation factor approach. The new approach is superior in that it (i) accounts for radionuclide competition for sorption sites and (ii) permits the consideration of spatially variable sorption and flow parameters. Competition for sorption sites means that dissolved radionuclide species compete for the available and fixed number of sites. Thus, as one radionuclide species dominates the utilization of available sorption sites, the sorption of other species is in essence blocked. The net effect is that some typically strongly sorbing radionuclides exhibit enhanced mobility. Illustrative transport calculations are presented for the case of ^{239}Pu and ^{238}U , which show the impact of sorption competition on radionuclide concentrations. This new methodology is expected to be used in the IPA Phase 3 exercise for YM.

As part of Task 2, a new computational technique was developed for solving the nonlinear governing equation for variably saturated flow in porous media. This equation is the basis for a number of NRC/CNWRA computer codes that are being extensively used to: (i) forecast infiltration and deep percolation rates for various climatic conditions, (ii) estimate water fluxes through the repository, and (iii) calculate groundwater travel times from the repository to the accessible environment. The new technique, which uses a simple transform, is a significant contribution because it provides more robust and computationally efficient computer calculations. To test the capability of the new technique, it has been applied to simulations of variably saturated flow using data from the YM, Hanford, and the Idaho National Engineering Laboratory sites. One illustrative application is presented which uses DOE/U.S. Geological Survey data for borehole UZ-16. The simulation results obtained using the new method were generated on an IBM PS/2 in about 3 minutes CPU time for a 241-node grid and time-marching to steady state. In contrast, previous attempts to simulate this problem with existing finite-difference codes utilizing conventional computational techniques failed to provide convergent results in a practical length of time.

1.5 VOLCANIC SYSTEMS OF THE BASIN AND RANGE

Characterization of the frequency and nature of past volcanic events in the Yucca Mountain Region (YMR) and assessment of the probability and consequences of future volcanism are critical aspects of prelicensing scientific investigation. The technical objectives of the Volcanic Systems of the Basin and Range Research Project are to (i) assess the probability of continued magmatic activity in the YMR, (ii) develop models that better predict the interaction between structure and volcanism in this tectonic setting, and (iii) develop scenarios for the impact of volcanism on the YM repository. Effective review of the Department of Energy license application will require insight into volcanic processes operating in the YMR on several scales. Investigations into the scale of volcanic processes includes assessment of: Western Great Basin (WGB) tectonic and structural controls on volcanism on local scales (10^2 to 10^3 km²), the longevity of cinder cone clusters and individual volcanoes in the WGB, and the relationship between specific mappable faults, joints, and fractures, and volcanic conduits, such as dikes and dike swarms. The WGB has been the site of recurring small-volume basaltic volcanism throughout the Quaternary. Modern analogs and theoretical studies have demonstrated convincingly that this activity encompasses a variety of eruption styles. The Volcanic Systems of the Basin and Range Research Project has been designed to assess the probability of future volcanism in the YMR, taking into account the range of activity and structural controls on activity that are an inherent part of WGB volcanism.

To test the applicability of methods for estimating the recurrence rates of volcanic events, a spatio-temporal near-neighbor model is used to identify and map variations in recurrence rate of volcanism in the Springerville Volcanic Field (SVF), Arizona; a large basaltic volcanic field along the southern boundary of the Colorado Plateau. Detailed mapping of individual lava flows and their associated vents, together with radiometric and paleomagnetic dating, demonstrates that 366 volcanic events produced the SVF. These volcanic events are represented by mapped eruptive units between 2.1–0.3 Ma over an area of 3,000 km². From data associated with the volcanic events, it appears that the SVF experienced waxing rates of vent formation prior to ≈ 1.0 Ma, near steady-state rates of vent formation during ≈ 1.0 –0.5 Ma, and waning rates of vent formation since ≈ 5 Ma. The highest rate of vent formation at ≈ 1.5 –1.0 Ma correlates with a shift in the locus of magmatism from west to east in the SVF and an increase in magma alkalinity. Magma output at uniform rates can be inferred from lava flow areas for 1.75–0.75 Ma. A spatio-temporal recurrence rate model with a 0.5-m.y. time window and seven near-neighbors reveals that areas of waxing and waning magmatism in the SVF are much more localized, and volcanic activity within these areas is much more intense than implied by broad temporal trends. Volcano clusters are 10–20 km in diameter and are commonly active for less than 0.25 Ma. This clustered and petrologically distinctive, rather than distributed or random, volcanic activity suggests that individual magma source regions also are localized and short-lived compared with the area and longevity of the entire field. Because volcanic activity is spatially and temporally clustered, forecasting subsequent activity is more successful using the spatio-temporal model than using average recurrence rates. This success indicates that spatio-temporal recurrence rate models are useful tools for the quantification of long-term patterns in volcanism in the SVF and should be applicable to YMR.

1.6 TECTONIC PROCESSES IN THE CENTRAL BASIN AND RANGE REGION

Geologic structure, structural deformation, and tectonic processes are important to long-term repository performance and preclosure operational safety. Tectonic processes represent potentially adverse conditions if they are characteristic of the controlled area or may affect isolation within the controlled area [10 CFR 60.122(c)]. The principal technical objectives of the Tectonics Research Project include: (i) compiling and integrating tectonic data for the central Basin and Range and YM regions, and (ii) developing and assessing models of tectonic processes in those regions. Of particular concern is the adequacy of existing and anticipated data for evaluating compliance with quantitative waste-isolation performance objectives. Information concerning models of tectonic processes (e.g., patterns and rates of historic and prehistoric faulting and seismicity) and structural features will be necessary to assess compliance with specific regulatory requirements as documented in LARP Sections 3.2.1.5 through 3.2.1.9 and 3.2.2.8. Important goals of the Tectonics Research Project include development and analyses of alternate tectonic models, evaluation of potential hazards due to fault displacement and seismic shaking, and initiation of field studies to address tectonic issues.

Significant accomplishments include: (i) collection and analysis of data to constrain the horizontal axis rotation of Bare Mountain (BM); (ii) generation of a partially restorable cross section through BM; (iii) construction of a new partially restorable subregional cross section that extends from the Bullfrog Hills across BM, Crater Flat, YM, Jackass Flat, and Little Skull Mountain; (iv) development of alternative models for the subsurface linkage between the Bare Mountain Fault (BMF) and the YM and Crater Flat faults; (v) preliminary paleomagnetic analyses that assist in constraining the amount and timing of rotation of BM around a vertical axis; (vi) analysis of apatite fission tracks to constrain the uplift history of BM; (vii) analyses of alluvial fan sedimentation patterns on the east and west sides of

BM that constrain the relative amounts and timing of motion on the BMF; (viii) field work to evaluate key structural elements that are used to constrain the regional tectonic setting of YM; (ix) construction of a structural analog deformation laboratory; (x) submittal of an article on slip-tendency analysis and fault reactivation to be considered for publication in *Geology*; (xi) submittal of an article that compares two calcite-twin based differential stress estimation techniques to be considered for publication in the *Journal of Structural Geology*; and (xii) submittal of a copyright application for the 3DSTRESS computer program, with which slip- and dilation-tendency analyses are performed. The first five items in the above list are the primary focus of this report.

There is considerable uncertainty regarding the three-dimensional (3D) structure and structural evolution of YM that is of direct importance for: (i) evaluation of potential earthquake sources; (ii) identification of faults that could trigger slip on YM faults; (iii) recognition of potential pathways for basaltic magma ascent; (iv) identification and characterization of potential barriers and fast pathways for groundwater flow; and (v) characterization of regional hydrostratigraphic units. Studies in tectonic research have been undertaken to develop and evaluate alternative models for the tectonic and neotectonic setting and structural evolution of YM. The BMF may be of major importance to YM in that it may link with YM faults at depth. There is evidence for late Quaternary to Holocene slip on splays of the BMF exposed in alluvium, but there is no consensus as to the amount or precise timing of this slip. Geometric modeling has been undertaken to determine the viable range of potential models for the tectonic development of BM. Paleomagnetic studies are being used to constrain the vertical and horizontal axis rotation of BM.

Two end-member models of fault linkage between BM and YM are possible. The first model assumes that the faults of YM developed as part of the Bullfrog Hills detachment system (BHDS) during the Miocene and were subsequently isolated by the rise of the BM and displacement of the BHDS by the BMF. The second model assumes that the east-directed BMF system generated the YM faults as antithetic faults in its hangingwall. Hybrids of these two end members are also geologically permissible. For example, YM faults may have originated as part of the BHDS, but may continue to accumulate slip because they are optimally oriented to accommodate antithetic shear in the hangingwall of the more recently active BMF. Knowledge of the precise nature of the linkage between the BMF and faults in its hangingwall is critical to assessing seismic and aseismic slip risks posed by the faults of YM.

Paleomagnetic analyses of an Oligocene dike and a fold in the Antelope Valley Formation in BM show that characteristic magnetization does not deviate from the expected directions for southwestern Nevada. If these preliminary results are confirmed by future work, then BM apparently has not rotated about a vertical axis since at least the Early Triassic and perhaps not at all. This possibility is in dramatic contrast to the current interpretation of approximately 90° clockwise rotation proposed by Snow (1994) and Snow and Prave (1994). More importantly, these results indicate that the Paleozoic carbonates, especially the Antelope Valley Formation, as well as the Cenozoic igneous rocks on BM are worthwhile candidates for more extensive paleomagnetic research. Preliminary paleomagnetic results also indicate the occurrence of an extensional faulting event that predates the magnetization of Oligocene dikes, but may postdate the Permian remagnetization of the Paleozoic carbonates on BM.

The Conejo Canyon and Fluorspar Canyon Faults in northwestern BM can be considered as part (possibly the bounding faults) of an anastomosing set of extensional detachments that stripped the pre-Tertiary miogeoclinal sequence and the Tertiary volcanic section westward from above the current surface of BM. The question of sense of displacement on the Conejo Canyon Fault system is of importance to the interpretation of the tectonic evolution of YM faults. If faults at YM developed as a part of the BHDS

that experienced only incipient extension during the Miocene, then they probably sole into subhorizontal detachments at or below the base-Tertiary unconformity. If the Conejo Canyon and associated faults are part of this west-directed (top to the west) Miocene detachment system, they represent the only well-exposed example of this deep detachment, and their characteristics may provide insight into the crustal levels at which this system developed.

New tectonic models and interpretations developed this period will aid in addressing two KTUs: (i) uncertainty in determining the 3D structure and tectonic setting of YM, and (ii) uncertainty in determining slip history of faults. In addition, these results are expected to be useful in evaluation of potential sources of seismicity, characterization of faults that could trigger slip on YM faults, identification of potential barriers or fast pathways for groundwater flow, and characterization of regional hydrostratigraphic units.

1.7 FIELD VOLCANISM

The basic objective of the Field Volcanism Research Project is to address some of the KTUs related to estimating effects of basaltic igneous activity on repository performance. Activities include investigations of the: (i) mechanics of basaltic eruptions, (ii) extent and characteristics of shallow hydrothermal systems and diffuse degassing associated with basaltic volcanoes, and (iii) nature of basaltic intrusive geometries in the shallow subsurface. Successful completion of the Field Volcanism Research Project, which began in April 1993, will require study of Neogene to Quaternary basaltic volcanoes in the western Great Basin and comparison with historically active basaltic volcanoes located elsewhere. The KTUs related to the Field Volcanism Research Project are (i) determining the consequence of igneous activity for repository performance, and (ii) determining the probability of igneous activity and resulting disruption of the candidate repository.

Activities designed to address issues related to the probability and consequence of igneous activity in the YMR that have been initiated or completed include:

- Field work at Cerro Negro volcano, Nicaragua, during the June 1995 eruption
- Detailed sampling and analysis of pyroclastic fall deposits from Lathrop Wells volcano, Nevada
- Compilation and preliminary analysis of soil-gas studies conducted between 1992 and 1994 at Cerro Negro, Nicaragua; Tolbachik, Russia; and Parícutin, Mexico volcanoes

Cerro Negro volcano, Nicaragua, is the site of the most recent small-volume basaltic eruptions at a cinder cone in the western hemisphere. These eruptions occurred in April 1992 and May–June 1995. Many previous eruptions of Cerro Negro were well documented and provide important information on the dynamic nature of basaltic cinder cone volcanism. Cerro Negro first erupted in 1850, with at least 20 documented eruptions occurring up through 1994. The current eruption of Cerro Negro began on May 24 with increased seismicity at and up to 15 km around the volcano and continued through May 28. Ash plumes to about 100 m high were first observed on May 28, with periodic eruptions occurring once or twice per hour. The eruptions correlated with periods of increased seismic activity. On June 1, the seismicity increased in frequency and intensity, with eruptions occurring about every 15 min. The preliminary conclusion that the May–June 1995 eruptions are dominantly phreatic (i.e., no new magma

erupted) is supported by continued analysis of the eruption and associated products. Ash deposits have an average grain size of about 0.1 mm and consist primarily of fragments of plagioclase, olivine, and pyroxene, with subordinate amounts of finely fragmented basalt; no juvenile (i.e., magmatic) basalt has been observed. Eruption repose times average 8 ± 5 min with no discernable correlation between observed column height and repose time. Ejection velocities of decimeter- to meter-sized blocks are about $100 \text{ m} \cdot \text{s}^{-1}$. These features are characteristic of dominantly phreatic activity. These data are expected to be used in performance assessment models to estimate the consequences (i.e., direct effects) of airborne releases resulting from volcanic eruptions.

Soil-gas radon samples collected in June 1995 at Cerro Negro have been processed and compared with samples from March and June 1994 studies. All three studies occurred in the same general areas around Cerro Negro, with many sample sites duplicated between studies. Background levels of about 2 pCi l⁻¹ were detected in March 1994, rising to about 17 pCi l⁻¹ in June 1994. In contrast, background concentrations were greater than 20 pCi l⁻¹ in June 1995, with anomalies characterized by order-of-magnitude increases in radon concentration relative to anomalies in previous studies. Soil mercury samples are being analyzed. These data are expected to be useful in modeling gas movement induced by volcanic eruptions and to assess indirect effects (e.g., accelerated corrosion) of volcanic gases on engineered barrier performance.

The May-June 1995 eruption of Cerro Negro was likely initiated by the injection of fresh basaltic magma to shallow levels at the volcano. This magma is required to produce the heat necessary to drive the steam-blast phreatic eruptions and to cause the observed increase in soil-gas flux. Thermal and soil-gas anomalies associated with the eruption extend for at least 0.75 km away from the vent, along major structural trends. Products of this eruption have an extremely low preservation potential in the geologic record. Cerro Negro has had at least 20 observed eruptions since formation in 1850, several of which were dominantly phreatic. This information will be useful in developing realistic models of volcanic eruptions which persist for 100 yr and exhibit multiple thermal and degassing pulses.

One of the main tasks in the Field Volcanism Research Project is to develop methods to determine eruption explosivities for basaltic volcanoes of the YMR. Many of the methods commonly used to determine eruption explosivities cannot be applied to YMR volcanoes due to the poor preservation of the eruption products. However, grain-size parameters of pyroclastic fall deposits often are used to determine eruption explosivities, although previous CNWRA research has shown several important limitations to these methods. The Lathrop Wells YMR volcano has incompletely preserved fall deposits up to 2.4 km away from the central vent. Of these deposits, 40 samples have been analyzed and compared to similar deposits from the Tolbachik volcano. Surprisingly, grain-size parameters from both of these volcanoes are very similar. Although there are currently no robust parameters to distinguish between normal strombolian and higher energy magmatic eruptions, the relative decrease in median diameter and sorting observed in both the Lathrop Wells and 1975 Tolbachik deposits may be controlled by eruption energetics. Future work will focus on developing more robust estimators of eruption explosivity through petrographic characteristics of scoria deposits at historically active and YMR volcanoes.

1.8 REGIONAL HYDROGEOLOGIC PROCESSES OF THE DEATH VALLEY REGION

The YM has been proposed as a potential site for a high-level nuclear waste repository, in part because of the favorable geochemical and hydrologic environment provided by its 700-m thick unsaturated

zone. Siting the repository in the unsaturated zone may significantly reduce the potential for waste canister corrosion and subsequent dissolution of the waste form. Moreover, the low water flux that is presumed to exist in the unsaturated zone reduces the likelihood that dissolved radionuclides would be rapidly transported to the accessible environment. Mechanisms that may saturate the repository horizon, and thus compromise favorable conditions provided by the YM site, include rapid infiltration of water from the surface through highly conductive fracture networks and an increase in the elevation of the regional water table. The first mechanism is being addressed in depth by the research project on Subregional Hydrogeologic Flow and Transport Processes. Elevation of the water table may occur due to increased recharge to the regional carbonate system along stream channels and mountain fronts in topographically closed basins 100 km to the north and northeast of YM, or by neotectonic disruption of structural or stratigraphic features that control the steep hydraulic gradient north of YM. Even if the elevation of the regional water table does not result in saturation of the repository block, the reduced thickness of the unsaturated zone has the potential to diminish travel times within the vadose zone. In addition, travel times in the saturated zone and the location of potential discharge areas for dissolved radionuclides down gradient from YM are performance-related issues addressed by this research project. The primary objectives of this research project are to: (i) analyze existing conceptual models and develop new conceptual models of the regional hydrogeologic flow regime in the Death Valley region that contains YM, and (ii) construct numerical models of regional flow that may be used to assess the potential for the water table beneath YM to rise in response to wetter climatic conditions or neotectonic disruption of hydraulic barriers.

The saturated zone feature that may have the greatest potential to compromise the performance of the repository is the presence of a relatively steep hydraulic gradient (0.15) located at the northern extreme of the perimeter of the proposed YM repository. If this steep hydraulic gradient is formed by the juxtaposition of high- and low-permeability units across a fault zone, there is concern that future tectonism may alter the flow across the fault and permit water levels to rise beneath YM. Numerical modeling studies suggest that disruption of the hydraulic barrier that forms the steep hydraulic gradient may cause a water table rise of 275 m beneath YM. Inasmuch as current construction plans call for the repository to be located approximately 300 m above the water table, a 275-m water table rise would dramatically decrease unsaturated zone travel times and may cause the repository to fail to meet the overall system performance standards. Several researchers have noted that the steep hydraulic gradient at YM appears to be part of a regional hydraulic feature that extends from just northeast of Bare Mountain, eastward to Shoshone Mountain, northward along the Eleana Range, and then eastward across Oak Spring Butte, at the north of Yucca Flat, and into the Groom Lake area. The steep eastward hydraulic gradient between the Eleana Range and Yucca Flat is due to thrust faulting that has placed portions of the highly permeable Paleozoic carbonate aquifer over the low-permeability argillite units of the Eleana Formation (upper clastic aquitard) and thus effectively compartmentalized the Paleozoic carbonate aquifer. Whether a similar geologic structure is responsible for the steep hydraulic gradient north of YM is an open question.

During this period, progress was made toward the development of alternative conceptual models of the steep hydraulic gradient at YM and the regional-scale steep hydraulic gradient. A hydrostratigraphic cross section was constructed that extends from the Eleana Range, east-southeast to the Las Vegas Range. Major structural features included in this cross section are the Belted Range Thrust to the northwest and the CP Thrust to the east-southeast. Where the Belted Range Thrust has led to a thick section of the lower clastic confining unit (LCCU) being placed above the lower carbonate aquifer (LCA), a relatively steep hydraulic gradient is predicted using a simplified flow model. Where the west-vergent CP Thrust has placed a small portion of the LCCU over the LCA and the upper carbonate

aquifer, a second relatively steep hydraulic gradient is predicted by the flow model. In the region between the Belted Range and CP Thrusts, the LCA attains its maximum thickness, which results in a comparatively mild hydraulic gradient. While the assumptions made in the construction of the flow model preclude determining the actual location of the free surface, the computed hydraulic head profile does provide an estimate of the horizontal variation of the vertically averaged head. The model therefore suggests that one plausible explanation for the cause of the regional steep gradient is the presence of the Belted Range or CP Thrusts. By extrapolation, one may also infer that the same structural features, buried beneath a thick sequence of Tertiary volcanics, may cause the steep gradient at YM.

1.9 SUBREGIONAL HYDROGEOLOGIC FLOW AND TRANSPORT PROCESSES

Research requirements dealing with such site characteristics as groundwater travel time (GWTT), favorable conditions (FACs), and potentially adverse conditions (PACs) relate to support of the NRC staff LARP. For example, understanding the subregional (site) and regional hydrogeology is required in order to determine the GWTT in the unsaturated and saturated zones. Other processes and phenomena of importance include, but are not limited to, the potential for flooding of the repository as a consequence of water table rise from meteorological or climatic changes, volcanism, or faulting. Furthermore, it will be necessary to assess the inherent variability and distribution of hydrogeologic and transport properties, initial and boundary conditions, hydro-geostratigraphic unit interfaces, location and characterization of structural features that significantly affect water and vapor movement, and coupled effects modeling strategies used by the DOE to support estimation of GWTT and moisture fluxes.

In the NRC LARP, these research requirements are expressed in the context of several KTUs that are influenced by, or pertain to, various subregional hydrogeologic flow and transport processes. These KTUs deal with: (i) Uncertainty in Determining Effects of Structural Deformation and Tectonic Processes on the Flow and Transport of Groundwater, (ii) Uncertainty in Identifying Geochemical Processes and Conditions That Affect Radionuclide Retardation and Determining and Predicting the Magnitude of the Effects at Yucca Mountain, (iii) Uncertainty in Developing a Conceptual and Mathematical Model for Transport of Vapor and Liquid Phase That is Representative of the Yucca Mountain Site Flow System, (iv) Uncertainty in Prediction on Future Changes to the Hydrologic System Resulting from a Combination of Climatic and Tectonic Changes and Human Activities (Including Heat Effects from Waste Emplacement and Future Groundwater Withdrawals), (v) Uncertainty in Determining the Fastest Path of Likely Radionuclide Travel From the Disturbed Zone to the Accessible Environment, (vi) Predicting Precipitation and Temperature (Climate) at the Yucca Mountain Site for 10,000 yrs into the Future, (vii) Uncertainties Associated with Variability of Model Parameter Values, and (viii) Uncertainties Associated with Development and Validation of Conceptual and Mathematical Models.

The research conducted under the Subregional Hydrogeologic Flow and Transport Processes Research Project is in direct response to NRC staff-identified research needs, supporting portions of the NRC LARP related to the review of the DOE site-scale groundwater flow and transport studies. The anticipated products of this research project will have a direct application to the LARP in the areas of: (i) evaluating overall system performance; (ii) appraising performance of the geologic setting; and (iii) determining compliance with various siting criteria (i.e., PACs and FACs). In particular, the Subregional Hydrogeologic Flow and Transport Processes Research Project deals with issues identified in the LARP sections on assessment of compliance with FACs and PACs for the hydrologic system (including 3.2.2.1—Nature and Rate of Hydrogeologic Processes; 3.2.2.4—Unsaturated Zone

Hydrogeologic Conditions; 3.2.2.3—GWTT Substantially Exceeding 1,000 yr; 3.2.2.9—Changes to Hydrologic Conditions; 3.2.2.12—Perched-Water Bodies; and 3.3—Assessment of Compliance with the GWTT Performance Objective). This research project will also contribute significantly to the execution of the Vertical Slice Implementation Plans, and in particular to resolution of the Key Technical Issue on “Location and Characterization of Structural Features which Significantly Affect Water and Vapor Movement.”

The activities of this research project address groundwater flow and transport assessment for selected technical issues associated with the following: (i) infiltration and recharge (both focused and distributed) processes, (ii) conditions and properties that contribute to perched-water zone development, (iii) thermally driven vapor-phase transport processes including coupled effects, and (iv) temporal and spatial distributions of initial and boundary conditions for site and repository-scale modeling.

During this period, research efforts have focused on: (i) developing approaches for evaluating uncertainties inherent in Geological Framework Models (GFM) of the YM site; (ii) continually updating the CNWRA databases, and associated models, with geological and hydrogeological information; (iii) developing an infiltration evaluation methodology, based on Geographic Information System technology; (iv) compiling, evaluating, and combining available isotopic and geochemical data with the existing 3D GFM for the YM site; (v) combining surface complexation models with mass transport; (vi) enhancing the numerical code CTOUGH so that it can handle atmospheric interactions in a computationally efficient manner; (vii) conducting a peer-review of the Project Plan; and (viii) interacting with the University of Arizona NRC contractors and coordinating the field studies at the Apache Leap Test Site (ALTS).

Specifically, image-processing techniques have been implemented for the evaluation of the realism and inherent uncertainty in iterative enhancements of GFM at YM. The methods developed can be applied to: (i) constrain the geologic units comprising the model of YM, (ii) provide the necessary framework over which geostatistical variability can be incorporated into the CNWRA GFM, and (iii) evaluate the unit outcrop spatial distributions which feed directly into an infiltration evaluation methodology. The GIS-based infiltration evaluation methodology has been developed, and a series of infiltration sensitivity analyses have identified processes that are expected to have a significant impact on predicted values of long-term net infiltration at the YM site. Isotopic and geochemical data compilation, evaluation, and combination with the existing 3D geological framework for the YM site provided a basis from which to evaluate the potential for perched water formation. The geochemical speciation code MINTQA2 was used to calculate sorption of U^{6+} and Np^{5+} on goethite in a batch system with pH ranging from 2–12. Finally, CNWRA staff interacted with the University of Arizona research group and provided a report describing the CNWRA data needs and a field testing plan for the ALTS.

1.10 HIGH-LEVEL WASTE NEAR-FIELD PROCESSES AND VARIATIONS

The objectives of the High-Level Waste Near-Field Project are to develop hypotheses for processes and variations that would develop in the near field of the proposed repository at YM, and to conduct research to address associated KTUs. Research in the Near-Field Project has focused initially on testing the hypothesis that releases of much of the radionuclide inventory from the engineered barrier system (EBS) will be controlled by the properties of secondary minerals composed of oxidized U (uranyl) and other components of the geologic environment. Despite this reasonable scenario, the role of secondary uranyl minerals is generally disregarded in evaluations of repository performance due in part

to the dearth of thermodynamic data for uranyl silicate minerals. Values for these properties reported in the literature are being evaluated, and experiments are being designed to generate new data of significance. KTUs that are directly addressed by this work are related to demonstration of repository performance with regard to cumulative release, subsystem performance objectives for containment and gradual release, and siting criteria related to groundwater conditions near and within the EBS.

Attempts to determine equilibrium solubilities of uranyl silicate minerals have been reported in the literature. These studies were critically reviewed, and the data were judged to be mostly unreliable. Dissolution studies for soddyite $[(\text{UO}_2)_2\text{SiO}_4 \cdot 2\text{H}_2\text{O}]$ provide the most likely basis for retrieval of reliable thermodynamic data. However, excess Si in the reactant material and in solution was assumed to be a consequence of the presence and dissolution of amorphous silica.

Thermodynamic properties for the uranyl hydrate, schoepite $(\text{UO}_3 \cdot 2\text{H}_2\text{O})$, are recommended in a recently published, comprehensive review of chemical thermodynamics of U. These data permit evaluation of the solubility of schoepite as a function of temperature. The equilibrium solubility of schoepite increases with decreasing temperature. In a progressively cooling repository near field, the solubility of schoepite would progressively increase. This process would provide a mechanism for subsequent release of U and other waste species sequestered in secondary schoepite.

Natural analog and laboratory studies indicate that uranophane $\{\text{Ca}(\text{UO}_2)_2[\text{SiO}_3(\text{OH})]_2 \cdot 5\text{H}_2\text{O}\}$ is a secondary uranyl mineral that is likely to form in the proposed repository at YM. Uranophane has been synthesized for potential use in solubility and coprecipitation studies. These studies are designed to derive thermodynamic parameters that can be used to make predictions of the role of uranophane in repository performance. No phases other than uranophane can be identified in the x-ray powder diffraction pattern of the synthetic uranophane. Solubility experiments will be conducted under conditions designed to maximize the potential for derivation of relevant data following additional chemical characterization of the synthetic reactant.

1.11 REFERENCES

- Ghosh, A., S. Hsiung, and A.H. Chowdhury. 1995. *Seismic Response of Rock Joints and Jointed Rock Mass*. CNWRA 95-013. San Antonio, TX: Center for Nuclear Waste Regulatory Analyses.
- Nuclear Regulatory Commission. 1994. *License Application Review Plan for the Review of a License Application for a Geologic Repository for Spent Nuclear Fuel and High-Level Radioactive Waste, Yucca Mountain Site, Nevada*. NUREG-1323. Washington, DC: Nuclear Regulatory Commission.
- Snow, J.K. 1994. Mass balance of basin and range extension as a tool for geothermal exploration. *Transactions of the Geothermal Resources Council*. Davis, CA: Geothermal Resources Council: 18: 23-30.
- Snow, J.K., and A.R. Prave. 1994. Covariance of structural and stratigraphic trends: Evidence for anticlockwise rotation within the Walker Lane Belt Death Valley region, California and Nevada. *Tectonics* (13): 712-724.

Sridhar, N., G.A. Cragolino, and D.S. Dunn. 1995. *Experimental Investigations of Failure Processes of High-Level Radioactive Waste Container Materials*. CNWRA 95-010. San Antonio, TX: Center for Nuclear Waste Regulatory Analyses.

2 GEOCHEMICAL NATURAL ANALOG RESEARCH

by James D. Prikryl, David A. Pickett, and English C. Percy

Investigators: James D. Prikryl, David A. Pickett, English C. Percy, William M. Murphy, and Ronald T. Green

NRC Project Officer: Linda A. Kovach

2.1 TECHNICAL OBJECTIVES

The technical objectives of the Geochemical Natural Analog Research Project are to develop an understanding of the utility and limitations of natural analog studies used to support a license application for a high-level nuclear waste (HLW) repository and to provide fundamental data on the long-term behavior of a HLW repository. These objectives are pursued through field, laboratory, theoretical, and interpretive analyses of natural systems that are analogous in many respects to the proposed HLW repository at Yucca Mountain (YM), Nevada. Many factors affecting the long-term behavior of waste forms, the engineered barrier system (EBS), and radionuclides in the environment of the proposed repository are poorly known. The absence of this basic information limits the confidence with which repository performance may be evaluated. Natural systems that have evolved for periods of time comparable to that required for HLW disposal (i.e., 10^3 – 10^4 yr and greater) (U.S. Environmental Protection Agency, 1989) provide unique opportunities to obtain observational knowledge of the behavior of HLW repository components. Such information provides important support to long-term predictive models of repository performance (Nuclear Regulatory Commission, 1987).

The Geochemical Natural Analog Research Project addresses uncertainties raised in several Compliance Determination Strategies (CDSs), which are outlined in the License Application Review Plan (Nuclear Regulatory Commission, 1994). Specific Compliance Determination Methods (CDMs) that may be supported with this research include those in CDSs for hydrogeologic processes (3.2.2.1), hydrologic conditions (3.2.2.9), perched water (3.2.2.12), geochemical conditions (3.2.3.2), mineral assemblages (3.2.3.3), geochemical processes (3.2.3.5), EBS performance (5.4), cumulative release (6.1), and individual protection (6.2). Data and interpretations developed within the Geochemical Natural Analog Research Project will help address Key Technical Uncertainty (KTU) topics including: (i) uncertainty in prediction of the effects of environmental conditions on the EBS during the post-containment period, (ii) uncertainty in identifying geochemical processes and conditions that affect radionuclide retardation and determining and predicting the magnitude of the effects at YM, (iii) uncertainty in developing a conceptual and mathematical vapor and liquid water phase transport model that is representative of the YM site flow system, (iv) uncertainty in predictions of effects of environmental conditions on the waste package during the containment period, and (v) uncertainties associated with development and validation of conceptual and mathematical models. Information presented in this chapter relates primarily to KTU topic (ii).

The Geochemical Natural Analog Research Project is an integrated effort combining expertise in geochemistry, hydrology, geology, and transport modeling, among others. The need for interdisciplinary input is reflected in a number of technical interfaces with other projects. For example, within the Geochemical Natural Analog Research Project, the hydrologic properties of welded silicic tuff from the Nopal I analog site have been measured, and the data have been analyzed within the Performance Assessment (PA) Research Project to allow more complete interpretation of long-term transport of uranium (U) through tuff at the site (Green et al., 1994). Observations and measurements from the Geochemical

Natural Analog Research Project are also being used within the Sorption Research Project (Chapter 3 of this document) for comparison to laboratory studies. Additionally, results from the Geochemical Natural Analog Research Project have been used in hypothesis development within the High-Level Waste Near-Field Processes and Variations Research Project (Chapter 10 of this document). Specifically, at the Nopal I site, it has been observed that alteration phases formed after uraninite (a spent fuel analog material) are dominated by the minerals uranophane, soddyite, and weeksite. The Nopal I analog suggests that these phases are likely to be important to radionuclide release and transport in a YM repository. Within the High-Level Waste Near-Field Processes and Variations Research Project, experiments are being conducted to determine thermodynamic properties of uranyl minerals so that their behavior and impact on repository performance may be evaluated.

The Geochemical Natural Analog Research Project addresses needs identified by the Office of Nuclear Material Safety and Safeguards concerning assessment of the degree to which data from analogous sites may be extrapolated to support modeling for a repository site. It also addresses the need for an evaluation of the extent to which repository modeling can be validated using data from natural analogs. Specific NRC research needs that may be met through this project include: (i) determining the geochemical effects on radionuclide transport within and beyond the thermally affected zone, and (ii) understanding the evolution of groundwater in the near-field environment.

Research in the Geochemical Natural Analog Research Project includes work at two sites: the Nopal I U deposit in the Peña Blanca district, Chihuahua, Mexico, and the Akrotiri archaeological site on Santorini, Greece. Earlier reports in this series documenting progress to date include Murphy et al. (1994); Percy et al. (1994a); Percy (1994b); Leslie et al. (1993a); Percy and Leslie (1993); Percy et al. (1993a, b); and Percy and Murphy (1990, 1991a-c). This report examines the role of secondary mineral formation in retarding radionuclide migration along a prominent fracture that crosscuts the Nopal I U deposit. Recent work at the Nopal I site indicates that U transport at the deposit occurs mainly along fracture pathways (Percy, 1994a, b). Data reported here are intended to address KTUs that deal with the ability of alteration mineral assemblages to inhibit radionuclide migration and may provide data that PA models can incorporate to constrain radionuclide transport in a YM-type environment.

2.2 SIGNIFICANT TECHNICAL ACCOMPLISHMENTS

The long-term safety of a HLW repository depends in part upon the effectiveness of the geological barrier, notably its ability to retain and retard the radionuclides that are released through engineered barriers. Migration of radionuclides along fluid-conducting fractures in the host rock of a repository is one mechanism by which hazardous radionuclides can be transported to the accessible environment. Retardation associated with fracture flow has been identified by recent NRC work as a critical issue in repository PA; however, uncertainties remain as to the appropriate implementation of fracture retardation as a parameter in transport models (Wescott et al., 1994). Diffusion from fractures into the rock matrix is a potentially important retardation mechanism and is a major conceptual basis of many radionuclide transport models. However, some studies have shown that diffusion of radionuclides from fractures into the adjacent rock matrix does not always take place and that very little of the rock adjacent to fractures may be available for diffusion (Heath et al., 1992; Neretnieks, 1980). Retention of radionuclides in iron minerals deposited in fractures may be a more important retardation mechanism than diffusion into the rock matrix. For example, at the El Berrocal (granite batholith) natural analog site in Spain, retention of U by secondary phases that line fracture walls is reported to dominate retardation processes (Ménager et al., 1994). At the Nopal I U deposit, measurement of the U contents of

microfracture infilling minerals (e.g., uranophane and goethite) and adjacent tuff matrix indicates that a high percentage (>95%) of U is retained in the microfractures (Pearcy, 1994a, b). The general objective of the work reported here is to evaluate the behavior and ability of secondary non-U minerals in retarding the transport of U at the Nopal I analog site.

The Nopal I U deposit is especially favorable for the study of mass transport in a geologic environment composed of fractured, igneous rocks. As a result a variety of field and laboratory studies are being carried out at the site. Features of the Nopal I deposit analogous to the proposed repository at YM include the fractured, silicic, volcanic host rocks; the semiarid climate; the unsaturated hydrology; and the chemically oxidizing environment (Pearcy and Murphy, 1991d; Pearcy and Murphy, 1992). Earlier research within this project has established the geologic, mineralogic, and hydrologic framework of the Nopal I Analog (Pearcy et al., 1993a-c). Secondary minerals produced by oxidative alteration of the primary mineral assemblage have been identified and described (Leslie et al., 1993a, b; Pearcy et al., 1993a-c; Pearcy et al., 1994a). The alteration processes were accompanied by mobilization of U, and the spatial distribution of U within and around the deposit has been measured and mapped (Leslie et al., 1993a, b; Pearcy and Leslie, 1993; Pearcy, 1994a, b).

The Nopal I U deposit is hosted by fractured, rhyolitic tuffs (Nopal and Coloradas Formations); the U mineralization extends approximately 100 m vertically and is located within a highly brecciated zone. Mining during the late 1970s and early 1980s exposed the deposit on two broad horizontal surfaces (Levels +00 and +10). Clearing, followed by geologic and radiometric mapping of the Level +00 and +10 surfaces, showed that the area of U mineralization is well defined, roughly elliptical in form, and has maximum horizontal dimensions of about 18×30 m (Figure 2-1). The cleared surfaces completely span the outcrop of the deposit and expose much of the surrounding host rock, providing an opportunity to study transport of U from the deposit out into the host tuff. A permanent 1×1 m grid with axes oriented NS and EW was constructed over the cleared areas and provides the location references in this report.

Recent work at Nopal I has examined the distribution of U in the host tuff at scales ranging from 10^{-6} to 10^1 m. The work indicates that U transport away from the deposit occurs mainly along fracture paths (Pearcy and Leslie, 1993; Pearcy, 1994a, b). It should be noted here that, although the dominant component of transport may have been vertical, data from the +10 level have been collected primarily along horizontal surfaces. The greatest horizontal transport distances (tens of meters) were observed along a few continuous mesofractures, whereas transport through generally fractured tuff containing less continuous microfractures achieved distances of meters. Initial analyses of a major EW fracture set located between 13 and 15 m N on the reference grid (Figure 2-1) noted the association of anomalous U concentrations with fracture-infilling minerals (Pearcy and Leslie, 1993; Prikryl and Pearcy, 1994). In previous reports, this fracture set has been referred to as the *13.5 m N fracture set* and will be referred to as such in this report. The 13.5 m N fracture set was selected for additional analyses including: (i) mineralogic characterization; (ii) U, Th, and trace element distributions; and (iii) U-series isotopic measurements. U-series disequilibrium measurements are capable of providing information on radionuclide mobility and geochronology of relatively recent (<1 Ma) geochemical events. Thus, their application in studies related to nuclear waste disposal is common (Ivanovich et al., 1992).

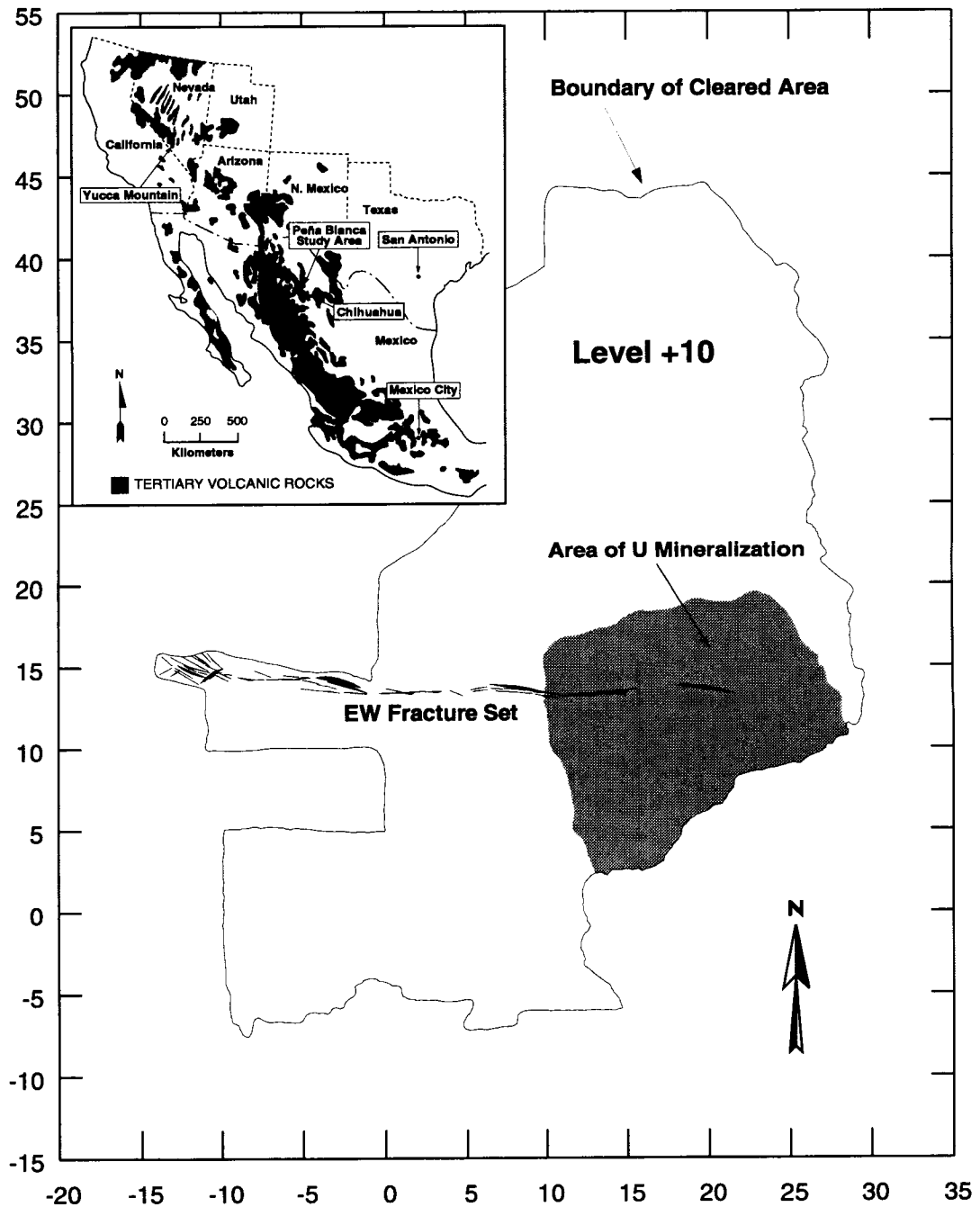


Figure 2-1. Map showing the location of the 13.5 m N fracture set on the Level +10 surface of the Nopal I deposit. The fracture set crosscuts the western margin of the deposit. Inset shows the location of the Peña Blanca district in relation to Yucca Mountain. Perimeter scales are in meters.

2.2.1 Background

2.2.1.1 Fracture Description

The 13.5 m N fracture set crosscuts the U deposit along its western margin and is the longest and most continuous fracture on the Level +10 surface (Figure 2-1). The fracture set is subplanar and has a near-vertical dip ($85\pm 5^\circ$ N). The horizontal trace of the fracture set extends about 20 m beyond the western margin of the deposit before branching into a series of less continuous fractures. The eastern extension of the fracture terminates within the deposit. Structurally, the 13.5 m N fracture set belongs to a set of EW-trending fractures that are the most recent among various fracture sets at Nopal I (Percy, 1994a, b). The 13.5 m N fracture is not offset or cut by internal features of the deposit, indicating that the fracture is younger than the deposit.

The 13.5 m N fracture set is filled with secondary minerals. The macroscopic assemblage of the fracture-infilling minerals is dominated by dark-colored Fe-oxides and Fe-hydroxides. The contrast of the dark-colored infill minerals against the light-colored host rock makes the fracture easily visible on the Level +10 surface. Fracture aperture (i.e., fracture-infilling material and open space) varies from 2 mm to 2.5 cm and tends to narrow with distance from the deposit. The amount of fracture-infilling minerals decreases with distance from the deposit and is associated with narrowing of the fracture aperture. The fracture displays some degree of macroscopic porosity, generally in the form of vugs, over its entire length. The vertical extension of the fracture is observed in an adit at the Level +00 horizon. When rainfall ponds on the Level +10 surface, water has been observed dripping from the ceiling of the adit along the trace of the fracture. This dripping of water indicates that the fracture is open with respect to fluid flow between Levels +10 and +00. The rate at which precipitation infiltrates downward through the fracture from the Level +10 surface to the ceiling of the adit (a distance of approximately 8 m) is relatively rapid (on the order of hours).¹

2.2.1.2 Analytical Methods

Fracture-infilling minerals were collected along the length of the 13.5 m N fracture at approximately 1-m intervals. Sampling was accomplished by either scraping fracture-infilling minerals from the rock surfaces using a steel pocket knife or by chiseling out bulk samples (i.e., fracture-infilling minerals attached to wall rock) and separating the fracture-infilling in the laboratory using a steel blade and pick.

Mineralogic characterization was performed by petrographic and x-ray diffraction (XRD) analysis. Standard polished thin sections were examined on a Nikon Optiphot-Pol transmitted/reflected light petrographic microscope. Higher resolution petrography employed an AMRAY Model 1645 scanning electron microscope (SEM) and a Phillips EM420 transmission electron microscope (TEM). The SEM was equipped with a Model 8502S Tracor Northern energy-dispersive x-ray analysis system for qualitative compositional analysis. Mineral identifications were confirmed using an automated (RADIX) Siemens D500 x-ray diffractometer (Cu tube, Ni filter, 40 kV, 37 mA; scan $2-70^\circ$ at 0.02° step; count 1.0 s). The graphics interface program JADE/MDI was used to provide output of the absolute intensity of the diffraction signal.

¹Ignacio Reyes, Autonomous University of Chihuahua, Chihuahua City, Mexico, personal communication, 1995.

Quantitative mineral compositions were measured using a Cameca SX-50 electron microprobe (EMPA). Standards used were: synthetic UO_2 for O and U; PbS for Pb; Fe_2O_3 for Fe; GaAs for As; CaSiO_3 for Ca; $\text{NaAlSi}_3\text{O}_8$ for Na; Al_2O_3 for Al; SiO_2 for Si; KAlSi_3O_8 for K; CaSO_4 for S; ThO_2 for Th; $\text{Mn}_3\text{Al}(\text{SiO}_4)_3$ for Mn; and TiO_2 for Ti. Analytical conditions were: 15-kV accelerating voltage, 200-nA beam current for U and Pb, 15-nA beam current for all other elements, and 1- μm spot.

Selected samples from the 13.5 m N fracture were analyzed by isotope dilution/alpha spectrometry for U (^{238}U , ^{234}U) and Th (^{232}Th , ^{230}Th) isotopes. Fracture-infilling minerals were subjected to the following procedure: (i) powdering in a SPEX 8000 Mixer/Mill using a tungsten carbide vial, (ii) spiking with a ^{232}U - ^{228}Th solution, (iii) acid digestion (CEM MDS-2000 microwave system with Teflon PFA vessels), (iv) iron hydroxide coprecipitation, (v) ion-exchange column separation and purification (BIORAD AG 1-x8 anion exchange resin), (vi) deposition on membrane filters, (vii) alpha counting, and (viii) data reduction and analysis. U and Th isotopes were measured on an EG&G ORTEC system that included model 676A and 576A spectrometers with ion-implanted silicon charged particle detectors, a model 920-16 multichannel buffer, ALPHAMAT analysis software for acquisition control, and MAESTRO II multichannel analyzer emulation software for analysis of spectral data.

2.2.2 Results

2.2.2.1 Mineralogic and Petrographic Characteristics

The mineralogic composition of the 13.5 m N fracture, determined by XRD methods, has been briefly described in earlier reports (Pearcy and Leslie, 1993; Pearcy, 1994a, b). The primary components of the fracture infilling material include goethite ($\alpha\text{-FeOOH}$), hematite (Fe_2O_3), jarosite [$\text{KFe}_3(\text{SO}_4)_2(\text{OH})_6$], kaolinite [$\text{Al}_2\text{Si}_2\text{O}_5(\text{OH})_4$], and quartz (SiO_2). Additional XRD analyses, supplemented by optical microscopy of samples at approximately 1 m spacing, reveal the distribution and paragenetic relationships of mineral phases over the length of the fracture.

Goethite is the earliest and most abundant secondary fracture-infilling mineral, and its abundance remains relatively constant over the length of the fracture (Figure 2-2). Textural evidence suggests that goethite forms by replacement of pyrite. Cubic goethite morphology indicates that goethite pseudomorphs pyrite (Figure 2-3). Locally, precursor pyrite crystals may be only partially replaced by goethite, leaving open space that is lined or filled by later forming mineral phases (e.g., hematite and jarosite). More commonly, goethite occurs as irregularly shaped crystalline masses (Figure 2-4). Evidence that these crystalline masses form by pyrite replacement is revealed by the occurrence of zoning (Figure 2-4). Zoning in goethite that forms as a result of pyrite oxidation suggests replacement of pyrite by two hydrous Fe-oxide phases [e.g., goethite and lepidocrosite ($\gamma\text{-FeOOH}$)] (Ramdohr, 1980). Goethite also occurs in the fracture as an intergrowth with micrometer-sized platelets of kaolinite. This goethite is also probably a result of pyrite oxidation and indicates that the original mineral assemblage in the fracture was a pyrite + kaolinite association.

Amorphous (i.e., noncrystalline) Fe-oxyhydroxide is the second most abundant fracture-infilling component. Due to its noncrystalline nature, the distribution of amorphous Fe-oxyhydroxide in the fracture could not be determined by XRD analysis. Optical observations indicate that the amount of amorphous Fe-oxyhydroxide increases significantly with distance from the deposit. The amorphous Fe-oxyhydroxide generally occurs as a gel-like crust that overgrows crystalline goethite (Figures 2-4 and 2-5). The occurrence of the amorphous phase overgrowing euhedral goethite crystals suggests that it formed after

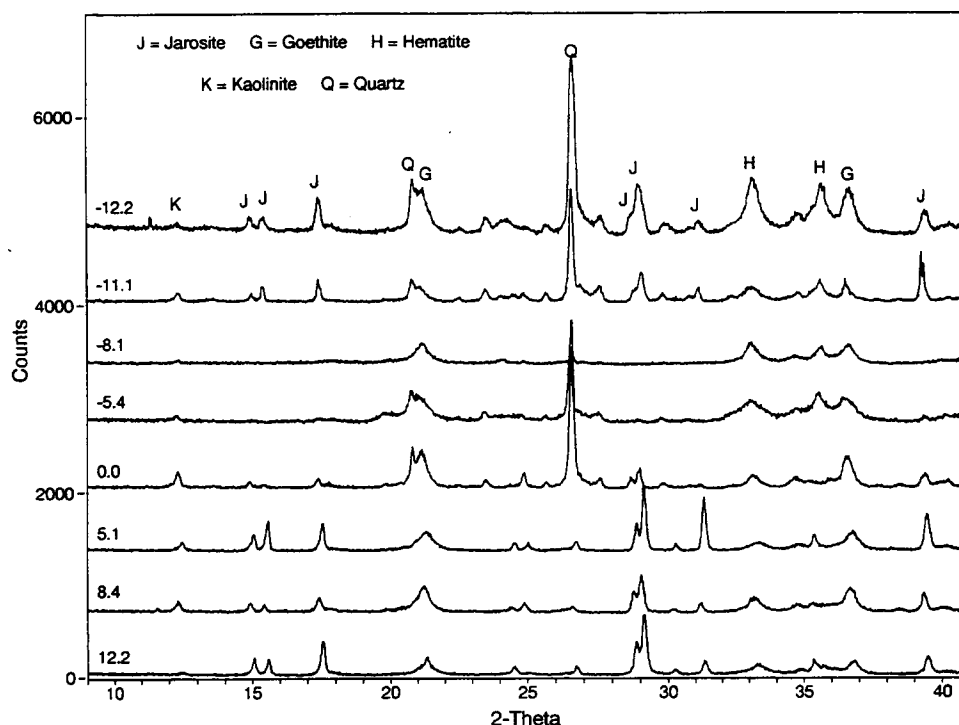


Figure 2-2. XRD patterns (2-theta vs counts) of bulk fracture-infilling minerals from the 13.5 m N fracture. The EW coordinate at which each sample was collected is displayed to the left of each pattern. Minerals identified include jarosite, goethite, hematite, kaolinite, and quartz. Goethite abundance is constant over the length of the fracture. The amount of hematite in the fracture generally increases with distance from the deposit (i.e., from east to west). The abundances of jarosite, kaolinite, and quartz are variable over the length of the fracture. The occurrence of quartz reflects the presence of tuff fragments in the bulk sample.

pyrite replacement. However, like goethite, amorphous Fe-oxyhydroxides are sometimes intergrown with kaolinite, which suggests that it may also form as a result of pyrite oxidation.

Hematite in the 13.5 m N fracture grows into open space from goethite and amorphous Fe-oxyhydroxide substrates and is easily identified by its colloform texture (Figures 2-4 and 2-5). Hematite abundance generally increases with distance from the deposit (Figure 2-2). Optically, this trend is reflected in a greater continuity and width of colloform hematite in samples farther from the deposit margin (compare Figure 2-3 with Figures 2-4 and 2-5). Goethite formation after colloform hematite has been observed in only one locality along the 13.5 m N fracture (inside the deposit at about 11.7 m E).

Jarosite is the latest forming mineral phase within the 13.5 m N fracture. Jarosite is present over the length of the fracture, but its abundance varies (Figure 2-2). Jarosite occurs as micrometer- to millimeter-sized euhedral, hexagonal crystals that partially or totally fill open spaces (Figures 2-5 and 2-6). Jarosite occurs most commonly in acidic, sulfate-rich environments developed as a result of pyrite oxidation during weathering (Bladh, 1982; Nordstrom, 1982) but has also been reported in hydrothermal ore deposits (Hayba et al., 1985).

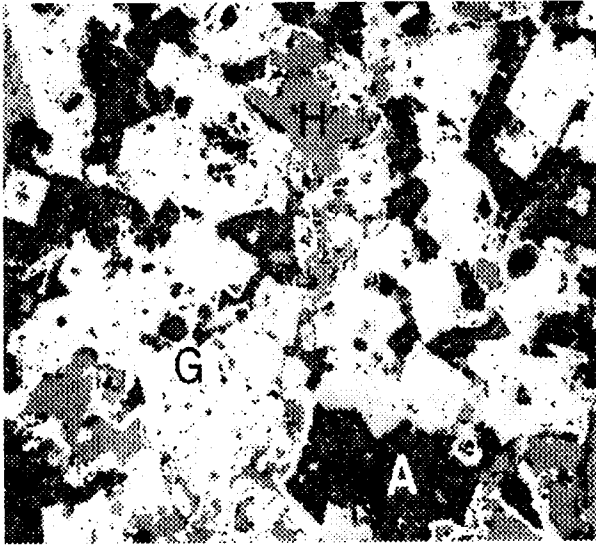


Figure 2-3. Reflected light photomicrograph of fracture-infilling consisting of goethite (G), hematite (H), and amorphous Fe-oxyhydroxide intergrown with kaolinite (A). This sample was collected at 6.1 m E along the 13.5 m N fracture. Goethite replaces precursor pyrite crystals. Colloform hematite forms a very thin, discontinuous rim on earlier formed goethite. Field of view is 0.65 mm.

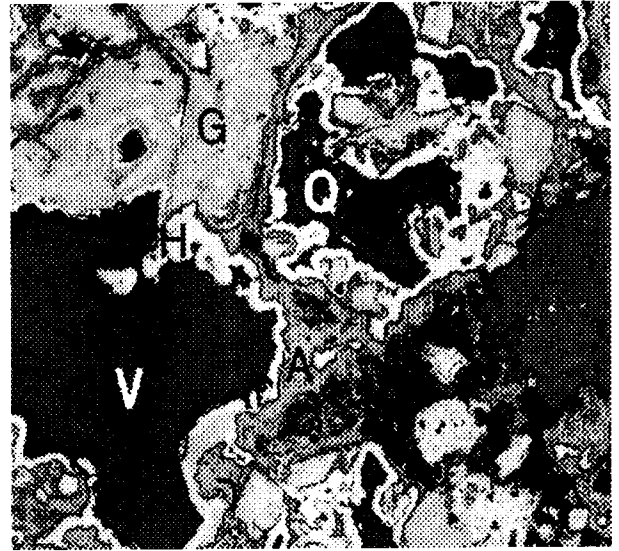


Figure 2-4. Reflected light photomicrograph of fracture-infilling collected from the 13.5 m N fracture at -10.1 m E. Hematite (H) forms a continuous colloform rim on goethite (G) and amorphous Fe-oxyhydroxides (A). Goethite shows zoning, which suggests replacement of precursor pyrite by two hydrous Fe-oxide phases. Material in open voids (V) is pre-dominantly quartz (Q) that was blown or washed into fracture openings. Field of view is 0.65 mm.

Quartz in the 13.5 m N fracture originates from siliceous rock fragments produced by fracturing of the tuff. Millimeter- to centimeter-sized tuff fragments cemented by fracture-infilling minerals (predominantly goethite) occur over the length of the fracture. As the fracture narrows with distance from the deposit, these tuff fragments are more difficult to separate from the fracture-infilling minerals as is shown by XRD analyses (Figure 2-2). Quartz is also present as micrometer- to millimeter-sized pieces of the host tuff that have been washed or blown into fracture openings (Figure 2-4).

Optical microscopy and XRD techniques were unable to identify U minerals within the 13.5 m N fracture. Examination of mineral phases by TEM indicates that discrete U minerals are absent even at nanometer scale. TEM examination included both the interiors of goethite, hematite, and kaolinite crystals and amorphous Fe-oxyhydroxides and the boundaries between mineral phases. The absence of discrete U minerals indicates that U is incorporated in the fracture-infilling by coprecipitation or sorption onto mineral surfaces.

Microscopic observations indicate that the fracture is porous and permeable over its entire length. Fracture porosity, as estimated petrographically, tends to decrease away from the deposit and is associated with narrowing of the fracture aperture. Vuggy porosity is produced by incomplete filling of the fracture by secondary mineral formation, which results in openings in the centers of fractures (Figures 2-4 and 2-5). Porosity also occurs as “gossan” (i.e., cellular masses) within the ore deposit or near the deposit

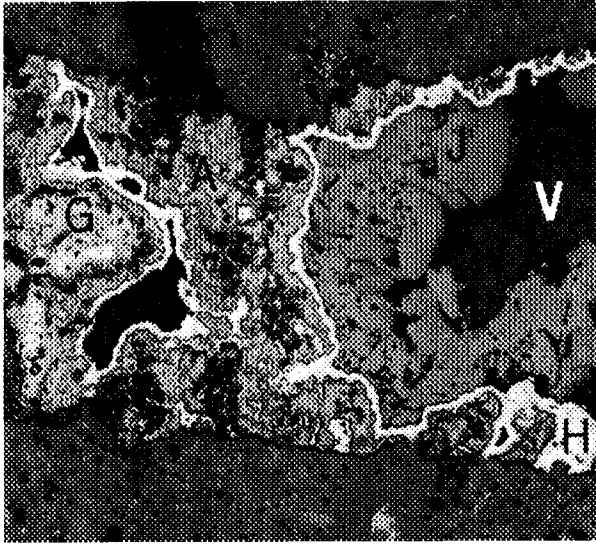


Figure 2-5. Reflected light photomicrograph of fracture-infilling collected at -10.1 m E. Hematite (H) forms a continuous rim on earlier formed goethite (G) and amorphous Fe-oxyhydroxide (A). Euhedral jarosite (J) crystals grow from hematite substrates into open voids (V). Field of view is 0.65 mm.

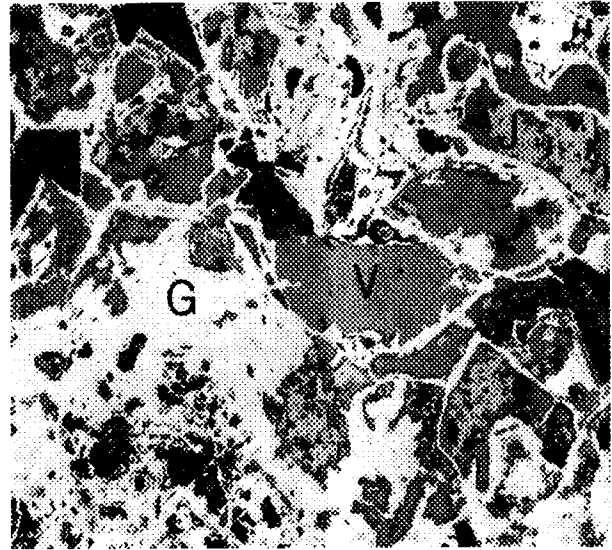


Figure 2-6. Reflected light photomicrograph of fracture-infilling collected at 6.1 m E. Goethite (G) forms a meshwork of gossan. Jarosite (J) partially fills the open voids (V) left by dissolution of pyrite and tuff fragments. Field of view is 0.65 mm.

margin, where fracture apertures are widest and fracture-infilling minerals are most abundant. Gossan is formed by oxidation and dissolution of precursor pyrite and acid leaching of siliceous tuff fragments (Figure 2-6). The meshwork of porous gossan remaining after pyrite and silicate removal is composed of goethite. Openings in the meshwork are commonly lined with colloform hematite or are partially or totally filled by jarosite (Figure 2-6).

2.2.2.2 U and Th Concentrations of Bulk Fracture-Infilling

The U and Th concentrations of the bulk fracture-infilling along the 13.5 m N fracture, measured by alpha-spectrometry, are reported in Table 2-1 and plotted in Figure 2-7. U concentrations generally decrease with distance from the deposit and range from 5,400 ppm inside the deposit to 375 ppm 20 m outside the deposit. This trend and range in U concentrations are similar to those of bulk fracture-infilling from the 13.5 m N fracture that were measured by gamma-counting (Percy and Leslie, 1993; Percy, 1994a, b). The U values of the bulk fracture-infilling indicate large enrichments in U relative to rocks from volcanic formations in the Peña Blanca district (8 to 14 ppm) and hydrothermally altered tuff from outside the orebody on the +10 Level of Nopal I (10 to 23 ppm) (Leslie et al., 1993a, b). The anomalously high U contents indicate that components of the fracture-infilling are capable of retaining U. The trend of decreasing U content with distance from the deposit suggests transport of U away from the deposit (noting, again, that data are from a horizontal transect).

Table 2-1. U and Th concentration and isotopic data of bulk fracture-infilling samples from the 13.5 m N fracture. Uncertainties in U and Th concentrations are $\pm 5\%$. Uncertainties in $^{234}\text{U}/^{238}\text{U}$ and $^{230}\text{Th}/^{234}\text{U}$ activity ratios are from counting statistics and are at the 2σ level (or 95% confidence level).

Sample	Location (m East)	U (ppm)	Th (ppm)	$^{234}\text{U}/^{238}\text{U}$	$^{230}\text{Th}/^{234}\text{U}$
NOPI-417	15.8	3,643	17	1.29 \pm 0.03	1.27 \pm 0.02
NOPI-144	12.2	5,374	19	1.15 \pm 0.02	1.03 \pm 0.01
NOPI-418	11.7	3,529	20	1.28 \pm 0.03	1.25 \pm 0.02
NOPI-142	10.1	1,719	139	1.40 \pm 0.02	1.19 \pm 0.01
NOPI-419	9.0	787	73	1.63 \pm 0.04	1.39 \pm 0.02
NOPI-302	8.4	1,481	111	1.34 \pm 0.03	1.10 \pm 0.02
NOPI-420	6.2	1,622	36	1.29 \pm 0.03	1.31 \pm 0.02
NOPI-139	6.2	1,412	25	1.14 \pm 0.02	1.24 \pm 0.01
NOPI-301	6.1	1,568	38	1.16 \pm 0.03	1.18 \pm 0.02
NOPI-137	3.8	1,156	39	1.16 \pm 0.02	1.06 \pm 0.01
NOPI-421	3.2	2,506	51	1.18 \pm 0.02	1.24 \pm 0.02
NOPI-422	1.1	1,716	40	1.08 \pm 0.03	1.21 \pm 0.02
NOPI-423	-2.1	472	28	1.12 \pm 0.03	1.31 \pm 0.03
NOPI-205	-3.0	818	108	1.11 \pm 0.02	1.14 \pm 0.02
NOPI-424	-6.1	768	32	1.05 \pm 0.04	1.23 \pm 0.05
NOPI-209	-7.3	1,095	40	1.30 \pm 0.08	1.16 \pm 0.05
NOPI-425	-9.8	455	27	1.11 \pm 0.03	1.33 \pm 0.03
NOPI-294	-10.1	375	15	1.12 \pm 0.03	1.23 \pm 0.03
NOPI-298	-12.2	484	55	1.10 \pm 0.02	1.15 \pm 0.02

The Th concentrations of the bulk fracture-infilling inside the deposit range from 16 to 20 ppm and are generally lower than those outside the deposit (Figure 2-7). Unlike U, there is no suggestion of a trend in Th with distance outside the deposit boundary. The highest Th concentrations, with one exception, were measured in samples at or directly outside the deposit boundary (within about 3 m) and range from about 70 to 140 ppm. These samples are enriched in Th when compared to volcanic rock formations in the Peña Blanca district (14 to 36 ppm) and hydrothermally altered tuff from the +10 Level of the Nopal I deposit (29 to 42 ppm) (Leslie et al., 1993a, b). At distances greater than 3 m outside the deposit, samples generally have Th concentrations between about 25 and 55 ppm, similar to hydrothermally altered tuff from Level +10, except for one sample at -3 m E with 110 ppm.

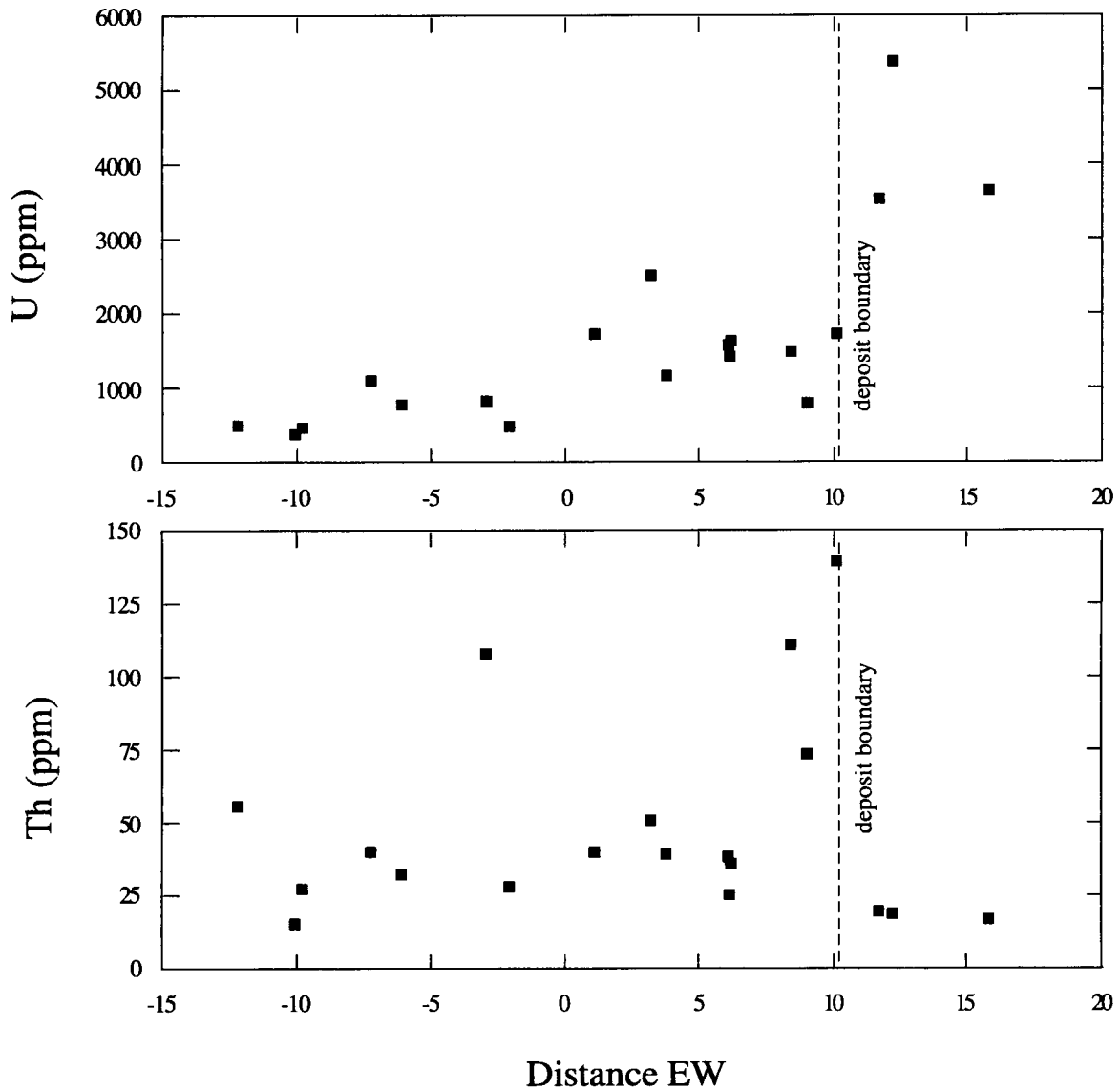


Figure 2-7. U and Th concentrations in bulk fracture-infilling samples along the 13.5 m N fracture

A plot of U versus Th concentrations for the bulk fracture-infilling samples indicates no correlation between these two radionuclides (Figure 2-8), probably reflecting differences in their transport behavior. Unlike U, which may be carried in solution as a complex ion, Th is almost chemically immobile in most natural waters due to its extremely low solubility (Gascoyne, 1992). The mobility of Th in natural waters is governed almost entirely by its movement as particulate or colloidal matter. This movement is controlled by the physical properties and flow velocity of the transporting medium. Enrichment of Th in fracture-infilling minerals directly outside the deposit may suggest that Th was transported away from the deposit. However, since Th contents of the fracture-infilling are similar to those of altered tuff on Level +10 at distances greater than about 3 m outside the deposit, any such advective transport of Th along the 13.5 m N fracture appears to have been limited to about 3 m from the deposit. It is not clear, on the basis of only three anomalous samples (and considering the high-Th sample further away from the deposit)

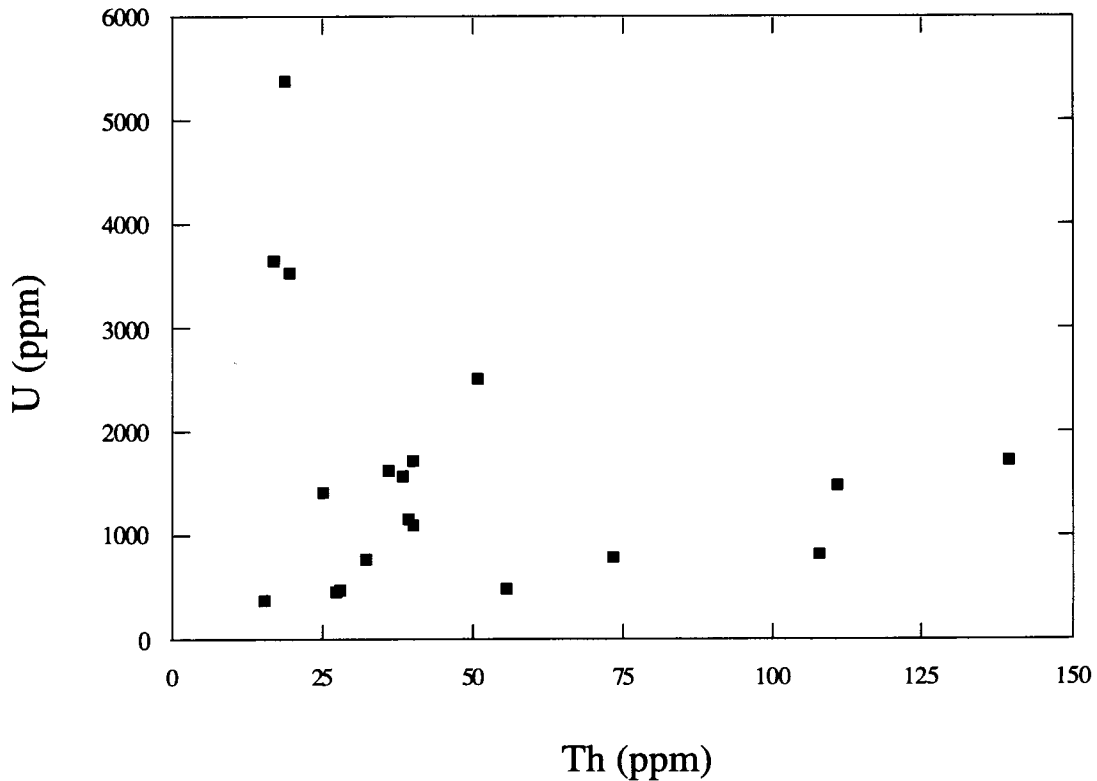


Figure 2-8. U versus Th concentrations in bulk fracture-infilling samples from the 13.5 m N fracture

that Th enrichment near the boundary is a significant feature. In any case, Th transport was not related to any concentration gradient (see the low Th from inside the deposit in Figure 2-7), in contrast to the situation for U.

2.2.2.3 U and Th Isotopic Profiles

Isotopic data for bulk fracture-infilling minerals along the 13.5 m N fracture are given in Table 2-1, and $^{234}\text{U}/^{238}\text{U}$ and $^{230}\text{Th}/^{234}\text{U}$ isotopic profiles are presented in Figure 2-9. $^{234}\text{U}/^{238}\text{U}$ and $^{230}\text{Th}/^{234}\text{U}$ activity ratios of the bulk fracture-infilling indicate disequilibrium for all samples analyzed. $^{234}\text{U}/^{238}\text{U}$ activity ratios are all greater than unity, with values ranging from 1.05 to 1.63. Radioactive disequilibrium between ^{234}U and ^{238}U in fracture-infillings indicates relatively recent U mobilization (i.e., <1 Ma). Excess ^{234}U accumulation in the fracture-infilling strongly suggests deposition (sorption or coprecipitation) of U from fluids with high $^{234}\text{U}/^{238}\text{U}$ ratios. Outside the deposit, there is a systematic decrease in $^{234}\text{U}/^{238}\text{U}$ activity ratios with distance from the deposit margin. Within the deposit, $^{234}\text{U}/^{238}\text{U}$ activity ratios of the fracture-infilling are lower than for samples directly outside the deposit margin (i.e., within about 3 m outside the deposit). These lower $^{234}\text{U}/^{238}\text{U}$ activity ratios are probably due to the larger mass of U in the bulk fracture-infilling within the deposit relative to the ^{234}U being added (see Figure 2-7). The systematic decrease in $^{234}\text{U}/^{238}\text{U}$ ratios with distance suggests a multistage mobilization process, such as remobilization of U from ^{234}U -enriched infill materials or differential transport of ^{234}U away from the deposit.

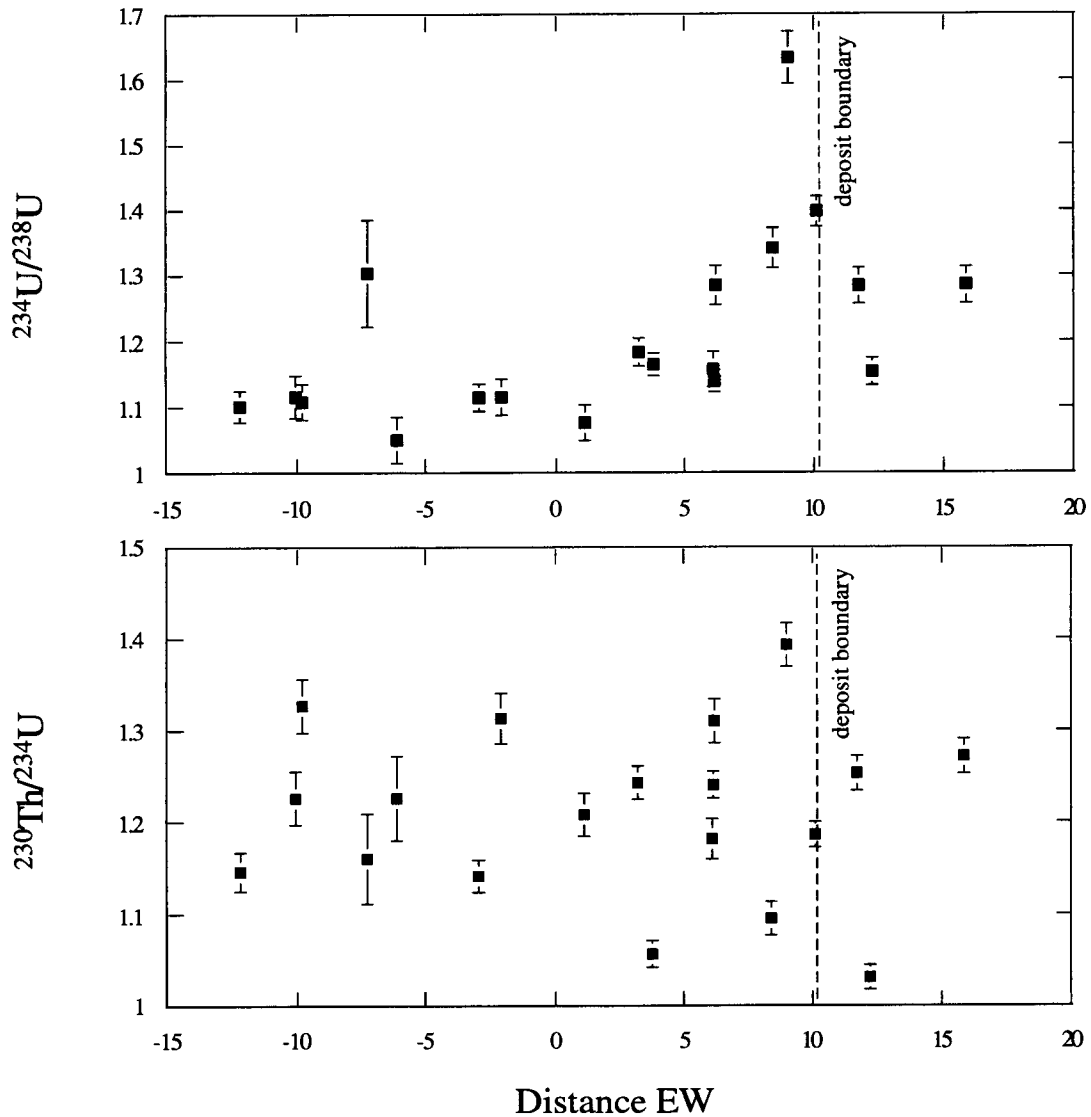


Figure 2-9. $^{234}\text{U}/^{238}\text{U}$ and $^{230}\text{Th}/^{234}\text{U}$ activity ratios of bulk fracture-infilling samples along the 13.5 m N fracture

Like $^{234}\text{U}/^{238}\text{U}$, $^{230}\text{Th}/^{234}\text{U}$ activity ratios of bulk fracture-infilling samples are also all greater than unity, ranging from 1.03 to 1.39 (Table 2-1). However, unlike $^{234}\text{U}/^{238}\text{U}$, $^{230}\text{Th}/^{234}\text{U}$ activity ratios show no spatial trend outside the deposit, which probably reflects the low mobility of Th in natural waters (Figure 2-9). The excess ^{230}Th accumulation in the bulk fracture-infilling probably results from preferential sorption of ^{230}Th generated by dissolved ^{234}U and/or remobilization of U from infill minerals after ^{230}Th ingrowth.

2.2.2.4 U and Trace Element Distribution

The results of chemical analyses for U, Pb, As, and S in goethite, hematite, and amorphous Fe-oxyhydroxides along the 13.5 m N fracture are summarized in Figure 2-10. These mineral phases were also analyzed for Ca, Si, Al, Na, Th, K, Ti, Mn, and Ba. Measured concentrations for Th, K, Ti, Mn, and Ba were below calculated detection limits for the EMPA conditions employed. The trace element content of amorphous Fe-oxyhydroxides was measured at only two locations along the fracture (at about 7.0 and -10.0 m E). EMPA analyses of jarosite indicated U contents below detection limits. Therefore, quantitative measurements for jarosite are limited and not included in Figure 2-10. Determination of the trace element content of kaolinite was precluded by its microcrystalline size and intergrowth with Fe-hydroxide phases.

The U contents of both goethite and hematite generally decrease with distance from the deposit (Figure 2-10a) and show a very similar trend to the measured U content of the bulk fracture-infilling (see Figure 2-7). This decreasing U concentration gradient with distance from the deposit again suggests transport of U away from the deposit. At any specific location along the fracture, the U content of goethite is greater than that of hematite (Figure 2-10a). This trend suggests that fluids were more enriched in U during goethite formation or that U has a greater affinity for goethite. The very high *in situ* U content of these Fe phases demonstrates that U in the bulk fracture-infilling is sited chiefly within the minerals, that is, the U was sequestered during mineral growth rather than sorbed on formed mineral surfaces.

Like U, the Pb and As contents of goethite, hematite, and amorphous Fe-oxyhydroxides are anomalously high (Figures 2-10b and 2-10c). The As content of goethite is generally greater than that of hematite. However, Pb contents show an opposite trend; goethite has lower Pb contents than hematite. These trends suggest that early solutions, which precipitated goethite, were more enriched in As and less enriched in Pb than later solutions, which precipitated hematite.

In contrast to U, the contents of other cationic constituents including Pb, As, Ca, Na, Si, and Al in goethite and hematite show no observable trends with distance from the deposit (see Figures 2-10b and 2-10c for Pb and As, respectively). This lack of a trend suggests that the mobility or geochemical transport characteristics of U along the 13.5 m N fracture are not wholly related to those of other trace elements. The occurrence of wulfenite (PbMoO_4) and an As-K-rich uranyl oxide hydrate phase tentatively identified as abernathyite [$\text{K}(\text{UO}_2)(\text{AsO}_4) \cdot 4\text{H}_2\text{O}$] (Percy et al., 1993c; Percy et al., 1994b) within the deposit suggests that the mobility of Pb and As are limited. Chemical analyses of uranophane [$\text{Ca}(\text{UO}_2)_2\text{Si}_2\text{O}_7 \cdot 6\text{H}_2\text{O}$] within the Nopal I deposit indicate As contents ranging from 1,090 to 11,570 ppm and suggest that As mobilized upon oxidation of the primary ore assemblage is readily incorporated into relatively stable uranyl silicates.

Ca concentrations in goethite, hematite, and amorphous Fe-oxyhydroxides range from about 500 to 2,500 ppm. The occurrence of uranophane as the predominant secondary U mineral at the Nopal I deposit (Percy et al., 1993c) and U-rich caliche on the premining surface adjacent to the deposit (Percy and Leslie, 1993; Percy, 1994a, b) indicates that the environment was rich in Ca during alteration and weathering of the deposit. Na, Si, and Al contents in fracture-infilling minerals show a high degree of variability. Na contents range from below detection limits to 4,200 ppm. Si and Al concentrations range from 7,230 to 41,500 ppm and 270 to 19,700 ppm, respectively. Leaching of constituents of the host tuff and tuff fragments within the fracture, which are composed of quartz, feldspar, and kaolinite, is the primary source of Na, Si, and Al in the fracture-infilling.

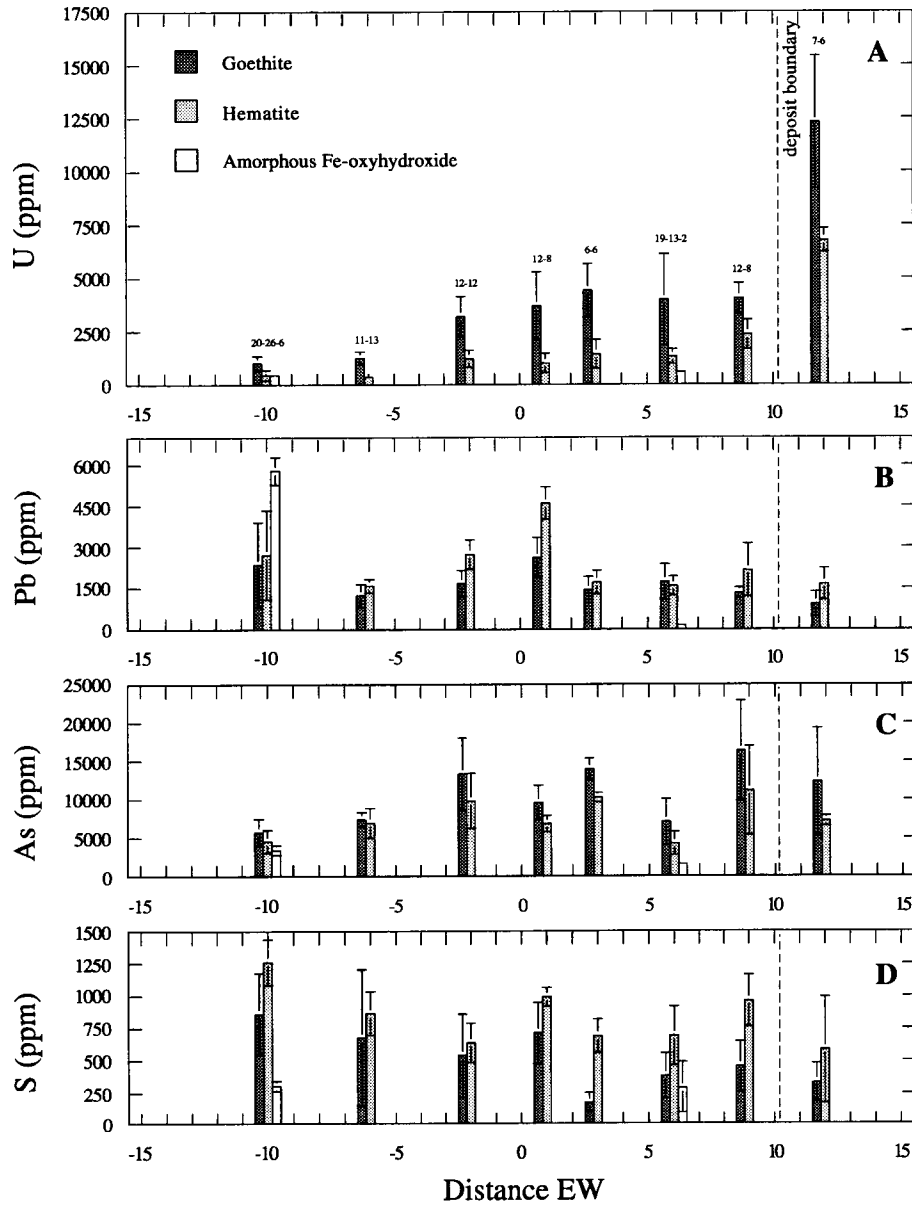


Figure 2-10. Average concentrations of (A) U, (B) Pb, (C) As, and (D) S in goethite, hematite, and amorphous Fe-oxyhydroxide along the 13.5 m N fracture. Numbers above bars in the plot for U (A) represent number of analyses on which the averages are based. Error bars show the variability (standard deviation) in the elemental concentrations.

The S content of goethite, hematite, and amorphous Fe-oxyhydroxides are generally less than the above mentioned cationic species (Figure 2-10d). The S contents range from about 200 to 1,400 ppm and show no concentration gradients with distance from the deposit (Figure 2-10d). Like Pb, the S content of hematite is greater than that of goethite and suggests that later solutions were more enriched in sulfate. The occurrence of jarosite growing from hematite substrates also indicates that the chemical environment was rich in sulfate subsequent to hematite deposition.

2.2.3 Discussion

Mineralogic and petrographic characterization indicates that mineral precipitation in the 13.5 m N fracture was a multistage process. Microscopic observations show replacement of pyrite by goethite (e.g., pseudomorphs of goethite after pyrite) over the length of the fracture. Kaolinite intergrown with goethite and amorphous Fe-oxyhydroxides also occurs throughout the fracture. Initial mineral precipitation likely consisted of pyrite and kaolinite deposited by reducing, hydrothermal solutions (Figure 2-11). The existing mineral assemblage in the 13.5 m N fracture is most likely the result of chemical weathering processes. In near-surface environments, chemical reactions between pyrite and oxygenated groundwater produce goethite, hematite, and jarosite (Bladh, 1982; Nordstrom, 1982). Environmental factors controlling the occurrence of the different mineral phases within the fracture are pH, Eh, and the availability of sulfur species. The sequence of mineralization observed in the 13.5 m N fracture suggests four distinct stages (Figure 2-11).

Stage 1—Oxidation of pyrite and replacement by goethite. The chemical processes leading to the formation of goethite during the weathering of pyrite are outlined by Bladh, 1982. Irreversible dissolution of pyrite by meteoric water is the first step in the process of chemical weathering. As pyrite dissolution proceeds, aqueous sulfur species oxidize and produce acidic groundwater. The aqueous complexes produced by pyrite dissolution are initially hydroxides. As Fe becomes fully oxidized in the acid waters, it eventually reaches saturation with goethite (Bladh, 1982).

The acidic groundwaters produced during chemical weathering of pyrite are also capable of dissolving silicate minerals. The gossan observed in the 13.5 m N fracture is probably developed during this stage as a result of dissolution of pyrite and siliceous tuff fragments within the fracture.

Stage 2—Precipitation of amorphous Fe-oxyhydroxides. Gel-like amorphous Fe-oxyhydroxides form a crust on crystalline goethite. As Eh increases at a constant pH, addition of hydroxide to a ferric salt in solution results in the precipitation of amorphous Fe-hydroxide of indeterminate water content (Garrels and Christ, 1965). These amorphous Fe-oxyhydroxides are unstable with respect to both hematite and goethite (Garrels and Christ, 1965; Nordstrom, 1982). Thus, with sufficient time, amorphous Fe-oxyhydroxides will dehydrate to much more stable hematite or goethite.

Stage 3—Hematite precipitation. Paragenetic relationships suggest that hematite formed after removal of pyrite. For example, colloform hematite is present in open spaces left by pyrite dissolution. The removal of pyrite within the 13.5 m N fracture is probably accompanied by a decrease in the activity of aqueous hydroxide, leading to a decrease in solution pH. As pH decreases under constant Eh conditions, hematite precipitation is favored over goethite precipitation (Garrels and Christ, 1965).

Stage 4—Jarosite precipitation. Jarosite most commonly precipitates in acidic, sulfate-rich environments (Nordstrom, 1982). Paragenetic relationships again indicate that jarosite precipitation within

Paragenesis of Minerals in the 13.5 m N Fracture

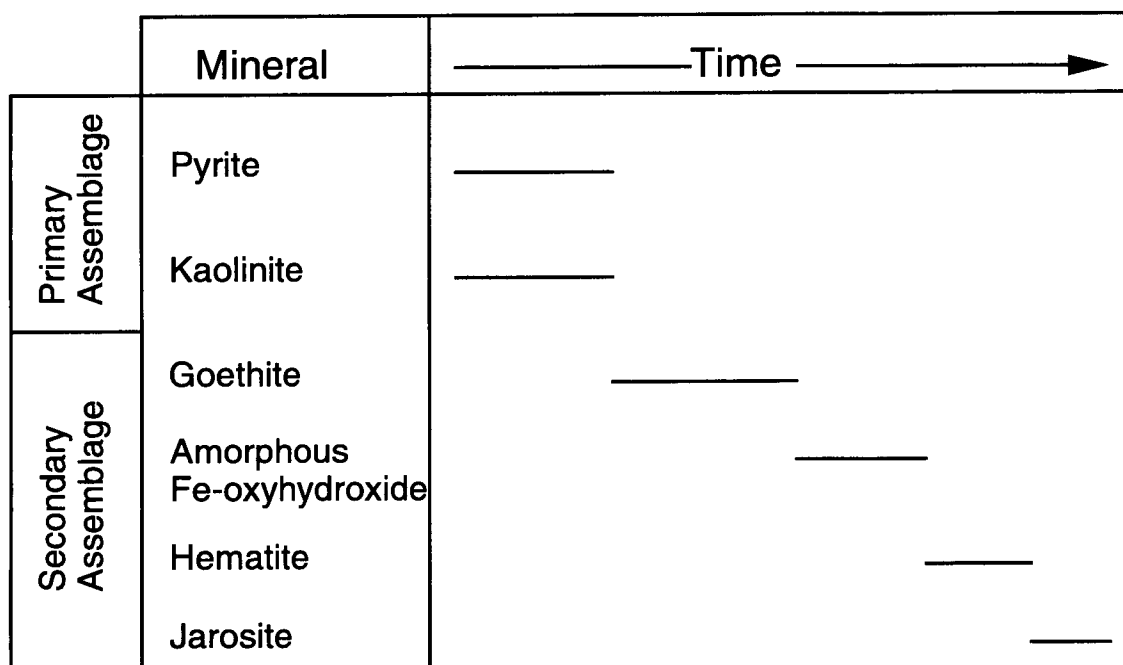


Figure 2-11. Relative sequence of formation of minerals in the 13.5 m N fracture

the 13.5 m N fracture occurred after removal of pyrite. For example, jarosite grows into open vugs from hematite substrates and is present in the open spaces of gossan, which results from pyrite dissolution (see Figures 2-5 and 2-6).

Increase in the abundance of hematite with distance from the deposit reflects variation in solution chemistry within the fracture. As the fracture aperture narrows with distance from the deposit, the abundance of fracture-infilling minerals decreases. Assuming that the rate of pyrite oxidation was constant over the length of the fracture, then pyrite removal would have occurred earlier at greater distance from the deposit. After pyrite is removed, a decrease in the activity of aqueous hydroxide, leading to a decrease in solution pH, would be expected. This decrease in solution pH would favor the precipitation of hematite over goethite or amorphous Fe-oxyhydroxides (Garrels and Christ, 1965). The general low abundance of hematite within and near the deposit margin suggests that acidic, hydroxide-rich conditions, possibly produced by oxidation of pyrite associated with the primary ore mineral assemblage (see below), dominate this part of the fracture.

Increase in the abundance of amorphous Fe-oxyhydroxides with distance from the deposit appears to be related to hematite formation. Farther from the deposit, hematite forms a thicker and more continuous colloform crust on amorphous Fe-oxyhydroxides, which effectively isolates the amorphous material from solutions moving through the fracture (see Figures 2-4 and 2-5). Even though the amorphous Fe-oxyhydroxides are unstable and will eventually dehydrate to form hematite or goethite, they are preserved by their isolation from fluids moving through the fracture.

The occurrence of euhedral jarosite precipitating in open spaces suggests that the 13.5 m N fracture was exposed to late-stage, acidic, sulfate-rich solutions. Paragenetic relationships indicate that pyrite at the Level +10 horizon was removed prior to jarosite formation. Therefore, sulfate and Fe for this late stage of mineral formation were probably derived from oxidation of pyrite elsewhere; most likely, pyrite within the deposit associated with the primary ore assemblage.

The primary U mineralization at Nopal I consists of a uraninite-pyrite-kaolinite-quartz assemblage deposited by hydrothermal solutions moving up along fractures (Pearcy et al., 1993c; Pearcy et al., 1994b). The apparent occurrence of a pyrite + kaolinite association in the 13.5 m N fracture suggests that the fracture may have been open to the hydrothermal solutions that formed the primary ore deposit. Within the U deposit, the presence in fractures of uranyl oxide hydrate and uranyl silicate minerals formed by uraninite oxidation is ubiquitous (Pearcy et al., 1993c; Pearcy et al., 1994b). On the other hand, U minerals are absent in the 13.5 m N fracture, even in the portion of the fracture within the deposit. In addition, no textural evidence exists that would indicate that uraninite or oxidized U minerals were ever constituents of the 13.5 m N fracture. It is possible that U minerals formed by oxidation of uraninite within the fracture were removed by acid leaching. For example, an area in the interior of the deposit between about 5 and 10 m N and 15 and 20 m E has undergone intense acid sulfate leaching. This area contains alunite [$KAl_3(SO_4)_2(OH)_6$], jarosite, hematite, and goethite but no visible U minerals, suggesting mobilization and removal of U. The occurrence of jarosite within the 13.5 m N fracture indicates that the fracture has been exposed to late-stage, acidic, sulfate-rich solutions, and these solutions may be capable of dissolving oxidized U minerals.

The absence of U minerals within the 13.5 m N fracture and the structural evidence that indicates the fracture is younger than the deposit (Pearcy, 1994a, b) suggest that subsequent hydrothermal solutions (i.e., solutions not associated with the primary U deposit) were responsible for the initial pyrite and kaolinite assemblage in the fracture. These solutions may have contained U leached from the volcanic host rock or from the U deposit itself. Therefore, U may have been available as a coprecipitate in pyrite within the fracture. Unfortunately, pyrite no longer exists in the 13.5 m N fracture; therefore, its original trace element content cannot be determined. Although the microcrystalline nature of kaolinite within the fracture precluded measurement of its U content, it is also capable of retaining U due to the sorptive properties of clay minerals. Dissolution of pyrite during oxidative chemical weathering would release any U present into solution. In addition, U sorbed onto kaolinite would be susceptible to leaching by acid groundwater produced by chemical weathering of pyrite. U released by these weathering processes would then be available for coprecipitation in secondary minerals forming within the fracture.

Chemical and isotopic analyses indicate that there are strong mineralogic controls on the distribution of U in the 13.5 m N fracture. These controls must be understood if the radionuclide retardation potentials of secondary minerals are to be assessed. The anomalous U contents measured in goethite, hematite, and amorphous Fe-oxyhydroxides within the 13.5 m N fracture indicate that these secondary minerals are capable of retaining U. Concentration profiles in both the bulk fracture-infilling and in goethite and hematite, which show systematic decreases in U contents with distance from the deposit, suggest that U within the 13.5 m N fracture was mobilized and transported away from the deposit. Because the U is most likely mobilized by episodic penetration of meteoric water, the concentration profiles probably represent U transport from more than one event.

The U deposit itself has undergone extensive chemical weathering as indicated by the pervasive occurrence of oxidized U minerals along with crystalline and amorphous Fe-oxides and Fe-hydroxides within fractures in the deposit. As mentioned earlier in this section, an area in the interior of the deposit

on the Level +10 surface contains alunite, jarosite, hematite, and goethite. However, the area contains no visible U minerals, which suggests mobilization and transport of U away from this area. There is also evidence for U mobilization and transport from the U deposit out into the surrounding host rock on other portions of the Level +10 surface. North of the deposit, gamma intensity mapping indicates the presence of anomalous U concentrations (i.e., U concentrations 4 to 10 times above local background values) that extend continuously from the deposit margin through fractured tuff for about 20 m (Pearcy, 1994a, b). Similar to the 13.5 m N fracture, anomalous U concentrations in generally fractured tuff along a 2-m traverse at 9.1 m N show systematic decreases with distance from the deposit (Pearcy and Leslie, 1993).

Mobilization and transport of U from the area of primary deposition is also supported by U-series measurements. $^{234}\text{U}/^{238}\text{U}$ disequilibrium in the generally fractured tuff along the 2-m traverse at 9.1 m N indicates U transport outside the deposit during the last 1 Ma (Pearcy and Leslie, 1993). U-series dating of U-enriched caliche collected on the premining surface and located about 30 m S of the 13.5 m N fracture indicates significant U transport at 53.6 ± 8 Ka, indicating that the U deposit has been subjected to hydrologically unsaturated, chemically oxidizing conditions for at least that period (Pearcy, 1994a, b). In addition, paragenetically late, U-rich opal collected from the deposit about 5 m S of the 13.5 m N fracture has been dated by U-series techniques at 54.3 ± 2 Ka.

In contrast to U, the concentration profiles of other trace elements in secondary mineral phases within the 13.5 m N fracture show no observable trends with distance from the deposit. It is likely that the source of trace elements such as As and Pb is similar to that of U (e.g., As and Pb in uraninite or U, As, and Pb in pyrite). Assuming that the primary U ore assemblage is a source of elements such as U, As, and Pb in the 13.5 m N fracture, then, like U, decreasing concentration gradients with distance from the deposit would be expected for As and Pb. The lack of correlation between the concentration profiles for these trace elements and U suggests that their mobility or geochemical transport characteristics are unrelated. Perhaps the geochemical conditions (i.e., pH and Eh) accompanying chemical weathering of the deposit do not favor transport of As and Pb. As mentioned earlier, the occurrence of Pb- and As-rich uranyl minerals within the deposit suggests that the mobility of these elements may be limited. If so, the primary source of As and Pb in secondary minerals in the 13.5 m N fracture may be the initial hydrothermally precipitated pyrite and kaolinite mineral assemblage.

U-series disequilibrium measurements provide additional information on U mobility along the 13.5 m N fracture. The $^{234}\text{U}/^{238}\text{U}$ activity ratios of all the bulk fracture-infilling samples from the 13.5 m N fracture are greater than unity and are indicative of "recent" U uptake from fracture fluids that carried excess ^{234}U . Interpretation of U mobilization and transport along the 13.5 m N fracture using U-series measurements requires an understanding of the mineralogic location and distribution of isotopes. The decreasing trend in $^{234}\text{U}/^{238}\text{U}$ activity ratios of the bulk fracture-infilling may be related to variations in the isotopic signatures of U-bearing minerals with distance from the deposit. For example, goethite is the dominant mineral near the deposit margin, whereas the abundance of hematite and amorphous Fe-oxyhydroxides increases with distance from the deposit. Selective leaching of samples from the 13.5 m N fracture for U and Th are currently under way and will provide information on the distribution of U-series isotopes in mineral phases of the fracture-infilling. Important insight into U mobilization and transport processes within the 13.5 m N fracture may be provided by this information.

Although the distribution of U-series isotopes in mineral phases within the 13.5 m N fracture is unknown at this time, U-series measurements of the bulk fracture-infilling provide insight into general U mobilization processes. The systematic decrease in $^{234}\text{U}/^{238}\text{U}$ activity ratios with distance from the deposit margin (with a notable exception at -7 m E) suggests a multistage mobilization process. A single

stage of U deposition in the fracture would have resulted in constant $^{234}\text{U}/^{238}\text{U}$ throughout. The $^{234}\text{U}/^{238}\text{U}$ trend may result from remobilization of U from ^{234}U -enriched infilling materials. Assuming that ^{234}U in the fracture-infilling is being mobilized (e.g., by differential leaching or alpha recoil) and transported away from the fracture at the Level +10 horizon (e.g., by downward infiltration of meteoric water) at a constant rate, a decreasing $^{234}\text{U}/^{238}\text{U}$ trend would be produced due to the smaller mass of U in the fracture-infilling with distance from the deposit. This condition would also be expected to produce a trend of *increasing* $^{230}\text{Th}/^{234}\text{U}$ away from the deposit. This trend could be less pronounced if the $^{234}\text{U}/^{238}\text{U}$ of the removed U is high. Alternatively, the trend of decreasing $^{234}\text{U}/^{238}\text{U}$ could have been produced had the recent U enrichment been superimposed on an earlier U enrichment, which had either produced no $^{234}\text{U}/^{238}\text{U}$ disequilibrium or had lost disequilibrium through decay. Higher $^{234}\text{U}/^{238}\text{U}$ near the deposit thus would indicate a greater degree of enrichment, consistent with the U concentration gradient. This model requires that the earlier enrichment produced rather uniform U concentrations (similar to the lower values at the west end of the fracture) throughout the fracture.

Regardless of the mechanism producing the $^{234}\text{U}/^{238}\text{U}$ trend, remobilization of ^{234}U from the fracture-infilling after ^{230}Th ingrowth (which would require on the order of 300 Ka assuming negligible initial ^{230}Th in the fracture) is consistent with the greater than unity $^{230}\text{Th}/^{234}\text{U}$ activity ratios observed along the fracture. This sequence can be summarized as follows: (i) U deposition in the fracture-infilling material from high- $^{234}\text{U}/^{238}\text{U}$ groundwater less than 1 Ma, but more than 0.3 Ma, before present; (ii) ingrowth of ^{230}Th toward equilibrium with ^{234}U , requiring at least 0.3 Ma and accompanied by a decrease due to decay in $^{234}\text{U}/^{238}\text{U}$; and (iii) remobilization of U out of the fracture-infilling, with or without preferential ^{234}U removal, resulting in an increase in $^{230}\text{Th}/^{234}\text{U}$ and unchanged or decreased $^{234}\text{U}/^{238}\text{U}$ (while still maintaining a memory of the original ^{234}U enrichment). The observed relative enrichment scheme of $^{230}\text{Th} > ^{234}\text{U} > ^{238}\text{U}$ requires such a multistage, open-system history. It is plausible that the latter two stages have operated concurrently to raise $^{230}\text{Th}/^{234}\text{U}$ and lower $^{234}\text{U}/^{238}\text{U}$ over the last few hundred thousand years. These stages represent a regime in which U retention and/or removal are dominant over U accumulation; this shift may be related to the cessation of growth of the secondary assemblage, which had provided for U accumulation by coprecipitation. Alternatively, this shift could be related to changes in the flow regime that effectively diminished the role of the ore deposit as a source of transported U.

It is important to note the implications of this model for the ages of the fracture-infilling minerals. It is apparent from Figure 2-10 that the U in these rocks is dominantly sited within, rather than sorbed onto, the minerals. The fact that these minerals maintain ^{234}U enrichments that are not confined to their surfaces requires that they be formed within the last 1 Ma. Considering that $^{234}\text{U}/^{238}\text{U}$ ratios of up to 1.4–1.6 are preserved, it is likely that they are significantly younger than that. A lower bound on their ages is provided by the necessity for an interval of approximately 0.3 Ma to elapse for $^{230}\text{Th}/^{234}\text{U}$ to evolve from very low values toward unity. Thus, this model implies that the fracture-infilling phases are between 1 and 0.3 Ma old. This age, in turn, implies that the oxidizing conditions that led to formation of the goethite-amorphous Fe-oxyhydroxide-hematite-jarosite assemblage have been in force for at least that long.

Differential transport of ^{234}U -enriched solutions away from the deposit is another mechanism that could produce the trend of decreasing $^{234}\text{U}/^{238}\text{U}$ ratios measured along the 13.5 m N fracture. U within the deposit is mobilized by episodic infiltration of meteoric water, which is likely enriched in ^{234}U by radiation-related processes such as alpha recoil. As indicated earlier in this section, because U is mobilized by episodic penetration of meteoric water, the decreasing U concentration gradients probably represent net U transport from more than one event. The distance that U travels away from the deposit in any one of these events depends on the residence time of meteoric water within the fracture. As

chemical weathering in the 13.5 m N fracture proceeds, secondary infilling minerals forming nearer the deposit are probably exposed to U-bearing meteoric water enriched in ^{234}U more often than secondary minerals farther from the deposit. The proximal portion of the fracture would thus be replenished in U with high- $^{234}\text{U}/^{238}\text{U}$ more frequently than the distal fracture, resulting in higher $^{234}\text{U}/^{238}\text{U}$ near the deposit as the $^{234}\text{U}/^{238}\text{U}$ ratios farther out are more strongly affected by decay. Without a subsequent U depletion event, this scenario requires excess ^{230}Th accumulation by some other means such as preferential sorption of ^{230}Th generated by dissolved ^{234}U .

Based on comparison with other studies (Ivanovich et al., 1992), and considering the unlikelihood of significant ^{230}Th enrichment by sorption in a U-rich environment, the first model of U-series evolution, involving initial U enrichment, ^{230}Th ingrowth, and U depletion, is preferred. It is likely that these processes did not occur as single events, but acted more or less continuously over different, though possibly overlapping, time periods. It is also possible that the preferential deposition of U near the deposit, as described in the previous paragraph, was also a factor in producing the $^{234}\text{U}/^{238}\text{U}$ gradient.

2.2.4 Conclusions

Among the processes that may contribute to retardation and retention of radionuclides released from a HLW repository is secondary non-U mineral formation. The objective of the current study was to establish if this process can be observed in a natural system. Secondary infilling minerals with anomalous U contents from a fracture that crosscuts the Nopal I U deposit on the Level +10 surface between 13 m and 15 m N were studied. A variety of analytical techniques were employed to elucidate the paragenetic history of the fracture, to determine the distribution and behavior of U in secondary minerals, and to examine evidence for U transport from a concentrated radionuclide source (i.e., the U deposit) out into the surrounding host rock.

The primary mineral assemblage in the 13.5 m N fracture is interpreted, based on textural evidence from petrographic observations, to consist of pyrite and kaolinite formed by hydrothermal solutions moving through the fracture. The secondary mineral assemblage within the 13.5 m N fracture includes goethite, hematite, amorphous Fe-oxyhydroxides, and jarosite, produced by chemical weathering of pyrite. Anomalous U concentrations (e.g., several hundred to several thousand ppm U) measured in goethite, hematite, and amorphous Fe-oxyhydroxides within the 13.5 m N fracture indicate that these secondary minerals are capable of retaining U. The very high *in situ* U contents of these Fe phases and the absence of U minerals within the fracture, even at nanometer scale, indicate that U was sequestered during secondary mineral growth.

Decreasing U concentration gradients in the bulk fracture-infilling and in goethite and hematite with distance from the deposit strongly suggest that U was mobilized and transported away from the deposit. These decreasing U concentration profiles probably represent net U transport from more than one event. U within the deposit was most likely mobilized and transported away from the deposit by episodic infiltration of meteoric water.

Disequilibrium $^{234}\text{U}/^{238}\text{U}$ ratios in bulk fracture-infillings along the 13.5 m N fracture indicate relatively recent U mobilization (i.e., <1 Ma). The greater than unity $^{234}\text{U}/^{238}\text{U}$ ratios measured in bulk fracture-infilling samples indicate U uptake from fracture fluids that carried excess ^{234}U . Systematic decreases in $^{234}\text{U}/^{238}\text{U}$ ratios with distance from the deposit margin suggest a multistage mobilization

process, such as remobilization of U from ^{234}U -enriched infill materials or differential transport of U-bearing solutions containing excess ^{234}U away from the deposit. The greater than unity $^{230}\text{Th}/^{234}\text{U}$ activity ratios measured in bulk fracture-infilling samples probably result from remobilization of U from infill minerals after ^{230}Th ingrowth or preferential sorption of ^{230}Th generated by dissolved ^{234}U .

2.3 ASSESSMENT OF PROGRESS TOWARD MEETING PROJECT OBJECTIVES

The Geochemical Natural Analog Research Project is making good progress toward the objectives listed in Section 4.1. Research results presented in this report and elsewhere (e.g., Percy et al., 1994a) have begun to provide a realistic understanding of the utility and limitations of natural analog studies when employed to support a license application for a HLW repository.

At Peña Blanca, fundamental data have been gathered and interpreted on U mineral characteristics, stabilities, and alteration sequences in a geologic environment comparable to that anticipated for the proposed YM repository. This information is required for development and evaluation of reasonable PA models for radionuclide transport. For example, data being gathered within the Geochemical Natural Analog Research Project on the matrix hydraulic properties of silicic tuff are being used within the PA Research Project to support modeling efforts. Additionally, progress has been made in evaluation of the roles of fracture and matrix transport of U in a YM-like environment. This information has been used in the development of CDS 3.2.3.3 (mineral assemblages), CDS 3.2.3.5 (geochemical processes), and CDS 5.4 (EBS performance).

The data in this report add to the understanding of a system in which radionuclides have been available for transport under conditions comparable to those anticipated for YM. Specifically, Iterative Performance Assessment has identified substantial conceptual uncertainties regarding appropriate implementation of fracture transport and fracture retardation. Results reported here identified specific mineral phases that have retained transported U under YM-comparable conditions. Likely processes by which U has been mobilized, transported, and retained by secondary minerals at the Nopal I deposit have been identified. These results will reduce conceptual uncertainties regarding U transport in future versions of PA models. For example, confirmation that model results for retention of U are scaled realistically can be derived from measurements of U retention in fractures at Nopal I. Additionally, the detailed characterization of a major fracture at Nopal I described in this report provides useful information for design and implementation of field-based hydraulic percolation tests. Such tests are planned to address the KTU identified in CDSs for hydrogeologic processes (3.2.2.1), hydrologic conditions (3.2.2.9), and perched water (3.2.2.12) concerning groundwater flow codes not tested against field data.

Results from the Akrotiri site have included development of constraints on models for hydraulic infiltration and runoff (e.g., Murphy et al., 1991; Murphy and Percy, 1994; Percy et al., 1993b; Percy et al., 1994a). An explicit role and objective of natural analog studies specified in 10 CFR Part 60 are to support models for repository performance. Models for repository performance range from conceptualizations of physical processes, to mechanistic models of specific processes, to probabilistic assessments designed to bound total-system performance and to evaluate uncertainty in the bound. Research at Akrotiri has demonstrated that natural analog studies can support these models by identification of important components and processes in a contaminant transport system and by quantitative evaluations of the long-term behavior of contaminants in a geologic environment (Murphy et al., 1994). This understanding is anticipated to provide essential input to development of CDMs 6.1 and 6.2 (KTU

topic: uncertainties associated with development and validation of conceptual and mathematical models); 3.2.2.1, 3.2.2.9 (KTU topic: uncertainty in developing a conceptual and mathematical vapor and liquid water phase transport model that is representative of the YM site flow system); and 3.2.3.5 (KTU topic: uncertainty in predictions of effects of environmental conditions on the waste package during the containment period).

The U.S. Department of Energy (DOE) has initiated analog research related to a YM repository. The DOE is studying water/rock interactions in hot springs in New Zealand in an attempt to validate the EQ3/6 computer code. In addition to these efforts, other DOE analog research is under consideration (e.g., Chapman et al., 1992). Center for Nuclear Waste Regulatory Analyses (CNWRA) work at Peña Blanca and at Akrotiri provides a strong base of experience from which to evaluate DOE analog studies. Results from CNWRA analog research allow informed comment on selection of sites, site characterization techniques, applications of the analog data, and use of the analog data for evaluation of models for the performance of a YM repository.

2.4 PLANS FOR NEXT REPORT PERIOD

Field research anticipated during the next report period (July 1, 1995 to December 31, 1995) will focus on the Peña Blanca site. At Peña Blanca, observations will be made, and samples will be collected to further investigate the partitioning of U among secondary, fracture-filling minerals within and near the Nopal I deposit. Detailed observations and measurements will be made of fracture patterns and fracture geometries in selected areas to improve conceptual models of transport through the Nopal I fracture network. An effort will also be made to collect groundwater from an apparent perched zone beneath the Level +10 surface, from seeps inside the Level +00 adit, and from wells in the area for geochemical and U-series isotopic analyses. These data will be useful for understanding present-day transport processes. These observations and measurements will also support planning for proposed field infiltration tests at the Nopal I site.

Laboratory research during the next period is planned to include U content and rare earth content measurements on samples from Peña Blanca. Optical microscopy, scanning electron microscopy, energy dispersive x-ray analyses, and powder diffraction x-ray analyses are planned for Peña Blanca samples. Ion probe measurements are planned for Nopal I uraninite and secondary uranyl minerals to determine rare earth element contents and to make isotopic measurements to allow radiometric ages to be interpreted. Gamma spectrometry measurements will be used to measure U-series disequilibria within Nopal I samples. Data interpretation activities planned for Peña Blanca during the next report period include quantitative modeling of the U-series data reported here, as well as interpretation of anticipated isotopic measurements to date samples from the Nopal I deposit. Conductivity data collected across the Nopal I cuesta will be further analyzed to interpret postulated perched water zones at and near Nopal I.

2.5 REFERENCES

- Bladh, K.W. 1982. The formation of goethite, jarosite, and alunite during the weathering of sulfide-bearing felsic rocks. *Economic Geology* 77: 176-184.
- Chapman, N., P.L. Cloke, J.-C. Petit, J.A.T. Smellie, and A.E.J. van Luik. 1992. *Applications of Natural Analogue Studies to Yucca Mountain as a Potential High Level Radioactive Waste Repository*. Las Vegas, NV: Office of Civilian Radioactive Waste Management: U.S. Department of Energy.

- Garrels, R.M., and L.C. Christ. 1965. *Solutions, Minerals, and Equilibria*. San Francisco, CA: Freeman, Cooper, and Company.
- Gascoyne, M. 1992. Geochemistry of the actinides and their daughters. *Uranium Series Disequilibrium: Applications to Earth, Marine, and Environmental Sciences*. 2nd ed. M. Ivanovich and R.S. Harmon, eds. New York, NY: Oxford University Press: 2: 34–61.
- Green, R.T., K. Meyer, and G. Rice. 1994. *Hydraulic Characterization of Hydrothermally Altered Nopal Tuff*. CNWRA 94-027. San Antonio, TX: Center for Nuclear Waste Regulatory Analyses.
- Hayba, D.O., P.M. Bethke, P. Heald, and N.K. Foley. 1985. Geologic, mineralogic, and geochemical characteristics of volcanic-hosted epithermal precious-metal deposits. *Geology and Geochemistry of Epithermal Systems*. B.R. Berger and P.M. Bethke, eds. El Paso, TX: The Economic Geology Publishing Company: 129–167.
- Heath, M.J., M. Montoto, A. Rodriguez Rey, V.G. Ruiz de Argandoña, and B. Menendez. 1992. Rock matrix diffusion as a mechanism of radionuclide retardation: A natural analogue study of El Berrocal granite, Spain. *Radiochimica Acta* 58/59: 379–384.
- Ivanovich, M., A.G. Latham, G. Longworth, and M. Gascoyne. 1992. Applications to radioactive waste disposal studies. *Uranium Series Disequilibrium: Applications to Earth, Marine, and Environmental Sciences*. 2nd ed. M. Ivanovich and R.S. Harmon, eds. New York, NY: Oxford University Press: 17: 583–630.
- Leslie, B.W., E.C. Percy, and J.D. Prikryl. 1993a. Geochemical natural analogs. *NRC High-Level Radioactive Waste Research at CNWRA January–June 1992*. W.C. Patrick, ed. NUREG/CR-5817. Washington, DC: Nuclear Regulatory Commission: 3(1).
- Leslie, B.W., E.C. Percy, and J.D. Prikryl. 1993b. Oxidative alteration of uraninite at the Nopal I deposit, Mexico: Possible contaminant transport and source term constraints for the proposed repository at Yucca Mountain. *Materials Research Society Proceedings*: Pittsburgh, PA: Materials Research Society: 294: 505–512.
- Ménager, M.T., M.J. Heath, M. Ivanovich, C. Montjotin, R. Barillon, J. Camp, and S.E. Hasler. 1994. Uranium migration/retention processes in core profiles from El Berrocal (Spain): Implications for matrix diffusion in fractured granite. *Radiochimica Acta* 66/67: 475–483.
- Murphy, W.M., and E.C. Percy. 1994. Performance assessment significance of natural analog studies at Peña Blanca, Mexico, and at Santorini, Greece. *Fifth Natural Analogue Working Group Meeting and Alligator Rivers Analogue Project (ARAP) Final Workshop*. H. von Maravic and J. Smellie, eds. Brussels: Commission of the European Communities: Final Report n° EUR 15178 EN: 219–224.
- Murphy, W.M., E.C. Percy, and P.C. Goodell. 1991. Possible analog research sites for the proposed high-level nuclear waste repository in hydrologically unsaturated tuff at Yucca Mountain, Nevada. *Fourth Natural Analogue Working Group Meeting and Pocos de Caldas Project Final*

Workshop. B. Come and N.A. Chapman, eds. Brussels: Commission of the European Communities: Final Report n° EUR 13014 EN: 267–276.

- Murphy, W.M., E.C. Percy, S. Mohanty, and J.D. Prikryl. 1994. Geochemical natural analog research. *NRC High-Level Radioactive Waste Research at CNWRA July–December 1994*. B. Sagar, ed. CNWRA 94-02S. San Antonio, TX: Center for Nuclear Waste Regulatory Analyses: 51–66.
- Neretnieks, I. 1980. Diffusion in the rock matrix: An important factor in radionuclide migration? *Journal of Geophysical Research* 85: 4,379–4,397.
- Nordstrom, D.K. 1982. Aqueous pyrite oxidation and the consequent formation of secondary iron minerals. *Acid Sulfate Weathering*. Madison, WI: Soil Science Society of America: Special Publication Number 10: 37–56.
- Nuclear Regulatory Commission. 1987. *Disposal of High-Level Radioactive Wastes in Geologic Repositories*. Title 10, Energy, Part 60 (10 CFR Part 60). Washington, DC: U.S. Government Printing Office.
- Nuclear Regulatory Commission. 1994. *License Application Review Plan for the Review of a License Application for a Geologic Repository for Spent Nuclear Fuel and High-Level Radioactive Waste Yucca Mountain Site, Nevada*. NUREG/CR-1323. Washington, DC: Nuclear Regulatory Commission.
- Pearcy, E.C. 1994a. Geochemical natural analog research. *NRC High-Level Radioactive Waste Research at CNWRA January–June 1994*. B. Sagar, ed. CNWRA 94-01S. San Antonio, TX: Center for Nuclear Waste Regulatory Analyses: 57–76.
- Pearcy, E.C. 1994b. *Fracture Transport of Uranium at the Nopal I Natural Analog Site*. CNWRA 94–011. San Antonio, TX: Center for Nuclear Waste Regulatory Analyses.
- Pearcy, E.C., and W.M. Murphy. 1990. Geochemical natural analogs. *Report on Research Activities for Calendar Year 1990*. W.C. Patrick, ed. NUREG/CR-5817. Washington, DC: Nuclear Regulatory Commission: 7-1 to 7-7.
- Pearcy, E.C., and B.W. Leslie. 1993. Geochemical natural analog research. *NRC High-Level Radioactive Waste Research at CNWRA January–June 1993*. B. Sagar, ed. CNWRA 93-01S. San Antonio, TX: Center for Nuclear Waste Regulatory Analyses: 7-1 to 7-19.
- Pearcy, E.C., and W.M. Murphy. 1991a. Geochemical natural analogs. *Report on Research Activities for the Quarter July 1 through September 30, 1991*. W.C. Patrick, ed. CNWRA 91-03Q. San Antonio, TX: Center for Nuclear Waste Regulatory Analyses: 7-1 to 7-9.
- Pearcy, E.C., and W.M. Murphy. 1991b. Geochemical natural analogs. *Report on Research Activities for the Quarter April 1 through June 30, 1991*. W.C. Patrick, ed. CNWRA 91-02Q. San Antonio, TX: Center for Nuclear Waste Regulatory Analyses: 7-1 to 7-7.

- Pearcy, E.C., and W.M. Murphy. 1991c. Geochemical natural analogs. *Report on Research Activities for the Quarter January 1 through March 31, 1991*. W.C. Patrick, ed. CNWRA 91-01Q. San Antonio, TX: Center for Nuclear Waste Regulatory Analyses: 7-1 to 7-7.
- Pearcy, E.C., and W.M. Murphy. 1991d. *Geochemical Natural Analogs Literature Review*. CNWRA 90-008. San Antonio, TX: Center for Nuclear Waste Regulatory Analyses.
- Pearcy, E.C., and W.M. Murphy. 1992. *Site Selection and Workplan Report for the Geochemical Natural Analog Research Project*. CNWRA 92-014. San Antonio, TX: Center for Nuclear Waste Regulatory Analyses.
- Pearcy, E.C., B.W. Leslie, W.M. Murphy, and R.T. Green. 1993a. Geochemical natural analogs. *Report on Research Activities for the Quarter July 1 through December 31, 1992*. W.C. Patrick, ed. CNWRA 92-02S. San Antonio, TX: Center for Nuclear Waste Regulatory Analyses: 7-1 to 7-27.
- Pearcy, E.C., W.M. Murphy, R.T. Green, B.W. Leslie, and J.D. Prikryl. 1993b. Geochemical natural analogs. *NRC High-Level Radioactive Waste Research at CNWRA for Calendar Year 1991*. W.C. Patrick, ed. NUREG/CR-5817. Washington, DC: Nuclear Regulatory Commission: 7-1 to 7-32.
- Pearcy, E.C., J.D. Prikryl, W.M. Murphy, and B.W. Leslie. 1993c. *Uranium Mineralogy of the Nopal I Natural Analog Site, Chihuahua, Mexico*. CNWRA 93-012. San Antonio, TX: Center for Nuclear Waste Regulatory Analyses.
- Pearcy, E.C., R.T. Green, and W.M. Murphy. 1994a. Geochemical natural analogs. *NRC High-Level Radioactive Waste Research at CNWRA July–December 1993*. W.C. Patrick, ed. CNWRA 93-02S. San Antonio, TX: Center for Nuclear Waste Regulatory Analyses: 5-1 to 5-16.
- Pearcy, E.C., J.D. Prikryl, W.M. Murphy, and B.W. Leslie, 1994b. Alteration of uraninite from the Nopal I deposit, Peña Blanca District, Chihuahua, Mexico, compared to degradation of spent nuclear fuel in the proposed U.S. high-level nuclear waste repository at Yucca Mountain, Nevada. *Applied Geochemistry* 9: 713–732.
- Prikryl, J.D., and E.C. Percy. 1994. The role of secondary mineral formation on uranium retardation and transport at the Nopal I deposit, Peña Blanca District, Chihuahua, Mexico. *Geological Society of America Abstracts with Programs–1994 Annual Meeting*. Boulder, CO: Geological Society of America.
- Ramdohr, P. 1980. *The Ore Minerals and Their Intergrowths*. New York, NY: Pergamon Press.
- Wescott, R.G., M.P. Lee, N.A. Eisenberg, and T.J. McCartin, eds. 1994. *Phase 2 Demonstration of the NRC's Capability to Conduct a Performance Assessment for a High-Level Waste Repository*. NUREG-1464. Washington, DC: Nuclear Regulatory Commission.
- U.S. Environmental Protection Agency. 1989. *Environmental Radiation Protection Standards for Management and Disposal of Spent Nuclear Fuel, High-Level and Transuranic Radioactive Wastes*. Title 40, Protection of the Environment, Part 191 (40 CFR Part 191). Washington, DC: U.S. Government Printing Office.

3 SORPTION MODELING FOR HIGH-LEVEL WASTE PERFORMANCE ASSESSMENT

by F. Paul Bertetti, David A. Pickett, and Roberto T. Pabalan

Investigators: Roberto T. Pabalan, David R. Turner, F. Paul Bertetti, David A. Pickett, and Michael G. Almendarez

NRC Project Officer: Phillip R. Reed

3.1 TECHNICAL OBJECTIVES

A fundamental concern in evaluating the stability of Yucca Mountain (YM), Nevada, as a repository for high-level nuclear waste (HLW) is the possibility of radionuclide migration from the repository to the accessible environment as dissolved constituents in groundwater. Sorption of radionuclides on minerals encountered along the flow paths could be an important mechanism for attenuating radionuclide migration. Sorption is specifically referred to in 10 CFR 60.122(b)(3) (Nuclear Regulatory Commission, 1992) as a favorable geochemical condition that could inhibit radionuclide migration and "favorably affect the ability of the geologic repository to isolate the waste." Conversely, geochemical processes that "would reduce sorption of radionuclides" are included [10 CFR 60.122(c)(8)] as potentially adverse conditions that could reduce the effectiveness of the natural barrier system.

To support the Nuclear Regulatory Commission (NRC) HLW program, the Center for Nuclear Waste Regulatory Analyses (CNWRA) is conducting research activities under the Sorption Modeling for HLW Performance Assessment (PA) Research Project. The broad objective of this project is to develop sufficient understanding of radionuclide transport issues so that timely precicensing guidance can be provided to the U.S. Department of Energy (DOE) and a sound basis is available for evaluating the DOE license application. The results will be used to support the preparation of the NRC License Application Review Plan, particularly Sections 3.2.3.2, 3.2.3.3, and 3.2.3.5, pertaining to favorable and potentially adverse geochemical conditions and processes at a potential repository site, and Section 3.4, which addresses the effectiveness of natural barriers against the release of radioactive material to the environment. Laboratory (Task 3) and modeling (Task 2) studies of radionuclide sorption, retardation, and transport, which are central to the Sorption Research Project, will provide independent bases for addressing Key Technical Uncertainties (KTUs), particularly uncertainties in identifying processes and conditions that affect radionuclide retardation and determining and predicting the magnitude of effects at YM. In addition, development of Compliance Determination Methods (CDMs) for determining compliance with the regulatory requirements will utilize data and models generated from this research project.

Results arising from this project will be integrated with those from other CNWRA activities. For example, data will be used in developing conceptual models for radionuclide transport/retardation in near- and far-field environments related to the PA Research Project (Chapter 4) and Iterative Performance Assessment (IPA) Phase 3. Results of activities undertaken during the first half of 1995 are discussed in the following sections. First, in Section 3.2, experiments that seek to characterize the oxidation states of plutonium in solution are discussed. Then Section 3.3 describes experiments investigating the sorption behavior of neptunium (Np) onto minerals relevant to YM.

3.2 PLUTONIUM EXPERIMENTS

Largely due to its complex, multivalent redox chemistry, much uncertainty remains regarding the sorption behavior of plutonium (Pu) in a repository environment. Few systematic studies of Pu sorption have been published (Sanchez et al., 1985; Righetto et al., 1991), and available data are insufficient for providing sorption coefficients to PA efforts with any degree of confidence. Following the same rationale used by the CNWRA in studies of other actinides, preparations were made to initiate experiments of sorption of Pu on mineral substrates under varying chemical conditions. Data on Pu sorption coefficients and their sensitivities to chemical conditions would be incomplete without information on the distribution of different Pu species or, at a minimum, the different oxidation states, in minerals and solution. Consequently, it was decided that an attempt would be made to track Pu oxidation states before and after sorption experiments. Tracking the oxidation states proved to be technically challenging because of the low Pu concentrations required for the experiments ($\leq 10^{-8}$ M). Due to these methodological challenges, Pu sorption experiments were not begun during the report period. Presented here is a brief summary of the preparation of experimental solutions and the results of efforts to characterize Pu oxidation states, including useful information on container sorption characteristics.

3.2.1 Plutonium Experimental Solutions

Solutions were prepared from a stock of ^{239}Pu HNO_3 solution obtained from Isotope Products Laboratories. Initial solutions were taken to near dryness repeatedly in HClO_4 in an attempt to oxidize the Pu to the Pu(VI) state. The resulting perchlorate solution was then diluted with water and HClO_4 to about 5×10^{-5} M Pu (~ 0.7 $\mu\text{Ci/g}$) in 1–2 M HClO_4 for analysis by spectrophotometry and liquid scintillation alpha counting (LSC). A portion of one of these Pu solutions was electrolytically converted to Pu(V) following the methods of Newton et al. (1986), Bennett et al. (1992), and Neu et al. (1994). Further dilutions were made using water, or 0.1 M NaClO_4 , with ^{239}Pu concentrations determined at each step by LSC. For bottle sorption experiments, pH was adjusted by the addition of HClO_4 or NaHCO_3 .

3.2.2 Plutonium Oxidation State Determination by Solvent Extraction

Because it is necessary to run Pu sorption experiments at concentrations of around 10^{-8} M (due to solubility limitations), conventional spectrophotometric methods are inadequate for Pu species determinations in experimental solutions. Progress has been made by other researchers (e.g., Okajima et al., 1991; Clark et al., 1994) in the utilization of laser photoacoustic spectroscopy for identifying Pu species at low concentrations. Preliminary discussions have begun concerning the use of such a facility for CNWRA experimental work. Technical capabilities at CNWRA, however, are currently limited to the use of chemical means for measuring oxidation states. A method of solvent extraction was tested that is reported to be capable of discriminating all four common oxidation states of Pu by way of four separate solvent extractions followed by LSC (Nitsche et al., 1994a). The accuracy of the method was checked by (i) spectrophotometric measurement of the concentration of Pu(VI), using the molar absorptivity value of Cohen (1961), in solutions of $>10^{-5}$ M Pu; (ii) dilution to concentrations of around 10^{-8} M Pu; (iii) solvent extraction of both concentrated and dilute solutions to determine molarities of Pu(III), Pu(IV), Pu(V), and Pu(VI); and (iv) comparison of results for Pu(VI). (Note that spectrophotometric determination of states other than Pu(VI) was precluded by low concentrations and molar absorptivities.)

Solvent extraction determination of the more concentrated solutions ($>10^{-5}$ M) necessitated dilution by a factor of ten, and extraction results were always consistent with spectrophotometry within

10 percent. It was thus concluded that the extraction method is accurate, at least for Pu(VI), down to concentrations of 10^{-6} M Pu. This conclusion is consistent with other studies (e.g., Neu et al., 1994). The method was unreliable, however, at 10^{-8} M Pu. Table 3-1 compares results of two separate tests, and in both cases the extraction method at $\sim 10^{-8}$ M yielded a much lower estimate of Pu(VI) than at $\sim 10^{-6}$ M. At low concentrations, the extraction overestimates Pu(V) mainly at the expense of Pu(VI). The method is also apparently inadequate for estimating "oxidized" (i.e., V+VI) versus "reduced" [i.e., III+IV+polymeric Pu (IV)]. In Test 2, for example, V+VI = 65 percent at high concentration, 83 percent at low. Therefore, it seems that the solvent extraction method is unreliable for Pu oxidation state estimates at Pu concentrations around 10^{-8} M; this unreliability may be related to impurities in the reagents¹. Other determinations of solutions expected to be dominated by Pu(VI) confirmed this conclusion. If Pu species of experimental solutions are to be estimated with a reasonable degree of accuracy, sensitive methods such as laser photoacoustic spectroscopy may be needed.

The solvent extraction method was also applied to a solution of 10^{-8} M Pu, which had equilibrated at pH 1.8 for 16 days. EQ3NR calculations for this solution (0.1 M NaClO₄ equilibrated with atmosphere) suggest that its Pu should be 100 percent in the VI state. The extraction method yielded 6 percent Pu(VI) and 82 percent Pu(V), further evidence of its unreliability.

3.2.3 Preparation of "Pure" Oxidation State Plutonium Solutions

The results in Table 3-1 for high-concentration solutions, as well as consistent spectrophotometric results, demonstrate a lack of success in preparing solutions of relatively pure Pu(VI). It is possible that HClO₄ fuming could be performed more extensively or aggressively. Autoradiolytic reduction of Pu(VI) to Pu(V) is a possible cause of Pu(VI) instability in concentrated solutions, but this reduction is a very slow process at concentrations of 10^{-5} M and lower (Newton et al., 1986); thus, rapid dilution following HClO₄ oxidation could improve results. Furthermore, the electrolytic method for preparing a Pu(V) solution from Pu(VI) yielded a solution of only 67 percent Pu(V); conditions were less than ideal for the process and can be improved in subsequent efforts.

Table 3-1. Comparison of solvent extraction results at different Pu concentrations

Oxidation State	Test 1		Test 2	
	9×10^{-7} M	9×10^{-9} M	7×10^{-6} M	1×10^{-8} M
Pu(III)	10%	2%	4%	5%
Pu(IV)	17%	14%	26%	8%
Pu(V)	9%	75%	3%	62%
Pu(VI)	58%	3%	62%	21%
p	4%	5%	3%	5%
p = "polymeric Pu(IV)" (Nitsche et al., 1988)				

¹D. Reed, Argonne National Laboratories, personal communication, 1995.

3.2.4 Container Sorption Experiments

Pu solutions at 10^{-8} M in 0.1 M NaClO_4 at varying pH were held for 11 days in bottles made of different materials. Polycarbonate bottles at pH 1.8, 3.5, and 7.8 sorbed 13–16 percent of the Pu, but none was sorbed at pH 9.3 [where EQ3NR (Wolery, 1992) calculations suggest Pu(VI) carbonate species are dominant]. At pH 7.8, Teflon-FEP sorbed 32 percent, and polypropylene sorbed 10 percent. It appears that polycarbonate bottles will be adequate for sorption experiments as long as container sorption effects are considered.

3.2.5 Calculated Plutonium Oxidation States

EQ3NR calculation results for the equilibrium abundances of Pu(V) and Pu(VI) of 0.1 M NaClO_4 solutions in equilibrium with atmosphere (likely to be used in sorption experiments) are shown in Figure 3-1. The most notable features of these calculations are (i) the dominance of Pu(V) and Pu(VI) at all pH, accounting for >96 percent of all Pu; and (ii) the peak in Pu(V) at the expense of Pu(VI) in the mid-pH range. This pattern results from the dominance of three aqueous Pu species under these conditions: PuO_2^{2+} at low pH, PuO_2^+ at moderate pH, and $\text{PuO}_2(\text{CO}_3)_2^{2-}$ at high pH. If accurate, these oxidation state shifts would have a profound influence on Pu sorption behavior, underscoring the importance of oxidation state information in the interpretation of sorption experiments.

3.3 NEPTUNIUM SORPTION EXPERIMENTS

To develop an understanding of radionuclide sorption processes and the important physical and chemical parameters that affect sorption behavior in the YM environment, experiments are being conducted to investigate the sorption behavior of Np and other actinides on geologic media. During this reporting period, experiments seeking to determine the effects of pH, initial Np concentration in solution, and partial pressure of $\text{CO}_2(\text{g})$ on the sorption of Np(V) onto quartz, clinoptilolite, and montmorillonite were performed. The minerals selected for these sorption experiments are representative of matrix and fracture lining minerals at YM and, in the case of quartz and clinoptilolite, are particularly abundant in some stratigraphic units.

Because of its long half-life (2.14×10^6 yr), suspected high radiotoxicity, occurrence in HLW, and reportedly low sorption characteristics, ^{237}Np is a particular concern to the safety suitability of YM as a repository. Though it may exist in one or more of four oxidation states (III, IV, V, and VI), under the oxidizing conditions typical of the YM environment, Np is expected to exist in solution primarily in one oxidation state (V) as the neptunyl species, NpO_2^+ (Allard et al., 1980). Previous studies indicate that the NpO_2^+ species forms relatively weak complexes (Patil et al., 1978; Fuger, 1992). As a result, the speciation of Np(V) in solution is somewhat simpler than U or Pu under similar conditions. However, uncertainties remain with respect to the stability of many of Np(V) species in solution. In fact, there is considerable debate over the value of the stability constant of the first hydrolysis product of Np, NpO_2OH^0 ; reported values vary by more than two orders of magnitude (Maya, 1983; Fuger, 1992; Tait et al., 1994). Studies by Allard, Bidoglio, and their respective co-workers (among others) have indicated that sorption of Np(V) occurs primarily at higher pH (7–12) and is low compared to that of Am, Pu, or U (e.g., Allard, 1984; Allard et al., 1984; Bidoglio et al., 1985, 1988; Thompson, 1988; Righetto et al., 1991; Triay et al., 1993). Here too, uncertainties are significant. For instance, reported results (expressed

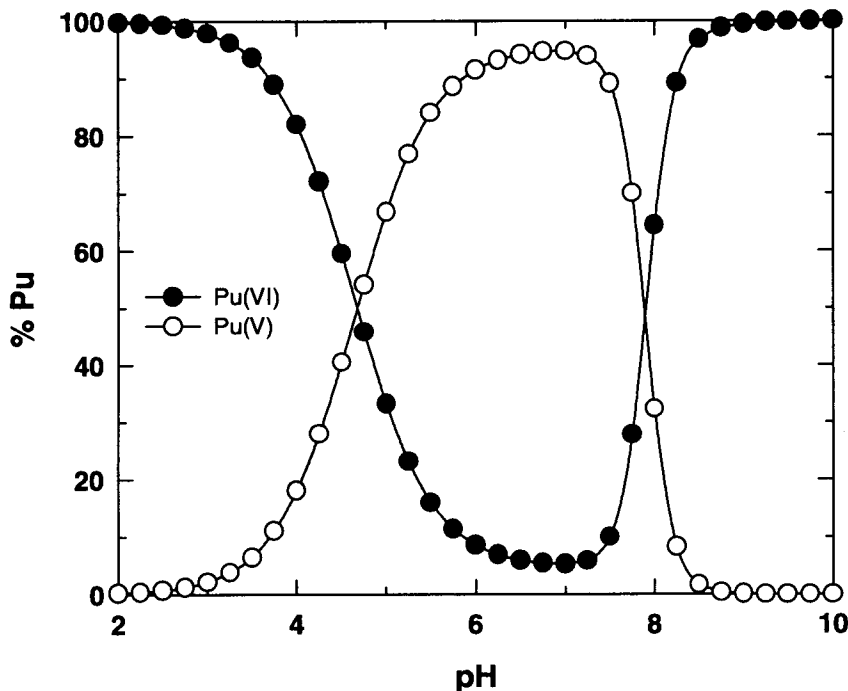


Figure 3-1. Estimated percent abundances of Pu(V) and Pu(VI) in dissolved Pu in 0.1 M NaClO₄ at varying pH in equilibrium with atmosphere. Calculations performed using EQ3NR (Wolery, 1992).

in terms of the distribution coefficient, K_D , in mL/g) for sorption of Np(V) onto similar mineral substrates can vary by over two orders of magnitude.

3.3.1 Mineral Preparation

3.3.1.1 Quartz

Quartz sand (Wedron #510) used in the experiments was obtained from Wedron Silica Co., Wedron, Illinois. A sieved size fraction (0.149 to 0.250 mm) representative of the bulk sand and relatively free of impurities was selected for use in the sorption experiments (Bertetti et al., 1995). The selected size fraction was chemically pretreated and cleaned to remove carbonate and Fe-oxide coatings on the sand grains and to remove nonquartz minerals. Pretreatment methods are described in detail in Bertetti et al. (1995). To provide a quartz substrate with a higher specific surface area, a subsample of the pretreated sand was separated and crushed using an agate mortar and pestle until the crushed quartz passed through a #325 sieve (0.044-mm mesh openings). The crushed quartz was then washed and cleaned using deionized H₂O (dH₂O) and an ultrasonic bath. Following washing, the crushed quartz was processed to remove particles less than 0.004 mm. To accomplish this removal, ~2-g aliquots of the crushed quartz were added to 30–40 mL of dH₂O and centrifuged in 50-mL polycarbonate tubes for 1 min at 1,500 rpm. Any remaining suspended quartz was decanted and discarded, and the process repeated. Removal of quartz less than 0.004 mm allows for separation of the quartz substrate and Np-bearing solution via centrifugation

(without the need for filtration of the solution) at the end of the experiment and helps to limit the amount of silica that will dissolve during experiment. The surface areas of the 0.149- to 0.250-mm and the 0.044- to 0.004-mm size fractions, as measured using a Coulter SA3100 surface area analyzer (N_2 -BET), were 0.02 ± 0.01 and 0.2 ± 0.03 m^2/g , respectively.

3.3.1.2 Clinoptilolite

Clinoptilolite powder was obtained by crushing, sieving, and chemically purifying a clinoptilolite-rich tuff from Death Valley Junction, California. Mineral pretreatment is described in detail in Pabalan (1994). Briefly, the 0.075- to 0.149-mm size fraction was separated, cleaned of carbonate and Fe-oxides, and treated using heavy liquids to remove mineral impurities. The clinoptilolite was then converted to near-homoionic Na form by reacting the powder with 3 M NaCl at 90 °C. The Na-clinoptilolite powder was then rinsed with dH_2O and stored over saturated NaCl solution in a desiccator to provide a constant zeolite water content prior to initiation of experiments. The measured surface area (N_2 -BET) of the Na-clinoptilolite was 10.1 ± 0.3 m^2/g .

3.3.1.3 Montmorillonite

Montmorillonite (SAz-1, "Cheto") used in the Np sorption experiments was obtained from the Source Clays Mineral Repository. The montmorillonite is a Ca-smectite and originated from Apache County, Arizona. Prior to its use in experiments, the montmorillonite was converted to Na-form and treated to isolate the fraction less than 0.002 mm in size. Na-montmorillonite was generated by treating 200-g batches of clay in approximately 1.5 L of 3 M NaCl. The clay-NaCl mixture was continuously stirred in a 2-L glass beaker. The NaCl solution was replaced every 3 d by discontinuing stirring, allowing the clay to flocculate and settle, decanting the used NaCl solution, and replacing it with fresh 3 M NaCl solution. After 2 wk, the clay was again allowed to settle, and most of the NaCl solution was decanted. The remaining clay-NaCl slurry was transferred in about 40-g aliquots to dialysis membranes (SpectraPor-4) that were tied off at each end. The membranes were placed in a glass beaker that contained warm (~40 °C) dH_2O . Water in the beaker was replaced twice daily for 1 wk and was heated using an electric hot plate. After 1 wk the dH_2O was tested using 0.1 M $AgNO_3$ to check for the presence of Cl^- . A negative test for Cl^- , as determined by a lack of $AgCl$ precipitate, was used as indication that the clay was rinsed of excess NaCl. The clay was then removed from the dialysis membranes and suspended in a 2-L glass beaker filled with dH_2O . No flocculation was observed over a period of 2 d. Then 40-mL aliquots of the clay suspension were collected and centrifuged for 2 min at 1,500 rpm using a Fisher-Marathon 21K centrifuge and a six-position fixed-angle rotor (effective radius 10 cm). The resulting suspension, which contained clay particles less than 0.002 mm, was decanted and saved. Clay remaining in each tube was mixed with dH_2O , vortexed thoroughly, and centrifuged again to recover any of the <0.002-mm fraction that had been entrained by larger particles. All clay removed from suspension by centrifugation at 1,500 rpm was discarded. The remaining suspended material was decanted and combined with the supernatant from previous separations. The <0.002-mm fraction was then collected by centrifuging aliquots of the suspension at 10,000 rpm for 20 min. Any particles that remained suspended following the high-speed centrifugation step were decanted and discarded. The wet, compacted clay was then freeze-dried for storage prior to use in sorption experiments. Freeze-drying effectively removes excess water from the clay but prevents undue collapse of the clay structure, which can be induced by drying under heat. X-ray diffraction analyses of the clay before and after Na-exchange, size fractionation, and freeze-drying showed a change in the interlayer spacing for montmorillonite consistent with ion exchange of Ca^{2+} for Na^+ . The measured surface area (N_2 -BET) of the freeze-dried Na-montmorillonite was 97 ± 1 m^2/g .

3.3.2 Neptunium Solutions

^{237}Np standard solutions were acquired in glass ampoules from Isotope Products Laboratories, Burbank, California. The standard solutions were composed of neptunyl nitrate in 4-M HNO_3 matrix and were carrier free. One standard solution was diluted with 0.1 molal NaNO_3 to make a stock solution of 1×10^{-6} M ^{237}Np (~237 ppb) for use in the sorption experiments. Since it was expected that the pH range of interest for sorption of Np(V) would be about pH 6 to 11, the pH of the stock solution was adjusted to ~pH 7 by addition of $\text{NaHCO}_3(\text{s})$ to minimize the volume and concentration of solutions that would need to be added to adjust the pH of experimental solutions. A factor of ten dilution of the stock solution was used to make 1×10^{-7} M ^{237}Np solutions used in lower concentration experiments. Np has been shown to exist in the (V) oxidation state in NaNO_3 solutions (Nakayama and Sakamoto, 1991). Under the pH and Eh conditions of the experiments reported here, the production and/or stability of the Np(IV) or Np(VI) is not favored (Figure 3-2; Lieser and Mühlenweg, 1988). A second standard solution was split to provide confirmation of the oxidation state of Np and the existence of NpO_2^+ in solution. Approximately 3 mL of the ^{237}Np standard solution were diluted using 0.1 molal NaNO_3 to make a 1×10^{-5} M ^{237}Np solution. Aliquots of this solution were analyzed in quartz cuvettes using a Perkin-Elmer Lambda 9 UV-VIS-NIR spectrophotometer. Upon analysis, a peak of 0.004 absorbance units, referenced to a blank of 0.1 molal NaNO_3 , at 981 nm was observed. The peak height and location correspond well to the expected presence and quantity of NpO_2^+ species in solution (Gauthier et al., 1983) and confirmed the existence of Np(V).

^{237}Np was analyzed by counting its alpha activity using a Packard 2505 TR/AB liquid scintillation analyzer (LSA). LSC of alpha particles is convenient because little chemical preparation of samples is required prior to analysis, and the LSA counts alphas at, or very near to, 100-percent efficiency. Unfortunately, the immediate daughter of ^{237}Np is a short-lived beta emitter, ^{233}Pa , which rapidly ingrows in solutions containing ^{237}Np . Radionuclides, like ^{233}Pa , that emit beta particles at average energies high enough (~100 keV) to conflict with the alpha decay spectrum (~100–400 keV) can cause significant interference in quantifying the alpha activity present. The Packard 2505 LSA is capable of discriminating alpha and beta decay events in the same solution, but solutions of the pure alpha and beta emitters must be used to optimize the LSA pulse decay discriminator. A split (~2 mL) of the second standard solution was used to generate the necessary samples. The standard solution split was separated into two ~1-mL aliquots. Based on a method modified from Pickett et al. (1994), the first aliquot was evaporated to dryness, taken up in a 1 M $\text{HCl}+0.5$ M HF matrix, loaded onto an AG1-X8 resin (Bio-Rad) anion exchange column, and eluted with a mixture of 9 M $\text{HCl}+0.05$ M HF . ^{233}Pa is eluted, while ^{237}Np is retained on the resin. The second aliquot was mixed with 6 M HNO_3 , loaded onto a separate silica gel column, and eluted with 6 M HNO_3 to isolate ^{237}Np preferentially based on a method modified from Hardy et al. (1958). The eluents were then evaporated, taken up in 0.02 M HNO_3 , and sampled for use in the LSA. Once optimized, the same LSA setting is used for all subsequent analyses of solutions containing ^{237}Np and ^{233}Pa as the primary radionuclides. Statistics of counting associated with analysis of ^{237}Np -bearing solutions are based upon the alpha activity only. All solutions were counted for a period of time such that the total number of alpha counts collected resulted in a maximum 2σ error of 2 or 3 percent for 1×10^{-6} and 1×10^{-7} M ^{237}Np solutions, respectively.

3.3.3 Experimental Procedure

The sorption experiments were conducted by reacting weighed amounts of quartz, clinoptilolite, or montmorillonite with 25 g of ^{237}Np -bearing solution in polycarbonate centrifuge tubes. Generally, the experimental solution was added to the tube followed by pH adjustment and, finally, addition of the solid

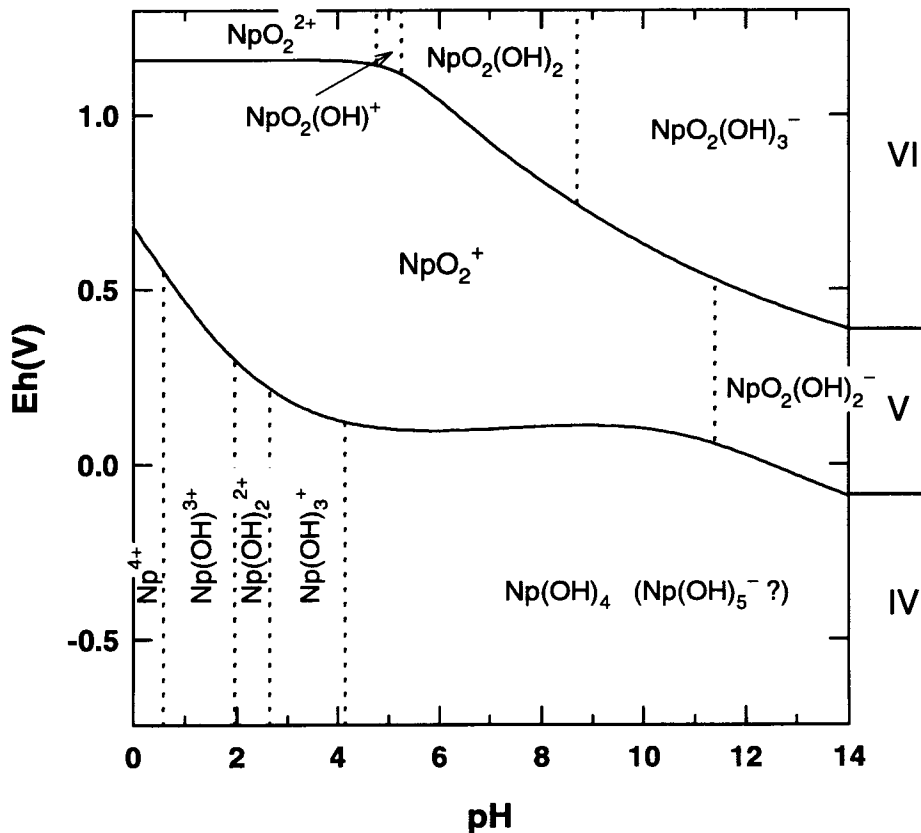


Figure 3-2. Eh-pH diagram of neptunium (adapted from Lieser and Mühlenweg, 1988)

phase. However, in cases where the amount of solid added was small (0.1 g or less), the solid was added first, followed by the solution and pH adjustment, to minimize introduced uncertainty associated with the determination (weighing by difference) of the actual amount of solid present. Each sorption experiment consisted of two parts, a sorption or forward component and a desorption or reverse component. The desorption component of the experiment provided information regarding potential container sorption of Np(V), confirmed reversibility of the sorption reaction, and provided mass balance for ^{237}Np . For all three minerals, experiments were conducted under equilibrium with atmospheric CO_2 or under conditions in which the solutions were undersaturated with respect to atmospheric CO_2 . By varying the partial pressure of $\text{CO}_2(\text{g})$ in equilibrium with solutions, the influence of carbonate complexation of Np(V) could be studied. Each experiment consisted of a set of 20–25 solutions adjusted to pH ~5–10.5 in ~0.25-pH increments. With the exception of two quartz experiments conducted at 1×10^{-7} M ^{237}Np , the initial concentration of ^{237}Np in all other experiments was 1×10^{-6} M. A summary of experiments and initial conditions is given in Table 3-2.

Experimental solution pH was adjusted by addition of predetermined quantities of HNO_3 , NaOH , or NaHCO_3 solutions. NaOH and NaHCO_3 solutions were freshly prepared using degassed dH_2O and stored in sealed glass containers to minimize introduction or loss of $\text{CO}_2(\text{g})$. The amount of reagent necessary to achieve the desired initial pH of the Np solutions was estimated using the EQ3NR geochemical equilibrium code (version 7.2a) and associated database Data0.com.R22a (Wolery, 1992).

Table 3-2. Summary of Np(V) sorption experiments

Experiment	Mineral	Mass Solid (g)	Vol. Soln. (mL)	Initial Conc. ²³⁷ Np (M)	CO ₂ Conditions	Mass Balance (%)
NpQ1	Quartz	2	25	1×10 ⁻⁷	Equil. atm.	-0.48±1.91
NpQ2	Quartz	1	25	1×10 ⁻⁷	Equil. atm.	-0.97±2.34
NpQ3	Quartz	1	25	1×10 ⁻⁶	Equil. atm.	0.10±0.78
NpQ4	Quartz	1	25	1×10 ⁻⁶	Undersaturated	-0.11±1.45
NpQ5	Crushed qtz	0.1	25	1×10 ⁻⁶	Undersaturated	-0.38±0.97
NpC1	Clinop.	0.1	25	1×10 ⁻⁶	Equil. atm.	-0.08±1.48
NpC2	Clinop.	0.1	25	1×10 ⁻⁶	Undersaturated	0.82±0.97
NpM1	Mont.	0.1	25	1×10 ⁻⁶	Undersaturated	0.35±1.24
NpM2	Mont.	0.1	25	1×10 ⁻⁶	Equil. atm.	0.24±1.36

After adjustment of pH, solutions were capped immediately to prevent further introduction of CO₂(g), or left loosely capped to allow solution equilibration with atmospheric CO₂. Experimental solution pH was determined at the end of the sorption experiment by direct measurement using a Ross combination pH electrode and Orion 920A expandable ion-analyzer. Experimental solutions were centrifuged as necessary, and samples were withdrawn for liquid scintillation counting prior to measurement of pH.

Previous kinetics studies of Np(V) sorption onto mineral surfaces have shown that sorption equilibrium was reached quickly (2–36 hr) (Bidoglio et al., 1987; Nakayama and Sakamoto, 1991). However, previous sorption studies conducted at the CNWRA have also shown that pH equilibration of solutions often takes up to 10 d (e.g., Pabalan and Turner, 1994); therefore, all experiments were allowed to equilibrate for at least 14 d. Following the 2-wk equilibration period, experimental solutions were sampled for ²³⁷Np concentration and pH. Prior to sampling, solutions containing montmorillonite or crushed quartz were centrifuged at 10,000 rpm for 20 min (other quartz and clinoptilolite solutions did not contain particles fine enough to remain suspended in solution under the influence of gravity). Solution sample aliquots of 0.5 mL were then withdrawn for analysis using an Eppendorf pipet and disposable tips. The aliquots were transferred to weighed 7-mL glass liquid scintillation vials to which 0.5 mL of 0.02 M HNO₃ had previously been added. Acidification of samples helps to minimize Np sorption onto the glass vials and thus minimize interference with counting results. Changes in Np concentration due to solution evaporation, dilution due to addition of acid or base, and variations in sample aliquot volume were accounted for by weighing experimental solution tubes and sample vials at each juncture. The amount of Np in solution was tracked by converting all measured concentrations to mass of Np, correcting for mass losses due to pH measurement, and comparing the calculated mass of Np initially added to each experimental solution with the mass of Np measured at the end of each experiment.

The potential for Np sorption onto experimental container walls was evaluated in two ways. First, control experiments were conducted at pH 8, 9, and 10 in which Np-bearing solutions were allowed to equilibrate, with and without atmospheric CO₂ present, in polycarbonate centrifuge tubes that contained no mineral substrate. After 2 wk, solutions in the tubes were sampled for Np, and pH was measured to determine if any Np had been lost from solution. Solutions were then transferred to separate containers and acidified with HNO₃. Acid solutions were also added to the original centrifuge tubes to effect desorption, if sorption had occurred, of Np from container walls. A second means of evaluating container sorption was accomplished via the desorption component of the sorption experiments. Following the forward sorption portion of the experiment, the mineral phase was transferred from the sorption tube. Solution remaining in the original polycarbonate tube was acidified and allowed to equilibrate for an additional 14 d. The solution was then sampled for Np content, and the difference in mass of Np before and after desorption was attributed to container wall sorption.

3.3.4 Results and Discussion

Results for the sorption of Np(V) onto quartz, clinoptilolite, and montmorillonite are presented in terms of a sorption coefficient (K_D), a surface area normalized sorption coefficient (K_A), or the fraction of total Np initially added to the system, which has been sorbed by the mineral (%Np sorbed). The K_D can be calculated by determining the ratio of the equilibrium concentration of Np sorbed onto the mineral phase to the equilibrium concentration of Np in solution.

$$K_D = \frac{\frac{\text{mass Np sorbed (g)}}{\text{mass solid (g)}}}{\frac{\text{mass Np solution (g)}}{\text{volume solution (mL)}}} \quad (3-1)$$

The K_D has the advantage of normalizing sorption results with respect to the solid-mass to solution-volume ratio used in each experiment. Dividing K_D by the mineral surface area per unit mass will give K_A . The K_A can be used to directly compare sorption on minerals of differing surface areas. Although least informative for the presentation of sorption results, the %Np sorbed is used in this report on a limited basis to provide comparison of experimental data to results of some previously published data sets and model calculations that are not easily converted to K_D or K_A values. In the results presented in the following sections, some negative K_D values are shown, the negative values occur primarily in regions where K_D is equal or nearly equal to zero. Calculation of a negative K_D is a consequence of the analytical uncertainties inherent in any sorption experiment, and in these experiments the negative K_D values result from an overestimate, due to ²³⁷Np counting error, of the amount of Np in solution at the end of an experiment. The magnitude of the total uncertainty is dependent on the analytical method(s) and the quantities of the analyte of interest. Error bars are shown to indicate the propagated total uncertainties (at the 2σ level) associated with the reported data.

3.3.4.1 Neptunium Sorption onto Quartz

Results of experiments investigating the sorption behavior of Np(V) onto quartz (Figures 3-3 and 3-4) show a strong pH dependence. Np sorption onto quartz begins at about pH 7 regardless of the CO₂ conditions established. For the experiments at equilibrium with atmospheric CO₂, sorption reaches a maximum about pH 8–8.5 and decreases again to a minimum by pH 9.5. Conversely, for conditions in which the solutions remain undersaturated with respect to atmospheric CO₂, sorption continues to increase

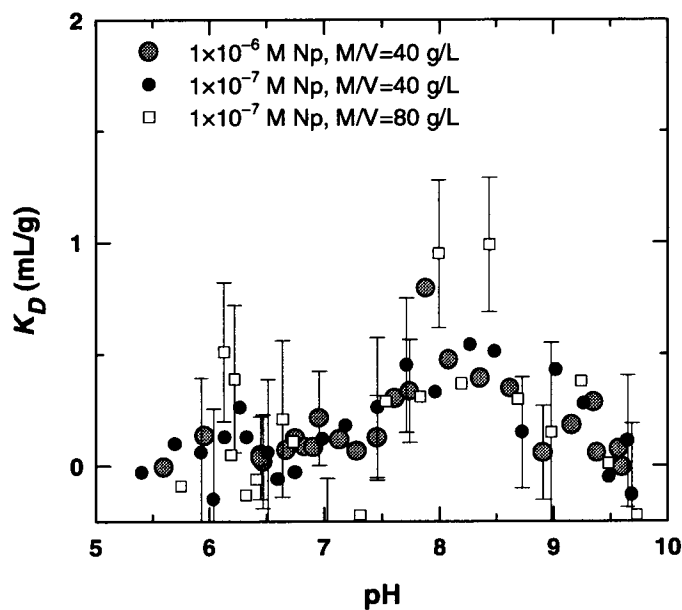


Figure 3-3. Sorption of Np(V) onto quartz as a function of pH, initial Np concentration, and solid-mass to solution-volume ratio (M/V). Error bars indicate calculated total uncertainties (2σ) for selected points.

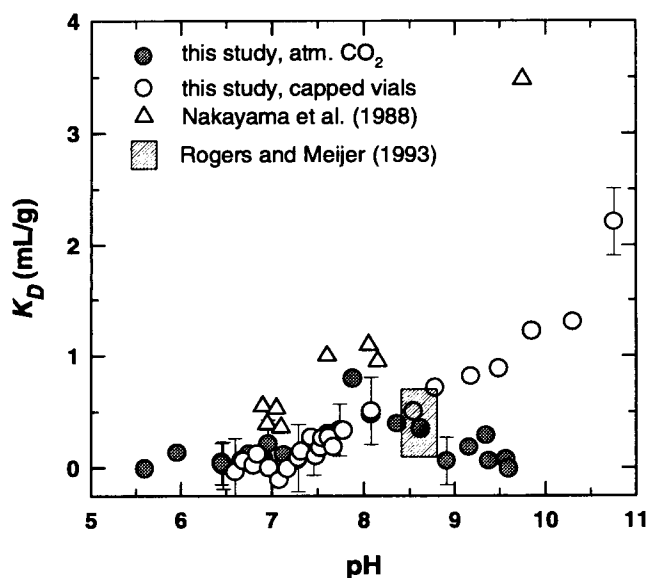


Figure 3-4. Sorption of Np(V) onto quartz as a function of pH and $\text{CO}_2(\text{g})$ equilibrium. Solutions were allowed to equilibrate with atmospheric CO_2 (filled circles) or capped immediately after pH adjustment, resulting in conditions undersaturated with respect to atmospheric CO_2 (open circles). Initial $[\text{Np}] = 1 \times 10^{-6} \text{ M}$. Error bars indicate total calculated uncertainties (2σ) for selected points. Also shown are data from low CO_2 quartz column experiments of Nakayama et al. (1988) and range of Np sorption onto devitrified tuffs reported by Rogers and Meijer (1993) (initial $[\text{Np}] \sim 4 \times 10^{-5} \text{ M}$ and in equilibrium with atm CO_2).

throughout the pH range studied. Changes in the initial concentration of Np(V) from 1×10^{-6} to 1×10^{-7} M ^{237}Np resulted in little discernible change in the magnitude of Np(V) sorption observed (Figure 3-3). Likewise, when results are normalized for the mass of solid in solution (in terms of K_D), changing the solid-mass to solution-volume ratio from 40 to 80 g/L made no difference in the magnitude of sorption observed (Figure 3-3). The results compare favorably to those reported in studies by DOE investigators of Np sorption onto devitrified tuff (primarily quartz and feldspar mineralogy), conducted under similar initial Np concentrations, and in equilibrium with atmospheric CO_2 (Figure 3-4; Rogers and Meijer, 1993; Triay et al., 1993). Likewise, the trend of increasing sorption with increasing pH throughout the range of pH studied has been observed for column-based studies of Np sorption onto quartz (Figure 3-4; Nakayama et al., 1988). Other studies have indicated much larger K_D s for sorption onto quartz (e.g., Allard, 1984; Righetto et al., 1991) but have used poorly characterized quartz material, poor specification of CO_2 conditions, high surface-area colloidal silica, or low initial concentrations of Np, all of which combine to make comparisons of results difficult. The effects of increasing quartz surface area were studied by reacting fine-grained crushed quartz (0.004–0.044 mm) with Np solutions undersaturated with atmospheric CO_2 (Figure 3-5). The finer grain sized quartz sorbs significantly more Np(V) from solution. However, when normalized for surface area differences (K_A), Np(V) sorption onto the fine-grained quartz is nearly indistinguishable from sorption onto the more coarse (0.149–0.250 mm) quartz sand (Figure 3-6).

Previously published reports have shown that representations of Np(V) sorption data using Surface Complexation Modeling (SCM) approaches such as the Diffuse-Layer Model (DLM) and the Triple-Layer Model (TLM) have been successful (Kohler et al., 1992; Turner, 1995). Turner (1995) used a DLM to fit the colloidal silica data of Righetto et al. (1991) and obtained good agreement between the model fit and experimental data when postulating sorption of two Np species, NpO_2^+ and NpO_2OH^0 , which are the predicted dominant Np species in solution under the experimental conditions specified (Figure 3-7). Kohler et al. (1992) modeled Np(V) sorption onto quartz using the TLM approach. Comparison of the Kohler et al. model prediction (surface site normalized) to the data obtained from the crushed-quartz experiment is also shown in Figure 3-7. Although the similarities in the magnitude of Np(V) sorption are somewhat fortuitous, the comparison is made to depict the correlation in the shape of the modeled sorption curve and the independently acquired sorption data. Kohler et al. postulated adsorption of only the NpO_2^+ species. Considering the successes of reproducing observed Np(V) sorption data with the SCM approach, it is probable that a DLM as described in Turner (1995), with the possible modification of employing two sorption sites, will be successful in describing the experimental data reported here.

3.3.4.2 Neptunium Sorption onto Clinoptilolite

Results for the experiments investigating sorption of Np(V) onto Na-clinoptilolite are shown in Figure 3-8. Similar to the observed Np(V) sorption behavior onto quartz, Np(V) sorption onto clinoptilolite is strongly influenced by solution pH. Significant sorption begins near pH 7 for conditions with and without atmospheric CO_2 present. For solutions at equilibrium with atmospheric CO_2 , Np sorption onto clinoptilolite reaches a maximum near pH 8 and decreases again to a minimum near pH 9.5. Experimental solutions undersaturated with respect to atmospheric CO_2 exhibit a continued increase in sorption as solution pH increases, with the maximum sorption ($K_D=28$ mL/g) attained at the highest pH studied (~10). Though clinoptilolite and quartz have different surface characteristics and compositions, the trends in Np sorption behavior are similar for both minerals. DOE-reported data for Np(V) sorption onto zeolitized tuff (Rogers and Meijer, 1993) are also shown in Figure 3-8. Within anticipated uncertainties, the DOE Np sorption values, collected under similar experimental conditions, are in agreement with the results observed for Np(V) sorption onto clinoptilolite.

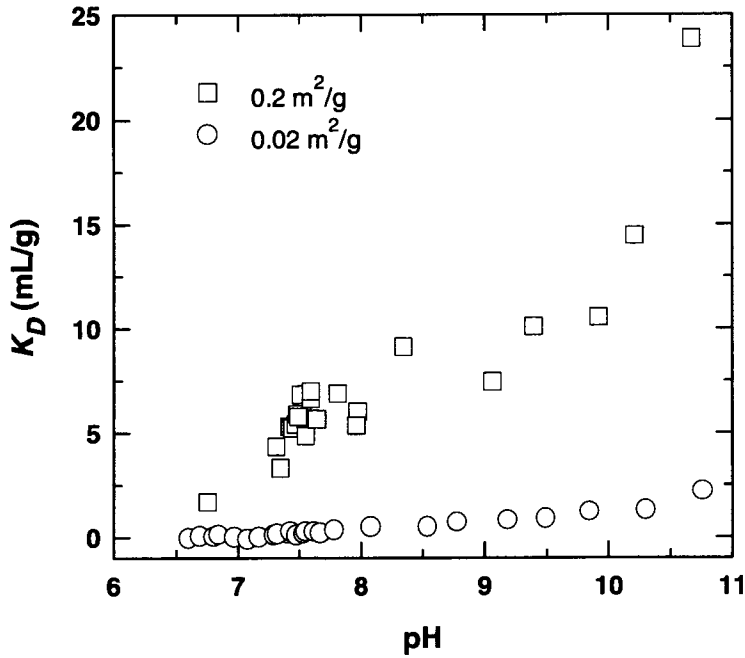


Figure 3-5. Sorption of Np(V) onto quartz as a function of pH and surface area. Initial $[\text{Np}] = 1 \times 10^{-6} \text{ M}$. Both experiments conducted with capped solution containers (low CO_2).

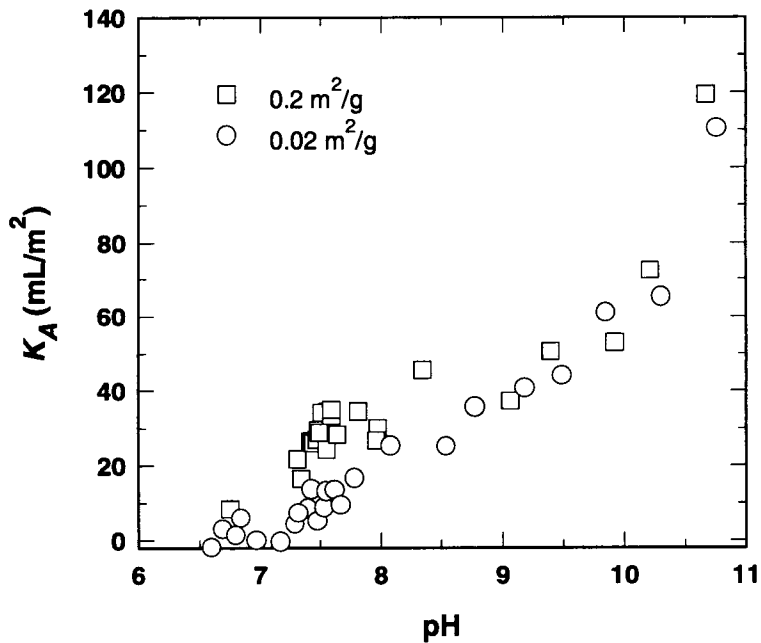


Figure 3-6. Sorption of Np(V) onto quartz as a function of pH and surface area after normalizing data from Figure 3-5 for surface area of quartz used in each experiment.

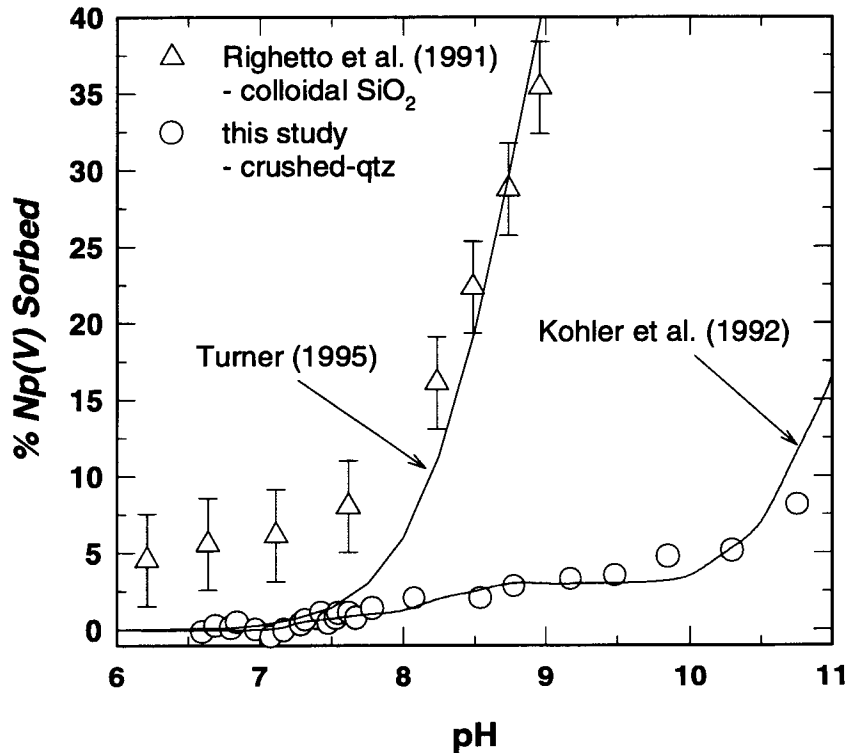


Figure 3-7. Comparison of surface-complexation model representations of Np(V) sorption onto quartz. Data from Righetto et al. (1991) collected with initial $[Np]=1\times 10^{-14}$ M, no CO_2 , and colloidal silica. Error bars show minimum uncertainty due to digitization of data. Model of Kohler et al. (1992) normalized to surface site concentration of 5×10^{-4} M.

3.3.4.3 Neptunium Sorption onto Montmorillonite

Over the entire pH range considered, the magnitude of Np(V) sorption onto Na-montmorillonite is greater than that observed for either quartz or clinoptilolite (Figure 3-9). However, the sorption trends with change in pH are very similar. Like the behavior observed for quartz and clinoptilolite, Np(V) sorption onto montmorillonite begins to increase at a solution pH of about 7. For solutions in equilibrium with atmospheric CO_2 , the magnitude of sorption peaks near pH 8–8.5 and decreases as the pH increases, forming a high pH sorption edge. Solutions that were capped and remained undersaturated with respect to atmospheric CO_2 show a continuous increase in sorption with increasing pH, at least through the pH range examined. Unlike the Np(V) sorption behavior observed in experiments with quartz and clinoptilolite, Np(V) sorption onto montmorillonite does not decrease to near zero at the low end of the pH range studied (~6). A net positive uptake is observed regardless of pH and CO_2 conditions. Studies of Np(V) sorption onto montmorillonite at pH values below 7 have attributed this net positive sorption to ion-exchange between NpO_2^+ and Na^+ in the clay (Kozai, 1994). A comparison of experimental data collected by Kozai (1994) for Na-smectite under similar solution conditions (Np concentration and ionic

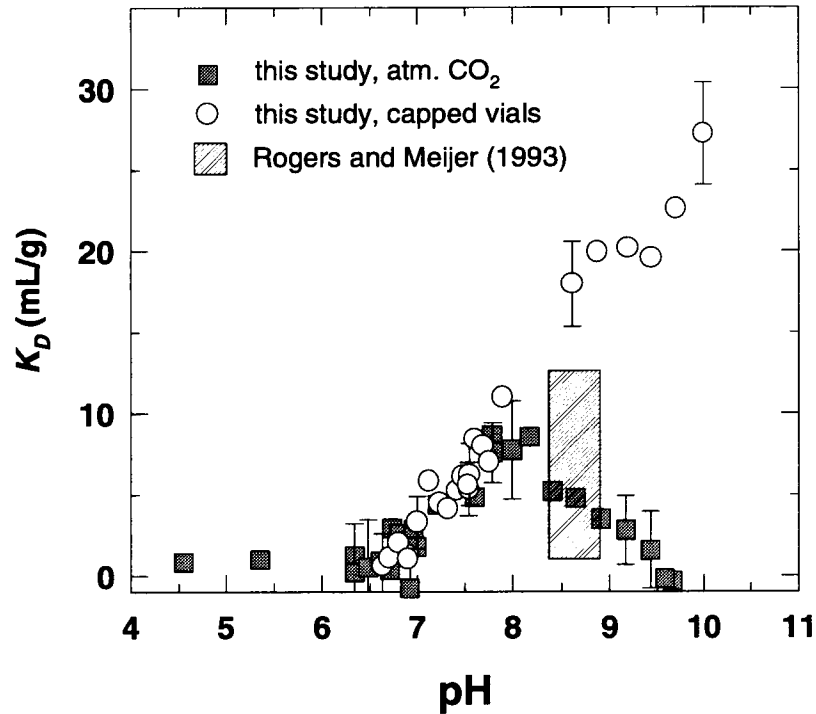


Figure 3-8. Sorption of Np(V) onto clinoptilolite as a function of pH and CO₂(g) equilibrium. Solutions were allowed to equilibrate with atmospheric CO₂ (filled squares) or capped immediately after pH adjustment, resulting in conditions undersaturated with respect to atmospheric CO₂ (open circles). Initial [Np]=1×10⁻⁶ M. Error bars indicate total calculated uncertainties (2σ) for selected points. Also shown are data from Np sorption onto zeolitized tuffs reported by Rogers and Meijer (1993) (initial [Np]~4×10⁻⁵ M and in equilibrium with atm. CO₂).

strength), but at lower pH values, shows good correlation between observed sorption of Np(V) at pH 6–7 (Figure 3-10). Though also postulated as further evidence for ion-exchange of NpO₂⁺ and Na⁺ (Kozai, 1994), reasons for the dramatic increase in Np(V) sorption at pH values below 4 are uncertain.

3.3.4.4 Neptunium Sorption onto Containers

Results of the control and container desorption experiments indicate that little or no Np(V) adsorbs onto container walls under the conditions studied. With no mineral substrate present, a maximum Np(V) loss from solution of 5 percent was observed. As might be expected, the maximum container sorption occurred with solutions of pH greater than 9 and when undersaturated with atmospheric CO₂. With a mineral phase present in solution, there were no measurable Np(V) losses to the container walls within the uncertainties associated with each experiment. Therefore, it was decided that corrections for loss of Np to the container walls were not needed.

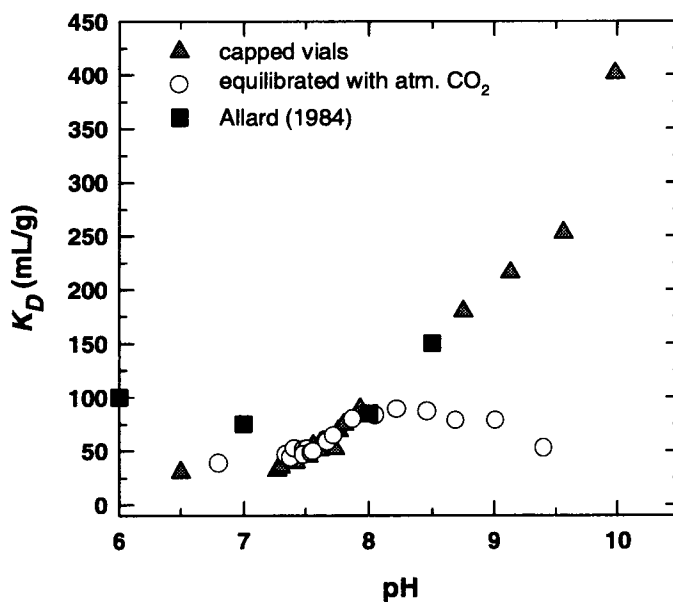


Figure 3-9. Sorption of Np(V) onto montmorillonite as a function of pH and CO₂(g) equilibrium. Solutions were allowed to equilibrate with atmospheric CO₂ (open circles) or capped immediately after pH adjustment, resulting in conditions undersaturated with respect to atmospheric CO₂ (filled triangles). Initial [Np]=1×10⁻⁶ M. Also shown are data from Allard (1984).

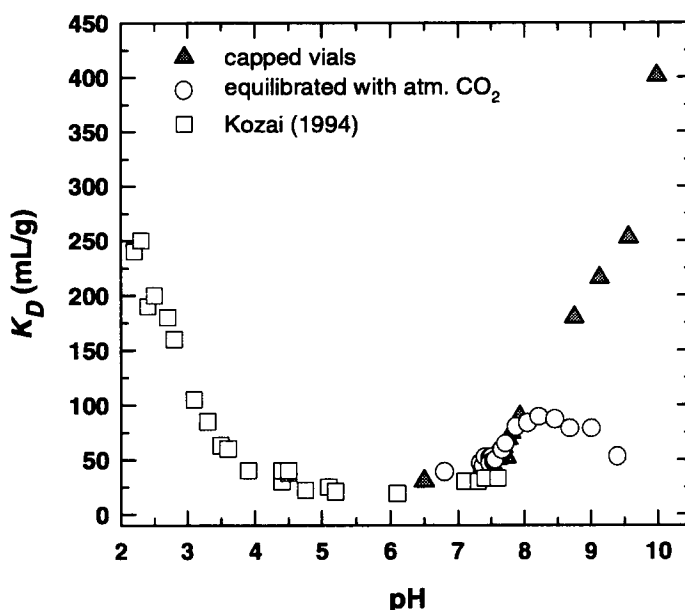


Figure 3-10. Sorption of Np(V) onto Na-montmorillonite over a large pH range. Filled triangles and open circles represent data from this study. Open squares are data from Kozai (1994). Sorption of Np(V) below about pH 7 is attributed to ion exchange.

3.3.5 Conclusions

Though minerals of distinct chemical composition and surface properties, the trends in observed Np(V) sorption behavior are extremely similar for the quartz, clinoptilolite, and montmorillonite studied. In each case, sorption of Np(V) increases significantly near pH 7 and, for conditions in which solutions are undersaturated with respect to atmospheric CO₂, continue to increase with an increase in pH over the entire pH range studied. Comparisons with solubility data for the limiting solids of NpO₂OH⁰ and Na-neptunyl-carbonates (Nitsche et al., 1994b; Itagaki et al., 1992) show that experimental solutions remained undersaturated with respect to these phases for all experimental conditions; therefore, the possibility of Np precipitation is unlikely. For experiments with solutions at equilibrium with atmospheric CO₂, a distinct sorption maximum and edges at low and high pH are observed for all three minerals. The pH of maximum sorption is 8–8.5, and sorption decreases with increasing pH to a minimum at pH~9.5. These results compare favorably with other studies that have correlated a decrease in Np(V) sorption with an increase in Np-carbonate complexation in solution (Bidoglio et al., 1985, 1987). It is interesting to compare Np(V) sorption behavior with the calculated speciation of Np(V) at a ²³⁷Np concentration of 1×10⁻⁶ M in a 0.1 molal NaNO₃ matrix and at equilibrium with atmospheric CO₂ (Figure 3-11). The solution is dominated by NpO₂⁺ at pH below 7. However, near pH~7 Np hydrolysis becomes significant, and the amount of the neptunyl hydroxyl species, NpO₂OH⁰, increases. The neutral hydroxyl species then reaches a maximum near pH 8.5 and decreases to a minimum near pH 9.5. The calculated behavior of the NpO₂OH⁰ species is distinctly similar to the observed sorption behavior of Np(V), in solutions at equilibrium with atmospheric CO₂, onto all three minerals. Also of note is the reported sorption behavior of Np(V) on other minerals such as biotite, α-alumina, hematite, and feldspar (e.g., Allard et al., 1984; Nakayama and Sakamoto, 1991; Righetto et al., 1991). Though reported magnitudes of sorption vary, the increase in sorption near pH 7 and the continued increase in sorption with increasing pH when solutions are undersaturated with respect to atmospheric CO₂ are also observed.

3.4 ASSESSMENT OF PROGRESS TOWARD MEETING PROJECT OBJECTIVES

The broad objective of this project is to develop sufficient understanding of issues of radionuclide sorption relevant to radionuclide transport modeling. An important mechanism for attenuating radionuclide transport could be sorption of radionuclides on minerals encountered along potential flow paths. Results of laboratory experiments on U(VI) and Np(V) sorption, combined with modeling efforts using surface-complexation models, are providing an understanding of the important parameters that control the sorption behavior of an actinide element. For example, the experimental results reported here and in previous CNWRA reports (e.g., Pabalan and Turner, 1994; Pabalan et al., 1994; Bertetti et al., 1995) demonstrate that U(VI) and Np(V) sorption on quartz, montmorillonite, clinoptilolite, and α-alumina is strongly dependent on pH. The presence of CO₂ also influences actinide sorption on these minerals. Sorption generally increases with increasing pH until carbonate complexation of the actinide becomes important, then the sorption of the actinide [U(VI) or Np(V)] decreases significantly with further increase in pH. The decrease in sorption is important for U(VI) and Np(V) because the reduction occurs over a pH range [7–8 for U(V), 8–9 for Np(V)] that is correlative with the pH range of most natural groundwaters, including those at YM. Moreover, sorption is reduced to near nil ($K_D=0$) in this pH range, especially for common YM minerals like quartz and clinoptilolite; thus little or no retardation would be expected. Since YM groundwaters are generally in equilibrium with levels of CO₂ above that of atmosphere, the pH where sorption decreases will likely be lower (Kohler et al., 1992) at YM. The implication is that, for all minerals studied in this project, sorption of U(VI) and Np(V) varies from maximum to minimum within

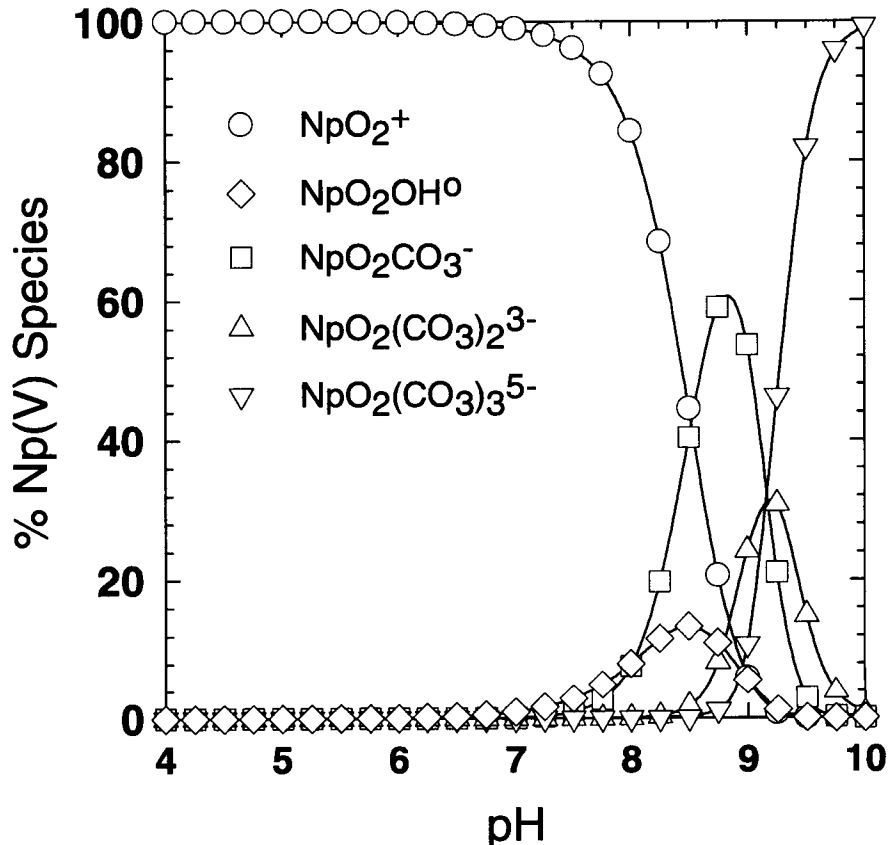


Figure 3-11. Speciation of Np(V) in solution in 0.1 m NaNO₃ at equilibrium with atmospheric CO₂, [Np]=1×10⁻⁶ M

the pH range of YM groundwaters. Additionally, the minimum values observed indicate that no effective retardation of these actinides would occur under the appropriate pH and CO₂ conditions. Because of the strong dependence of actinide sorption on pH, sorbent concentration, and surface area, modeling of sorption processes will likely require that changes in groundwater chemistry and in rock/fluid ratio be properly accounted for in PA calculations if retardation by sorption processes is included. However, the successes of SCMs in describing and predicting actinide sorption on quartz, montmorillonite, and other minerals suggest that SCMs offer a scientifically defensible approach that may be useful for PA calculations.

The similarity in the pH-dependence of Np(V) sorption on quartz, montmorillonite, and clinoptilolite is important, especially considering the distinct differences in the surface properties of the minerals. It may help identify simplified approaches to modeling sorption and thus help in the development of CDMs relevant to the KTUs identified in Section 3.2 and in developing conceptual models related to the PA Research Project and IPA Phase 3. Additionally, knowledge of Np(V) sorption behavior on minerals representative of the YM environment can provide information regarding realistic bounding estimates used in IPA modeling for the magnitude of Np sorption along potential transport paths.

3.5 PLANS FOR NEXT REPORTING PERIOD

Experiments that focus on ^{237}Np sorption onto quartz, clinoptilolite, and montmorillonite will continue. Experiments will be expanded to investigate the dependence of Np sorption on initial Np concentration, variations in ionic strength, presence of competing cations such as Ca^{2+} , and presence of dissolved silica and alumina. In addition, experiments studying Np(V) sorption on clinoptilolite and montmorillonite under CO_2 -free conditions will be conducted primarily as a means to develop sorption-binding constants and thus begin effective modeling of Np(V) sorption. Results will be presented in the next semi-annual report. Experiments to investigate the sorption behavior ^{239}Pu will be delayed pending access to techniques and/or methodologies that will provide better characterization of the oxidation state of ^{239}Pu .

A formal peer-review of the Sorption Project was held June 19–20, 1995. Findings and recommendations of the peer-review panel are scheduled to be delivered during the next reporting period. A summary of the peer-review findings will appear in the next semi-annual report. Preliminary recommendations (e.g., influence of Ca^{2+}) made by the panel have been incorporated into plans for upcoming experiments. The data generated from all these experiments will continue to be utilized in both the modeling activities being conducted in this project and extended the radionuclide transport models used in IPA.

3.6 REFERENCES

- Allard, B. 1984. Mechanisms for the interaction of Americium(III) and Neptunium(V) with geologic media. *Scientific Basis for Nuclear Waste Management VII*. Materials Research Society Symposium Proceedings 26. Pittsburgh, PA: Materials Research Society: 899–906.
- Allard, B., G.W. Beall, and T. Krajewski. 1980. The sorption of actinides in igneous rocks. *Nuclear Technology* 49: 474–480.
- Allard, B., U. Olofsson, and B. Torstenfelt. 1984. Environmental actinide chemistry. *Inorganica Chimica Acta* 94: 205–221.
- Bennett, D.A., D. Hoffman, H. Nitsche, R.E. Russo, R.A. Torres, P.A. Baisden, J.E. Andrews, C.E.A. Palmer, and R.J. Silva. 1992. Hydrolysis and carbonate complexation of dioxoplutonium(V). *Radiochimica Acta* 56: 15–20.
- Bertetti, F.P., R.T. Pabalan, and D.R. Turner. 1995. Sorption modeling for HLW performance assessment. *NRC High-Level Radioactive Waste Research at CNWRA July–December 1994*. B. Sagar, ed. CNWRA 94-02S. San Antonio, TX: Center for Nuclear Waste Regulatory Analyses: 67–81.
- Bidoglio, G., G. Tanet, and A. Chatt. 1985. Studies on neptunium(V) carbonate complexes under geologic repository conditions. *Radiochimica Acta* 38: 21–26.
- Bidoglio, G., P. Offermann, and A. Saltelli. 1987. Neptunium migration in oxidizing clayey sand. *Applied Geochemistry* 2: 275–284.
- Bidoglio, G., A. Avogadro, A. De Plano, and G.P. Lazzari. 1988. Reaction pathways of Pu and Np in selected natural water environments. *Radiochimica Acta* 44/45: 29–32.

- Clark, D.L., S.A. Ekberg, D.E. Morris, P.D. Palmer, and C.D. Tait. 1994. *Actinide(IV) and Actinide(VI) Carbonate Speciation Studies by PAS and NMR Spectroscopies: Yucca Mountain Project Milestone Report 3031-WBS 1.2.3.4.1.3.1*. LA-12820-MS. Los Alamos, NM: Los Alamos National Laboratory.
- Cohen, D. 1961. The absorption spectra of plutonium ions in perchloric acid solutions. *Journal of Inorganic and Nuclear Chemistry* 18: 211–218.
- Fuger, J. 1992. Thermodynamic properties of actinide aqueous species relevant to geochemical problems. *Radiochimica Acta* 59: 89–91.
- Gauthier, R., V. Ilmstadter, and K.H. Lieser. 1983. Simultaneous determination of the various oxidation states of neptunium at low concentrations by spectrophotometry. *Radiochimica Acta* 33: 35–39.
- Hardy, C.J., D. Scargill, and J.M. Fletcher. 1958. Studies on protactinium(V) in nitric acid solutions. *Journal of Inorganic and Nuclear Chemistry* 7: 257–275.
- Itagaki, H., S. Nakayama, S. Tanaka, and M. Yamawaki. 1992. Effect of ionic strength on the solubility of neptunium(V) hydroxide. *Radiochimica Acta* 58/59: 61–66.
- Kohler, M., E. Wieland, and J.O. Leckie. 1992. Metal-ligand-surface interactions during sorption of uranyl and neptunyl on oxides and silicates. *Proceedings of the 7th International Symposium on Water-Rock Interaction–WRI-7. Volume 1: Low Temperature Environments*. Y.K. Kharaka and A.S. Maest, eds. Rotterdam, The Netherlands: A.A. Balkema: 51–54.
- Kozai, N. 1994. Performance of engineered barrier materials: Sorption characteristics of neptunium by smectite. *Progress Report on Safety Research on Radioactive Waste Management for the Period April 1992 to March 1993*. S. Muraoka, M. Senoo, and K. Sekine, eds. JAERI-M 94-027. Tokai, Japan: Japan Atomic Energy Research Institute: 39–41.
- Lieser, K.H., and U. Mühlenweg. 1988. Neptunium in the hydrosphere and in the geosphere 1. Chemistry of neptunium in the hydrosphere and sorption of neptunium from groundwaters on sediments under aerobic and anaerobic conditions. *Radiochimica Acta* 43: 27–35.
- Maya, L. 1983. Hydrolysis and carbonate complexation of dioxoneptunium(V) in 1.0 M NaClO₄ at 25 °C. *Inorganic Chemistry* 22: 2,093–2,095.
- Nakayama, S., and Y. Sakamoto. 1991. Sorption of neptunium on naturally-occurring iron-containing minerals. *Radiochimica Acta* 52/53: 153–157.
- Nakayama, S., H. Arimoto, N. Yamada, H. Moriyama, and K. Higashi. 1988. Column experiments on migration behaviour of neptunium(V). *Radiochimica Acta* 44/45: 179–182.
- Neu, M.P., D.C. Hoffman, K.E. Roberts, H. Nitsche, and R.J. Silva. 1994. Comparison of chemical extractions and laser photoacoustic spectroscopy for the determination of plutonium species in near-neutral carbonate solutions. *Radiochimica Acta* 66/67: 251–258.

- Newton, T.W., D.E. Hobart, and P.D. Palmer. 1986. *The Preparation and Stability of Pure Oxidation States of Neptunium, Plutonium, and Americium*. LA-UR-86-967. Los Alamos, NM: Los Alamos National Laboratory.
- Nitsche, H., S.C. Lee, and R.C. Gatti. 1988. Determination of plutonium oxidation states at trace levels pertinent to nuclear waste disposal. *Journal of Radioanalytical and Nuclear Chemistry, Articles* 124(1): 171–185.
- Nitsche, H., K. Roberts, R. Xi, T. Prussin, K. Becraft, I. Al Mahamid, H.B. Silber, S.A. Carpenter, and R.C. Gatti. 1994a. Long term plutonium solubility and speciation studies in a synthetic brine. *Radiochimica Acta* 66/67: 3–8.
- Nitsche, H., K. Roberts, T. Prussin, A. Müller, K. Becraft, D. Keeney, S.A. Carpenter, R.C. Gatti, and C.F. Novak. 1994b. *Measured Solubilities and Speciations from Oversaturation Experiments of Neptunium, Plutonium, and Americium in UE-25p#1 Well Water from the Yucca Mountain Region*. Milestone Report 3329-WBS 1.2.3.4.1.3.1. LA-12563-MS UC-802. Los Alamos, NM: Los Alamos National Laboratory.
- Nuclear Regulatory Commission. 1992. *Disposal of High-Level Radioactive Wastes in Geologic Repositories*. Title 10, Energy, Part 60 (10 CFR Part 60). Washington, DC: Nuclear Regulatory Commission.
- Okajima, S., D.T. Reed, J.V. Beitz, C.A. Sabau, and D.L. Bowers. 1991. Speciation of Pu(VI) in near-neutral solutions via laser photoacoustic spectroscopy. *Radiochimica Acta* 52/53: 111–117.
- Pabalan, R.T. 1994. Thermodynamics of ion exchange between clinoptilolite and aqueous solutions of Na^+/K^+ and $\text{Na}^+/\text{Ca}^{2+}$. *Geochimica et Cosmochimica Acta* 58: 4,573–4,590.
- Pabalan, R.T., and D.R. Turner. 1994. Sorption modeling for HLW performance assessment. *NRC High-Level Radioactive Waste Research at CNWRA July–December 1993*. B. Sagar, ed. CNWRA 93-02S. San Antonio, TX: Center for Nuclear Waste Regulatory Analyses: 6-1 to 6-23.
- Pabalan, R.T., D.R. Turner, and F.P. Bertetti. 1994. Sorption modeling for HLW performance assessment. *NRC High-Level Radioactive Waste Research at CNWRA January–June 1994*. B. Sagar, ed. CNWRA 94-01S. San Antonio, TX: Center for Nuclear Waste Regulatory Analyses: 77–95.
- Patil, S.K., V.V. Ramakrishna, and M.V. Ramaniah. 1978. Aqueous coordination complexes of neptunium. *Coordination Chemistry Reviews* 25: 133–171.
- Pickett, D.A., M.T. Murrell, and R.W. Williams. 1994. Determination of femtogram quantities of protactinium in geologic samples by thermal ionization mass spectrometry. *Analytical Chemistry* 66: 1,044–1,049.
- Righetto, L., G. Bidoglio, G. Azimonti, and I.R. Bellobono. 1991. Competitive actinide interactions in colloidal humic acid-mineral oxide systems. *Environmental Science and Technology* 25(11): 1,913–1,919.

- Rogers, P.S.Z., and A. Meijer. 1993. Dependence of radionuclide sorption on sample grinding, surface area, and water composition. *Fourth Annual International High-Level Radioactive Waste Management Conference Proceedings*. La Grange Park, IL: American Nuclear Society and American Society of Civil Engineers: 1,509–1,516.
- Sanchez, A.L., J.W. Murray, and T.H. Sibley. 1985. The adsorption of plutonium IV and V on goethite. *Geochimica et Cosmochimica Acta* 49: 2,297–2,307.
- Tait, C.D., D.L. Clark, M.P. Neu, S.A. Ekberg, and P.D. Palmer. 1994. Temperature dependence of the hydrolysis and carbonate complexation reactions of NpO_2^+ . *Geological Society of America Abstracts with Programs—1994 Annual Meeting*. Boulder, CO: Geological Society of America 26(7): A-101.
- Thompson, J.L. 1988. Actinide behavior on crushed rock columns. *Journal of Radioanalytical and Nuclear Chemistry* 130: 353–364.
- Triay, I.R., B.A. Robinson, R.M. Lopez, A.J. Mitchell, and C.M. Overly. 1993. Neptunium retardation with tuffs and groundwaters from Yucca Mountain. *Fourth Annual International High-Level Radioactive Waste Management Conference Proceedings*. La Grange Park, IL: American Nuclear Society and American Society of Civil Engineers: 1,504–1,508.
- Turner, D.R. 1995. *A Uniform Approach to Surface Complexation Modeling of Radionuclide Sorption*. CNWRA 95-001. San Antonio, TX: Center for Nuclear Waste Regulatory Analyses.
- Wolery, T.J. 1992. *EQ3/6, A Software Package for Geochemical Modeling of Aqueous Systems: Package Overview and Installation Guide*. UCRL-MA-110662 PT1. Livermore, CA: Lawrence Livermore National Laboratory.

4 PERFORMANCE ASSESSMENT RESEARCH

by Robert G. Baca, Mark S. Jarzempa, and Stuart A. Stothoff

Investigators: Robert G. Baca, Ronald T. Green, Mark S. Jarzempa, Ronald W. Janetzke, Randall D. Manteufel, Sitakanta Mohanty, Budhi Sagar, and Stuart A. Stothoff (CNWRA); Ashok Nedungadi (SwRI); Evaristo J. Bonano, Mohan Seth, and Hoa G. Nguyen (Consultants)

NRC Project Officer: John D. Randall

4.1 TECHNICAL OBJECTIVES

Performance Assessment (PA) will have a central role in the review of the U.S. Department of Energy (DOE) license application for the proposed high-level waste (HLW) repository at Yucca Mountain (YM), Nevada. In conducting its technical review, the Nuclear Regulatory Commission (NRC) will use a hierarchy of PA models and codes. In the past, the development and application of these models and codes have largely been performed under the NRC Division of Waste Management (DWM) Iterative Performance Assessment (IPA) activity. While PA model applications will continue under IPA, reliance on the NRC research programs to make greater contributions to model and code development is becoming increasingly important.

The scope and objectives of the PA Research Project have been tailored to more directly fulfill the NRC needs in the area of PA modeling technology. With the programmatic goal of providing tools for compliance determination, the PA Research Project is focusing on three technical topical areas: (i) formulation and evaluation of conceptual models of key phenomena and future system states (under Task 1—Conceptual Model Development); (ii) development of efficient computational and computer methods for use in total-system and subsystem PA codes (under Task 2—Computational Model Development); and (iii) evaluation of NRC and DOE models through benchmark testing and comparisons with available data (under Task 3—Model Evaluation).

One of the primary programmatic objectives of the PA Research Project is to provide modeling technology that will benefit the ongoing NRC IPAs, with particular emphasis on improving the Total-System Performance Assessment (TPA) computer code (Sagar and Janetzke, 1993). Another, and equally important, programmatic objective is to provide the knowledge base necessary for supporting: (i) revision of the postclosure PA Compliance Determination Strategies (CDSs) (i.e., CDSs 6.1, 6.2, and 6.3), and (ii) development of postclosure performance Compliance Determination Methods (CDMs) that will be incorporated into appropriate sections of the License Application Review Plan (Nuclear Regulatory Commission, 1994). Specifically, this research project is contributing to the knowledge base for addressing Key Technical Uncertainties (KTUs) associated with: (i) variability of model parameter values, (ii) predicting future system states, and (iii) developing and validating conceptual and mathematical models.

At present, the first KTU resulted in the associated CDS being classified as Review Level 4, while the CDS associated with the second KTU is classified as Review Level 5; these KTUs are broadly addressed in Tasks 1 and 2 of this research project. The last KTU requires a type Level 5 Review of CDS 6.1—Assessment of Compliance with the Requirement for Cumulative Releases of Radioactive Materials. This KTU is being addressed in a focused effort under Task 3 of this research project. In addition, the

practical experience and expertise gained from this research project will place the NRC and the Center for Nuclear Waste Regulatory Analyses (CNWRA) in a position to thoroughly and independently evaluate the DOE PA models and codes.

Because of its multidisciplinary nature, the PA Research Project is an integrated programmatic effort drawing on expertise from many technical disciplines such as hydrology, geochemistry, structural geology, volcanology, seismology, climatology, computational fluid dynamics, and computer science. At present, the PA Research Project is closely integrated with the DWM IPA activity and three other Office of Nuclear Regulatory Research (RES) projects: (i) the Geochemical Analog of Contaminant Transport in Unsaturated Rock Research Project, (ii) the Sorption Modeling for High-Level Waste Performance Assessment Research Project, and (iii) the Subregional Hydrogeologic Flow and Transport Processes Research Project. In conjunction with the Geochemical Analog of Contaminant Transport in Unsaturated Rock Research Project, data from rock cores obtained from the Peña Blanca field site are being analyzed to improve conceptual and mathematical models of: (i) variably saturated flow in the fractured porous tuff, and (ii) radionuclide transport in discrete fractures and diffusion into and out of the rock matrix. In addition, data on diffusion and adsorption coefficients, compiled under the Sorption Modeling for High-Level Waste Performance Assessment Research Project, are contributing to conceptual/mathematical model development of radionuclide transport phenomena. Studies recently initiated under the Subregional Hydrogeologic Flow and Transport Processes Research Project have identified a number of PA technology needs associated with: (i) computational aspects that currently limit the practical application of detailed hydrologic codes (e.g., BIGFLOW) to the YM site, and (ii) modeling variably saturated flow in tuff rocks with interconnected fracture systems. Work conducted under Task 2 of the PA Research Project is being focused to reduce or remove these modeling limitations.

The PA Research Project is designed to address a number of user needs identified by the DWM for postclosure PA. Specific research needs include: (i) enhancement of means for identifying and screening scenarios, (ii) integration of improved mathematical models into repository PA methodology, (iii) validation of mathematical models, (iv) evaluation of mathematical models, (v) evaluation of flow and transport models applicable to unsaturated fractured rock and application to a range of scales of heterogeneities, and (vi) appraisal of the applicability of existing mathematical models of hydrologically and chemically coupled transport.

Research conducted under the PA Research Project is divided among three major tasks. The first task, Conceptual Model Development, focuses on developing conceptual/mathematical models in two areas: (i) flow and transport phenomena, and (ii) disruptive scenarios. Under the second task, Computational Model Development, research is directed toward the development of advanced numerical methods necessary to implement PA conceptual and mathematical models. Under the third task, Model Evaluation, model testing and confidence-building techniques are being developed, fully utilizing the experience gained from participation in the INTRAVAL project. Work completed on these tasks has been reported in previous semi-annual research reports. This chapter describes the results of the PA Research Project for the first half of 1995.

4.2 SIGNIFICANT TECHNICAL ACCOMPLISHMENTS

Significant progress was made toward the technical objectives of the three major tasks of the PA Research Project. In Conceptual Model Development (Task 1), for example, two research activities related to flow and transport in unsaturated media were completed. The first activity was conducted as an integrated effort with the Geochemical Analog of Contaminant Transport in Unsaturated Rock Research Project and provided analyses of hydraulic properties and model predictions for a proposed infiltration experiment at the Peña Blanca field site. The second activity produced a new conceptual and mathematical approach for describing radionuclide adsorption in porous media. This new modeling approach will be expanded to include ion exchange phenomena and surface interaction in unsaturated media and is expected to be used in IPA Phase 3. Under Computational Model Development (Task 2), research was performed on advanced computational methods for solving the nonlinear flow equation and on the use of Parallel Virtual Machine technology in TPA. As part of Model Evaluation (Task 3), benchmark testing of DOE thermohydrologic codes was performed using a set of challenging test cases.

In the following subsections, the accomplishments of two specific research activities are highlighted. The first activity described is on a novel approach to modeling the migration of radionuclides that are simultaneously competing for adsorption sites. Parametric calculations are presented to illustrate the importance of adsorption site competition on radionuclide transport. A second activity is summarized that presents a new computational method for solving Richards' equation for variably saturated flow in porous media. The superiority of this new method over numerical techniques currently in use is demonstrated with applications to test cases based on data from the YM site.

4.2.1 Methodology for Modeling Radionuclide Adsorption

An improved methodology for modeling the effects of radionuclide adsorption in saturated porous media was recently developed. The improved model presented herein is superior to the classical retardation factor approach in that it is capable of: (i) accounting for the competitive nature of radionuclide adsorption, and (ii) incorporating spatially variable flow and adsorption parameters. This work is expected to be extended to account for simultaneous ion exchange and adsorption (i.e., sorption), and to accommodate variably saturated media. The improved model extends previous work of other investigators (Blue et al., 1995; Turner, 1995; Jeong and Lee, 1992) that considered the competitive effects of sorption.

4.2.1.1 Model Development for Totally Saturated Media

The improved model was developed by writing the mass balance equations for the population density of radionuclide species i (species meaning that radionuclide i may exist in several chemical forms) in both the adsorbed and fluid-bound state for a medium that is totally saturated with water.

$$\frac{\partial}{\partial t} n_i(\vec{r}, t) = [k_i^0(\vec{r})] \left[1 - \frac{\sum_i n_i(\vec{r}, t)}{n_T(\vec{r})} \right] c_i(\vec{r}, t) + \sum_j \lambda_{j \rightarrow i}^P n_j(\vec{r}, t) - \lambda_i^P n_i(\vec{r}, t) - \lambda_i^C n_i(\vec{r}, t) \quad (4-1)$$

$$\frac{\partial}{\partial t} c_i(\vec{r}, t) = \frac{\lambda_i^C}{\epsilon(\vec{r})} n_i(\vec{r}, t) - \lambda_i^P c_i(\vec{r}, t) + \sum_j \lambda_{j-i}^P c_j(\vec{r}, t) - \sum_j R_{i-j} c_i(\vec{r}, t) + \sum_j R_{j-i} c_j(\vec{r}, t) \quad (4-2)$$

$$- \frac{[k_i^0(\vec{r})]'}{\epsilon(\vec{r})} \left[1 - \frac{\sum_j n_j(\vec{r}, t)}{n_T(\vec{r}, t)} \right] c_i(\vec{r}, t) - \vec{\nabla} \cdot [\vec{U}(\vec{r}, t) c_i(\vec{r}, t)] + \vec{\nabla} \cdot D_i(\vec{r}) \vec{\nabla} c_i(\vec{r}, t)$$

where:

- $n_i(\vec{r}, t)$ - the number of atoms of radionuclide species i that are adsorbed rock surfaces per unit total volume (volume of rock plus pores)
- $n_T(\vec{r})$ - the number of adsorber sites per unit total volume (volume of rock plus pores)
- $[k_i^0(\vec{r})]'$ - the number of atoms of radionuclide species i adsorbed per unit total volume per unit time per unit concentration of radionuclide species i in the groundwater, in the absence of any adsorbed atoms on the rock surfaces
- λ_{j-i}^P - the probability per unit time that radionuclide j decays resulting in the production of radionuclide i
- λ_i^P - the radioactive decay constant for radionuclide i
- λ_i^C - the desorption rate constant for radionuclide species i
- $c_i(\vec{r}, t)$ - the concentration of radionuclide species i in the groundwater
- $\epsilon(\vec{r})$ - the rock porosity, or the volume of pore space per unit total volume
- R_{j-i} - the reaction rate (per unit concentration) of radionuclide species j with other groundwater constituents that results in the production of radionuclide species i
- $\vec{U}(\vec{r}, t)$ - the pore velocity of the interstitial fluid (water) as a function of position and time
- $D_i(\vec{r})$ - the diffusion coefficient of radionuclide species i in the media as a function of position and time, where $D_i(\vec{r}) = f[\epsilon, \vec{r}, \tau(\vec{r})] \cdot D_{wi}$
- $f[\epsilon, \vec{r}, \tau(\vec{r})]$ - an empirical function relating the diffusion coefficient of radionuclide species i in the porous media to the diffusion coefficient of radionuclide species i in air. Various forms of this function can be found in Jury et al. (1991).

- $\tau(\bar{r})$ - the tortuosity of the media
- D_{wi} - the diffusion coefficient of radionuclide species i in water

The first term on the right-hand side of Eq. (4-1) accounts for the adsorption rate of radionuclide species i from groundwater onto adsorption sites. The expression in the brackets of the first term accounts for the blocking of adsorption sites for radionuclide species i by all radionuclide species (degradation of the adsorption media due to competition). The second term accounts for the ingrowth of radionuclide species i due to decays of parent nuclei assuming that the daughter remains adsorbed. The third term accounts for the radioactive decay rate of radionuclide i while in the adsorbed state. The fourth term accounts for the desorption rate of radionuclide species i from the adsorbed state.

The first term on the right-hand side of Eq. (4-2) accounts for the desorption of radionuclide species i , from the adsorbed state, into water in the pore space. The second term accounts for the radioactive decay of radionuclide species i in the groundwater. The third term accounts for the ingrowth of radionuclide species i in the groundwater from radioactive parents. The fourth and fifth terms account for the outgrowth and ingrowth of radionuclide species i in the groundwater due to chemical reaction with other constituents in the groundwater, resulting in the production of a new chemical species. The sixth term accounts for the adsorption of radionuclide species i from the groundwater onto adsorber sites that are covered with water. The seventh and eighth terms account for the movement of radionuclide species i from one differential volume to another via mass flow and diffusion, respectively.

The same type of modeling could be performed for an unsaturated medium by writing differential equations for $n_i(\bar{r}, t)$ in both the water-covered and water-uncovered state (since radionuclides that adsorb and then are uncovered by decreasing moisture content will have no opportunity to desorb). Unsaturated modeling is not considered here, but will be addressed in future work at the CNWRA.

The above model has the ability to accommodate the competitive nature of radionuclide adsorption, as each adsorbed radionuclide blocks an adsorption site for use by another nuclide. Another important feature of this improved model is that it has the ability to calculate adsorption for spatially variable flow regimes. The flow velocity term in Eq. (4-2) can be a function of position, thus accounting for increased or decreased flow of groundwater in rock fractures. More importantly, a modified experimentally determined adsorber site density can be used for volumes that contain rock fractures (as opposed to those that contain only matrix porosities) to account for adsorption in the fractures.

Equation (4-2) does not account for precipitation of radionuclide species nor dissolution of nuclides in solid phases. Competition with naturally occurring ions could be important as well; therefore, the concentrations and adsorbed population densities of naturally occurring (nonradionuclide species) ions should also be tracked. It may prove possible to model these naturally occurring ions as constant in concentration, so that accounting for their effects could be accomplished by reducing $(k_i^0)'$. It should also be noted that many of the parameters in Eqs. (4-1) and (4-2) are presented as constants. For example, the chemical reaction constants could be functions of the concentration of whatever radionuclide species i is reacting with; however, without going into the specific reactions, these constants would be impossible to quantify. It is anticipated that parameters $(k_i^0)'$, λ_i^c , and $n_T(\bar{r})$ could be functions of solution characteristics, such as pH (Turner, 1993; 1995). Also, rather than assuming the adsorbing species forms

a monolayer, $n_T(\vec{r})$ could be made a function of the adsorbed population density to describe the process of radionuclides adsorbing on top of other radionuclide layers at the cost of further complicating the model. It appears that a monolayer assumption accounts for the situation fairly accurately (Turner, 1995).

Equations (4-1) and (4-2) may be too complex to incorporate into existing PAs. Perhaps the utility of this model with respect to PA could be increased by assuming that steady-state conditions exist, that there is no ingrowth of radionuclides from parent radioactive decay, and that chemical reactions in the groundwater can be neglected (i.e., all radionuclides exist in one, or perhaps, an average chemical form). Under these assumptions, the differential equation describing the concentration of radionuclide species i in the groundwater becomes:

$$0 = \left[\frac{\lambda_i^P}{\epsilon(\vec{r})} \right] \left\{ \frac{\frac{[k_i^0(\vec{r})]'}{\lambda_i} c_i(\vec{r})}{1 + \frac{1}{n_T(\vec{r})} \sum_j \frac{[k_j^0(\vec{r})]'}{\lambda_j} c_j(\vec{r})} \right\} - \lambda_i^P c_i(\vec{r}) \quad (4-3)$$

$$- \vec{\nabla} \cdot [U(\vec{r}) c_i(\vec{r})] + \vec{\nabla} \cdot D_i(\vec{r}) \vec{\nabla} c_i(\vec{r})$$

where $\lambda_i = \lambda_i^P + \lambda_i^C$, which is somewhat more computationally traceable for PA calculations. One should note from Eq. (4-3) that the denominator of the term in square brackets on the right-hand side describes the competitive effects of adsorption; neglecting this term, as will be shown, could have adverse consequences for groundwater radionuclide concentration calculations. One will also note that Eq. (4-3) is only a function of the concentrations of the competing species and not of the adsorbed species population density, thus simplifying the model.

4.2.1.2 Data Extraction

In order to extract the data that the improved adsorption model [i.e., $(k_i^0)'/\lambda_i$] needs from existing data (namely K_d) for the example to follow, a one-species, spatially homogeneous, steady-state saturated system in which the species does not radioactively decay is considered. This analysis assumes that ion exchange is negligible and the water is at rest. Under these circumstances, and dropping the subscript for simplicity, Eqs. (4-1) and (4-2) both reduce to

$$c = \frac{n\lambda^C}{(k^0)' \left(1 - \frac{n}{n_T} \right)} \quad (4-4)$$

Since there are two unknowns (c and n) and only one equation, another equation must be derived to completely describe the system. Consider an introduction of s_0 atoms per unit volume of the radionuclide being investigated:

$$c = s_0 - n \quad (4-5)$$

Recall that K_d , the distribution coefficient, is defined as the ratio of the number of atoms in the adsorbed state per mass of adsorption media to the number of atoms in solution per volume of solution at equilibrium. Or, in terms of the parameters listed above,

$$K_d = \frac{n}{\rho_b c} \quad (4-6)$$

where ρ_b equals the bulk density of the adsorbing media.

Using the assumptions listed in the first paragraph of this section and the above stated definitions leads to an expression for the distribution coefficient

$$K_d = \frac{n}{\rho_b c} = \frac{\left[\frac{\lambda^C}{(k^0)'} + \frac{s_0}{n_T} + 1 \right] - \sqrt{1 + 2 \left[\frac{\lambda^C}{(k^0)'} - \frac{s_0}{n_T} \right] + \left[\frac{\lambda^C}{(k^0)'} + \frac{s_0}{n_T} \right]^2}}{\rho_b \left\{ \left[-\frac{\lambda^C}{(k^0)'} + \frac{s_0}{n_T} - 1 \right] + \sqrt{1 + 2 \left[\frac{\lambda^C}{(k^0)'} - \frac{s_0}{n_T} \right] + \left[\frac{\lambda^C}{(k^0)'} + \frac{s_0}{n_T} \right]^2} \right\}} \quad (4-7)$$

One should note that the expression in Eq. (4-7) has the expected form with respect to increasing s_0 (at small values of s_0 , K_d is approximately constant and at exceedingly large values of s_0 , K_d approaches zero).

In the low atomic concentration limit, Eq. (4-7) becomes

$$K_d = \frac{1}{\rho_b} \frac{(k^0)'}{\lambda^C} \quad (4-8)$$

As an example, consider the cases of Pu and U that will be used in the following sections. Wilson et al. (1994) reports a median K_d of 2.5 g/cm³ for U and 125 g/cm³ for Pu. Assuming that these values denote the low atomic concentration ($s_0 \rightarrow 0$) distribution coefficients for U and Pu ions, and using a bulk rock density of 2 g/cm³, one finds:

$$\frac{(k_1^0)'}{\lambda_1} \approx \frac{(k_1^0)'}{\lambda_1^C} = 5 \quad (4-9)$$

$$\frac{(k_2^0)'}{\lambda_2} \approx \frac{(k_2^0)'}{\lambda_2^C} = 250 \quad (4-10)$$

where radionuclide 1 is U, radionuclide 2 is Pu, and it is assumed that radioactive decay is negligible when compared with chemical desorption.

4.2.1.3 Significance of the New Model

To illustrate the significance of this new methodology for radionuclide adsorption, consider a system composed of ^{238}U (radionuclide 1), ^{239}Pu (radionuclide 2), water, and rock. In the following sections, the predictions of the new model (assuming ion exchange is negligible) and a model using a retardation factor approach are compared. Both models are used to predict the concentration of Pu in groundwater as a function of distance from a source. The comparison highlights potential for nonconservative estimates of radionuclide releases inherent in the widely used retardation factor approach.

Groundwater Pu Concentrations as Calculated Using Constant Retardation Factors.

The method currently used for calculating the concentration of radionuclides in the groundwater at some point along the transport path assumes that the radionuclide travels with some constant, reduced velocity (as compared to the groundwater travel velocity), independent of adsorbed radionuclide populations, that is due to the effects of adsorption. The ratio of the groundwater travel velocity to the radionuclide travel velocity is called the retardation factor. Under this type of modeling, the concentration of Pu in the groundwater at some point along the steady-state travel path is given by:

$$c_2(x) = c_{2,0} \exp[-\lambda_2^P \cdot R_f^{\text{Pu}} \cdot t_w(x)] \quad (4-11)$$

where:

$c_{2,0}$ - the concentration of Pu in the groundwater at $x=0$

R_f^{Pu} - the retardation factor for Pu

$t_w(x)$ - the time required for the groundwater to travel from the system origin ($x=0$) to a point x

In order to make this calculation more physically meaningful for the case of YM, it is further assumed that:

- (i) The repository inventory of ^{239}Pu equals 2.1×10^7 Ci (Lozano et al., 1994).
- (ii) The rate of water flow through the repository is spatially uniform and equals 9.43×10^4 L/yr (Duguid et al., 1994).
- (iii) The solubility of Pu equals 10^{-5} moles/L and that the water flowing through the repository becomes saturated and is not diluted along its path to the accessible

environment (Kerrisk, 1985). Alternatively one could perform the same calculation per unit input concentration (concentration of the radionuclide at $x=0$). The stated solubility of Pu is used as an upper limit.

- (iv) R_f^{Pu} equals 251 (Wilson et al., 1994), assuming a bulk rock density of 2 g/cm^3 , a pore water fraction of unity, and a median K_d for devitrified tuff of $125 \text{ cm}^3/\text{g}$.
- (v) t_w ($x=5,000 \text{ m}$) equals 1,000 yr.

With assumptions (i), (ii), and (iii), the concentration of Pu in the groundwater at $x=0$ is:

$$c_{2,0} = 6.0 \times 10^{18} \left(\frac{\text{atoms}}{\text{L}} \right) \quad (4-12)$$

Groundwater Pu Concentrations as Calculated Using the Proposed Model.

Using the improved model, as described by Eqs. (4-1) and (4-2), one finds that the groundwater concentration of Pu is

$$c_2(x) = c_{2,0} \exp \left\{ - \frac{\lambda_2^P}{U_0} \left[1 + \frac{1}{\epsilon} \frac{(k_2^0)'}{\lambda_2} \frac{\lambda_1}{(k_1^0)'} \frac{n_T}{c_{1,0}} \right] x \right\} \quad (4-13)$$

Equation (4-13) was derived from Eqs. (4-1) through (4-3) using the previously listed assumptions and the following:

- (i) n_T is less than 10^{20} \#/L^*
- (ii) $\frac{(k_1^0)'}{\lambda_1 n_T} c_1(x) > 1$ and $\frac{(k_1^0)'}{\lambda_1 n_T} c_1(x) > \frac{(k_2^0)'}{\lambda_2 n_T} c_2(x)$
- (iii) The solubility of U is $2 \times 10^{-3} \text{ (moles/L)}$ and the water flowing through the repository is saturated with U (Kerrisk, 1985)
- (iv) The repository inventory of ^{238}U is $2.1 \times 10^4 \text{ Ci}$ (Lozano et al., 1994)

* Because data for this parameter for devitrified tuff were unavailable, a range was chosen that is at least an order of magnitude lower than that for U.S. Environmental Protection Agency activated charcoal (from Blue et al., 1995).

These assumptions lead to a solution for $c_{1,0}$ of:

$$c_{1,0} = 1.2 \times 10^{21} \left(\frac{\text{atoms}}{\text{L}} \right) \quad (4-14)$$

In Eq. (4-14) it has been further assumed that there is negligible radioactive decay of U in transport, as the half-life of ^{238}U is long (4.5×10^4 yr) when compared to an estimate of the maximum radionuclide travel time through the media of $R_f * t_w$ (6,000 yr).

The groundwater concentration of Pu and U as a function of distance into the media as calculated by the retardation factor method and the new method (with n_T as a parameter) is shown in Figure 4-1. As one can see, accounting for the competitive degenerative nature of adsorption has significant effects on groundwater concentration predictions.

4.2.1.4 Interpretation of Results

The model presented here addresses two of the shortcomings of the classical retardation model currently used in YM PA work by accounting for the competitive nature of radionuclide adsorption and the degeneration of the adsorption capabilities of geologic media due to occupation of adsorption sites by other radionuclides. The model presented in this report should work well provided that the monolayer adsorption approximation is valid. Data presented in Turner (1995), as fit by the diffuse layer surface complexation model, would suggest that this approximation is valid for the general case.

Using the derived model instead of a simple retardation factor approach leads to significant impacts on calculations of groundwater radionuclide concentrations. There was approximately a three order of magnitude difference between groundwater ^{239}Pu concentration calculations at 5,000 m into a geologic medium using the two different models for a simple system composed of ^{238}U , ^{239}Pu , water, and rock typical of YM, as ^{238}U was able to block enough of the adsorber sites such that ^{239}Pu was able to pass through unimpeded by adsorption. The mathematical simplifications made during these calculations were intended to make the calculations transparent to the reader. Although these simplifications are realistic in the context presented, in general the differential equations would be solved numerically to incorporate this adsorption model into existing PA methodology.

It is envisaged that this model can be directly coupled to models that predict the flow velocity of groundwater in geologic media, as the groundwater velocity term and the adsorption site density directly couple into the adsorption equations. Accordingly, the model could be incorporated into existing PA models provided that sufficient data exist.

Future work on this topic will include generalizing the model to account for adsorption in unsaturated media. Generalization will be accomplished by writing differential equations for adsorbed radionuclide species in both the fluid-covered and fluid-uncovered state. It will be assumed that any adsorption radionuclide species not covered by fluid is trapped on the adsorption site since there will be no fluid into which they can desorb. Future modeling work will also include the ion exchange property of the media.

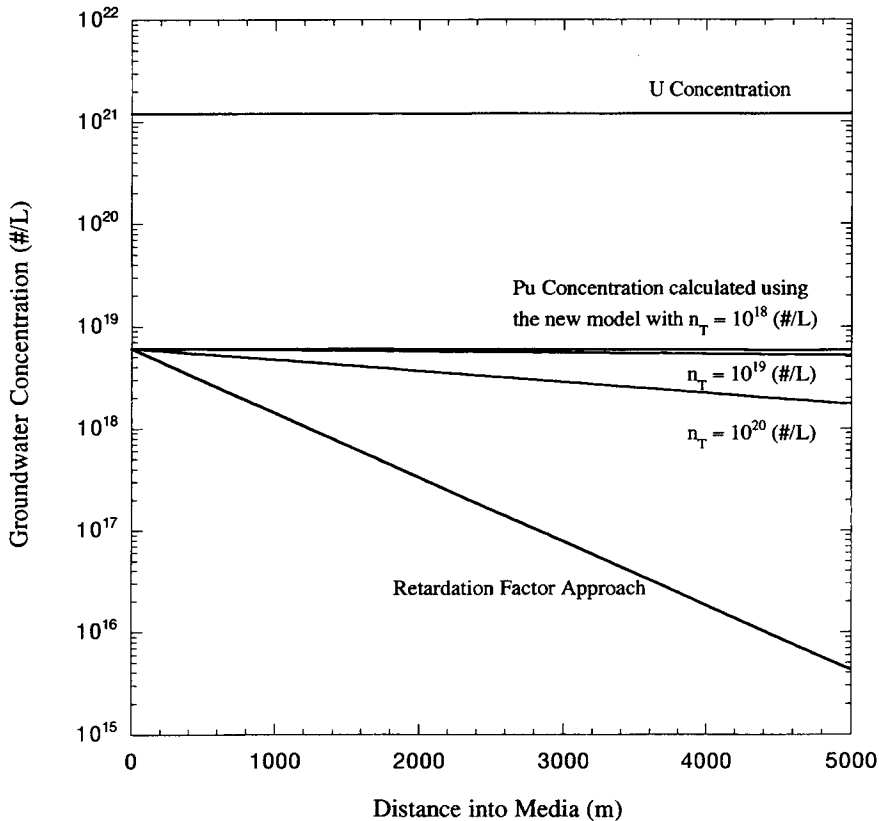


Figure 4-1. A comparison of groundwater Pu concentrations with the retardation factor method and the new method with n_T as a parameter

4.2.2 Advanced Computational Methods

Performance assessments of the proposed YM site involve extensive utilization of numerical models to predict fluid flow and contaminant transport. Models of infiltration and deep percolation, for example, are playing a central role in the NRC IPA studies. Numerical models are currently being applied to forecast infiltration rates that may occur as a result of future climate changes (typically spanning thousands of years) (Stothoff, 1995). In steady-state analyses, Monte Carlo simulations of flow are generally performed to develop probabilistic estimates of water fluxes (Childs and Long, 1992) and travel times (Bagtzoglou and Baca, 1994). Such models require fast, accurate, and robust numerical algorithms in order for these specialized applications to become routine. This use of detailed simulation of flow in unsaturated media has motivated research to pursue improved numerical techniques to solve the governing flow equation, that is, Richards' equation, in a more efficient manner.

A new transform-based approach has been tested using data from the YM site, Hanford site, and the Idaho National Engineering Laboratory. A comparative study of various transforms was recently completed, and the results of that study will be documented in a future journal article. All of those test cases reflect flow conditions of great computational difficulty such as: (i) large infiltration rates into very dry soils, (ii) flow through soil layers with large permeability contrasts, and (iii) flow involving the

formation and dissipation of perched-water zones. In this section, the essential mathematical theory of the new method is presented, along with an application to one of the test cases developed using data from the YM site.

4.2.2.1 Mathematical Theory of New Transform-Based Approach

The mixed form of Richards' equation for transient flow in variably saturated porous media is a well-known nonlinear parabolic equation. A modified form of this equation, which has significant advantages, is obtained by making a simple change of variable in the spatial term. For one-dimensional flow, the modified or "transformed" Richards' equation is expressed as:

$$\frac{\partial \theta}{\partial t} = \frac{\partial}{\partial z} \left(\kappa \frac{\partial \chi}{\partial z} - K \right) \quad (4-15)$$

where $\theta(\psi)$ is the volumetric water content (cm^3/cm^3), κ is $K \partial \psi / \partial \chi$, $K(\psi)$ is the hydraulic conductivity (cm/s), ψ is the pressure head (cm), z is the depth (cm) taken positive downward, and t is time. In this formulation, fluid storage associated with compressibility of both the porous medium and fluid is neglected. The new dependent variable χ is defined as a generalized "partitioned transform," namely

$$\chi = \begin{cases} \psi & \psi \geq \psi_0 \\ \alpha_1 f(\theta, \psi) + \alpha_2 & \psi < \psi_0 \end{cases} \quad (4-16)$$

where $f(\theta, \psi)$ is an analytic function, yet to be specified, and ψ_0 is an arbitrary match point. The fundamental idea of this approach is to select an analytic function that transforms ψ into a "compressed" state variable χ . This compression results in a smooth and more gradually varying solution space. In turn, the smoother solution space allows more accurate calculation of the spatial gradients of χ . Four transforms that can be written in partitioned form are: (i) natural log, (ii) inverse hyperbolic sine, (iii) algebraic, and (iv) mixed (which uses both θ and ψ).

To formulate a numerical solution method for the transformed Richards' equation, an iterative algorithm must be used because of its strong nonlinearity. An iterative algorithm can be directly embedded in a finite element approximation by using the Newton-Galerkin method (Baca et al., 1995). This method requires that the product of a set of weighting functions, $\omega_j(z)$, and the first order Taylor series expansion of the residual, ϵ , be orthogonal under integration. Specifically, the Newton-Galerkin method requires

$$\int_{\Omega} \omega_j(z) \left(\epsilon^k + \frac{\partial \epsilon^k}{\partial \psi} \Delta \psi \right) dz = 0 \quad 1 < j \leq N \quad (4-17)$$

where Ω denotes the spatial domain $0 \leq z \leq L$, N is the number of basis functions, and ϵ^k is obtained directly from the transformed Richards' equation, namely

$$\epsilon^k = \frac{\partial \theta}{\partial t} - \frac{\partial}{\partial z} \left(\kappa \frac{\partial \chi}{\partial z} - K \right) \quad (4-18)$$

In this expression, the spatial variation of θ , χ , κ , and K is approximated using a set of linear basis functions; these functions are chosen to be identical to the set of weighting functions $\omega_j(z)$. It is important to note that the numerical solution is in terms of ψ rather than θ or χ , both of which are often discontinuous at layer interfaces where the unsaturated hydraulic properties change. Substituting Eq. (4-18) into Eq. (4-17) and rearranging, the following system of algebraic equations is produced for an arbitrary element e :

$$[J_e] \{ \Delta \psi \} = - \{ R_e \} \quad (4-19)$$

where the right-hand side vector is:

$$\begin{aligned} \{ R_e \} = & \frac{1}{\Delta t} \int_{\Omega_e} \{ \omega \} \{ \omega \}^T dz \{ \Delta \theta^k \} + \int_{\Omega_e} \left\{ \frac{\partial \omega}{\partial z} \right\} \hat{\kappa} \left\{ \frac{\partial \omega}{\partial z} \right\}^T dz \{ \chi \} \\ & - \int_{\Omega_e} \left\{ \frac{\partial \omega}{\partial z} \right\} \{ \omega \}^T dz \{ K \} - \begin{Bmatrix} q_{e1}^{bc} \delta_{e1} \\ -q_{eM}^{bc} \delta_{eM} \end{Bmatrix} \end{aligned} \quad (4-20)$$

and the Jacobian matrix is:

$$\begin{aligned} [J_e] = & \frac{1}{\Delta t} \int_{\Omega_e} \{ \omega \} \{ \omega \}^T dz \{ \Delta \theta^k \} \left\{ \frac{1}{\partial \psi^{n+1}} \right\}^T \\ & + \int_{\Omega_e} \left\{ \frac{\partial \omega}{\partial z} \right\} \hat{\kappa} \left\{ \frac{\partial \omega}{\partial z} \right\}^T dz \{ \chi \} \left\{ \frac{\partial}{\partial \psi^{n+1}} \right\}^T - \int_{\Omega_e} \left\{ \frac{\partial \omega}{\partial z} \right\} \{ \omega \}^T dz \{ K \} \left\{ \frac{\partial}{\partial \psi^{n+1}} \right\}^T \end{aligned} \quad (4-21)$$

where $\hat{\kappa} = \{ \omega \}^T \{ \kappa \}$, the Kronecker deltas for the boundary flux q^{bc} are defined as $\delta_{e1} = 1$ for the first element and is zero elsewhere, while $\delta_{eM} = 1$ for the last element only. The fully integrated forms of $\{ R_e \}$ and $[J_e]$ can be found in Baca et al. (1995).

4.2.2.2 Example Application of New Computational Method

To illustrate the capability of the new computational approach, we consider the problem of simulating flow in a multilayer system. The test problem selected is taken from the INTRAVALEX exercise for the YM site. This test problem is based on data collected by the DOE/U.S. Geological Survey for borehole UZ-16, which is drilled to a depth of 490 m and terminates just below the water table. Specific model parameters developed for UZ-16 are summarized in Table 4-1 (Table 7-2 in Baca et al., 1994).

Table 4-1. Hydrostratigraphy and van Genuchten-Mualem parameters for UZ-16 (Baca et al., 1994)

Top (m)	Bottom (m)	α (m ⁻¹)	n	K_s (m/s)	θ_s	θ_r	Lithology
0.00	-10.80	0.1	1.3	1.0×10^{-6}	0.098	0.0001	Alluvium
-10.80	-17.80	0.031	1.5	7.1×10^{-13}	0.057	0.003	TC Lower Lithophysal
-17.80	-34.10	0.0024	1.82	7.8×10^{-10}	0.071	0.007	TC Hackly
-34.10	-42.60	0.0024	1.82	3.9×10^{-13}	0.072	0.007	TC Colmn. Densely Welded
-42.60	-44.40	0.86	1.3	5.8×10^{-8}	0.28	0.001	TC Colmn. Mod. Welded
-44.40	-48.40	0.86	1.3	1.6×10^{-6}	0.42	0.001	TC Shardy Base
-48.40	-49.30	3.69	1.33	5.5×10^{-5}	0.52	0.01	TC Bedded Tuffs
-49.30	-52.30	1.40	1.28	4.3×10^{-6}	0.41	0.008	TC Yucca Mt. Member
-52.30	-58.00	0.76	1.34	3.4×10^{-6}	0.45	0.009	TC Bedded Tuffs
-58.00	-66.30	0.22	2.35	3.3×10^{-6}	0.57	0.011	TS Nonwelded
-66.30	-69.60	0.22	1.8	5.0×10^{-7}	0.46	0.01	TS Mod. Welded
69.60	-71.90	0.0076	1.8	3.7×10^{-11}	0.042	0.0004	TS Vitric Caprock
-71.90	-100.70	0.14	1.42	1.8×10^{-8}	0.16	0.004	TS Rounded
-100.70	-165.60	0.105	1.36	1.4×10^{-11}	0.14	0.004	TS Upper Lithophysal
-165.60	-203.30	0.0074	1.64	4.5×10^{-13}	0.10	0.01	TS Middle NonLithophysal
-203.30	-285.80	0.053	1.46	6.9×10^{-12}	0.14	0.008	TS Lower Lithophysal
-285.80	-328.30	0.25	1.23	2.4×10^{-12}	0.11	0.01	TS Lower NonLithophysal
-328.30	-338.30	0.25	1.23	7.0×10^{-12}	0.096	0.008	TS Smectite Zone
-338.30	-354.80	0.0076	1.8	3.7×10^{-11}	0.063	0.006	TS Basal Vitrophyre
-354.80	-367.50	0.021	2.65	2.0×10^{-11}	0.24	0.003	TS Nonpart. Welded
-367.50	-446.80	0.0051	1.68	3.0×10^{-11}	0.32	0.005	Calico Hills Nonwelded Zeolitic
-446.80	-454.80	0.0026	1.4	2.5×10^{-11}	0.24	0.002	CH Bedded Tuff
-454.80	-482.20	0.006	2.4	2.3×10^{-12}	0.29	0.003	Prow Pass Nonwelded Zeolitic
-482.20	-490.00	0.004	1.46	6.5×10^{-12}	0.20	0.002	PP Mod. Welded Devit.

As in the INTRAVAL exercise, the hydrostratigraphic model for this borehole consists of 24 layers, and the hydraulic properties of each layer are described by van Genuchten-Mualem relations:

$$S_e = \frac{\theta - \theta_r}{\theta_s - \theta_r} = \left[\frac{1}{1 + (\alpha |h|)^n} \right]^m \quad (4-22)$$

$$K = K_s S_e^{1/2} \left[1 - (1 - S_e^{1/m})^m \right]^2 \quad (4-23)$$

where θ_r and θ_s are residual and saturated water contents, respectively, K_s is the saturated hydraulic conductivity, and α , n , and m are model parameters with $m = 1 - 1/n$.

Each of the 24 layers was discretized into 10 finite elements, which produced a variable grid of 241 nodes. Simulations of steady-state flow were accomplished by performing a transient simulation for a 10^6 -yr period. The surface boundary condition was a constant flux of 0.0086 mm/yr with the initial conditions assumed to be uniform and set to -10^4 cm. The bottom boundary was fixed at a pressure head corresponding to the measured moisture content. The flow simulations for this test problem were performed on an IBM PS/2 Model 95 (486/66). The total CPU time to perform this simulation was about 3 min. The simulation results are shown in Figure 4-2, which compares the computed and measured moisture content profiles.

It is important to note that previous attempts to simulate this INTRAVAL test problem using available CNWRA finite difference codes were largely unsuccessful (Baca et al., 1993), as time steps required for convergence were impractically small. The test case is computationally challenging because of: (i) the strongly nonlinear nature of Richards' equation, (ii) the large variations in van Genuchten parameters, and (iii) the very dry initial conditions. The results of this test case and others documented in a forthcoming journal article illustrate that the new method is significantly more robust and computationally efficient than the popular modified Picard method (Celia et al., 1990). The incorporation of this new computational method into the CNWRA flow codes (e.g., BREATH, BIGFLOW, PORFLOW, CTOUGH) will significantly extend their utility and simulation capability.

4.3 ASSESSMENT OF PROGRESS TOWARD MEETING PROJECT OBJECTIVES

As indicated previously, one of the main programmatic objectives of the PA Research Project is to provide enhanced PA models and codes for use in the NRC IPA exercises. A second and equally important objective is to provide PA methodology that can be used as CDM analysis tools. During this reporting period, noteworthy progress was made toward both of these objectives. A set of NUREG/CR reports are soon to be published that document some of the recent accomplishments of the PA Research Project.

Research on the adsorption process produced a new conceptual model that provides a more realistic description of the chemical effects on radionuclide transport. This new approach overcomes one of the major limitations of the classical " K_d " approach to adsorption. A summary of the conceptual and mathematical model is presented in Section 4.2.1 of this chapter; a more detailed description of the theory is contained in a paper currently being finalized for submittal to a peer-reviewed journal. This new

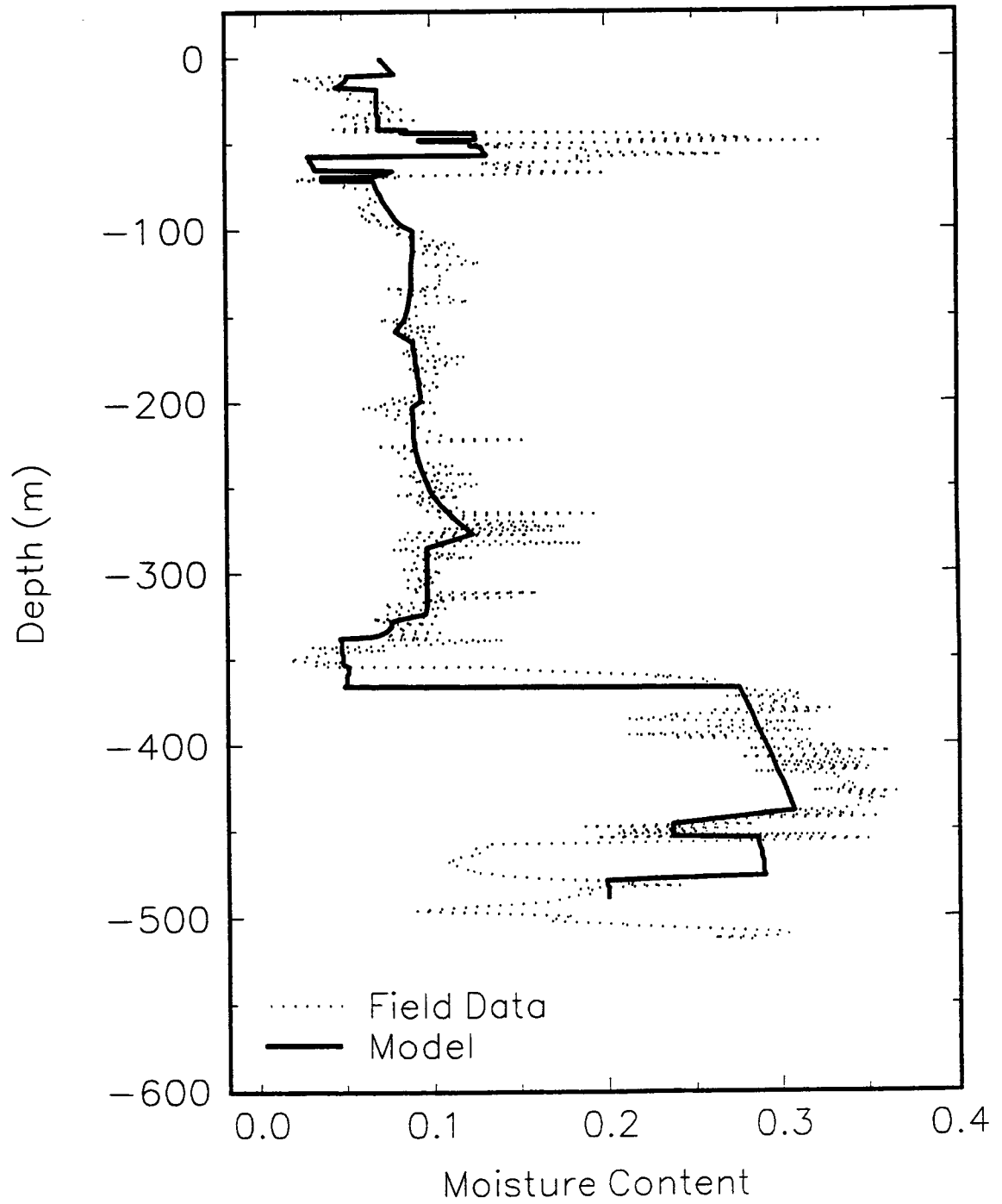


Figure 4-2. Comparison of computed and measured moisture content profiles for UZ-16

adsorption model is expected to be incorporated in the transport module of the TPA code (Sagar and Janetzke, 1993).

Significant progress was made on the development of advanced computational and computer modeling techniques. In particular, a new computational method was developed for solving the strongly nonlinear equation for flow in unsaturated media. This new method is very robust, accommodates a wide variety of flow regimes, and is four to five times faster than numerical techniques (Celia et al., 1990) currently in wide use. This new computational method is described in a paper (Baca et al., 1995) recently submitted for journal publication. It is expected that the new method will significantly improve the computational speed and robustness of such multidimensional flow codes as BIGFLOW, PORFLOW, and DCM3D. Significant progress was made on the evaluation of PVM computing technology. Current findings suggest that PVM is very well suited to the Monte Carlo simulation approach used in PA codes. In addition, significant progress was made on a relatively new sensitivity analysis method referred to as the Variance-Based Sensitivity Method (McKay and Beckman, 1994). This new method of conducting sensitivity analysis is expected to be used in the IPA Phase 3 exercise.

Benchmark testing of DOE and NRC/CNWRA thermohydrologic codes was conducted, and comparative results were obtained for several isothermal and nonisothermal flow problems. Two DOE codes, FEHMN and TOUGH2, were tested on progressively difficult problems. Simulation results produced by codes were compared with results obtained with the NRC/CNWRA codes CTOUGH and PORFLOW. The experience gained with these DOE codes will have direct benefit to the forthcoming NRC review of the DOE Topical Report on Process Models and future technical reports on the repository thermal-loading strategy.

4.4 PLANS FOR NEXT REPORTING PERIOD

A number of new and challenging research topics will be pursued in the next period. These topics were chosen to meet the priority modeling needs of IPA and subsystem PA. Research on these topics will be performed in a manner that fully utilizes and integrates the knowledge base, models, and data from the technical assessment activities under DWM and from various research projects (e.g., Subregional Hydrogeology, Geochemical Analogs, Volcanic Systems, Rock Mechanics) under RES. New and improved PA methodologies developed under this project will be documented in CNWRA technical reports, NUREG/CR reports, peer-reviewed journals, and conference proceedings.

Within the scope of Task 1, research efforts will be devoted to three major topics. The first topic deals with radiocolloid transport in the unsaturated zone. Utilizing the results from the recent literature review (Manaktala et al., 1995), a conceptual model will be developed that describes the genesis, interaction, and transport of colloids. This conceptual model will be used in formulating a mathematical model of multicomponent and multiphase mass transport through the fractured-porous tuff. The second topic will involve the new methodologies for scenario analysis. In particular, the "influence diagram" and "Rock Engineering System Matrix" techniques developed by the Swedish Nuclear Fuel and Waste Management Company (Eng, 1995) will be evaluated for possible use in scenario analysis for YM. The third topic will examine flow in fractured-porous media and will delve into the nature of matrix-fracture interactions. Research on these three topics will be coordinated with the NRC IPA Phase 3 exercise and aimed at providing information that can be used in precicensing reviews of DOE activities.

As part of Task 2, research will be directed to methods of complementary cumulative distribution function (CCDF) construction and evaluation of advanced computational and computer methods. A study will be conducted to examine alternate approaches to CCDF construction for the

purpose of determining the advantages, underlying assumptions, and potential limitations. Results of this study will provide the basis for a future NRC Staff Technical Position. New and emerging computational and computer methods that may significantly improve computing efficiency of the IPA and subsystem PA codes will be examined. In addition, it is expected that recently developed sensitivity analysis methods will also be studied and evaluated for potential use in IPA- and PA-related CDMs.

Under the scope of Task 3, model evaluation studies will concentrate on two topics: (i) benchmark testing of DOE PA codes, and (ii) demonstration of the NRC/SKI model validation strategy. The current testing of the DOE thermohydrologic codes (e.g., FEHMN and TOUGH2) and the NRC thermohydrologic codes (e.g., CTOUGH and PORFLOW) will be completed and documented in a technical report. In addition, the DOE/USGS codes for modeling flow in the unsaturated zone (e.g., VS2D) will be acquired and rigorously tested against the NRC/DOE flow codes (e.g., BIGFLOW, BREATH, and DCM3D). The results of this benchmark testing will be directly beneficial to the future review of the DOE topical report on the DOE process models (U.S. Department of Energy, 1994).

4.5 REFERENCES

- Baca, R.G., G.W. Wittmeyer, R.T. Green, and S. Mohanty. 1993. Performance assessment research. *NRC High-Level Radioactive Waste Research at CNWRA January-June 1993*. B. Sagar, ed. CNWRA 93-01S. San Antonio, TX: Center for Nuclear Waste Regulatory Analyses.
- Baca, R.G., R.D. Manteufel, S. Mohanty, S.A. Stothoff, and G.W. Wittmeyer. 1994. Performance assessment research. *NRC High-Level Radioactive Waste Research at CNWRA July-December 1993*. B. Sagar, ed. CNWRA 93-02S. San Antonio, TX: Center for Nuclear Waste Regulatory Analyses: 7-1 to 7-29.
- Baca, R.G., J.N. Chung, and D.J. Mulla. 1995. Mixed transform finite element method for solving the equation for variably saturated flow. *International Journal for Numerical Methods in Fluids*. In Review.
- Bagtzoglou, A.B., and R.G. Baca. 1994. Probabilistic calculations of groundwater travel time in heterogeneous three-dimensional porous media. *Materials Research Society Symposium Proceedings*. Boston, MA: Materials Research Society 333: 849-854.
- Blue, T.E., M.S. Jarzempa, and A.W. Fentiman. 1995. Steady-state response of a charcoal bed to radon in flowing air with water vapor. *Health Physics* 68(6): 809-816.
- Celia, M.A., E.T. Bouloutas, and R.L. Zarba. 1990. A general mass-conservative numerical solution for the unsaturated flow equation. *Water Resources Research* 26(7): 1,483-1,496.
- Childs, S.W., and A. Long. 1992. Model and calculations for net infiltration. *Third Annual International High-Level Radioactive Waste Management Conference Proceedings*. La Grange Park, IL: American Nuclear Society: 1,633-1,642.
- Duguid, J.O., R.W. Andrews, E. Brandstetter, T.F. Dale, and M. Reeves. 1994. *Calculations Supporting Evaluation of Potential Environmental Standards for Yucca Mountain*. B00000000-01717-2200-00094-Rev. 01. Las Vegas, NV: INTERA Inc.

- Eng, T. 1995. Recent scenario development methodologies within SKB. *Sixth Annual International High-Level Radioactive Waste Management Conference Proceedings*. La Grange Park, IL: American Nuclear Society: 394–396.
- Jeong, C.W., and K.J. Lee. 1992. Propagation of concentration waves through a sorption medium with simultaneous ion exchange and electrolyte adsorption. *Waste Management* 12: 61–73.
- Jury, W.A., W.R. Gardner, and W.H. Gardner. 1991. *Soil Physics*. New York, NY: John Wiley and Sons, Inc.
- Kerrisk, J.F. 1985. *An Assessment of the Important Radionuclides in Nuclear Waste*. LA-10414-MS. Los Alamos, NM: Los Alamos National Laboratory.
- Lozano, A.S., H. Karimi, J.P. Cornelius, R.D. Manteufel, and R.W. Janetzke. 1994. *INVENT: A Module for the Calculation of Radionuclide Inventories, Software Description, and User Guide*. CNWRA 94-016. San Antonio, TX: Center for Nuclear Waste Regulatory Analyses.
- Manaktala, H., D. Turner, T. Ahn, V. Colten-Bradley, and E. Bonano. 1995. *Potential Implications of Colloids on the Long-Term Performance of a High-Level Radioactive Waste Repository*. CNWRA 95-015. San Antonio, TX: Center for Nuclear Waste Regulatory Analyses.
- McKay, M.D., and R.J. Beckman. 1994. Using variance to identify important inputs. *Proceedings of the Joint Statistical Meetings*. Toronto, Canada: LAUR 94-566. Los Alamos, NM: Los Alamos National Laboratory.
- Nuclear Regulatory Commission. 1994. *License Application Review Plan for the Review of a License Application for a Geologic Repository for Spent Nuclear Fuel and High-Level Radioactive Waste, Yucca Mountain Site, Nevada*. NUREG-1323. Washington, DC: Nuclear Regulatory Commission.
- Sagar, B., and R. Janetzke. 1993. *Total System Performance Assessment Computer Codes: Description of Executive Module*. CNWRA 93-017. San Antonio, TX: Center for Nuclear Waste Regulatory Analyses.
- Stothoff, S.A. 1995. *BREATH Version 1.1—Coupled Flow and Energy Transport in Porous Media, Simulator Description and User Guide*. NUREG/CR-6333. Washington, DC: Nuclear Regulatory Commission.
- Turner, D.R. 1993. *Mechanistic Approaches to Radionuclide Sorption Modeling*. CNWRA 93-019. San Antonio, TX: Center for Nuclear Waste Regulatory Analyses.
- Turner, D.R. 1995. *A Uniform Approach to Surface Complexation Modeling of Radionuclide Sorption*. CNWRA 95-001. San Antonio, TX: Center for Nuclear Waste Regulatory Analyses.
- U.S. Department of Energy. 1994. *Yucca Mountain Site Characterization Project Five-Year Plan Fiscal Years 1996-2000, Predecisional Draft*. Washington, DC: U.S. Department of Energy.

Wilson, M.L., J.H. Gauthier, R.W. Barnard, G.E. Barr, H.A. Dockery, et al. 1994. *Total-System Performance Assessment for Yucca Mountain-SNL Second Iteration (TSPA-1993)*. Vol. 1 and 2. SAND93-2675. Albuquerque, NM: Sandia National Laboratories.

5 VOLCANIC SYSTEMS OF THE BASIN AND RANGE

by Charles B. Connor

Investigators: Charles B. Connor, Brittain E. Hill, Gerry Stirewalt, F. Michael Conway, Peggy Hunka, Ron Martin (CNWRA), and Christopher D. Condit (University of Massachusetts)

NRC Project Officer: Linda Kovach

5.1 OVERALL TECHNICAL OBJECTIVES

Characterization of the frequency and nature of past volcanic events in the Yucca Mountain Region (YMR) and assessment of the probability and consequences of future volcanism are critical aspects of precensuring scientific investigation. The technical objectives of the Volcanic Systems of the Basin and Range Research Project are to (i) assess the probability of continued magmatic activity in the YMR, (ii) develop models that better predict the interaction between structure and volcanism in this tectonic setting, and (iii) develop scenarios for the impact of volcanism on the Yucca Mountain (YM) repository. Effective review of the Department of Energy license application will require insight into volcanic processes operating in the YMR on several scales. Investigations into the scale of volcanic processes include assessment of: Western Great Basin (WGB) tectonic and structural controls on volcanism on local scales (10^2 to 10^3 km²), the longevity of cinder cone clusters and individual volcanoes in the WGB, and the relationship between specific mappable faults, joints, and fractures, and volcanic conduits, such as dikes and dike swarms. The WGB has been the site of recurring small-volume basaltic volcanism throughout the Quaternary. Modern analogs and theoretical studies have demonstrated convincingly that this activity encompasses a variety of eruption styles. The Volcanic Systems of the Basin and Range Research Project has been designed to assess the probability of future volcanism in the YMR, taking into account the range of activity and structural controls on activity that are an inherent part of WGB volcanism.

Insight gained through the Volcanic Systems of the Basin and Range Research Project will be used to support specific sections of the License Application Review Plan (LARP). Research on Basin and Range volcanism will form an integral part of the description of the site and site characterization activities (Evidence of igneous activity as a potentially adverse condition, Section 3.2.1.9, and Impact of volcanism on groundwater movement, Section 3.2.2.7), and the description of overall system performance (assessment of compliance with the requirement for cumulative releases of radioactive materials, Section 6.1). Compliance Determination Strategies (CDSs) for these LARP sections are currently under development. However, the CDS associated with evidence of Quaternary volcanism is of Type 5, indicating that the Nuclear Regulatory Commission (NRC) may need to conduct independent research to evaluate Key Technical Uncertainties (KTUs) associated with volcanism and that volcanism poses a high risk of noncompliance with 40 CFR Part 191 as set forth by the U.S. Environmental Protection Agency, and Parts 10 CFR 60.122(c)(15) and 10 CFR 60.122(c)(3) as determined by the NRC. Consequently, this project will assist in the resolution of specific KTU topics, including: (i) prediction of future system states (disruptive scenarios), (ii) prediction of future changes in the hydrologic system (due to tectonism), (iii) determining the probability of igneous activity and resulting disruption of the candidate repository. Of these KTUs, (i) and (iii) are focused upon most strongly in the Volcanic Systems of the Basin and Range Research Project.

Efforts in the Volcanic Systems of the Basin and Range Research Project are primarily directed toward the development of probability models of potential volcanic events in the YMR, based as far as possible on geologic insight into tectonic processes operating in the WGB and geologic controls on areal cinder cone volcanism in general. Key elements of the research design include the development of robust probability models for cinder cone volcanism and creation of a comprehensive database on cinder cone volcanism in the southwestern United States. Review of the regional tectonic setting of cinder cone volcanism in the Great Basin, Task 1 of this project, is provided by Stirewalt et al. (1992). Connor and Hill (1993) discuss initial work on probability model development and the nature of cinder cone volcanism in the YMR. This report describes research activities accomplished during January 1, 1995 to June 30, 1995.

5.2 SIGNIFICANT TECHNICAL ACCOMPLISHMENTS

Several major milestones have been delivered since January 1, 1995. These major milestones include:

- A critical review of the Volcanism Geographic Information System (GIS) Database (Stirewalt et al., 1995)
- Three nonhomogeneous Poisson models for the probability of basaltic volcanism: Application to Yucca Mountain, Nevada (Connor and Hill, 1995)
- Recurrence rates of volcanism in basaltic volcanic fields: An example from the Springerville Volcanic Field, AZ, USA (Condit and Connor, 1995)

Both the Volcanic Systems of the Basin and Range and the Field Volcanism Research Projects were reviewed by a panel of five world-renown volcanologists in October and November of 1994. The results of this review were delivered to the NRC in January 1995 as an intermediate milestone (Hill, 1995).

Research has recently focused on evaluation of spatio-temporal probability models that the Center for Nuclear Waste Regulatory Analyses (CNWRA) staff have developed and applied to volcanism in the YMR (Connor and Hill, 1993; 1995). These models have been tested and evaluated using the Springerville Volcanic Field (SVF), Arizona. The SVF is a larger volcanic field than the YMR, and it provides a robust data set to evaluate volcano probability models. The results of this research were submitted to the NRC in the form of a manuscript written for publication in the peer-reviewed literature (Condit and Connor, 1995). In order to present these models to NRC staff in a timely and convenient manner, much of this paper is presented in the following sections.

5.2.1 Recurrence Rates of Basaltic Volcanism

Many recurrence rate models depend on temporal patterns of volcanism observed in individual volcanic fields. Bacon (1982) observed that cumulative erupted volume in the Coso Volcanic Field since about 0.4 Ma is remarkably linear in time. Successive eruptions occur at time intervals that depend on the cumulative volume of the previous eruptions. This linear relationship was used by Bacon (1982) to forecast the timing of future eruptions and to speculate about processes, such as strain rate, that may govern magma supply and output in the Coso Volcanic Field. Kuntz et al. (1986) successfully applied

this volume-predictable model to several areas on the Snake River Plain, where recurrence rates of late Quaternary volcanism are much higher than in the Coso Volcanic Field, but cumulative volumetric rate of basaltic magmatism is nonetheless linear in time. Other recurrence rate models depend on the number of volcanoes formed, or number of volcanic events, through time. Ho (1991) and Ho et al. (1991) describe a set of models based on several statistical estimators of recurrence rate, including maximum likelihood estimators and the Weibull-Poisson distribution. In this approach, the recurrence rate of volcanism depends on the time elapsed between successive eruptions within some specified time interval. These statistical estimators are used to evaluate whether volcanism within a specific region is temporally waxing, waning, or steady state, and to place bounds on the certainty with which these trends in activity can be determined.

The broad and comparatively uniform temporal trends identified in some volcanic fields are in marked contrast to spatial patterns that reveal the clustered, episodic character of small-volume basaltic volcanism. Cinder cones and related basaltic vents are not randomly distributed within continental volcanic fields, but form clusters and alignments (Connor, 1990; Lutz and Gutmann, 1995). Shifts in the locus of volcanism within these fields also appear to be common (Duffield et al., 1980; Tanaka et al., 1986; Condit et al., 1989a; Foland and Bergman, 1992). These spatial patterns exist because recurrence rate is not uniform across a volcanic field at a given time even if volumetric output in the field as a whole is steady state. Such spatial patterns reflect basic geologic controls on magma generation and ascent processes.

Recurrence rate models can take these spatial patterns in volcanic activity into account. For example, zones may be defined within which the recurrence rate of volcanism is thought to be greater than elsewhere in the field (Smith et al., 1990). Alternatively, recurrence rate models can incorporate spatial information directly. These spatial and spatio-temporal models evaluate recurrence rate as a function of area, or time and area, on subregional scales. Wadge et al. (1994) used this technique to estimate the probable locations of future lava-flow boccas on Mt. Etna. Connor and Hill (1995) used a set of three spatial and spatio-temporal models to map probability of future volcanism in the YMR. In these models, both the timing and distribution of past volcanic events are used to estimate the long-term volcanic hazard probabilistically.

Here, temporal and spatial patterns of volcanism in the SVF are analyzed using a spatio-temporal recurrence rate model. The model is used to track the Plio-Quaternary development of this large Colorado Plateau volcanic field (Figure 5-1) and to quantify the relationship between recurrence rate of vent formation, volume, and change in the major petrologic characteristics of basalts. By constraining the spatio-temporal model with a robust data set, we are able to map areas of waxing and waning volcanism within the SVF for discrete time intervals and areas. This approach provides a much more complete view of the development of the SVF than is otherwise possible. The utility of the recurrence rate model as a tool in hazard analysis is then evaluated by forecasting subsequent volcanic events within the SVF at discrete time intervals.

The lavas of the SVF are distributed over an area of about 3,000 km². Approximately 409 vents in the area consist mostly of cinder cones and include five maars, four fissure vents, two shield volcanoes, and several spatter mounds. Mapping at the 1:24,000 scale by Condit (1995) shows that of the 3,000 km² area of the field, 2,166 km² is volcanic outcrop (Figure 5-2).

For several reasons, the SVF provides excellent possibilities for evaluation of both probability models of volcanism and uncertainties inherent in the application of these models. The SVF is one of the

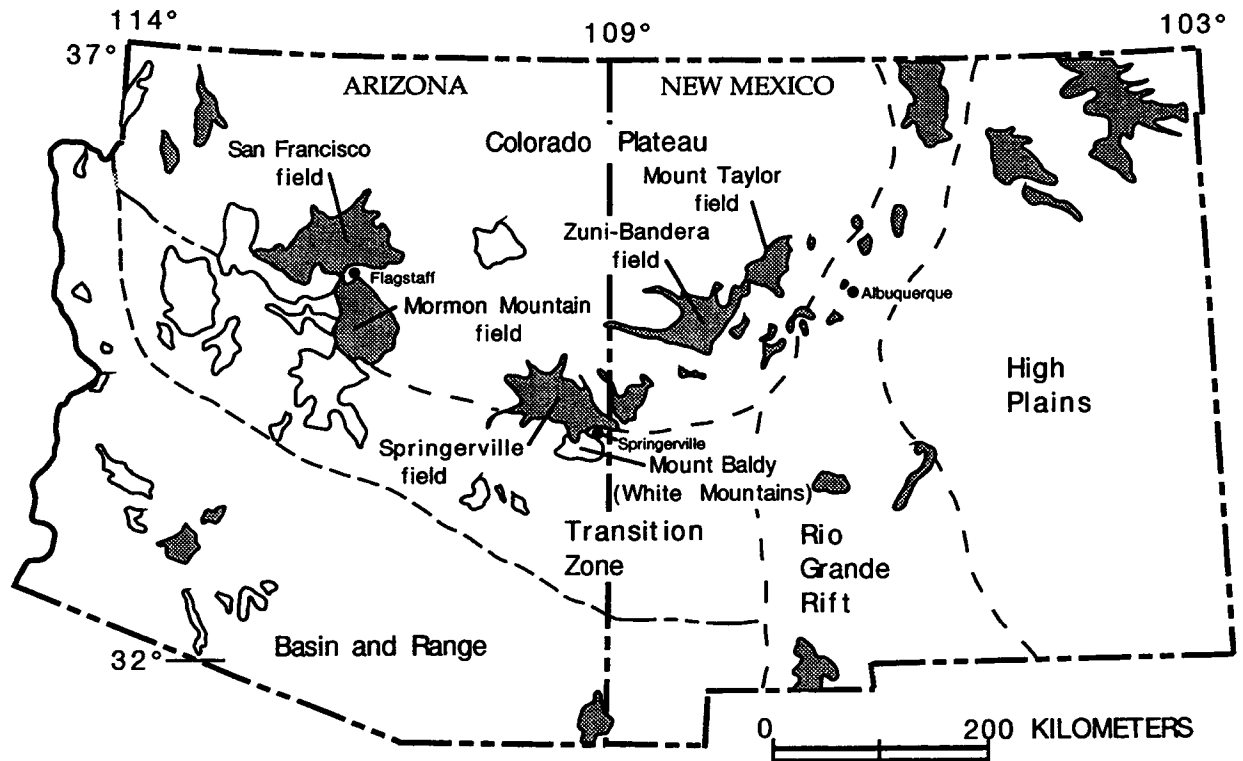


Figure 5-1. Physiographic provinces and distribution of late Cenozoic basaltic volcanic fields in Arizona and New Mexico (adapted from Luedke and Smith, 1978). Stippled areas represent volcanic rocks of Pliocene to Holocene age (< 5 Ma); outlined areas represent volcanic rocks of Miocene or older age.

few continental cinder cone fields that has been mapped (Condit, 1991; 1995; Condit et al., in press) using criteria designed to identify units as individual flow fields and to correlate units with source vents (Aubele et al., 1987; Condit et al., 1989b; Ulrich et al., 1989; Crumpler et al., 1994). Forty-two K-Ar age determinations have been made on the basalts in the SVF. In addition, extensive stratigraphy and magneto-stratigraphy studies further constrain the ages of flows for which radiometric age determinations have not been made (Condit, 1984; 1991; 1995).

Geology and geochemistry of SVF basalts have been discussed by Condit (1984; 1995), Condit et al. (1989a), and Ulrich et al. (1989). The six oldest lavas in the SVF suggest that older Pliocene and Miocene basaltic volcanism may have been substantial. Two flows found on the southwest edge of the field and dated at 8.66 ± 0.19 and 8.97 ± 0.19 Ma (Condit and Shafiqullah, 1985) have a source on the Mount Baldy shield volcano (Condit, 1984; Nealey, 1989). A 50-km^2 tholeiitic flow in the northern SVF is dated at 5.31 ± 0.11 Ma (Cooper et al., 1990; Cooper, 1991). Other older Pliocene flows range in age from 7.6 ± 0.4 Ma¹ to 2.94 ± 0.14 Ma (Laughlin et al., 1979) and are tholeiites to hawaiites in composition. Voluminous tholeiites erupted early in the latest episode ($\approx 2.1\text{--}0.3$ Ma) of volcanism in the field, followed by increasing volumes of transitional and olivine-alkaline basalts. The eruption of more

¹R.J. Miller, personal communication, 1991.

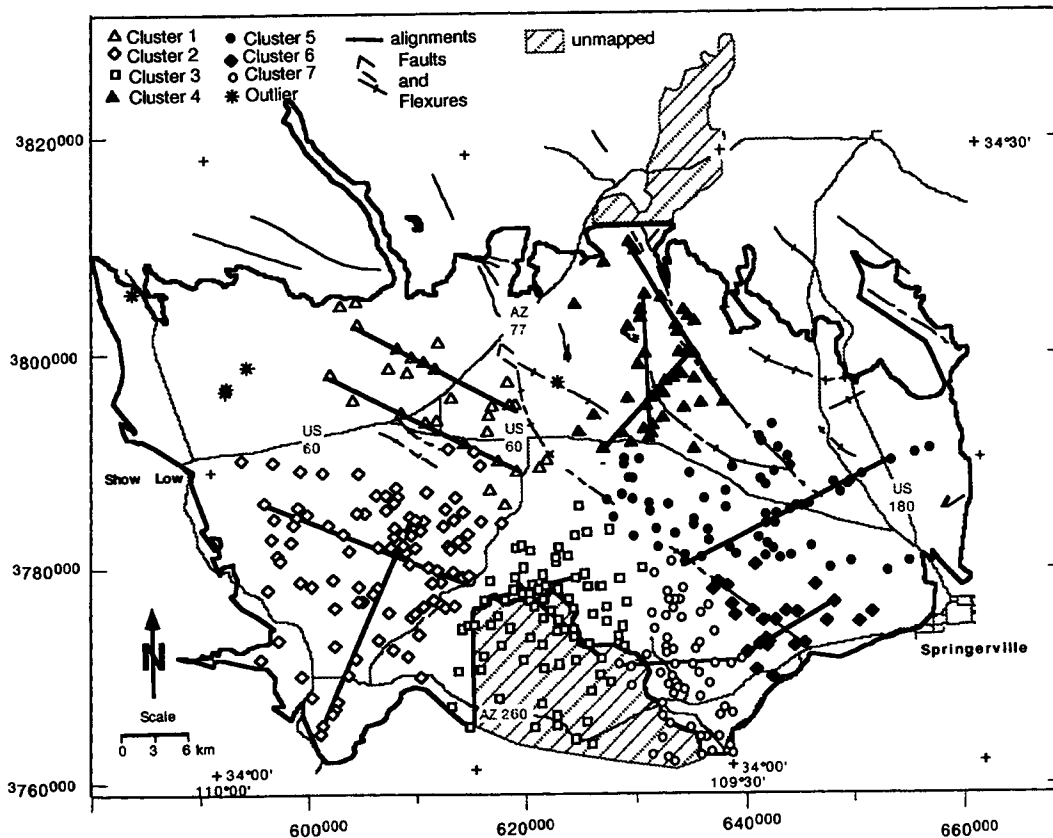


Figure 5-2. Outline of SVF with vent clusters and vent alignments identified by Connor et al. (1992) and faults and flexures mapped by Crumpler et al., (1994). Field outline is in black, unmapped areas are crosshatched. Map coordinates are Universal Transverse Mercator.

evolved alkaline basaltic rocks, including hawaiite, mugearite, and benmoreite, reached a maximum at 1.5–1.0 Ma. Note that in rock classification, Hawaiites are mildly alkaline basalts with 45–52 percent SiO_2 . Mugearites have higher SiO_2 , and alkalinity and benmoreites higher still. Condit et al. (1989a) noted that a west-east shift in the locus of volcanism occurred through time in the field at approximately plate tectonic rates (1–3 cm/yr), but identified little or no other systematic spatial variation in basalt geochemistry. However, additional geochronological constraints (e.g., Cooper et al., 1990), coupled with spatial analysis of vent distribution (Connor et al., 1992) suggested spatio-temporal geochemical trends exist and are important in the development of the SVF. Analysis of geochemical data in light of spatio-temporal recurrence rates elucidates these trends.

5.2.2 Defining Volcanic Events in the Springerville Volcanic Field

It is critical to define the “event” used to describe volcanic activity in any recurrence rate model. Definitions of volcanic events vary widely in the literature (Condit et al., 1989a; McBirney, 1992; Bemis and Smith, 1993; Lutz and Gutmann, 1995; Connor and Hill, 1995). Ideally, volcanic events would correspond to eruptions. Unfortunately, subsequent geologic processes often obliterate evidence of previous eruptions from the geologic record (e.g., Walker, 1993). Consequently, volcanic events in the SVF are defined as mappable eruptive units and documented by detailed field mapping.

A total of 357 vents are documented in the mapped area. As discussed below, more than one flow unit is associated with some of these vents, giving a total of 366 volcanic events. These units are less than 2.1 Ma. Fifty-two additional known vents in the SVF have been identified based on topographic expression in the unmapped area in the southern part of the field (Figure 5-2). Because there is no age control on these vents, they are not included as volcanic events in the following analysis. In an area of intense magmatism, such as the SVF, subsequent activity buries or destroys vents. This destruction of the vents means that recurrence rate estimates based on mapped features will be lower than actual recurrence rates. Units older than 2.1 Ma are excluded from the analysis, primarily because these units have been buried substantially.

5.2.2.1 Mapping Volcanic Events

Identification of volcanic events is based on mapping in which the basic map unit was defined as a discernible eruptive unit. Each of these units was distinguished using lithologic (type, size, and abundance of phenocrysts) and morphologic criteria that are detailed in Condit (1995) and Condit et al. (in press). Mapping included correlation of flows to source vents in order to best characterize the physical volcanology of the units. Vents include all features in the SVF that exhibit evidence of eruption and that could be depicted as mappable features at 1:24,000 scale. Vents are commonly cinder cones, but also include maar craters, fissures that fed flows, and shield volcanoes. Vents on some of the older units include isolated spatter mounds that form distinctive topographic highs.

Stratigraphic and volcanologic relationships are essential to determine the number of volcanic events represented by mappable units. Most flow units could be traced to their source at a single cone; these flow-vent units represent single volcanic events. Seventy-four isolated vents could not be associated with flows. Each of these vents is taken to represent single volcanic events.

In many cases, multiple vents correlate with single lava flow units, some of which have multiple flow lobes. A total of 26 lava flow units correlate to vent pairs. Other lava flow units correlate with up to six vents. Units that are a composite of multiple flow lobes were defined because discontinuous flow fronts or flow edges were recognized within an area of otherwise uniform lithology and flow morphology. Both volcanological relationships and historical analogy suggest that these flow units are likely little separated in time. The 1975 Tolbachik cinder cones are a modern example of a brief episode of dike injection resulting in the formation of a similar alignment of several closely spaced vents and associated composite lava flows (Tokarev, 1983).

In a few cases, composite units consist of different flow-lobe lithologies that could not be broken out as discrete units because of poor exposures or other complicating factors. Some composite units of mixed lithologies may represent a magma of varied phenocryst content emplaced during a single eruptive episode (Wilcox, 1954), although these types of composite units are probably rare in the SVF. In all cases in which more than one vent has been assigned to a single map unit, vents are assigned the same age, and each of these vents is defined as a volcanic event. In the most extreme case, six vents correlate with a single flow unit. This single flow unit represents six discrete events, all of which are assigned the age of the dated lava flow.

Conversely, in some cases multiple flow lobes are clearly traceable back to a single vent. Seven vents within the SVF erupted more than one mappable flow lobe. Where these flow lobes could be distinguished, single vents appear more than once in the data set as volcanic events, each correlated in time with its mapped eruptive unit. A total of six of these vents erupted two distinct, mappable units,

representing a total of twelve volcanic events. One vent has four distinct eruptive units, and therefore produced four events. Based on radiometric age determinations, stratigraphy, flow morphology, and paleomagnetism, it is likely that little time elapsed between the emplacement of any of these flow lobes. One example of this style of eruptive activity is Cerro Negro, Nicaragua, which has erupted 10 lava flows since 1850 A.D. (McKnight et al., 1994; Simkin and Siebert, 1994). Although vents that have multiple flow lobes are weighted more in the analysis because they include more than one volcanic event, they are few in number and do not significantly alter recurrence rate estimates.

5.2.2.2 Dating Volcanic Events

Given the number of units in the SVF, it was not tenable to make radiometric age determinations on each unit. However, map and stratigraphic information coupled with radiometric age determinations on key stratigraphic units well constrain the development of the field. Thirty-four K/Ar age determinations have been made on flows <2.1 Ma that cover slightly more than 30 percent of the SVF. The possible age ranges of the remaining units <2.1 Ma can be inferred with varying degrees of precision, using stratigraphic, magneto-stratigraphic, and to a lesser degree, geomorphologic correlation with dated flows (Aubele et al., 1986; Pierce et al., 1979). In some cases, age ranges of undated flow units are estimated quantitatively, for example, where a unit is bounded solely by magnetic polarity reversals. Where possible, a further attempt was made to bound flow and vent ages using additional field data. For example, the degree of soil development between flows provides an indication of the time elapsed between successive eruptions. Thus, age range-charts for all flows and their associated vents were developed for subregions within the SVF. Detailed unit descriptions and details of the stratigraphic correlation are available in Condit (1995).

It is assumed that there is equal probability of a vent forming throughout its estimated age range. Undated units may have erupted immediately after the stratigraphically lower lava erupted, or immediately before the overlying lava erupted, or at some intermediate time. Under these circumstances, application of the uniform distribution is best for estimating ages of stratigraphically bounded units. A confidence interval for the age of each flow unit, and vent, was established in this manner.

The Morgan Mountain area illustrates the procedure of estimating ages. In the Morgan Mountain area, a lava flow and vent sequence of 18 units lies stratigraphically between two other dated flows: Qme and QTsf (Figure 5-3). QTsf is a reversely polarized composite unit dated at 1.90 ± 0.06 and 2.00 ± 0.11 Ma in the Morgan Mountain area. Elsewhere in the SVF, K-Ar dates on the composite QTsf lavas indicate slightly younger ages. Thus, this unit is assigned a mean estimated age of 1.95 ± 0.13 Ma, based on radiometric age determinations and rock magnetic polarity. Qme erupted at 0.49 ± 0.03 Ma. In addition, two intermediate units in the Morgan Mountain area are dated radiometrically and seven units sampled for magnetic polarity.

These age data are used to estimate the permissible age range for each flow in the Morgan Mountain area. For example, unit Qmc4 directly overlies QTsf, underlies Qme, and is reversely polarized. No other stratigraphic information definitively bounds the age of this unit, and it may have formed at any time between 1.95 and 0.73 Ma, with the exception of during the Jaramillo and Olduvai normal-polarity subchrons (Figure 5-3). Parenthetically, lavas upslope of Qmc4 vent V9313 indicate that an additional Qmc4 vent must be present but buried beneath Qme or Qmb6; this inferred vent is not included in the analysis. Unit Qmb4 is reversely polarized, also overlies QTsf and underlies both Qmh and Qmg. Units Qmb4, Qmh, and Qmg are all overlain by Qmb6, which is dated at 1.01 ± 0.02 Ma (Figure 5-3). Each of these units (Qmb4, Qmh, and Qmg) may have erupted between 1.95 ± 0.13 and

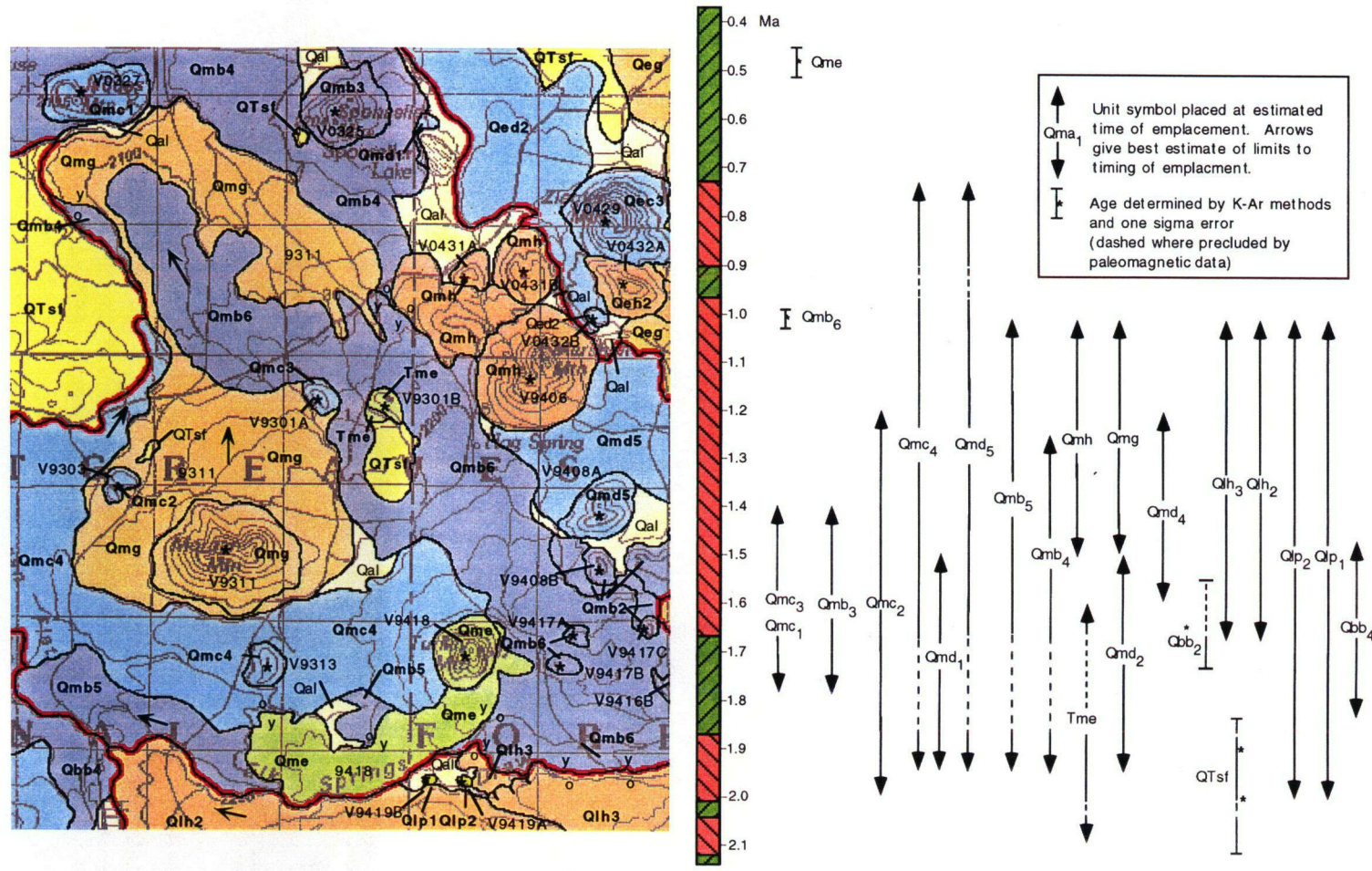


Figure 5-3. Timing of volcanic events in the SVF is constrained by mapped stratigraphic relationships, rock magnetic polarity, and radiometric ages. Here a geologic map of part of the Morgan Mountain area is shown (Condit, 1995) as an example of the stratigraphic relationships used to constrain the age range of each eruptive unit. See text for examples. Map units are colored by lithologic type. The paleomagnetic time scale is shown (red: reversed polarity time intervals; green: normal polarity time intervals).

1.01 ± 0.02 Ma. However, differences in soil development at the contact and flow surface morphology indicate that Qmb4 is considerably older than either Qmh or Qmg. Using these geological criteria, Qmb4 is assigned an age range of 1.95–1.25 Ma, exclusive of the Olduvai isochron, and Qmh and Qmg are each assigned an age range of 1.5–1.01 Ma.

After determining the permissible age range for each vent and lava flow in the mapped area, the data were subdivided into 0.25-m.y. intervals. Subdividing the development of the SVF into 0.25-m.y. intervals yields a relatively equal number of radiometric age determinations per interval. Between 2 and 0.75 Ma, four to eight lava flows and their associated vents per interval have radiometric age determinations; three flows between 0.5 and 0.75 Ma and two lava flows between 0.25 and 0.5 Ma are dated. Errors associated with placing units in specific intervals are easily propagated through the analysis. For example, the mean estimated age of Qmb5 is 1.4 Ma, but this unit has a large age range (Figure 5-3). Based on the age range of Qmb5, there is a 34-percent chance that Qmb5 erupted between 1.25 and 1.5 Ma. Also, there is a 32-percent chance that Qmb5 erupted 1.0–1.25 Ma; a 23-percent chance, 1.5–1.75 Ma; and an 11-percent chance, 1.75–2.0 Ma. The cumulative impact of these uncertainties is evaluated in the following section.

5.2.3 Temporal Trends in Volcanism

One way to represent the temporal pattern of volcanism in the SVF is by plotting the cumulative number of volcanic events through time (Figure 5-4). This plot was made at 0.25-m.y. intervals and used expected, minimum, and maximum ages for the 366 volcanic events. Despite the uncertainty in the age determinations, it is clear that the SVF has gone through a waxing stage, prior to about 2 Ma, a steady state phase, in which the numbers of volcanic events were relatively constant, and a waning stage since 0.75 Ma. The youngest dated vents are approximately 0.3 Ma.

Based on mean estimates of the ages of volcanic events, the recurrence rate of volcanism was highest between 1.5 and 1.0 Ma, when it averaged approximately 3.0×10^{-4} volcanic events/yr (v/yr). Using maximum vent ages, the highest recurrence rate of vent formation in the field occurred between 2.0 and 1.5 Ma and averaged 3.7×10^{-4} v/yr. Using minimum vent ages, the highest recurrence rate of vent formation in the field occurred between 1.0 and 0.5 Ma and averaged 3.6×10^{-4} v/yr. The timing of the maximum recurrence rate of volcanic events for the SVF lies within the envelope defined by these two extremes and, given the large number of vents, likely occurred close to 1.5–1.0 Ma.

The areal extent of lava flows and vents is used to estimate magma output rate, rather than flow volume. Lava flow thickness is highly variable on individual flows and has not been estimated for each unit in sufficient detail. Flow thickness is a difficult parameter to estimate from outcrop mapping because partial flow thickness, obtained at flow edges, is all that is normally observable. Flow and vent areas, on the other hand, are well known through mapping.

Cumulative area covered by lava flows is plotted in Figure 5-5. The total area covered by lavas with mapped vents less than 2.1 Ma is approximately 1,700 km². These data suggest that the magma output rate in the field is remarkably steady through time. The magma output rate in the SVF is essentially constant between 1.75 and 0.75 Ma, a long period of time compared with steady-state volumetric trends identified previously in other volcanic fields (e.g., Bacon, 1982). In contrast, the frequency of volcanic events, or vent formation, increases later in this interval at approximately 1.5 Ma. Thus, rates of magma output and rate of vent formation are not equivalent during the development of the SVF.

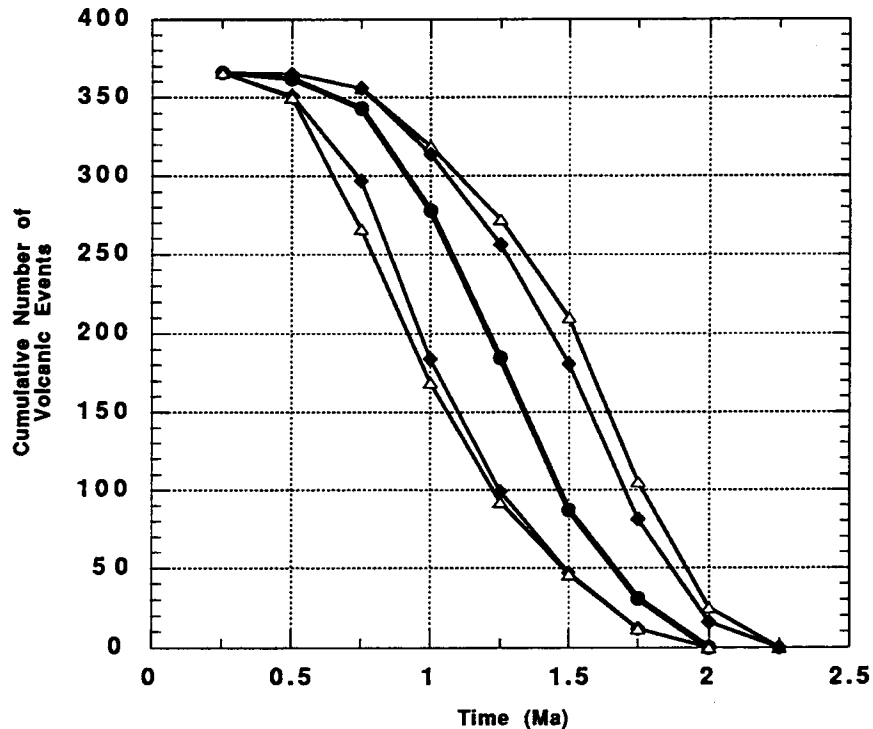


Figure 5-4. Cumulative number of vents in the SVF estimated at 0.2-Ma intervals. The center curve (solid circles) shows the frequency of vent formation using mean estimates of unit ages. This curve is bounded by curves of the frequency of vent formation made using the maximum and minimum estimated ages of individual units (open triangles), and an 84-percent confidence envelope (solid diamonds).

Major element analyses exist for 257 of the mapped eruptive units (volcanic events) between ≈ 2.1 and 0.3 Ma (Condit, 1995). These 257 volcanic events are further classified (Condit et al., 1989a; modified from Le Bas et al., 1986) by petrologic type as: tholeiite, transitional basalt, alkali-olivine basalt, hawaiite, mugearite, and benmoreite. The eruption of transitional, alkali-olivine basalts, and hawaiites, that together make up about 80 percent of the total units, follows the trend defined by the cumulative number of volcanic events (Figure 5-4). In contrast, tholeiites erupted predominantly between 1.75 and 1.5 Ma. Eruption of the most evolved basalts in the field increased after 1.5 Ma, reaching a maximum at 1.25–1.0 Ma.

Geochemical patterns also emerge through plotting the change in the alkalinity index (AI) of basalt through time (Condit et al., 1989a). The AI is the difference between sample alkalinity ($\text{Na}_2\text{O} + \text{K}_2\text{O}$) and the alkaline-subalkaline boundary of Irvine and Baragar (1971) at the same SiO_2 concentration (Condit et al., 1989a). Here, lavas are classified on the basis of observed alkalinity into subalkaline ($\text{AI} < 0$), mildly alkaline ($0 \leq \text{AI} < 1$), alkaline ($1 \leq \text{AI} < 1.75$), and highly alkaline ($1.75 \leq \text{AI}$). The AI of basaltic rocks in the SVF has a normal distribution, with 80 percent of the analyzed samples falling at $0 \leq \text{AI} < 1.75$. Roughly 10 percent of the 257 units analyzed in the SVF are subalkaline, and an equal percentage is highly alkaline.

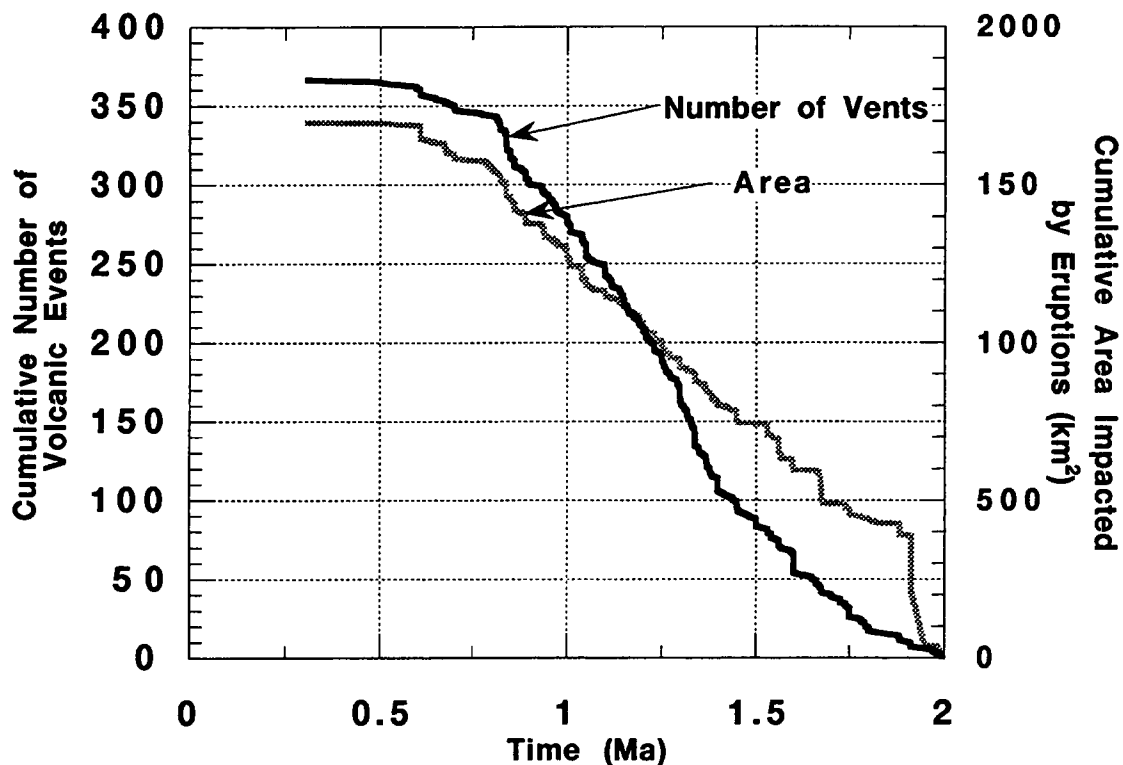


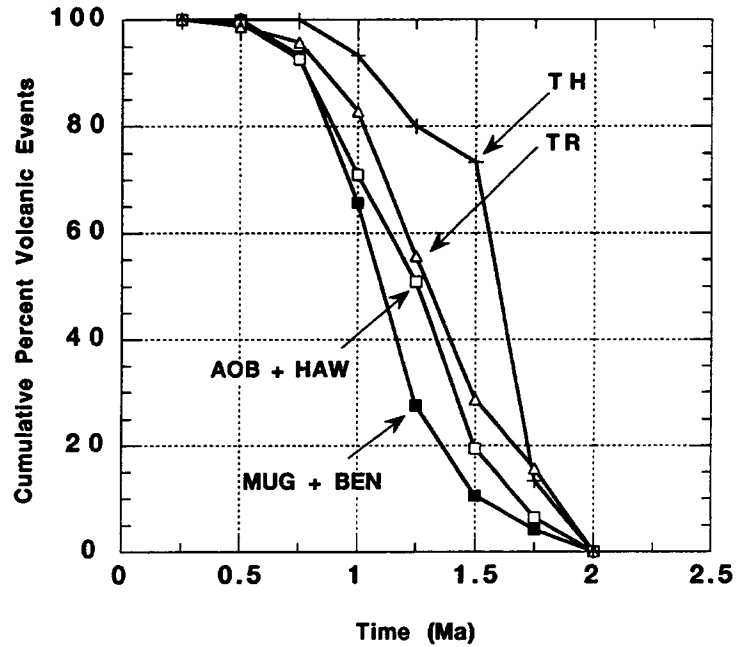
Figure 5-5. Cumulative area covered by lava flows, a proxy for volume estimates, is remarkably steady in the field between 1.75 and 0.75 Ma. In contrast, the rate of volcanic events increases at approximately 1.5 Ma. Both volume and vent formation rates decrease abruptly after about 0.75 Ma.

The cumulative percent of basalts erupted is plotted by AI in Figure 5-6(b) using mean ages for the basalts at 0.25-Ma intervals. Naturally, the mildly alkaline to alkaline rocks that constitute 80 percent of the field track the cumulative rate of vent formation. Subalkaline and highly alkaline rocks show a very different pattern. Subalkaline rocks represent a small number of vents but a large volume of lava flows. Most of these basalts erupted between 1.75 and 1.5 Ma; comparatively few erupted since 1.5 Ma. Highly alkaline basalts show a very similar trend, but erupted later. Comparatively few highly alkaline basalts erupted before 1.5 Ma, whereas 50 percent of these vents formed between 1.5 and 1.25 Ma.

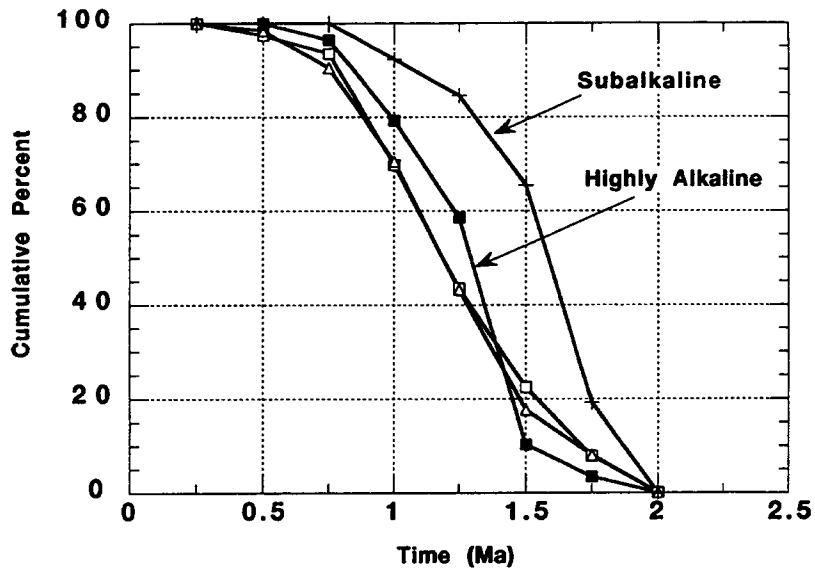
This increase in the rate of highly alkalic, predominantly mugearitic and benmoreitic, volcanic events correlates well with the decrease in the rate of eruption of tholeiites, and with an increase in the rate of volcanic events overall [Figures 5-6(a) and 5-6(b)]. The total volumetric output of the field remained constant during this transition (Figure 5-5).

5.2.4 Spatial Trends in Volcanism

The relationship between the occurrence of volcanic events, volumetric output, and petrology of basalts is further elucidated by mapping vent density in the field for individual 0.25-m.y. time intervals. Vent density is quantified using a kernel estimation technique (Lutz and Gutmann, 1995;



(a)



(b)

Figure 5-6. Cumulative percent of volcanic events by (a) petrologic type: TH—tholeiite, TR—transitional basalt, AOB + HAW—alkali-olivine basalt and hawaiiite, MUG + BEN—mugearite and benmoreite, and (b) alkalinity index: plus sign—subalkaline ($AI < 0$), open triangle—mildly alkaline ($0 \leq AI < 1$), open square—alkaline ($1 < AI \leq 1.75$), solid square—highly alkaline ($1.7 \leq AI$). Note the transition in petrological type and alkalinity approximately at 1.5 Ma.

Connor and Hill, 1995), which provides a simple and consistent way to map the density of volcanic events per unit area in a field within each time interval. This technique provides a basis for comparison of the density and distribution of volcanic events during the development of a volcanic field.

In the kernel estimation technique, spatial variation in the intensity of the volcanic events is estimated from the distance to nearby volcanoes and a smoothing constant, h , using a kernel function. The choice of a kernel function has little impact on the density estimation, but an Epanechnikov kernel is widely used (Silverman, 1986; Cressie, 1991; Lutz and Gutmann, 1995) and is adopted for this analysis. The shape of the resulting map of vent density depends on the value of the smoothing constant, h , chosen. Using a large smoothing constant results in a map that shows little variation in vent density, whereas choosing a small smoothing constant maximizes the variation in vent density. For the following maps, $h=5$ km. This smoothing constant is small relative to the area of the field, but is much larger than the average vent spacing and therefore provides a robust measure of density variation (Silverman, 1986).

Density maps are shown for four time intervals [Figures 5-7(a) through 5-7(d)]. These maps illustrate the spatial development of the field by 0.25-Ma time intervals during the period in which the SVF was most active, that is, 1.75–0.75 Ma. The maps reveal great spatial variation in the density of volcanic events across the SVF 1.75–0.75 Ma.

Vents formed between 1.75 and 1.5 Ma are comparatively few and widely distributed. The greatest concentration of vents is in the western portion of the field. In five areas the vent density is as high as 0.05 volcanic events/km² (v/km²), and in one area is greater than 0.15 v/km² [Figure 5-7(a)]. More than 50 percent of the tholeiites in the SVF erupted during the 1.75- to 1.5-Ma time interval, and then tholeiite flows cover large areas.

The pattern of volcanism changes dramatically in the interval 1.5–1.25 Ma [Figure 5-7(b)], as the recurrence rate increases. These new vents are highly concentrated in several discrete clusters, mostly in the eastern portion of the field. Vent density is 0.1–0.25 v/km² within these clusters. Elsewhere in the field, the vent density is generally less than 0.05 v/km² at this time, with a diffuse zone of >0.1 v/km² in the western part of the SVF. This change in vent distribution correlates to the main eruptions of mugearites and benmoreites; 50 percent of the highly alkaline (AI ≥ 1.75) basalts mapped in the field erupted 1.5–1.25 Ma. All the mugearites and benmoreites erupted at this time are located in parts of the field in which vent density and recurrence rate are the highest (Figure 5-7(b)). In contrast, comparatively few subalkaline basalts (<20 percent) erupted during this time interval. These subalkaline basalts consist of one tholeiite and several transitional basalts. Subalkaline basalts occur in lower density areas.

The pattern of development of the SVF between 1.5 and 1.25 Ma continued during the next 0.5 Ma [Figures 5-7(c) and 5-7(d)]. This pattern is characterized by a comparatively low density (<0.05 v/km²) of new vents forming throughout about 50 percent of the volcanic field, and discrete areas of much more active vent formation (0.1–0.25 v/km²). Mugearites and benmoreites are nearly all limited to the most active clusters in the field, and subalkaline basalts are more widely dispersed.

5.2.5 Modeling Patterns of Basaltic Volcanism in the Springerville Volcanic Field

The previous analyses indicate that models of the recurrence rate of volcano formation in the SVF must take into account several basic patterns in activity. Models must account for the overall temporal trend of vent formation, including steady-state volcanism prior to 0.75 Ma and waning

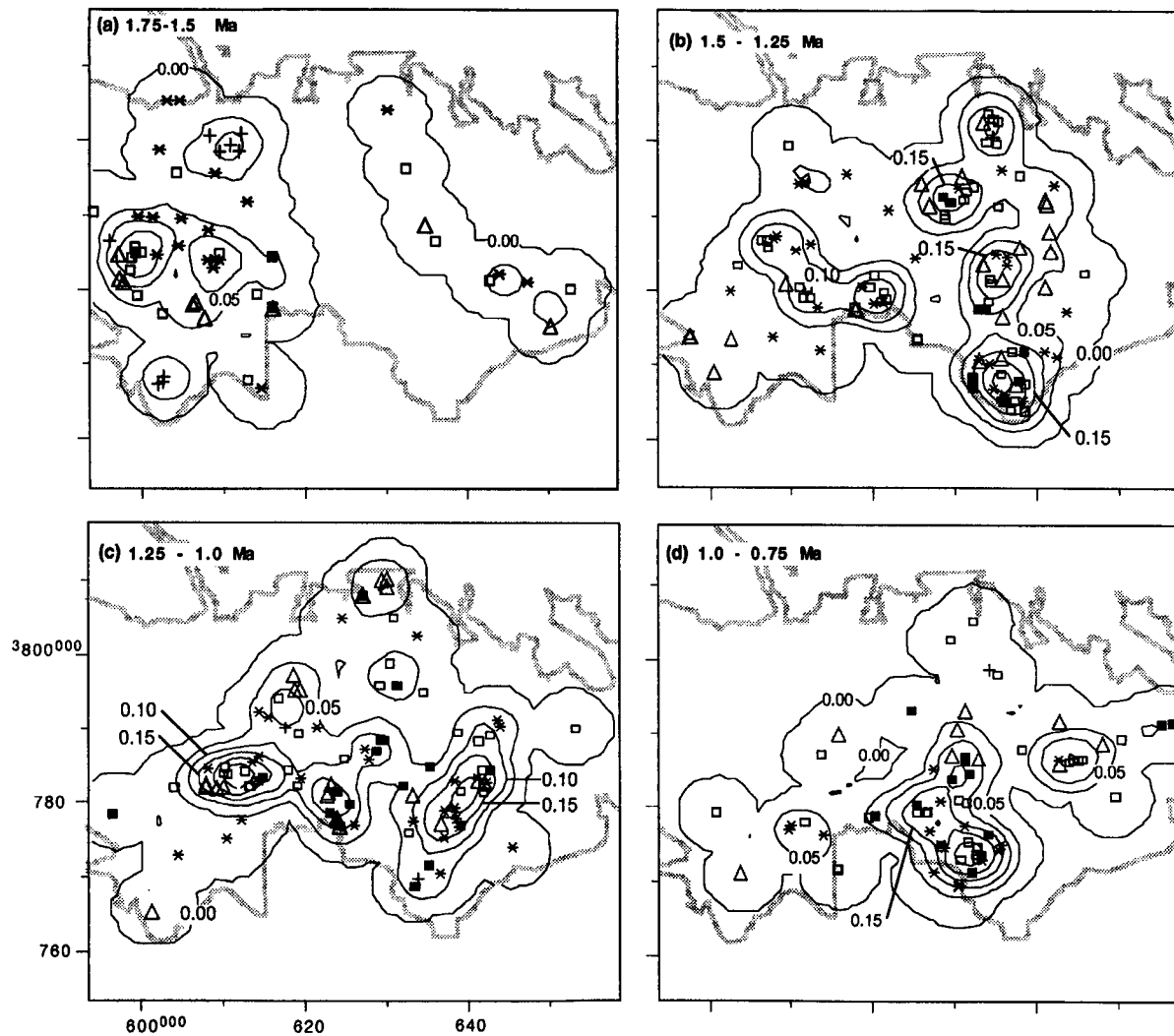


Figure 5-7. Density of mapped volcanic events in the SVF: (a) 1.75–1.5 Ma, (b) 1.5–1.25 Ma, (c) 1.25–1.0 Ma, and (d) 1.0–0.75 Ma, based on mean estimated ages of vents and lava flows and using an Epanechnikov kernel ($h=5$ km). Vents are plotted by basalt type: plus sign—tholeiite, open triangle—transitional basalt, open square—alkali-olivine basalt and hawaiiite, solid square—mugearite and benmoreite, and asterisk—no analysis. Contour interval is 0.05 v/km^2 . Map coordinates are Universal Transverse Mercator.

volcanism since that time. In addition, the model must account for the spatial change in the intensity of volcanism within the field because recurrence rate was by no means uniform throughout the SVF at any particular time. Furthermore, the model must be amenable to comparison with observed volumetric and geochemical trends in volcanism.

Connor and Hill (1993; 1995) applied several spatial and spatio-temporal recurrence rate models to volcano formation in the YMR, Nevada. Here, one of these models of recurrence rate, a spatio-temporal near-neighbor model, is applied to the recurrence rate of vent formation. In this model, recurrence rate per unit area surrounding a point p is estimated by m near-neighbor volcanoes determined as the minimum of $u_i t_i$, where t_i is the time elapsed since the formation of the i^{th} near-neighbor vent, and u_i is the area of a circle whose radius is the distance between volcano i and point p , with $u_i \geq 1 \text{ km}^2$ (Connor and Hill, 1995). In practice, recurrence rates, $\lambda_n(p)$, are calculated on a grid, and these values are summed over a region extending slightly beyond the volcanic field.

Calculations were made using $m=6, 7, 8,$ and 10 near-neighbor vents. Calculations were made at 0.25 m.y. intervals, using only vents erupted prior to the time of the calculation in order to compare the near-neighbor estimates with the recurrence rates calculated from age data. The near-neighbor models track the variation in estimated recurrence rate, increasing before 1.25 Ma , and decreasing after 1.0 Ma (Figure 5-8). The $m=7$ and 8 near-neighbor models provide the best estimates of the regional recurrence rate before 0.75 Ma . In contrast, the $m=10$ near-neighbor model underestimates and the $m=6$ near-neighbor model overestimates the recurrence rate in the SVF.

After 0.75 Ma , all these near-neighbor models underestimate the decrease in recurrence rate as volcanism wanes. This underestimation is in part due to the nature of the estimation technique. Using this spatio-temporal model, the recurrence rate estimate can never decrease to zero. Therefore, the near-neighbor estimation technique has a tendency to overestimate the recurrence rate when waning magmatism occurs over a relatively short period of time.

Overestimation of recurrence rate during the rapidly waning stages of activity in a volcanic field can be addressed by including only those volcanoes formed during some time interval, such as 0.5 m.y. , prior to the time for which the calculation is made. For example, in making an estimate of recurrence rate for the SVF at 1.0 Ma , only vents formed between 1.5 and 1.0 Ma might be used to determine near-neighbor volcanoes, rather than including all vents formed in the field prior to 1.0 Ma . During successive calculations, this time interval shifts, windowing the interval used to determine near-neighbor vents and to estimate recurrence rate at a particular time. As a result, geographically nearby volcanoes that are too old to be included within the time window are not included in the recurrence rate estimate. This modification has little impact on recurrence rate estimates during waxing or steady-state magmatism, but decreases the recurrence rate estimate during waning magmatism.

Figure 5-9 shows a comparison of the observed change in recurrence rate and $m=7$ and 8 near neighbors, using a 0.5-m.y. time window. These two curves better fit the observed recurrence rate curve after 1.0 Ma than models that do not use 0.5-m.y. time windows (Figure 5-8). Thus, the $m=7$ near-neighbor model with a 0.5-m.y. time window best matches the overall trend in recurrence rate, although it overestimates the cumulative number of volcanic events slightly. Using $m=7$ near neighbors and a 0.25-m.y. time window, recurrence rate is underestimated during the last 1.0 Ma (Figure 5-9). The $m=8$

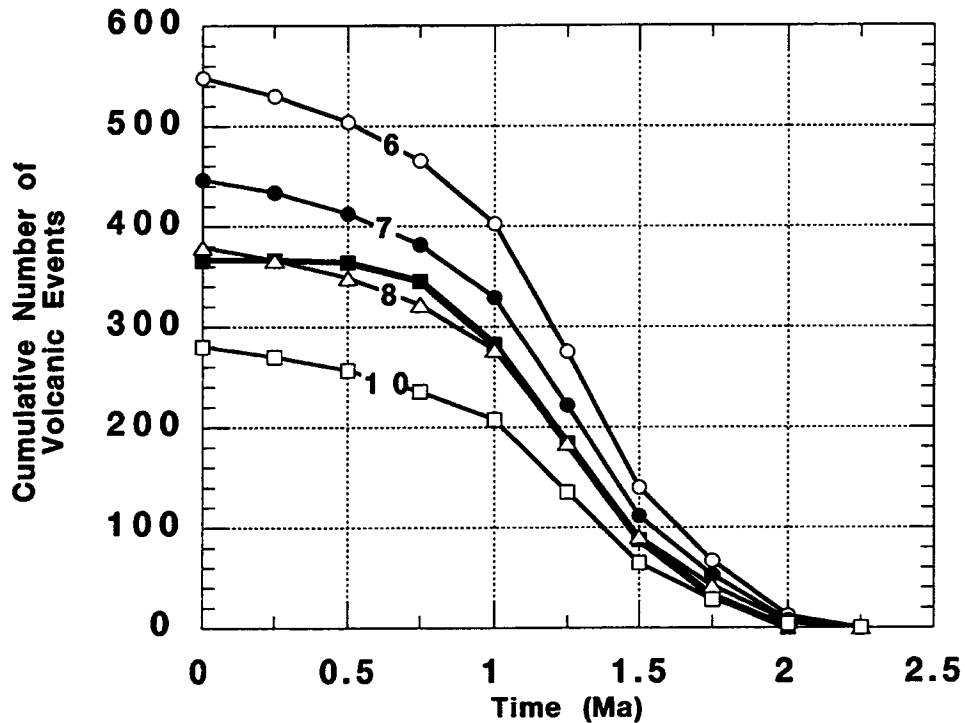


Figure 5-8. Comparison of recurrence rate estimates based on $m=6$, 7, 8, and 10 near-neighbor model (labeled lines) and the observed mean estimate of recurrence rate (heavy line with solid squares). The $m=7$ and 8 near-neighbor models best reflect recurrence rate before 1.0 Ma, given the uncertainty in the vent ages. The rate of decrease in recurrence rate after ≈ 0.75 Ma is not well captured by these models.

near-neighbor model without a time window gives the best fit before 1.0 Ma. However, this model underestimates the rate of change in volcanism after 1.0 Ma, and overestimates the future rate of volcanism (Figure 5-8).

5.2.6 Recurrence Rate and Probability Maps

This spatio-temporal technique provides a basis for mapping the local recurrence rate of vent formation across the area and identifying areas of waxing or waning magmatism during a given time interval. The density maps [Figures 5-7(a)-(d)] indicate that the smooth variation in temporal recurrence rate of vent formation does not fully capture the pattern of volcanism. Rather, specific areas within the field experience much more intense volcanism than others during a given time interval. This variation is cast in terms of spatio-temporal recurrence rate ($v \text{ yr}^{-1} \text{ km}^{-2}$). Iterative calculations using varying numbers of nearest-neighbor vents and time windows indicates that a $m=7$ near-neighbor model with a 0.5-m.y. time window provides the best estimate of the change in recurrence rate of vent formation across the SVF.

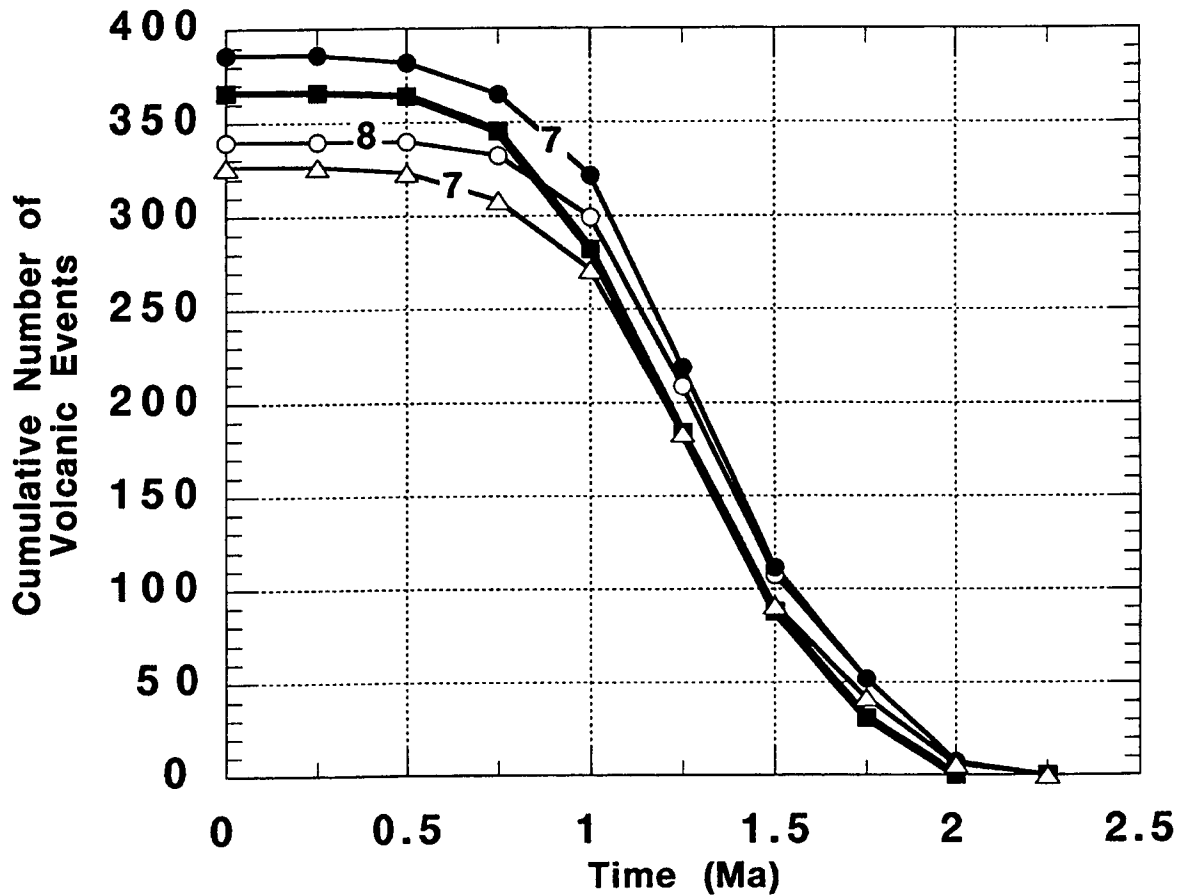


Figure 5-9. Volcanism has waned in the SVF since about 0.75 Ma. This decrease in observed recurrence rate, based on mean age determinations (heavy solid line with solid squares), m is captured by near-neighbor models using a 0.5-m.y. time window, rather than all of the volcanoes formed prior to the time for which the calculation is made. Near-neighbor models $m=7$ (solid circles) and $m=8$ (open circles) are shown. Using $m=7$ near-neighbor vents and a time window of 0.25 m.y. underestimates recurrence rate since 1.0 Ma (open triangles).

These maps of recurrence rate of volcanism in the SVF are useful for two reasons. First, these maps make it possible to identify areas of waxing and waning magmatism within the volcanic field. Second, recurrence rate can be recast in terms of probability. Using recurrence rate, or probability maps, variations in volcanic hazard across a region can be assessed.

The change in recurrence rate through time is calculated from the difference in recurrence rate ($v \text{ yr}^{-1} \text{ km}^{-2}$) between successive time intervals. The difference in recurrence rate between successive intervals is plotted in Figure 5-10 to identify where volcanism is developing (or waxing) most clearly. Dark areas show where volcanism is waning the most rapidly, and red areas show where it is steady through time, including parts of the field in which no volcanism at all is occurring. So, for example, the waning in the SE corner of the field 1.5–1.75 Ma occurs because of a small group of vents formed in this area 2.0–1.75 Ma. Volcanism did not continue in this area during the next time interval.

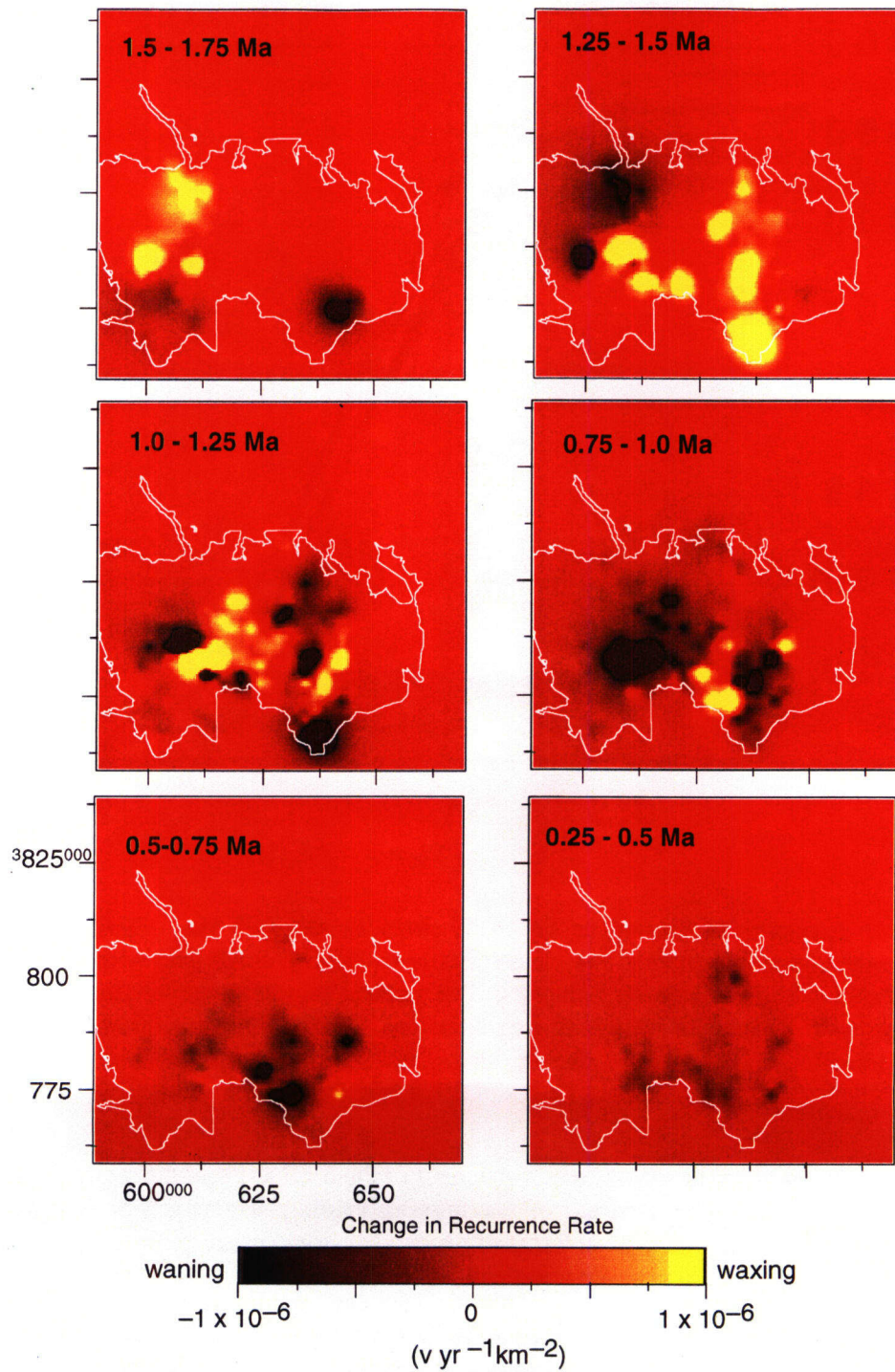


Figure 5-10. Areas of waxing and waning basaltic volcanism in the SVF are delineated through application of the recurrence rate model. Maps for successive 0.25-m.y. intervals are differenced to illustrate spatial and temporal change in recurrence rate. The outline of the SVF is shown in white. Map coordinates are Universal Transverse Mercator.

Probabilities are calculated from the recurrence rate values using Poisson's equation:

$$P[N = 1 \text{ volcanic event}] = 1 - \exp[-t\alpha\lambda_n(p)] \quad (5-1)$$

where t is the time interval of the probability estimate, α is the area about point p for which probability is estimated based on recurrence rate at point p , and $\lambda_n(p)$ is the recurrence rate estimate at p . Use of Eq. (5-1) implies that $\lambda_n(p)$ does not vary significantly within the time interval t or over the area α , and that the probability of more than one volcanic event in this area and time interval is very small.

Probability maps were made from the $m=7$ near-neighbors and 0.5-m.y. time window probability model to test the utility of the model in forecasting subsequent volcanic events in the SVF. The maps were made by contouring the probability [Eq. (5-1)] of a new volcanic event within $t = 50,000$ yr and $\alpha = 10 \text{ km}^2$ for each estimate of $\lambda_n(p)$. For example, the probability of volcanic events was calculated and contoured for the SVF at 1.75 Ma using the timing and locations of volcanic events before 1.75 Ma [Figure 5-11(a)]. Based only upon these mapped volcanic events, two zones of higher probability of future volcanic events were identified: one broad zone in the western portion of the field and a smaller zone in the southeastern portion of the field.

The success of this probability model can be evaluated based on the timing and distribution of subsequent volcanic events. These subsequent events are readily identified by stratigraphic relationships. Although the timing of these events is uncertain, they are the next volcanic events to occur in the SVF and, of course, are not used in the probability estimate. The mean ages of these subsequent events are 0.05–0.1 m.y. younger than the date of the probability calculation. Volcanic events that occurred within 0.05–0.1 m.y. after 1.75 Ma, based on stratigraphic relationships and mean ages, correlate well with probability zones estimated from previous eruptions [Figure 5-11(a)].

Maps constructed in a similar manner for other time intervals are shown in Figures 5-11(b) through 5-11(d). Based on these and similar maps, some observations about the relationship between probability maps and subsequent volcanic activity can be made. Nearly all the next volcanic events to occur are located within zones where $P[\text{volcanic event} | \alpha = 10 \text{ km}^2, t = 50,000 \text{ yr}] > 0.03$. During most time intervals after 1.5 Ma [e.g., Figures 5-11(c) and 5-11(d)], new vents are preferentially located in areas where $P[\text{volcanic event} | \alpha = 10 \text{ km}^2, t = 50,000 \text{ yr}] > 0.1$.

The utility of the spatio-temporal recurrence rate model can be further evaluated by comparing the estimated recurrence rate at the location of a subsequent volcanic event with average recurrence rate in the field, as might result from a purely temporal model. Average recurrence rate may be determined in several ways (Ho, 1991; Connor and Hill, 1993). One estimate of the average recurrence rate is

$$\bar{\lambda}(p) = \frac{n}{At} \quad (5-2)$$

where n is the number of volcanic events, based on mean estimated ages, that occurred in the preceding time interval $t = 0.25$ m.y. A is the area of the volcanic field, the selection of which is somewhat subjective. Here, the area used is the minimum area of a convex hull polygon that encloses all of the mapped vents in the SVF with the exception of three outlying vents in the NW portion of the field

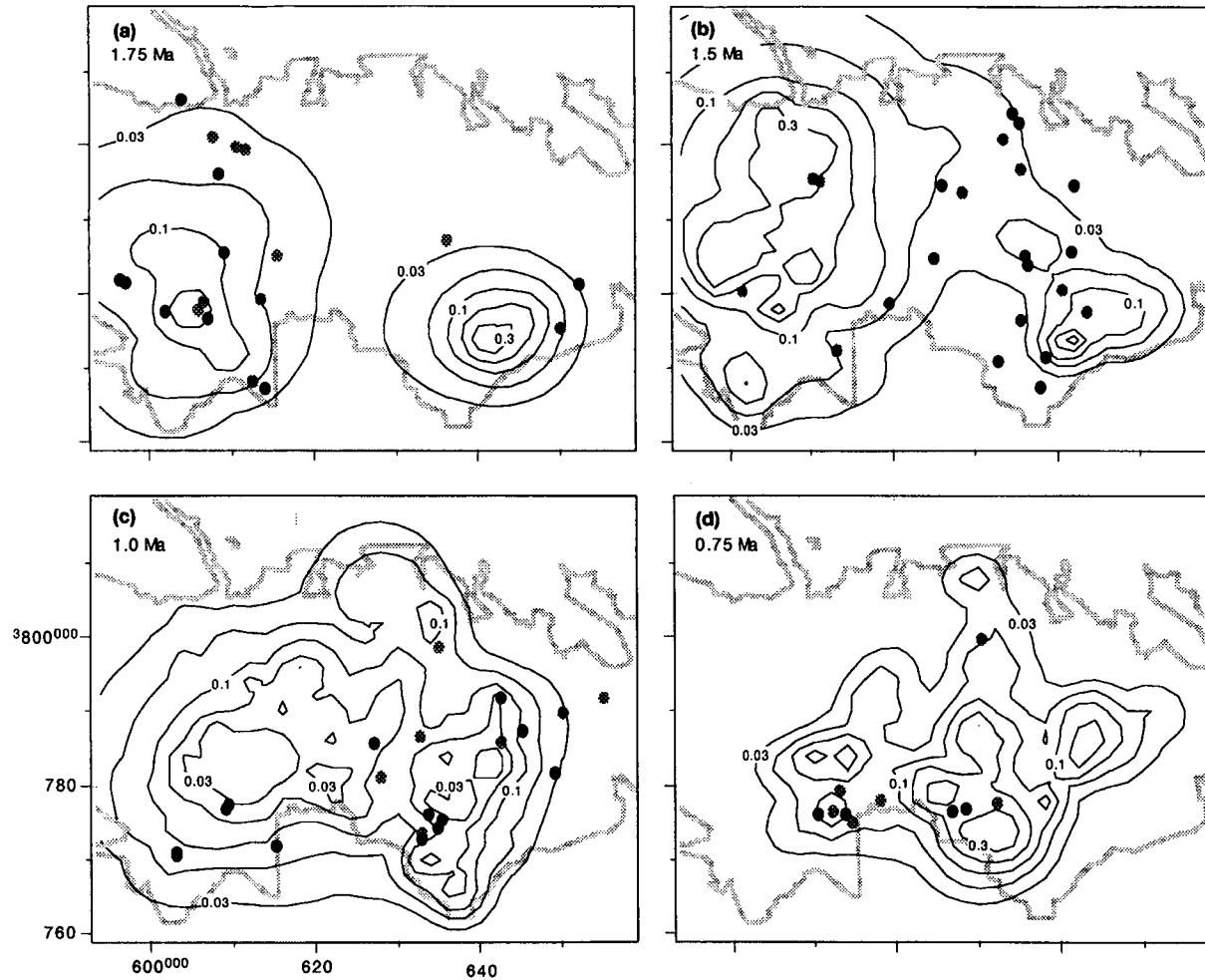


Figure 5-11. Probability maps of volcanism in the SVF calculated using the near-neighbor model. $P[\text{volcanic event} \mid a=10 \text{ km}^2, t=50,000 \text{ yr}]$ is contoured using volcanoes formed (a) before 1.75 Ma, (b) 2.0–1.5 Ma, (c) 1.5–1.0 Ma, and (d) 1.25–0.75 Ma. Ages labelled on each plot are the times for which probability estimates were made, using the timing and distribution of volcanic events that occurred during the previous 0.5 m.y. The locations of subsequent volcanic events are also plotted (solid circles—vents formed within the next 50,000 yr; shaded circles—vents formed 50,000–100,000 yr later, based on mean vent ages). Map coordinates are Universal Transverse Mercator.

(Figure 5-2). This area is $\approx 3,000 \text{ km}^2$. Average recurrence rates may also be calculated from the spatio-temporal model:

$$\bar{\lambda}_t(p) = \frac{\lambda_t}{A} \quad (5-3)$$

where λ_t is the regional recurrence rate and A is the area of the volcanic field ($3,000 \text{ km}^2$). The values of $\bar{\lambda}_t(p)$ and $\bar{\lambda}(p)$ differ slightly due to variation in the fit of the model (Figure 5-9).

At 1.75 Ma, the regional recurrence rate was $1.8 \times 10^{-4} \text{ v/yr}$ and $\bar{\lambda}_t(p) = 6.0 \times 10^{-8} \text{ v yr}^{-1} \text{ km}^{-2}$. Based on the number of volcanic events 2.0–1.75 Ma, $\bar{\lambda}(p) = 4.1 \times 10^{-8} \text{ v yr}^{-1} \text{ km}^{-2}$. The next 19 vents to form are located in areas with $\lambda_n(p) = 5.8 \times 10^{-8} - 6.6 \times 10^{-7} \text{ v yr}^{-1} \text{ km}^{-2}$, with 11 of the 19 vents formed in locations of $\lambda_n(p) > 1 \times 10^{-7} \text{ v yr}^{-1} \text{ km}^{-2}$. At 1.75 Ma, the spatio-temporal model forecasts the locations of subsequent volcanic events significantly better than simply averaging the regional recurrence rate over the entire field [Figure 5-12(a)]. The spatial-temporal model does equally well at 0.75 Ma [Figure 5-12(d)], and nearly as well at 1.0 Ma [Figure 5-12(c)].

The probability model does a poor job of forecasting the location of future volcanic events at 1.5 Ma. Based on the model, the probability of future eruptions was high in the western portion of the field at this time [Figure 5-11(b)]. However, most volcanism occurred in the central portion of the SVF during the next 50,000 yr, in areas where $P[\text{volcanic event} | a = 10 \text{ km}^2, t = 50,000 \text{ yr}] < 0.05$. The regional recurrence rate at this time was $2.4 \times 10^{-4} \text{ v/yr}$ or $\bar{\lambda}_t(p) = 8.0 \times 10^{-8} \text{ v yr}^{-1} \text{ km}^{-2}$, and $\bar{\lambda}(p) = 7.4 \times 10^{-8} \text{ v yr}^{-1} \text{ km}^{-2}$. Approximately 40 percent of subsequent volcanic events occur in areas in which the recurrence rate is estimated to be less than these values [Figure 5-12(b)]. In other words, at 1.5 Ma the spatio-temporal model performed no better than assuming subsequent volcanic events would have a random distribution in the field. This decrease in the effectiveness of the model results from a major change in the locus of volcanism in the field around 1.5 Ma. A change in alkalinity [Figures 5-6(a) and 5-6(b)] and an increase in the rate of new vent formation (Figure 5-4) also occurred at this time. Therefore, a major shift in paragenesis is accompanied by a new pattern in the distribution and timing of volcanism.

Even in cases in which the spatio-temporal model is effective (e.g., 1.75, 1.0, and 0.75 Ma), it is important not to over interpret the probability maps. Numerous maxima occur on many of the probability plots [e.g., Figure 5-11(d)] within which $P[\text{volcanic event} | a = 10 \text{ km}^2, t = 50,000 \text{ yr}] > 0.3$. These areas have been the site of comparatively intense volcanism during the previous 0.5 m.y. Often, subsequent volcanism does not occur within these maximum, but is instead offset from these maxima by 5–10 km. This pattern is clear in the eastern portion of the field at 1.0 Ma [Figure 5-11(c)] and the western and central portions of the field at 0.75 Ma [Figure 5-11(d)]. In general, subsequent volcanic activity does not occur in areas of very high or low recurrence rate in any of the time intervals [Figures 5-12(a) through 5-12(d)].

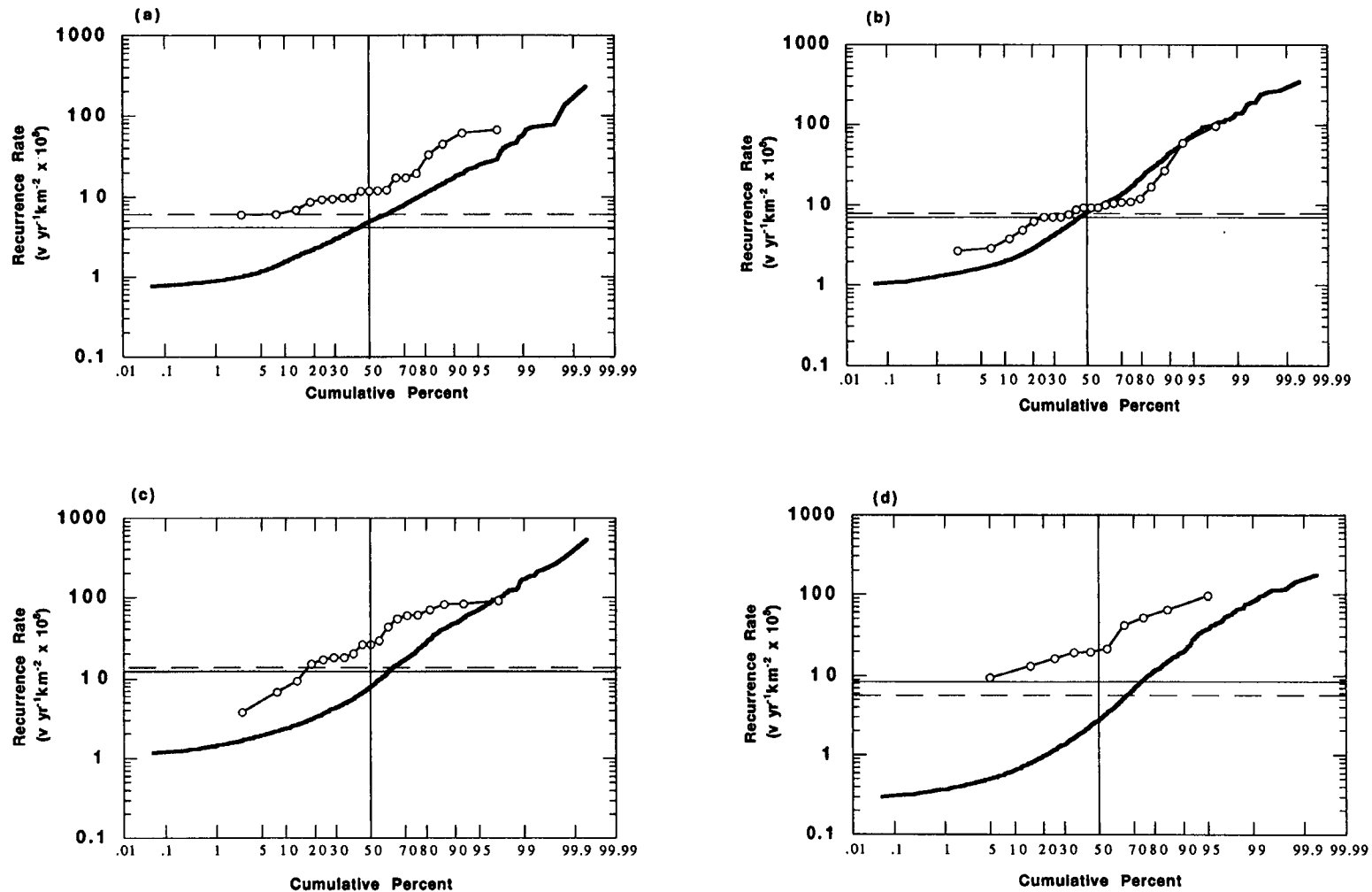


Figure 5-12. The relative success of the spatio-temporal model can be evaluated by comparing the recurrence rates estimated by the model at the locations of subsequent volcanic events (open circles) with the average recurrence rates of volcanism, $\lambda_t(p)$ (dashed line) and $\lambda(p)$ (solid line). The distribution of model recurrence rates, $\lambda_n(p)$ in the entire SVF is also shown (heavy solid line) for comparison at (a) 1.75 Ma, (b) 1.5 Ma, (c) 1.0 Ma, and (d) 0.75 Ma. Recurrence rates in the areas of subsequent volcanic events, estimated using the spatio-temporal model, are significantly greater than average values at 1.75, 1.0, and 0.75 Ma, and not significantly different at 1.5 Ma. Subsequent volcanic events for each interval are mapped in Figures 5-12(a)-(d).

5.2.7 Discussion

Patterns in volcanic activity in the SVF were identified through detailed mapping and analysis. Although details of the stratigraphy and volcanology of the field are well known, it is critical to evaluate possible bias in the analysis due to assumptions about the timing and distribution of volcanic events. The dense effusion of basalts in the field over the last 2 m.y. likely buried or destroyed numerous older vents. Burial and destruction may have occurred preferentially in highly active parts of the volcanic field. For example, numerous eruptions occurred in the central portion of the SVF between approximately 1.0 and 0.75 Ma [Figure 5-7(d)]. These eruptions may have buried numerous older vents accounting, in part, for the pattern of basaltic eruptions observed during earlier time intervals [e.g., Figure 5-7(a)]. However, the observed tightly clustered pattern in volcanism argues against the severity of this problem. Inspection of Figure 5-11 indicates that areas of waxing volcanism occur over limited zones within the SVF at all time intervals. Certainly these intense, clustered episodes of volcanism bury some older vents. It would be quite fortuitous, however, if these relatively few zones of intense volcanism completely buried similar, older zones of intense volcanism, given the deduced pattern of activity (Figure 5-10).

Experimentation with the uncertainty in the ages of the units indicates that some shift in the timing of episodes of volcanism in the SVF is possible, as exemplified by the uncertainty in cumulative rate of volcanic events (Figure 5-4). However, stratigraphic relationships preclude the possibility that the relative timing of major trends, such as the change from tholeiitic to more alkaline magmatism, are inverted. Similarly, although some variation in the exact timing of cluster formation is permissible, the relative timing of formation of clusters is closely and unambiguously constrained by stratigraphic and radiometric age data.

5.2.7.1 Patterns of Volcanism in the Springerville Volcanic Field

Although additional geochronological information will no doubt improve the resolution of recurrence rate models, the basic temporal and spatial patterns of volcanism in the SVF are evident. These patterns include: (i) waxing, steady-state, and waning rates of vent formation; (ii) steady-state magma output for more than 1 m.y.; (iii) a change in major element geochemistry accompanying an increase in rate of vent formation, without a change in total magma output; and (iv) formation of vent clusters that are discrete in time and space. These clusters form on timescales of 0.5 Ma or less and in areas that are commonly 10–20 km in diameter (Figure 5-10), during episodes in which the recurrence rate commonly exceeds $1 \times 10^{-7} \text{ v yr}^{-1} \text{ km}^{-2}$. Episodes of cluster formation took place against a background recurrence rate throughout the SVF that was much lower (e.g., $\leq 2 \times 10^{-8} \text{ v yr}^{-1} \text{ km}^{-2}$ during a given 0.25-m.y. interval; Figures 5-7(a) through 5-7(d). Even during waning magmatism in the SVF as a whole (1.0–0.5 Ma; Figure 5-10), specific areas of the field still had much higher recurrence rates than average.

Two possible explanations for this localization of vents are: (i) zones of high vent density reflect the same basic areal distribution of zones of melt generation in the mantle, and (ii) melt generation is more regional, but crustal structures or crustal stress state enhance transport at particular locations and at particular times. Several lines of evidence help differentiate between these two explanations. Generally, stress states are thought to have been uniform, or rotated slightly, during the Quaternary in the southern Colorado Plateau region (Thompson and Zoback, 1979; Zoback and Zoback, 1989) and the region of the SVF contains few and subtle structures (Crumpler et al., 1989). Although only about 20 percent of vents in the SVF are part of vent alignments, the vent alignments that are present are regional in extent and

likely reflect large-scale crustal structures (Figure 5-2). These vent alignments transect the field, develop over time, and have orientations consistent with regional stress orientation and a vertical σ_1 (Connor et al., 1992). Although ascending magmas appear to interact locally with these structures, there is no evidence to indicate that the regional crustal stress state changes or structures develop on the temporal and spatial scales of observed changes in volcanic activity. This lack of evidence argues against regional structural control on the development of vent clusters.

Alternatively, rapid changes in the local stress state likely resulted from dike intrusion, and this in turn may affect subsequent dike intrusions (Parsons and Thompson, 1991). Such local changes in crustal stress may enhance magma transport in some areas, for example, between two intrusions (e.g., Ryan, 1990; Takada, 1994). Thus, dike injection may affect the pattern of vent distribution in and near vent clusters, where dike density is likely to be high. However, changes in stress state due to dike injection cannot account for shifts in activity across the entire SVF, as occurred between 1.5 and 1.25 Ma, or the intensity of volcanism in local areas following periods of relative quiescence (Figure 5-10).

Instead, given the distinct petrology of some clusters, their timing and distribution, and lack of association with known structure, the pattern of vent formation is more likely related to localized melt generation. Localized melt generation throughout the development of the SVF is a dramatically different picture than would emerge if vents were assumed to be randomly distributed in the field. Patterns of volcanism in other continental basaltic fields (Heming, 1980; Tanaka et al., 1986; Connor, 1990; Connor and Hill, 1995), although often less well constrained, indicate that this nonhomogeneity in timing and distribution of vents, and hence melt generation, is common and may be ubiquitous. Thus, the application of a spatio-temporal recurrence rate model provides a more complete view of the development of the field than is possible through identification of temporal (Condit et al., 1989a) or spatial (Connor et al., 1992) trends alone.

Significant changes in petrogenesis occur with changes in the timing and intensity of volcanism in the SVF. The observed change in alkalinity may result from some combination of a decrease in the degree of partial melting, increase in the depth over which partial melting occurred, or increased open-system behavior of the magmas (e.g., Best and Brimhall, 1974; Morse, 1980; Fitton et al., 1988). We do not attempt to differentiate between these mechanisms in this report. However, the increase in the rate of vent formation with increasing alkalinity but constant volume output for the entire volcanic field does imply that with smaller percentages of partial melting, more numerous magma batches reach the surface. These relatively small batches of magma can only form, or at least reach the surface, in those areas in which heat flux and magma generation are sufficiently localized to generate and transport these magmas. Comparing areas of waxing volcanism over time in the SVF (Figure 5-10) indicates little change in the clustered nature of volcanism despite large changes in petrogenesis. Persistent vent clustering and constant magma output indicate that a model of early intense heating, resulting in widespread tholeiitic volcanism, followed by waning and increasingly alkalic magmatism (Best and Brimhall, 1974; Fitton et al., 1988; Condit et al., 1989a), does not capture essential details of the development of the SVF.

5.2.7.2 Hazard Models

The patterns of volcanic activity in the SVF indicate that hazard models must account for spatial and temporal nonhomogeneity in recurrence rate. Recurrence rate varied by more than two orders of magnitude across the SVF at any given time during its development [Figures 5-12(a) through 5-12(d)]. Consequently, averaging the recurrence rate over the entire SVF would significantly overestimate hazard

in some regions and underestimate hazard in others. Application of the near-neighbor spatio-temporal recurrence rate model to the SVF offers an opportunity to evaluate the utility of these models at various times during the development of the field as the locus and intensity of volcanism changes, and through changes in petrogenesis.

Several assumptions are made in the application of the spatio-temporal recurrence rate model. Iterative calculation of the local and regional recurrence rates, λ_r and $\lambda_n(p)$, indicates that the model is sensitive to changes in the number of near-neighbor volcanic events used. There are no geologic criteria for choosing among these different numbers of near-neighbor vents, and for much of the early history of the SVF, $m=6-10$ near-neighbors work nearly equally well, given the uncertainty in the age determinations of specific units (Figure 5-8). However, the use of many near-neighbor events, for example $m \geq 10$, tends to include volcanic events in the recurrence rate estimate even when they are far away or are old. Use of a large number of near-neighbor vents results in a low recurrence rate estimate that cumulatively results in a strong divergence between the model and the true cumulative number of volcanic events through time. Conversely, use of few near-neighbors preferentially weights very recent or nearby volcanic events. Use of few near-neighbors tends to increase recurrence rate estimates and, ultimately, overestimates the total number of volcanic events. In the SVF, $m=7-8$ near-neighbors best models recurrence rate throughout most of the < 2.1 Ma volcanic activity. In other volcanic fields, with different recurrence rates and vent distributions, different numbers of near-neighbor volcanoes could provide better estimates of the observed recurrence rate.

Empirical observation (Figure 5-9) indicates that implementation of a 0.5-m.y. time window better models the waning system than longer or shorter time windows. Older events are much less relevant to patterns in volcanic activity in the SVF than younger events, but only up to a point. For example, in the SVF a zone of intense volcanism is no more likely to experience eruptions than another nearby area after 1 m.y. of quiescence. In contrast, 0.25 Ma of quiescence is not sufficient to preclude future activity in the immediate area. The duration of this time window suggests a limit to the duration of melt generation in a particular region of the SVF, despite persistent activity in the field as a whole. In a less active volcanic system, or one which is more strongly episodic in time, trends are often not as apparent as they are in the SVF (e.g., Ho et al., 1991; Connor and Hill, 1995). In these areas in which the estimation of an appropriate time window is difficult, it may be conservative to apply various windows, or not window the recurrence rate estimate at all, realizing that recurrence rates and therefore hazard may be under- or overestimated.

At most time intervals, the near-neighbor model does a better job of identifying areas of subsequent volcanic activity than simply averaging recurrence rate, $\bar{\lambda}_r(p)$ or $\bar{\lambda}(p)$, across the entire field [Figures 5-12(a) through 5-12(d)]. This performance was generally maintained despite shifts in the locus of volcanism and changes in the regional recurrence rate, λ_r . A large percentage of subsequent events take place in areas with more than twice the average recurrence rate of the SVF at the time. Thus, the spatio-temporal recurrence rate and probability maps have a definite advantage in evaluating long-term hazards over area averaging techniques.

However, hazards are not significantly greater at local maxima $P[\text{volcanic event} \mid a=10 \text{ km}^2, t=50,000 \text{ yr}] > 0.5$ than in nearby areas. Subsequent volcanic activity occurs close to, but not usually directly within, areas that have experienced intense volcanic activity in the past. Several geological factors may account for this shift in intensity, including a shift in the location of zones of partial melting due to

migration in the source of heat or depletion of mantle, or changes in the stress state of the crust due to multiple dike injections (e.g., Parsons and Thompson, 1991). Based on these considerations, it is best to treat the areas of extreme recurrence rate, either maxima or minima, with caution when estimating the locations of future eruptions and identifying hazard zones.

The model does not perform significantly better than the average recurrence rate at 1.5 Ma. This period was a time of rapid change in the SVF, with a shift in the locus of volcanism from west to east, an increase in the recurrence rate of volcanic events, and an increase in the eruption of more highly alkaline basaltic magmas. It makes sense that this major shift in volcanic activity is not well forecast by the method because the recurrence rate estimate depends on the timing and distribution of past events. With a comparatively major change in petrogenesis and possibly other processes governing magma transport, recent patterns in activity are a less reliable indicator of future activity. Conversely, the correlation between petrogenesis and patterns in activity implies that hazard models can be improved if petrogenesis and processes governing magma transport can be taken into account directly.

5.2.8 Conclusions

The SVF developed through episodes of volcanism that occurred at discrete times and locations within the field. These episodes typically are focused in areas 10–20 km in diameter and are less than 0.5 m.y. in duration, possibly representing the area and longevity of magma source regions. Cumulatively, these discrete episodes resulted in waxing rates of vent formation prior to 1.5 Ma, near steady-state rates of vent formation at 1.5–0.75 Ma, and waning rates of vent formation since 0.75 Ma. The increase in rate of vent formation at about 1.5 Ma occurred at a time of shift in the locus of magmatism from west to east in the field and a significant increase in alkalinity of magmas erupted in the most active clusters of vents in the SVF. The volume of erupted magmas, inferred from lava flow areas, was steady state between 1.75–0.75 Ma.

An $m=7$ near-neighbor spatio-temporal recurrence rate model with a 0.5-m.y. time window most accurately describes a plot of the cumulative rate of volcanic events versus time in the SVF. Application of this spatio-temporal recurrence rate model reveals that areas of waxing and waning magmatism in the field are much more localized and volcanic activity within these areas much more intense than implied by broad temporal trends. Because volcanic activity is spatially and temporally clustered, the model is more successful at forecasting subsequent activity in specific locations than is possible using average recurrence rates. These results indicate that spatio-temporal recurrence rate models are useful tools for quantification of long-term volcanic hazards in continental basaltic volcanic fields.

5.3 ASSESSMENT OF PROGRESS TOWARD MEETING PROJECT OBJECTIVES

The three major milestones submitted to the NRC since January 1, 1995, represent a substantial effort to advance our understanding of the application and utility of probabilistic methods in long-term volcanic hazard assessment. One of the principal findings of this work is that significant and previously unrecognized uncertainty exists in probability estimates. These uncertainties result from spatial variation in recurrence rate of volcanic activity in the YMR. Although the probability of volcanic disruption of the YMR site is $1-5 \times 10^{-4}$ in 10,000 yr, based on many estimation techniques, this probability varies by more than two orders of magnitude within 20 km of the site (Connor and Hill, 1995). Such large variation in probability over a distance on the scale of many geologic structures indicates the actual range

of probability of volcanic activity at the repository site in the next 10,000 yr is 1×10^{-5} to 1×10^{-3} . This range is based on several assumptions, such as that a volcano must form within 500 m of the repository boundary in order to impact performance at all, and that the regional recurrence rate of volcanism is less than 10 volcanoes/m.y. The range in probability based on currently available data is large enough that these assumptions must be examined in greater detail, particularly because uncertainty can be reduced through geological investigation.

Several avenues of investigation were proposed by the expert panel that reviewed the CNWRA research program in volcanology in 1994 (Hill, 1995). The project plan for this research project has been revised to take into account the specific technical recommendations of this panel with the goal of further bounding probability estimates and reducing uncertainty. These goals have led to the addition of two tasks to the Volcanic Systems of the Basin and Range Research Project and the revision of a third. These tasks include:

- Task 6—Petrogenesis of Neogene and Quaternary basalts
- Task 7—Development of dike zones in small-volume basaltic systems
- Task 4—Tectonic setting of basaltic volcanic has also been revised and expanded based on the expert panel recommendations. The purpose of this revision is to focus on several issues that are most likely to impact volcanic hazard models for YM.

5.4 PLANS FOR NEXT REPORTING PERIOD

Activities in Task 4 will concentrate on analysis of the development of the Big Pine Volcanic Field and the San Francisco Volcanic Field during the next 6 mo. Both of these fields are associated with major structural features. Geological investigations in these areas will concentrate on the relationship between the timing of deformation and the timing of volcanic activity on subregional (100–1,000 km²) scales. Spatial controls on volcanism due to the presence of major structures will also be investigated on several scales. In addition to these activities, sampling and analysis of Neogene and Quaternary basalts in the YMR will proceed. It is anticipated that all of the Plio-Quaternary basalt units within 100 km of YM will be sampled within the next 6 mo.

5.5 REFERENCES

- Aubele, J.C., L.S. Crumpler, and M. Shafiqullah. 1986. K-Ar ages of late Cenozoic rocks of the central and eastern parts of the Springerville volcanic field, Arizona. *Isochron/West* 46: 3–5.
- Aubele, J.C., L.S. Crumpler, and C.D. Condit. 1987. Tectonic deformation of the Late Cenozoic Springerville volcanic field, southern margin of the Colorado Plateau, Arizona. *Geological Society of America Abstracts with Programs—1987 Annual Meeting*. Boulder, CO: Geological Society of America: 19: 576.
- Bacon, C.R. 1982. Time-predictable bimodal volcanism in the Coso Range, California. *Geology* 10: 65–69.

- Bemis, K.G., and D.K. Smith. 1993. Production of small volcanoes in the Superswell region of the South Pacific. *Earth and Planetary Science Letters* 118: 251-262.
- Best, M.G., and W.H. Brimhall. 1974. Late Cenozoic alkalic basaltic magmas in the western Colorado Plateau and the Basin and Range transition zone, U.S.A., and their bearing on mantle dynamics. *Geological Society of America Bulletin* 85: 1,677-1,690.
- Condit, C.D. 1984. *The Geology of the Western Part of the Springerville Volcanic Field, East-Central Arizona*. Unpublished Ph.D. Dissertation. Albuquerque, NM: University of New Mexico: 453.
- Condit, C.D. 1991. Lithologic map of the western part of the Springerville volcanic field, east-central Arizona (1:50,000). U.S. Geological Survey MI Map I-1993, 2 sheets. Reston, VA: U.S. Geological Survey.
- Condit, C.D. 1995. *Dynamic Digital Map: The Springerville Volcanic Field*. Digital Publication Series DPSM01MC (CD-ROM for the Macintosh). Boulder, CO: Geological Society of America.
- Condit, C.D., and C.B. Connor. 1995. Recurrence rates of volcanism in basaltic volcanic fields: An example from the Springerville volcanic field, AZ, USA. *Geological Society of America Bulletin* Submitted.
- Condit, C.D., and M. Shafiqullah. 1985. K-Ar ages of late Cenozoic rocks of the western part of the Springerville volcanic field, east-central Arizona. *Isochron/West* 44: 3-5.
- Condit, C.D., L.S. Crumpler, and J.C. Aubele. In press, Lithologic, age-group, magnetopolarity and geochemical maps of the Springerville volcanic field, east-central Arizona (1:100,000). U.S. Geological Survey MI Map I-2431, 4 sheets. Reston, VA: U.S. Geological Survey.
- Condit, C.D., L.S. Crumpler, J.C. Aubele, and W.E. Elston. 1989a. Patterns of volcanism along the southern margin of the Colorado Plateau: The Springerville Field. *Journal of Geophysical Research* 94: 7,975-7,986.
- Condit, C.D., L.S. Crumpler, and J.C. Aubele. 1989b. Field trip road log for the Springerville volcanic field, southern margin of the Colorado Plateau. *Field Excursions to Volcanic Terranes in the Western United States, Volume I: Southern Rocky Mountain Region*. C. Chapin and J. Zidek, eds. Socorro, NM: New Mexico Bureau of Mines and Mineral Resources: 46: 33-38.
- Connor, C.B. 1990. Cinder cone clustering in the TransMexican volcanic belt: Structural and petrologic implications. *Journal of Geophysical Research* 95: 19,395-19,405.
- Connor, C.B., and B.E. Hill. 1993. Estimating the probability of volcanic disruption at the Yucca Mountain site using nonhomogeneous Poisson models. *Focus '93*. La Grange Park, IL: American Nuclear Society: 174-181.
- Connor, C.B., and B.E. Hill. 1995. Three nonhomogeneous Poisson models for the probability of basaltic volcanism: Application to the Yucca Mountain Region, Nevada, USA. *Journal of Geophysical Research* 100: 10,107-10,126.

- Connor, C.B., C.D. Condit, L.S. Crumpler, and J.C. Aubele. 1992. Evidence of regional structural controls on vent distribution: Springerville volcanic field, Arizona. *Journal of Geophysical Research* 97: 12,349-12,359.
- Cooper, J.L. 1991. *The Springerville Volcanic Field: A Case Study of Crust/Mantle Evolution and Magma Genesis in a Tectonophysical Transition Zone* Ph.D. Dissertation. Oxford, OH: Miami University: 298 p.
- Cooper, J.L., J.L. Aronson, C.D. Condit, and W.K. Hart. 1990. New K-Ar ages of lavas from the Colorado Plateau-Basin and Range transition zone, east-central Arizona. *Isochron/West* 55: 28-31.
- Cressie, N.A.C. 1991. *Statistics for Spatial Data*. New York, NY: John Wiley and Sons: 900 p.
- Crumpler, L.S., J.C. Aubele, and C.D. Condit. 1989. Influence of Quaternary tectonic deformation on volcanism in the Springerville volcanic field, Colorado Plateau, USA. *Bulletin of the New Mexico Bureau of Mines and Mineral Resources* 131: 64.
- Crumpler, L.S., J.C. Aubele, and C.D. Condit. 1994. Volcanoes and neotectonic characteristics of the Springerville volcanic field, Arizona, Mogollon Slope. *New Mexico Geological Society Guidebook*. Socorro, NM: New Mexico Geological Society: 147-164.
- Duffield, W.A., C.R. Bacon, and G.B. Dalrymple. 1980. Late Cenozoic volcanism, geochronology, and structure of the Coso Range, Inyo County, California. *Journal of Geophysical Research* 85: 2,381-2,404.
- Fitton, J.R., D. James, P.D. Kempton, D.S. Ormerod, and W.P. Leeman. 1988. The role of lithospheric mantle in the generation of late Cenozoic basic magmas in the western United States. *Journal of Petrology, Special Lithosphere Issue* 331-349.
- Foland, K.A., and S.C. Bergman. 1992. Temporal and spatial distribution of basaltic volcanism in the Pancake and Reveille ranges north of Yucca Mountain. *Third Annual International High-Level Radioactive Waste Management Conference Proceedings*. La Grange Park, IL: American Nuclear Society: 2,366-2,371.
- Heming, R.F. 1980. Patterns of Quaternary basaltic volcanism in the northern North Island, New Zealand. *New Zealand Journal of Geology and Geophysics* 23: 335-344.
- Hill, B.E. 1995. *Expert-Panel Review of CNWRA Research Programs*. CNWRA 95-002. San Antonio, TX: Center for Nuclear Waste Regulatory Analyses.
- Ho, C.-H. 1991. Time trend analysis of basaltic volcanism at the Yucca Mountain site. *Journal of Volcanology and Geothermal Research* 46: 61-72.

- Ho, C.-H., E.I. Smith, D.L. Feuerbach, and T.R. Naumann. 1991. Eruptive probability calculation for the Yucca Mountain site, USA: Statistical estimation of recurrence rates. *Bulletin of Volcanology* 54: 50-56.
- Irvine, T.N., and W.R.A. Baragar. 1971. A guide to the chemical classification of the common volcanic rocks. *Canadian Journal of Earth Science* 8: 523-548.
- Kuntz, M.A., D.E. Champion, E.C. Spiker, and R.H. Lefebre. 1986. Contrasting magma types and steady-state, volume-predictable, basaltic volcanism along the Great Rift, Idaho. *Geological Society of America Bulletin* 97: 579-594.
- Laughlin, A.W., D.G. Brookins, P.E. Damon, and M. Shafiqullah. 1979. Late Cenozoic volcanism of the central Jemez zone, Arizona-New Mexico. *Isochron/West* 25: 5-8.
- Le Bas, M.J., R.W. Le Maitre, A. Streckeisen, and B. Zanettin. 1986. A chemical classification of volcanic rocks based on the total alkali-silica diagram. *Journal of Petrology* 27: 745-750.
- Luedke, R.G., and R.L. Smith. 1978. Map showing distribution, composition, and age of late Cenozoic volcanic centers in Arizona and New Mexico: U.S. Geological Survey Miscellaneous Investigations Series Map I-1091-A, scale 1:100,000 and 1:500,000, 2 sheets. Reston, VA: U.S. Geological Survey.
- Lutz, T.M., and J.T. Gutmann. 1995. An improved method of determining alignments of point-like features and its implications for the Pinacate volcanic field, Mexico. *Journal of Geophysical Research*. In press.
- McBirney, A.R. 1992. Volcanology. *Techniques for Determining Probabilities of Geologic Events and Processes*. R.L. Hunter and J.C. Mann, eds. International Association for Mathematical Geology, Studies in Mathematical Geology No. 4. New York, NY: Oxford University Press: 167-184.
- McKnight, S.B., K. Roggensack, and S.N. Williams. 1994. Historical eruption dynamics, volumes, and geochemistry of a young volcano, Cerro Negro, Nicaragua. *EOS, Transactions of the American Geophysical Union* 75 (44): 731.
- Morse, S.A. 1980. *Basalts and Phase Diagrams*. New York, NY: Springer Verlag: 493.
- Nealey, L.D. 1989. Field trip road log for the White Mountains volcanic field, southeastern Colorado Plateau. *Field Excursions to Volcanic Terranes in the Western United States, Volume I, Southern Rocky Mountain region*. C. Chapin and J. Zidek, eds. Socorro, NM: New Mexico Bureau of Mines and Mineral Resources Memoir 46: 221-225.
- Parsons, T., and G.A. Thompson. 1991. The role of magma overpressure in suppressing earthquakes and topography: Worldwide examples. *Science* 253: 1,399-1,402.
- Pierce, H.W., P.E. Damon, and M. Shafiqullah. 1979. An Oligocene(?) Colorado Plateau edge in Arizona. Plateau Uplift; Mode and Mechanism. T.R. McGetchin, ed. *Tectonophysics*: 61: 1-24.

- Ryan, M.P. 1990. The physical nature of the Icelandic magma transport system. *Magma Transport and Storage*. M.P. Ryan, ed. New York, NY: John Wiley and Sons: 175-224.
- Silverman, B.W. 1986. *Density Estimation for Statistics and Data Analysis*. London, England: Chapman and Hall: 175 p.
- Simkin, T., and L. Seibert. 1994. *Volcanoes of the World*. Second Edition. Tucson, AZ: Geosciences Press: 349 p.
- Smith, E.I., T.R. Naumann, D.L. Feuerbach, and J.E. Faulds. 1990. The area of most recent volcanism near Yucca Mountain, Nevada: Implications for volcanic risk assessment. *International High-Level Radioactive Waste Management Conference Proceedings*. La Grange Park, IL: American Nuclear Society: 81-90.
- Stirewalt, G.L., S.R. Young, and K.D. Mahrer. 1992. *A Review of Pertinent Literature on Volcanic-Magmatic and Tectonic History of the Basin and Range*. CNWRA 92-025. San Antonio, TX: Center for Nuclear Waste Regulatory Analyses.
- Stirewalt, G.L., B.E. Hill, C.B. Connor, and C. Lin. 1995. *A Critical Review of Data in the CNWRA Volcanism Geographic Information System (GIS) Database*. CNWRA 95-003. San Antonio, TX: Center for Nuclear Waste Regulatory Analyses.
- Takada, A. 1994. The influence of regional stress and magmatic input on styles of monogenetic and polygenetic volcanism. *Journal of Geophysical Research* 99: 13,563-13,574.
- Tanaka, K.L., E.M. Shoemaker, G.E. Ulrich, and E.W. Wolfe. 1986. Migration of volcanism in the San Francisco volcanic field, Arizona. *Geological Society of America Bulletin* 97: 129-141.
- Tokarev, P.I. 1983. Calculation of the magma discharge, growth in the height of the cone and dimensions of the feeder channel of Crater I. *The Great Tolbachik Fissure Eruption, Geological and Geophysical Data, 1975-1976*. S.A. Fedotov and Ye.K. Markhnin, eds. New York, NY: Cambridge University Press: 27-35.
- Thompson, G.A., and M.A. Zoback. 1979. Regional geophysics of the Colorado Plateau. *Tectonophysics* 61: 149-181.
- Ulrich, G.E., C.D. Condit, K.J. Wenrich, E.W. Wolfe, R.F. Holm, L.D. Nealey, M. Conway, J.C. Aubele, and L.S. Crumpler. 1989. Miocene to Holocene volcanism and tectonism of the southern Colorado Plateau. *Field Excursions to Volcanic Terranes in the Western United States, Volume I: Southern Rocky Mountain Region*. C. Chapin and J. Zidek, eds. Socorro, NM: New Mexico Bureau of Mines and Mineral Resources Memoir 46: 1-2.
- Wadge, G., P.A.V. Young, and I.J. McKendrick. 1994. Mapping lava flow hazards using computer simulation. *Journal of Geophysical Research* 99: 489-504.

- Walker, G.P.L. 1993. Basaltic-volcano systems. *Magmatic Processes and Plate Tectonics*. H.M. Prichard, T. Alabaster, N.B.W. Harris, and C.R. Neary, eds. Geological Society Special Publication No. 76. Boulder, CO: Geological Society of America: 3-38.
- Wilcox, R.E. 1954. *Petrology of Parícutin Volcano*. U.S. Geological Survey Bulletin 965C. Reston, VA: U.S. Geological Survey: 281-353.
- Zoback, M.L., and M.D. Zoback. 1989. Tectonic stress field of the continental United States. *Framework of the continental United States*. L.C. Pakiser and W.D. Mooney, eds. Memoir. Boulder, CO: Geological Society of America: 172: 523-539.

6 TECTONIC PROCESSES IN THE CENTRAL BASIN AND RANGE REGION

by David A. Ferrill, Alan P. Morris, John A. Stamatakos, and Kathy H. Spivey

*Investigators: David A. Ferrill, D. Brent Henderson, John A. Stamatakos, Kathy H. Spivey,
(CNWRA), Alan P. Morris (Consultant)*

NRC Project Officer: Edward O'Donnell

6.1 TECHNICAL OBJECTIVES

The principal technical objectives of the Tectonics Research Project include: (i) compiling and integrating tectonic data for the central Basin and Range and Yucca Mountain Regions (YMR), and (ii) developing and assessing models of tectonic processes in those regions. Of particular concern is the adequacy of existing and anticipated data for evaluating compliance with quantitative waste-isolation performance objectives.

Geologic structure, structural deformation, and tectonic processes are important to long-term repository performance and preclosure operational safety because tectonic processes represent potentially adverse conditions if they are characteristic of the controlled area or may affect isolation within the controlled area [10 CFR 60.122(c)]. Design criteria for the Geologic Repository Operations Area (GROA) require design of structures, systems, and components such that natural phenomena (e.g., earthquakes and ground rupture associated with fault slip) anticipated at the GROA will not interfere with the necessary safety functions [10 CFR 60.131(b)(1)]. The tectonic setting of Yucca Mountain (YM) presents numerous potential hazards for the proposed repository, such as, seismicity, fault disruption, basaltic volcanism, magma channeling along pre-existing faults, and faults and fractures that may serve as conduits or barriers to groundwater flow.

Information concerning models of tectonic processes (e.g., patterns and rates of historic and prehistoric faulting and seismicity) and structural features will be necessary to assess compliance with specific regulatory requirements as documented in License Application Review Plan (LARP) Sections 3.2.1.5 through 3.2.1.9 and 3.2.2.8. Key Technical Uncertainties (KTUs) that have been or will be addressed by the Tectonics Research Project include:

- Uncertainty in determining three-dimensional structure and tectonic setting of YM (see LARP Section 3.2.1.5)
- Uncertainty in determining spatial and temporal patterns of seismicity (see LARP Sections 3.2.1.7 and 3.2.1.8)
- Uncertainty in determining the slip history of faults (see LARP Sections 3.2.1.5, 3.2.1.7, and 3.2.1.8)
- Uncertainty in determining effects of structural deformation and tectonic processes on the flow and transport of groundwater (see LARP Section 3.2.2.8)

- Uncertainty in determining magnitude of fault slip and associated seismic shaking at surface and shallow subsurface locations (see LARP Section 3.2.1.7)
- Uncertainty in determining effects of structural deformation and tectonic processes on rock mass properties (see LARP Section 3.2.1.5)
- Uncertainty in determining the probability of igneous activity and resulting disruption of the candidate repository

Important goals of the Tectonics Research Project include development and analyses of alternate tectonic models, evaluation of potential hazards due to fault displacement and seismic shaking, and initiation of field studies to address tectonic issues. Field studies will focus on the following topics: (i) identification and analysis of structural/tectonic analogs for YM, (ii) development and assessment of alternative structural/tectonic models for the central Basin and Range and YMR, (iii) assessment of interaction of faulting and igneous activity (collaboration with Volcanology Research), and (iv) determination and analysis of structural/tectonic controls on regional groundwater flow (collaboration with Regional Hydrology Research). Descriptions of key tasks of the Tectonic Processes of the Central Basin and Range Research Project are available in the project plan (Ferrill and Stirewalt, 1995).

The material presented in this chapter primarily addresses the following KTUs: (i) uncertainty in determining three-dimensional (3D) structure and tectonic setting of YM and (ii) uncertainty in determining the slip history of faults.

6.2 SIGNIFICANT TECHNICAL ACCOMPLISHMENTS

Significant technical accomplishments by the Tectonics Research Project prior to the present reporting period include: (i) development of digital terrain models of the YM and central Basin and Range regions; (ii) production of integrated maps of Quaternary faults, Quaternary basaltic volcanic fields, historic earthquake seismicity, and *in situ* stress data for the central Basin and Range region using the Tectonics Geographic Information System; (iii) compilation of an initial database of geodetically measured regional strain and geologically determined slip rates for individual fault systems in the central Basin and Range region; (iv) evaluation of historic earthquakes in southern California and Nevada with emphasis on the relationships between earthquakes and mapped faults, temporal and spatial clustering of earthquakes, and the 1992 Landers earthquake sequence in the southern Mojave desert; (v) sampling at Bare Mountain, Nevada, for fission track analyses; (vi) field reconnaissance in the Black Mountains, California; (vii) participation in the Nuclear Regulatory Commission/CalTech YM/Death Valley Global Positioning System Survey; (viii) research, in collaboration with the Regional Hydrology Research Project, on the effects of *in situ* stress on transmissivity and regional groundwater flow in the YM and Death Valley region; (ix) development of an interactive computer program to analyze slip tendency and dilation tendency for mapped faults and fractures; (x) analyses of slip tendency of existing fault sets (including YM faults) to evaluate potential for slip in a contemporary stress state; (xi) analyses of dilation tendency for faults and fractures, to investigate potential for magma channeling by faults and extension fractures and to evaluate potential effects of *in situ* stress on transmissivity and regional groundwater flow; (xii) field research on fault and dike interaction along the Mesa Butte Fault in the San Francisco Volcanic Field, Arizona; (xiii) sampling at Bare Mountain, Nevada, for paleomagnetic and microstructural analyses; and (xiv) collaborative research, with Volcanism Research, to develop a volcanic hazard map of the YM area that combines volcanic probability models and dilation tendency analysis of YM area faults.

Significant accomplishments during the present reporting period include: (i) collection and analysis of data to constrain horizontal axis rotation of Bare Mountain; (ii) generation of a partially restorable cross section through Bare Mountain; (iii) construction of a partially restorable, subregional cross section that extends from the Bullfrog Hills across Bare Mountain, Crater Flat, YM, Jackass Flat, and Little Skull Mountain; (iv) development of alternative models for the subsurface linkage between the Bare Mountain Fault (BMF) and the YM and Crater Flat Faults; (v) preliminary paleomagnetic analyses that assist in constraining the amount and timing of rotation of Bare Mountain around a vertical axis; (vi) analysis of apatite fission-tracks to constrain the uplift history of Bare Mountain; (vii) analyses of alluvial fan sedimentation patterns on the east and west sides of Bare Mountain that constrain the relative amounts and timing of motion on the BMF; (viii) field work to evaluate key structural elements that are used to constrain the regional tectonic setting of YM; (ix) construction of a structural analog deformation laboratory; (x) submittal of an article on slip-tendency analysis and fault reactivation to be considered for publication in *Geology*; (xi) submittal of an article that compares two calcite-twin based differential stress estimation techniques to be considered for publication in the *Journal of Structural Geology*; and (xii) submittal of a copyright application for the 3DSTRESS computer program, with which slip- and dilation-tendency analyses are performed. The first five items in the above list are the primary focus of this chapter.

6.2.1 Tectonic Setting and Significance of Bare Mountain

Bare Mountain, Nevada, is approximately 16.5 km west of the proposed site of the high-level nuclear waste (HLW) repository at YM (Figure 6-1). It consists of a folded, faulted, tilted, and uplifted sequence of rocks that range in age from late Proterozoic through Devonian and possibly Mississippian with few unconformities. This block of Precambrian to Paleozoic rocks forms the footwall of two fault systems that are important to the YMR: (i) The Bullfrog Hills Detachment System (BHDS), and (ii) the Bare Mountain Fault. The Fluorspar Canyon Fault, which bounds Bare Mountain on its northern end, is part of the BHDS, west-directed (top to the west) extensional detachment system (Figure 6-2). The BHDS was active during the Miocene (13–7.5 Ma) and accommodated as much as 275-percent extension of the Tertiary volcanic sequence within the Bullfrog Hills to the northwest of Bare Mountain (Hamilton, 1988; Carr and Monsen, 1988; Scott, 1990; Maldonado, 1990). The BMF, which defines the eastern boundary of Bare Mountain, is an east-directed (top to the east) normal fault with approximately 2 km of throw that may have been active during the Holocene (Snyder and Carr, 1984; Swadley et al., 1984; Reheis, 1986). The proximity of the recently active BMF to the site of the proposed HLW repository gives rise to the following three uncertainties: (i) the potential seismic hazard of the BMF; (ii) the potential for triggered deformation on the west-directed normal faults of the YM area resulting from slip on the BMF (seismic or otherwise); and (iii) the role of steep faults in providing conduits for magma ascent from deep crustal levels. In order to address these uncertainties, it is necessary to understand the genesis of the BMF, determine the history of slip on the BMF, and generate realistic models of linkage (or non-linkage) between the BMF and faults to the east.

Although it is predominantly of low metamorphic grade and has no highly mylonitised carapace, Bare Mountain is considered to be a form of metamorphic core complex (e.g., Burchfiel et al., 1992). It probably owes its current high elevation to tectonic removal of the overlying Tertiary volcanic sequence and some thickness of the Paleozoic section during the Miocene (Hamilton, 1988; Scott, 1990). This extension was accomplished as Bare Mountain became involved in the extreme extension of the Death Valley region during the last 36 m.y. (Snow, 1994).

4094932 m

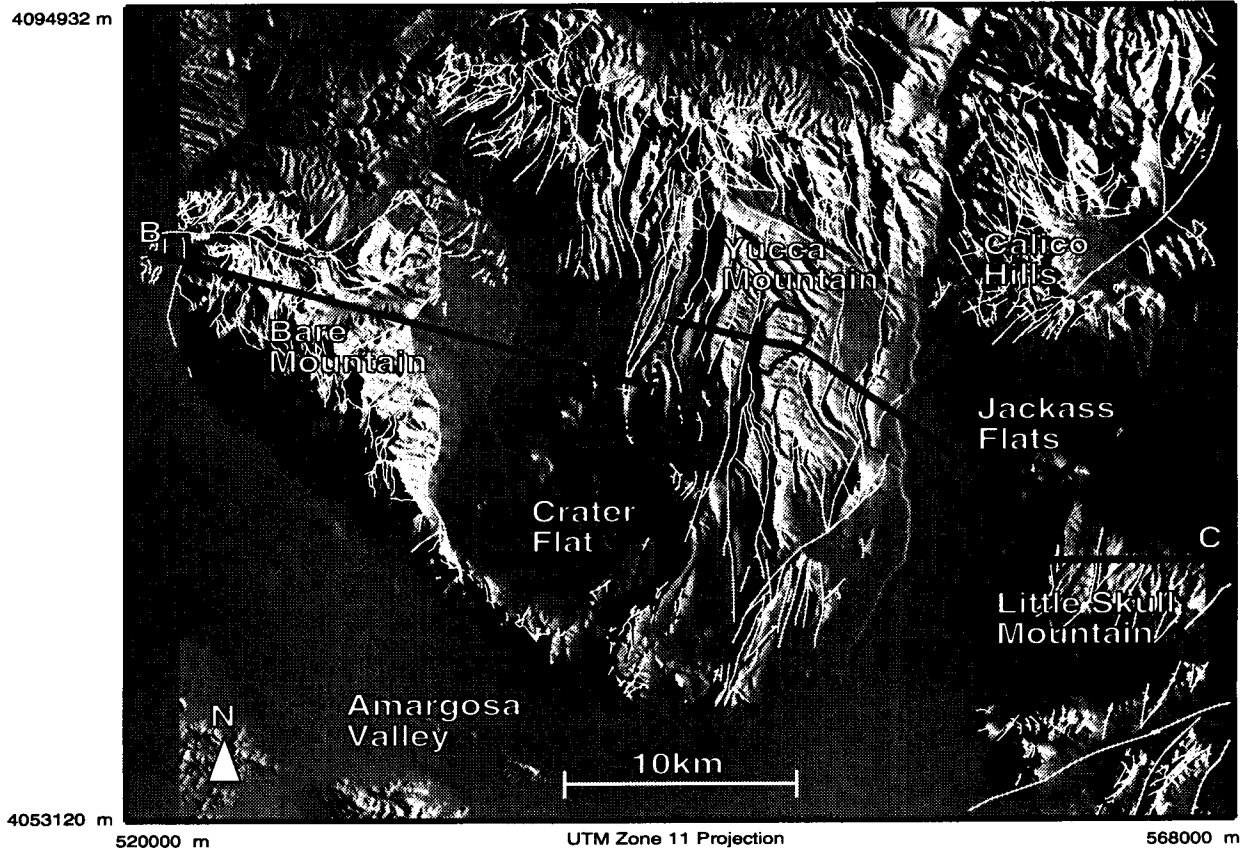


Figure 6-1. Digital elevation map of Bare Mountain, Nevada, and surrounding region. The line of the subregional cross section (Figure 6-3) is shown. Map coordinates are Universal Transverse Mercator.

Two end-member models of fault linkage between Bare Mountain and YM are possible [Figure 6-3(a) and 6-3(b)]. The first model [Figure 6-3(a)], based on conceptual models of Scott (1990) and Hamilton (1988) and quantitative modeling of Young et al. (1993), assumes that the faults of YM developed as part of the BHDS during the Miocene and were subsequently isolated by the rise of the Bare Mountain block (e.g., Scott, 1990). YM faults are considered to have formed during mid-late Miocene as a little extended (12 to 20 percent in YM compared with 275 percent in the Bullfrog Hills) “headwall” portion of the Bullfrog Hills-Fluorspar Canyon detachment system. Subsequent motion on the Bare Mountain Fault, cutting to greater crustal depths, truncated the older west-directed detachment system. The depths to detachment are modeled using the regional geometry of the Paintbrush Tuff and assuming vertical shear as the hangingwall deformation mechanism (see e.g., Young et al., 1993). The greater depth to detachment of the Bare Mountain Fault compared with the YM faults is geometrically required by the rollover within the Crater Flat graben, which is constrained by geophysical and geological data (Snyder and Carr, 1984; Faulds et al., 1994). The second model [Figure 6-3(b)] assumes that the east-directed BMF system generated the YM faults as antithetic faults in its hangingwall after conceptual models (Carr and Mosen, 1988; and Gilmore, 1992). In this second model, YM faults are considered to have formed to accommodate hangingwall deformation required by movement on the Bare Mountain Fault. YM faults can be modeled to these depths by increasing the dips of the near-surface segments of the faults from about 70° to 80–85°. This procedure can be justified on the grounds that few major faults are exposed in

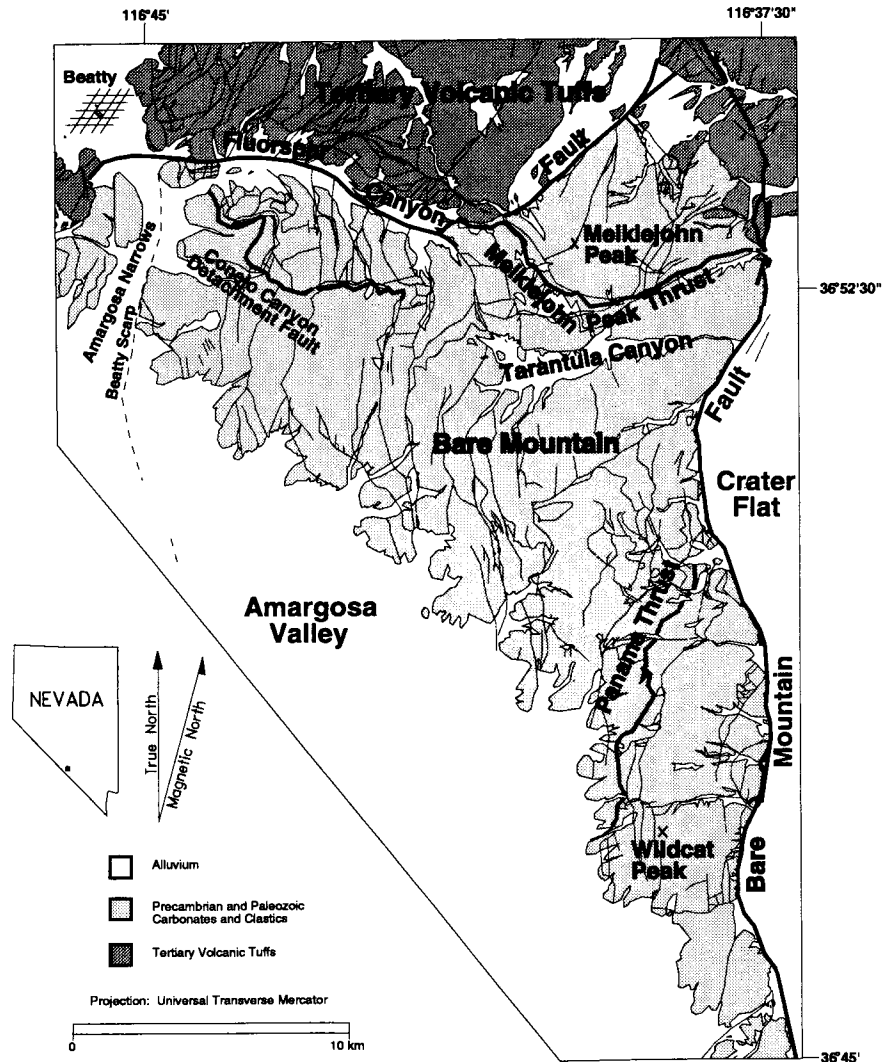


Figure 6-2. Bare Mountain, Nevada, physiography and important features referred to in the text

bedrock at the surface, and there is considerable uncertainty as to the dips of many of the YM faults. Hybrids of these two end members are also permissible. For example, YM faults may have originated as part of the BHDS, but may continue to accumulate slip because they are optimally oriented to accommodate antithetic shear in the hangingwall of the more recently active BMF. Knowledge of the precise nature of the linkage between the BMF and faults in its hangingwall is critical to assessing seismic and aseismic slip risks posed by the faults of YM. A combination of geometric and finite-element modeling has been undertaken to determine the viability of the range of potential models for the tectonic development of Bare Mountain (e.g., Ofoegbu and Ferrill, 1995).

The BMF may penetrate the entire thickness of the seismic crust to depths exceeding 15 km (9 mi) or it may sole into a subhorizontal detachment at shallower crustal levels (7 km, 4 mi) (Gilmore, 1992; Scott, 1990). In either case, if it is still active, then it is likely to be a source of earthquake activity. Any slip on it may be translated into dependent slip on the faults of the YM area regardless of whether these latter faults originated as part of the BHDS or as later antithetic faults to accommodate deformation of the BMF hangingwall.

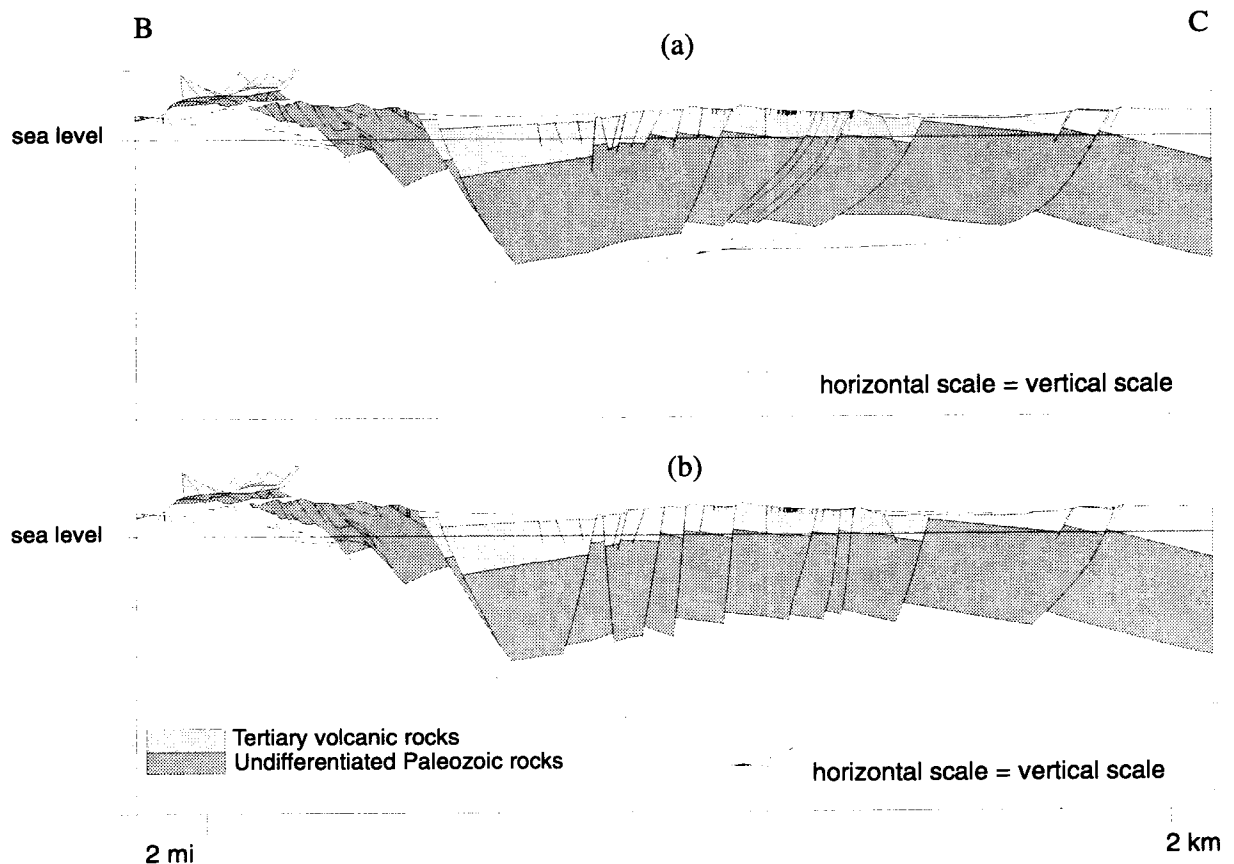


Figure 6-3. Semi-restorable cross sections through Bare Mountain and YM from B to C (Figure 6-1) illustrating two alternative interpretations of the deep BMF-YM fault system

6.2.2 Stratigraphy of Bare Mountain

Bare Mountain exposes a 7.4-km (4.6-mi) thick section of pre-Tertiary sedimentary rocks with minor igneous intrusions (Monsen et al., 1992) (Figures 6-4 and 6-5). The upper Proterozoic to lower Paleozoic rocks of Bare Mountain were deposited on the western margin of the North American craton (e.g., Poole et al., 1992; Burchfiel et al., 1992). They represent the more cratonward (eastern) facies of the Cordilleran miogeocline and can be divided into three tectono-stratigraphic groups. The lower part of the sequence, from upper Proterozoic (about 600 Ma) to lower middle Cambrian, is dominated by clastic sediments, quartzites, and argillites, that were shed westward from the rift-related thermal bulge on the craton (Burchfiel et al., 1992; Poole et al., 1992). They represent sediment accumulation after initial rifting of the Cordilleran margin. The middle part of the sequence is composed mainly of middle Cambrian through Devonian carbonates that represent the shallow continental shelf environment, which evolved as the continental margin subsided and as the source of terrigenous sediment was depleted. The upper part of the sequence consists of upper Devonian-Mississippian clastics (argillites, chert-pebble conglomerates, and detrital limestones) that accumulated in a foredeep basin. Sediment source was to the west from highlands formed by the collision of an island arc with the western edge of the miogeocline during the late Devonian-Mississippian Antler orogeny.

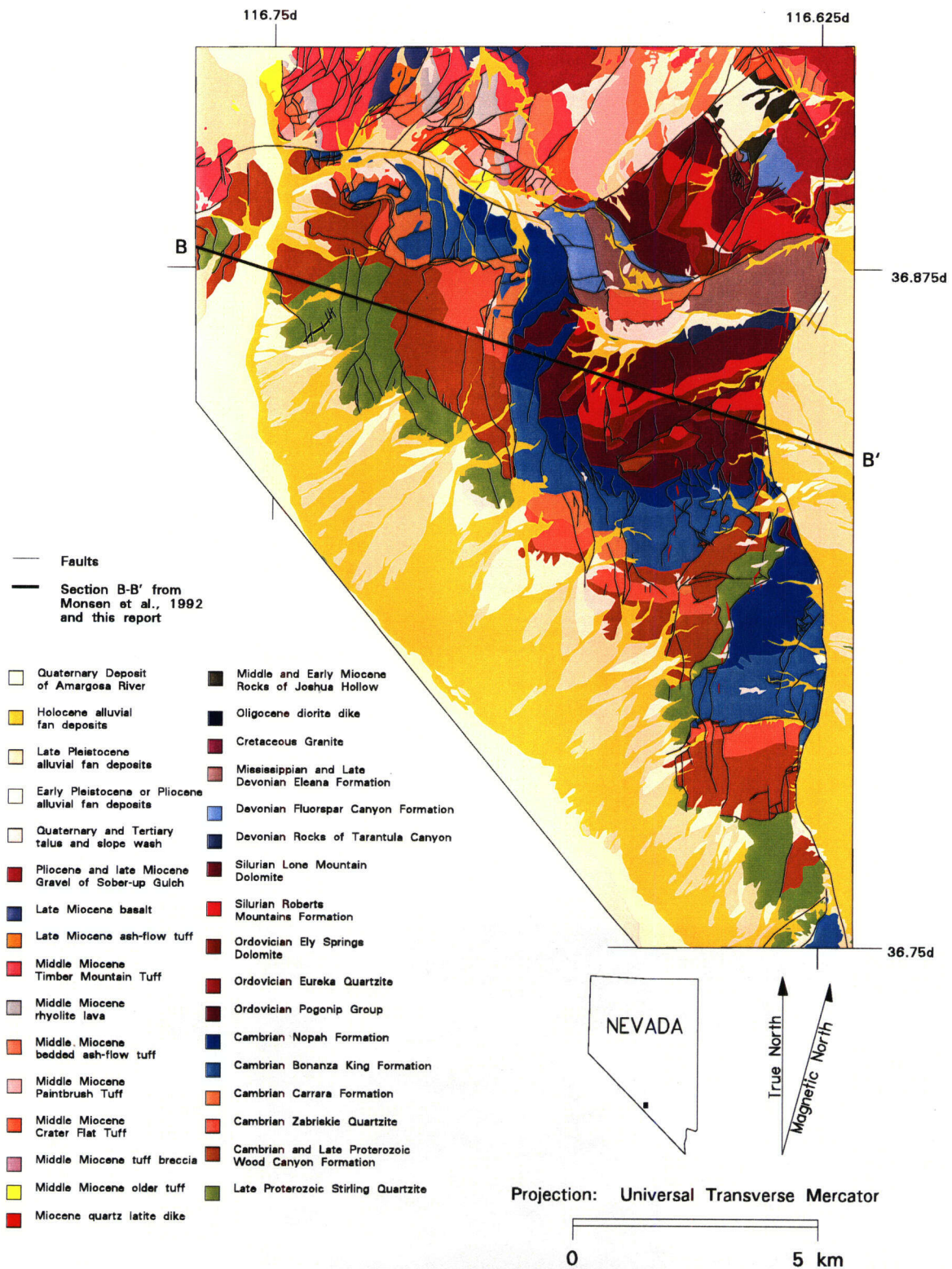


Figure 6-4. Geological map of Bare Mountain (after Mosen et al., 1992) showing the line of section B-B'

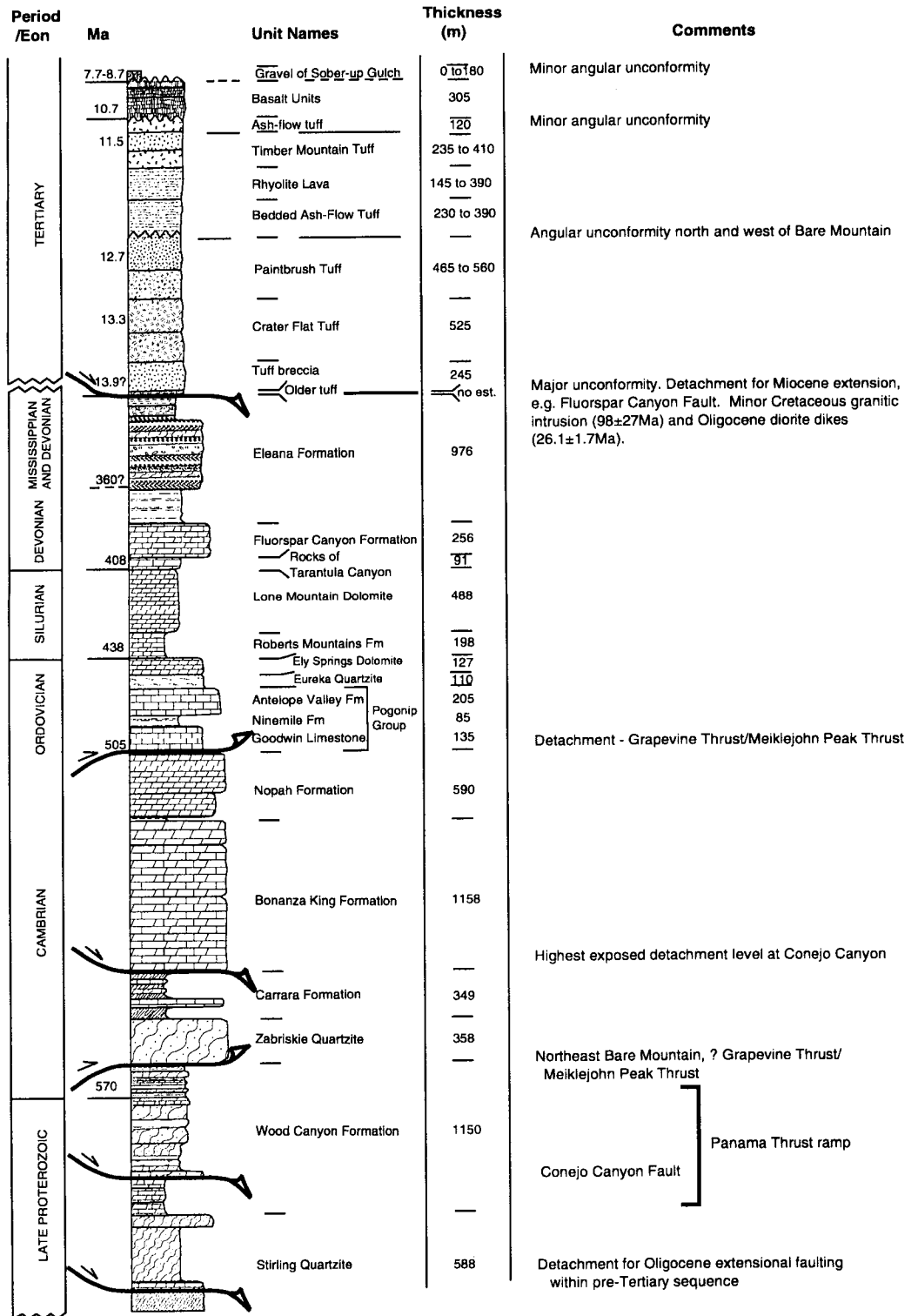


Figure 6-5. Stratigraphic section of Bare Mountain (after Mosen et al., 1992; Sawyer et al., 1994), with interpretations of weathering profile and compressional and extensional detachments

With the exception of a small Cretaceous (98 ± 27 Ma; from Monsen et al., 1992) granitic intrusion, there is a major hiatus in sedimentation and igneous activity at Bare Mountain between the Mississippian and the Oligocene, when a number of north-northeast trending, subvertical diorite dikes were emplaced. Following this emplacement, in the Early and Middle Miocene (15–11.45 Ma, Sawyer et al., 1994), and roughly coeval with the onset of extreme regional extension, was the eruption of a variety of pyroclastic rocks and minor rhyolitic lava flows. Toward the top of this 1,400–1,900 m thick sequence are minor basaltic flow units. Within the post-Oligocene volcanic sequence are two angular unconformities representing significant fault movement at about 11.6–11.4 Ma and later than 10.7 Ma (Frizzell and Shulters, 1990; Monsen et al., 1992; Sawyer et al., 1994).

6.2.3 Structure of Bare Mountain

Bare Mountain is a roughly triangular inlier of Late Proterozoic to Paleozoic rocks bounded on the west by Quaternary alluvial cover, on the east by the BMF and Quaternary alluvial cover, and on the north by the Fluorspar Canyon Fault, a west-directed Miocene extensional fault system carrying Miocene volcanic rocks over the inlier (Figure 6-2).

The pre-Tertiary sequence is part of the miogeoclinal wedge of the North American craton and lies at the margin between the hinterland and the frontal thrust zone of the Mesozoic fold-thrust belt of the Cordillera near its southernmost limit. Lying toward the east of the miogeoclinal wedge, Bare Mountain records only the stratigraphic effects of the Devonian-Mississippian Antler orogeny, in the form of the clastic Eleana Formation. Pre-Late Cretaceous fold-thrust structures are preserved in the form of the south-vergent Meiklejohn Peak Thrust (“Grapevine Thrust,” Miller et al., 1992) and the north-vergent Panama Thrust and associated folds (Zhang and Schweickert, 1991). Timing of the contractional event(s) that generated these structures is contentious; they are assigned either to the Permian (Snow, 1992; Snow and Wernicke, 1993) or to the Late Jurassic-Late Cretaceous Sevier orogeny (e.g., Miller et al., 1992; Stone and Stevens, 1993).

The onset of Cenozoic extension at Bare Mountain is manifested by a series of east-dipping normal faults, inferred by Monsen et al. (1992) to have been active or reactivated (Carr and Monsen, 1988) in the mid-Miocene, that cut the Late Proterozoic to Paleozoic rocks of the inlier exclusively. Figure 6-6 illustrates the structure of Bare Mountain projected onto a plane normal to the plunge of the mountain. The east-dipping normal fault system appears in Figure 6-6 as a listric fan of normal faults in which individual faults have displacements of hundreds of m to >2 km. This listric fan appears to be cut by an east-dipping normal fault, with more than 3 km displacement, that placed the Cambrian Ordovician carbonate sequence against the Late Proterozoic-Cambrian clastic sequence. Two complex detachment systems, one carrying a dismembered sequence of uppermost Late Proterozoic to lowermost Paleozoic rocks [the Conejo Canyon-Wildcat Peak detachment of Zhang and Schweickert (1991)] and the other carrying the Tertiary volcanic sequence (BHDS), are also exposed. Detachment faults have been mapped within the pre-Tertiary sequence in the Conejo Canyon and Wildcat Peak areas of Bare Mountain. These faults have been interpreted by Zhang and Schweickert (1991) to be part of a once continuous fault system, although there is no clear evidence for this correlation. The Conejo Canyon-Wildcat Peak detachment (CCWPD) is inferred by Zhang and Schweickert (1991) to be pre-Miocene in age; however, field relationships (Monsen et al., 1992) indicate that the CCWPD cuts the east-dipping normal fault set inferred by them to have been active in the mid-Miocene (see also Carr and Monsen, 1988). Zhang and Schweickert (1991) interpret the CCWPD as having a top to the south sense of displacement.

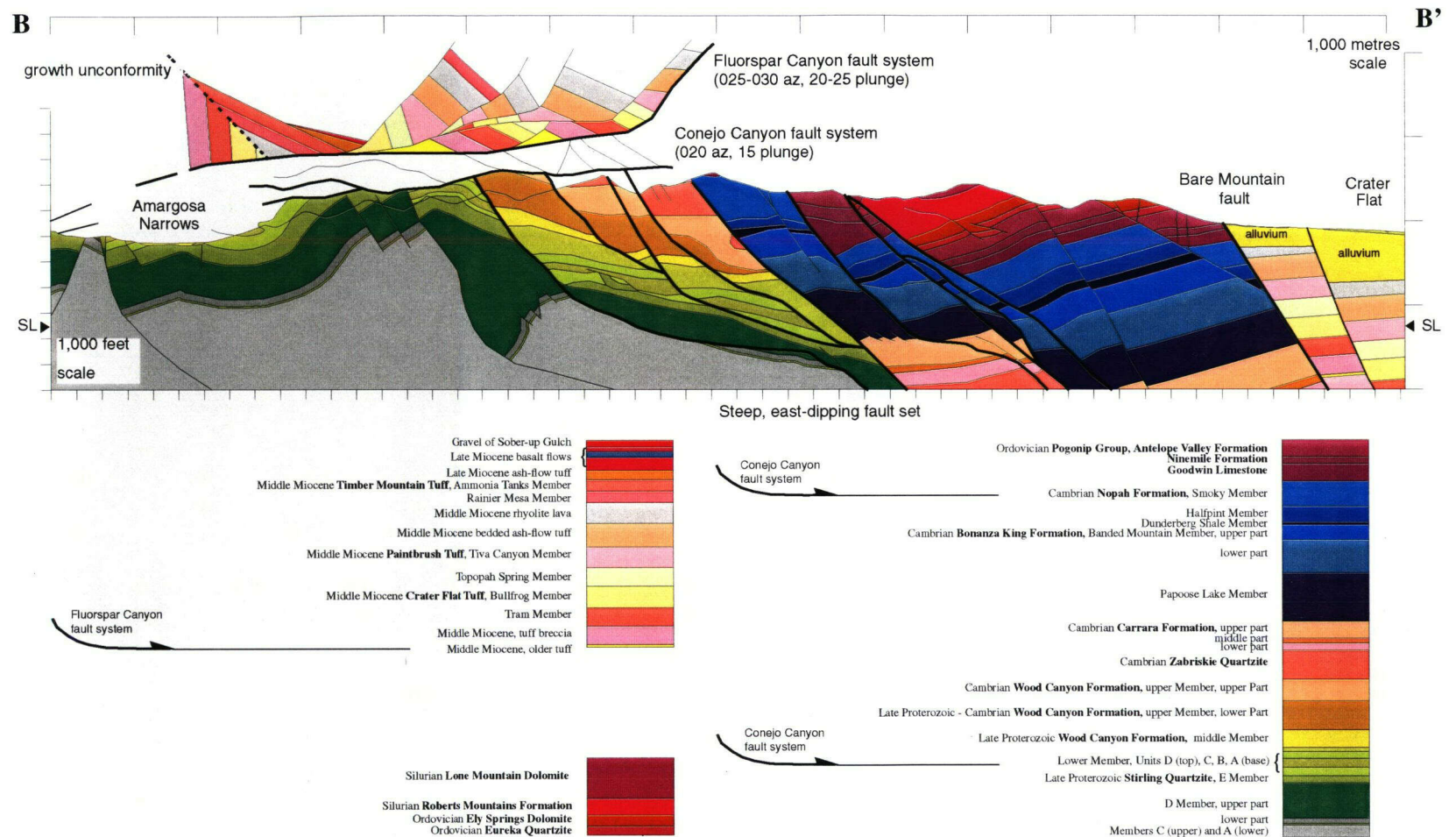


Figure 6-6. Plunge-perpendicular cross section of Bare Mountain along section line BB' (Figure 6-4, after Monsen et al., 1992). The pole to the cross section plane is 030° azimuth, 30° plunge, which is approximately the plunge of the predominant extensional fault system within the pre-Tertiary sequence (see text for discussion of the steeply east-dipping fault system). Pre-Tertiary structures are projected along the pole to the cross-section plane. The Conejo Canyon detachment system was projected along 020° azimuth, 15° plunge, and the hangingwall of the Flourspar Canyon Fault was projected along 025-030° azimuth, 20-25° plunge. Details of the structure within the Conejo Canyon system are not well represented by this cross-section plane because they strike east-west.

The Fluorspar Canyon Fault at the north end of Bare Mountain carried mid-Miocene volcanic rocks over the pre-Tertiary sequence. Although the Fluorspar Canyon Fault cannot be mapped continuously to the Bullfrog Hills, it likely connects with the BHDS to the west (Hamilton, 1988; Maldonado, 1990; Scott, 1990). There is broad agreement on the Miocene age and top to the west-northwest sense of displacement of the BHDS. Eastward tilting (40 to 70°) of the older Miocene volcanic rocks occurred as a result of movement on the Fluorspar Canyon and related faults (around an approximately north-northeast horizontal axis) (Figure 6-6). Most authors consider movement on the BHDS to have been the probable cause of the tectonic denudation of Bare Mountain and the subsequent rise of the Bare Mountain block (e.g. Hamilton, 1988; Scott, 1990).

Following Miocene faulting, but with unknown time of initiation, shallow, east-dipping normal faults displaced parts of the pre-Tertiary mountain core. One of these faults is also expressed in early Pleistocene and or Pliocene alluvial fan material on the east side of Bare Mountain (Monsen et al., 1992). The BMF, which marks the eastern edge of the mountain block may have more than 2 km of vertical displacement (Snyder and Carr, 1984). Based on the occurrence of megabreccia of Paleozoic rock between the 12.7-Ma Tiva Canyon Member and the 11.6-Ma Rainier Mesa Member, it has been inferred that the BMF was active prior to 11.6 Ma, which exposed Bare Mountain and produced a source for the megabreccia (Carr and Parrish, 1985; Faulds et al., 1994). The BMF may be a buttress unconformity between younger tuffs deposited in Crater Flat and the pre-Tertiary rocks of Bare Mountain. The most recent slip on the BMF is interpreted by Reheis (1986) to have been during the Holocene. However, Klinger and Anderson (1994) interpreted that the most recent slip on the BMF was >100 Ka based upon alluvial fan morphology.

6.2.4 Salient Points and Problems in the Tectonic History of Bare Mountain

- (i) Whatever the age of the pre-Tertiary contractional deformation, the north-vergent Panama fold-thrust system is used as a basis for regional correlations in palinspastic reconstructions of Bare Mountain and adjacent mountain ranges (Snow and Wernicke, 1989; Caskey and Schweickert, 1992; Snow and Prave, 1994; Snow, 1994). The Panama fold-thrust system (which is bounded to the north by the Panama Thrust, the southern boundary of domain XI) is correlated with the White Top Mountain backfold and the Winters Peak anticline, (e.g., Snow, 1994) both west-vergent structures in a generally east-vergent fold-thrust belt. The current east-west trend and northward vergence of the Panama structure (Figure 6-7, domains XIII, XIV, XV) are used to constrain a 90° clockwise rotation of Bare Mountain within the last 30 m.y., as the Death Valley region experienced extreme extension. Structural correlation of the Panama Thrust with the Striped Hills anticline in the Striped Hills (southeast of YM) has been used to infer > 20 km right-lateral strike slip along a fault that extends from Crater Flat to the south-southeast of the Stewart Valley-Stateline Fault Zone (Caskey and Schweickert, 1992).
- (ii) The east-dipping fault set described by Monsen et al. (1992) and inferred by them to be mid-Miocene (14 Ma) or older in age is truncated by the CCWPD, which Zhang and Schweickert (1991) consider to be pre-Miocene (Carr and Monsen, 1988). Zhang and Schweickert (1991) also interpret the CCWPD as a southward-directed (top to the south) system. We favor a pre- to early-Miocene age for the east-dipping fault set because it is clearly truncated by the Conejo Canyon Fault (CCF) of the CCWPD and nowhere cuts Miocene volcanic rocks. The east-dipping fault set is best exposed in the central portion

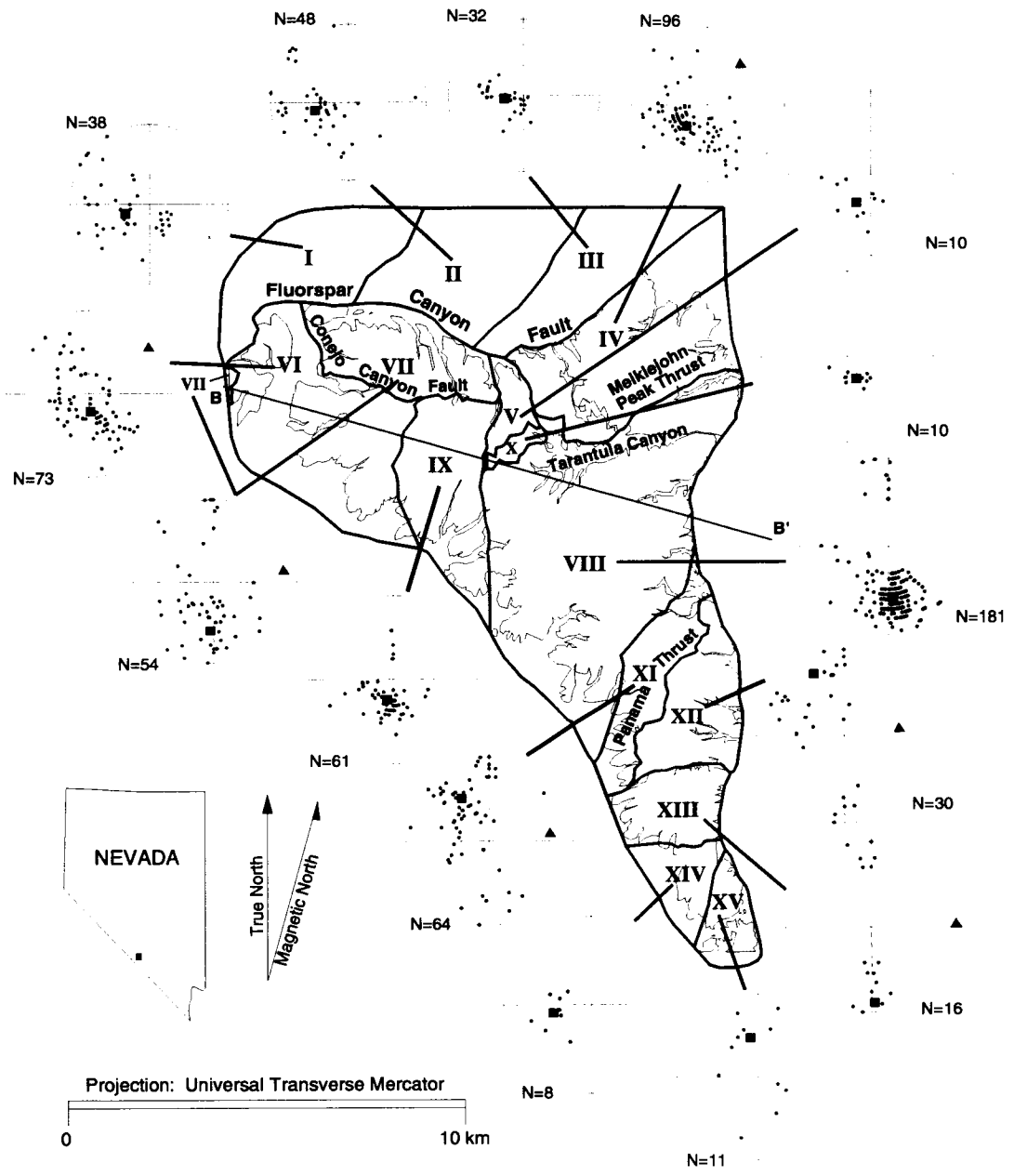


Figure 6-7. Structural domain map of Bare Mountain based on data in Monsen et al. (1992). Domain boundaries are drawn primarily on the basis of major faults. Lower hemisphere, equal-area projections are plotted for poles to bedding for each domain, and superimposed on these projections are the mean pole orientations (maximum eigenvector of distribution, filled squares). Also plotted for domains where meso- to macro-scopic folds occur are best-fit great-circles to the poles (dashed lines), and the pole to the best fit great-circle (minimum eigenvector of the distribution, filled triangles), which represents the average fold axis for that domain (Fisher, 1953; Woodcock, 1977; Ramsay, 1967).

of the mountain (Figure 6-7, domains VIII and IX), but may be responsible for the overall outcrop pattern of the mountain. The broad structure of the pre-Tertiary core of Bare Mountain is that of a north-dipping homocline. In Tarantula Canyon, a large anticline in the Ordovician Antelope Valley Formation plunges 30° to the northeast (Figure 6-7, domain IV). Folds in domain VI share this plunge direction (Figure 6-7). Cutoff lines of bedding against the east-dipping fault set plunge 25–35° to the northeast, and branch lines of intersecting faults in this set plunge generally 30° to the northeast. These orientation data indicate that the east-dipping fault set developed as northeasterly trending (in present-day coordinates), down-to-the-east normal faults in a subhorizontal sequence, and has since acquired a northeasterly plunge. These faults actually form a listric fan with substantial overall displacement, and probably sole into an east-directed detachment that has now been disrupted by the BMF (Figures 6-3 and 6-6). The age of this faulting is problematic. Carr and Monsen (1988) regard them as old, but reactivated during the Miocene. Preliminary paleomagnetic results (see Section 6.2.5.4) indicate that the postfaulting plunge predates the magnetization of Oligocene dikes exposed at Bare Mountain, but may postdate Permian remagnetization of the Paleozoic carbonates.

- (iii) The sense of displacement inferred for the CCWPD by Zhang and Schweickert (1991) is open to question. Late Proterozoic rocks between the CCF and the Fluorspar Canyon section of the BHDS have steep north-northeastward dips (Figure 6-7, domain VII), and rocks below the CCF have similar but shallower dips (Figure 6-7, domains VI and IX). It is possible to derive the dips of the rocks in domain VII above the CCF by clockwise (looking west) rotation about an east-west trending axis from rocks of domains VI and IX. This observation is consistent with a south-directed (top to the south) detachment as suggested by Zhang and Schweickert (1991). However, the CCF can be projected across Amargosa Narrows and connected with the Lower Detachment of Maldonado (1990). In this interpretation, the CCF of the CCWPD represents part of the BHDS (of which the Fluorspar Canyon Fault is a part), which cut deeper into the crust than the base of the Tertiary volcanic sequence. Thus, the CCF and Fluorspar Canyon Fault can be considered as part (possibly the bounding faults) of an anastomosing set of extensional detachments that stripped pre-Tertiary miogeoclinal sequence and the Tertiary volcanic package westward (Figure 6-6), which is in general agreement with the regional interpretation of Scott (1990). Monsen (1983), however, demonstrates that the low angle faults of Conejo Canyon do not represent discontinuities in either metamorphic grade or structural history, and tentatively suggests top to the east displacements.

The question of sense of displacement on the CCWPD is of importance to the interpretation of the tectonic evolution of YM. If the faults at YM developed as a part of the Bare Mountain detachment system that experienced only incipient extension during the Miocene (e.g., Hamilton, 1988), they probably sole into subhorizontal detachments at or below the base Tertiary unconformity (Scott, 1990; Young et al., 1993). If the CCF and associated faults are part of the west-directed (top to the west) Miocene detachment system, they represent the only well exposed example of this deep detachment, and their characteristics may provide insight into the crustal levels at which this system developed.

- (iv) Low-angle, down to the east normal faults occur on the eastern side of Bare Mountain and either merge with or are cut by the steeply (60–70°) east-dipping BMF (Carr and Monsen, 1988). One of these shallow faults cuts older Quaternary alluvium on the north side of the

entrance to Chuckwalla Canyon (Carr and Mosen, 1988). Slip on the BMF is documented for the period 270,000–9,000 yr ago (Swadley et al., 1984), but questions about the initiation of the BMF, its current activity, and how it is linked to the faults of YM remain unresolved.

6.2.5 Vertical Axis Rotation of Bare Mountain

6.2.5.1 Background

Paleomagnetic techniques are applicable to tectonic problems, particularly in mobile belts with complex displacement histories, because, among other constraints on deformation, paleomagnetism provides both absolute and relative estimates of vertical-axis rotations. The technique utilizes the earth's magnetic field as a reference frame, which, when averaged over 2,000 to 5,000 yr (the averaged secular field), is essentially that of a geocentric axial dipole. Field lines of this dipole originate from the geographic south pole and re-enter at the geographic north pole (or vice versa) depending on the polarity of the field (normal or reversed). This magnetic reference frame is described by two angles between the magnetic field lines and the earth's latitude and longitude reference frame, declination and inclination. Declination is the horizontal projection of the field lines relative to the north and south poles. Inclination is the vertical projection relative to the earth's surface. Values of declination range from 0 to 360° measured clockwise (positive) from north. Inclination values range from –90 to 90° (negative up and positive down). On the surface of the earth, declination points either north (0°) or south (180°) depending on the polarity of the earth's magnetic field. Inclination is related to latitude through the dipole equation:

$$\tan(I) = 2 \times \tan(\lambda) \quad (6-1)$$

where I is the inclination and λ is the latitude. The sign of λ changes, depending on polarity.

Most rocks contain a fraction of magnetic minerals (magnetite and hematite are the most common) that records information on the intensity, polarity, and orientation of the earth's geomagnetic field through geologic time. The record of reversals of the earth's magnetic field as recorded by the striped pattern of ocean magnetic anomalies is the best known example. For igneous rocks, the magnetic minerals acquire a thermo-remanent magnetization as they cool through their Curie temperature. For the two most common magnetic minerals, magnetite and hematite, the Curie temperatures are 580 and 696 °C, respectively (Merrill and McElhinny, 1983). Sedimentary rocks acquire a detrital remanent magnetization by alignment of the magnetic minerals parallel to the magnetic field during sedimentation. Rocks can also acquire a chemical remanent magnetization (CRM) by authigenic growth of magnetic minerals during diagenesis.

Remanent magnetizations are vectors, and as long as they remain fixed with respect to the rock, any translation or rotation of the rock will result in an equivalent translation or rotation of the magnetic vector. Because most rocks preserve remanent magnetizations that can be measured in the laboratory, remanent magnetizations provide a quantifiable measurement of these movements. In the case of vertical axis rotations, the angular difference between the remanent magnetization of the rock in question and that of a known reference direction (e.g., true north or that of another rock) yields the amount and sense of absolute (relative) rotation.

Difficulties in paleomagnetism arise because diagenesis or geothermal activity significantly younger than the rock often produce magnetic phases that partially or completely overprint the original (primary) magnetization. In such cases, the measured natural remanent magnetization (NRM) is the vector sum of the constituent magnetic components. Isolating single components of known geologic age requires demagnetization techniques that can decompose the composite signal. These demagnetization techniques take advantage of differences in the magnetic properties of the various magnetic phases. For example, if the secondary and primary magnetizations are carried by magnetic mineral phases with different unblocking-temperature spectra, then progressive thermal demagnetization and measurement can be employed to isolate them from the composite NRM. As is often the case, the vector removed at the lower unblocking temperatures is the secondary magnetization, while the vector removed at the higher unblocking temperatures is the characteristic (and maybe primary) magnetization. Standard practice is to use vector endpoint diagrams (Zijderveld, 1967) to graphically display the demagnetization results. Individual components are determined numerically from principal component analysis of linear portions of the demagnetization trajectories (Kirschvink, 1980).

Paleomagnetic data can be evaluated in one of two coordinate systems. In a directional coordinate system, the reference field and paleomagnetic vectors are represented by the two angles of declination and inclination described above. Directions are specific to the site location, and any reference directions used for comparisons need to be transformed via the site coordinates using the full dipole formula (see Butler, 1992, p 157–159).

Alternatively, remanence directions can be converted to their corresponding geomagnetic poles (the position of the magnetic pole indicated by the remanence direction, holding the site fixed). This system is the basis for the construction of *apparent polar wander* (APW) paths and their use in the description of plate motions through geologic time. The wander is *apparent* because it displays motion of the north or south magnetic pole relative to a fixed set of lithospheric plates, opposite to the theory of continental drift. The advantage in using APW paths is that large amounts of paleomagnetic data can be presented in a simple diagram (in contrast to a cumbersome set of paleogeographic maps). Because we are using the paleomagnetic data at Bare Mountain to constrain tectonic and structural problems specific to the YMR, data in this report will be presented in directional space. We simply point out the alternatives of APW and geomagnetic poles because they are often confused with paleomagnetic directions.

6.2.5.2 Uncertainties

There are four fundamental sources of uncertainty associated with paleomagnetic measurements, (i) sample orientation errors, including uncertainties in structural corrections; (ii) fidelity of the signal; (iii) unaveraged secular variation (i.e., that individual samples do not fully record enough geologic time to adequately average the instantaneous geomagnetic field to be coincident with the geocentric dipole); and (iv) age of the magnetization.

In general, igneous rocks tend to provide highly precise records of the magnetic field, but are limited by orientation errors (especially in nonbedded plutonic rocks that may have tilted since emplacement). In addition, igneous rock may not always incorporate enough geologic time to average secular variations (an advantage if details of the secular field are being studied). In contrast, sedimentary rocks tend to have weaker and less well recorded magnetizations, but are easily oriented within an external reference frame, for example, sedimentary bedding. Because they tend to incorporate a larger span of geologic time, secular variation is more easily averaged in sedimentary rocks, sometimes even within a

single paleomagnetic sample. In both igneous and sedimentary rocks, the age of magnetization must also be established because of the possibility that younger CRMs completely mask the primary magnetization.

Sampling strategies for paleomagnetic studies are designed to mitigate these uncertainties. In general, samples are collected and resultant magnetizations averaged in an hierarchical fashion; n samples per site and N sites per geologic unit studied. The proper choices of n and N depend on the specific limitations of the rock type, as outlined above. Such sampling schemes also provide statistical estimates of precision and error. Paleomagnetism employs a form of spherical statistical analysis (Fisher, 1953) analogous to Gaussian statistics for planar coordinate systems. The two most common of these Fisher statistics are the precision parameter, k (an estimate of the true precision K ; larger k means increased precision), and the semiangle of the cone of 95 percent confidence about the mean direction, α_{95} (analogous to two standard errors about the mean in a Gaussian normal distribution). In pole space, these are written as K and A_{95} . In addition, paleomagnetic field tests have been developed to constrain the timing of magnetization relative to other geologic phenomena (e.g., folding, conglomerate deposition, and igneous intrusion).

In folded terrains, the age of the magnetization can be compared to the age of folding by examining the change in the distribution of remanent directions as the tilted rocks are restored to paleohorizontal. The underlying assumption is that the remanent directions on differently dipping limbs of folds best cluster at the point of unfolding that corresponds to the time the rocks acquired their magnetization. The three general categories of fold test results are before folding (prefolding), after folding (postfolding), or during folding (synfolding).

Conglomerate tests check whether rocks have been remagnetized by the scatter of the remanence directions of the clasts relative to those in the matrix. If the conglomerate has been remagnetized after deposition, then both clasts and matrix should have similar, well-grouped remanence directions. On the other hand, if the magnetization in the conglomerate is primary, then the clasts should display a random pattern of remanence directions.

Baked contact tests look for changes in magnetization directions away from the altered zone around igneous intrusions. If the region has been remagnetized after intrusion, then all rocks, regardless of their proximity to the intrusion and even within the intrusion itself, should have similar remanent directions. Otherwise, the unaltered country rock should preserve a different (older) magnetization than the intrusion, with a mixture of magnetizations in the contact aureole. Distinguishing these magnetizations relies upon a measurable difference in the orientations of the two magnetizations.

Further age constraints, especially for Paleozoic and Mesozoic magnetizations, are derived by comparison of the inclination with a set of known reference inclinations (derived from reference APW paths).

6.2.5.3 Sampling and Experimental Methods

As part of the evaluation of the kinematic study of the 3D displacement paths for the YMR, we initiated a paleomagnetic study of several of the Paleozoic and Cenozoic rock units exposed at Bare Mountain (Figure 6-8). This distribution of rock types and ages to be sampled was selected in order to test the proposed Miocene and younger vertical-axis rotations of Bare Mountain (Snow and Prave, 1994). We sampled 11 sites in Middle Miocene quartz-latitude dikes (13.9 ± 0.2 Ma based upon a conventional

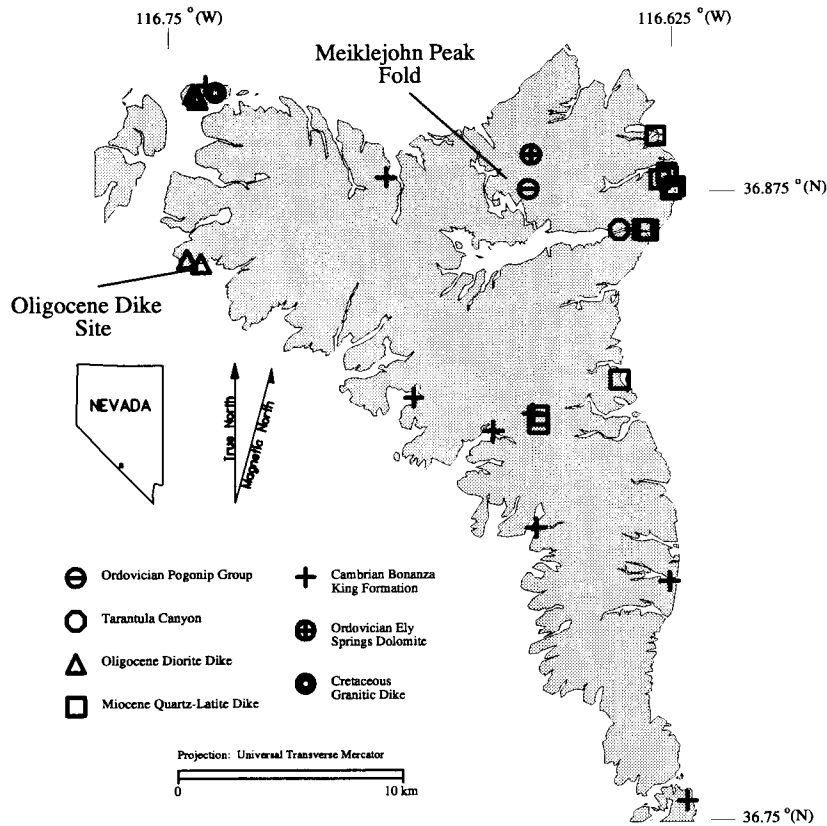


Figure 6-8. Map of Bare Mountain showing the distribution of paleomagnetic sites. The sampled Oligocene dikes at the northwesternmost corner of BM are presently unmapped.

potassium-argon age from biotite, Monsen et al., 1992), 5 sites in Oligocene diorite and mafic dikes (26.1 ± 1.7 Ma based upon a conventional potassium-argon date of hornblende, Monsen et al., 1992), 1 site in a Cretaceous granite dike intrusion (98 ± 27 Ma; U-Pb intercept age, from concordia plot, Monsen et al., 1992), and 13 sites in Paleozoic carbonates (Cambrian Bonanza King, Ordovician Pogonip Group and Ely Springs Dolomite, and Devonian Tarantula Canyon Formation) (Figure 6-8).

In this study, the timing of magnetization in the Antelope Valley Formation is constrained by a fold test. Future age constraints will be determined from fold tests, conglomerate tests, and baked contact tests. Samples were either drilled in the field with a portable diamond-coring drill or in the lab from oriented hand samples. Samples were oriented with a magnetic compass after field checks showed that the rocks were too weakly magnetized to significantly bias compass readings. Progressive thermal demagnetization was performed on all samples using an ASC thermal demagnetizer. Measurements were made on a three-axis cryogenic magnetometer housed in the magnetically shielded laboratory at the University of Michigan.

6.2.5.4 Paleomagnetic Results

For this report, we present preliminary results from one of the Oligocene diorite dikes, located in the northwestern corner of Bare Mountain and two sites on opposite limbs of a fold in the Ordovician

Antelope Valley Formation of the Pogonip Group. We wish to emphasize that these results are preliminary and that conclusions drawn from these results are primarily being used to guide our future research.

Samples from the Oligocene diorite dike exhibit strong NRM intensities between 100 and 400 mA/m. Thermal demagnetization revealed two remanence components: (i) a secondary magnetization parallel to the present earth field with unblocking temperatures up to 350 °C and (ii) a characteristic magnetization with unblocking temperatures between 350 and 580 °C [Figure 6-9(a)]. The strong NRMs and 580 °C unblocking temperature suggest that the dominant magnetic phase is magnetite.

The low-unblocking temperature component is interpreted as a present-day viscous remanent magnetization (VRM) and is not useful for constraining Bare Mountain kinematics. The characteristic directions, in *in situ* coordinates, are either north-northwest and moderately down or south-southeast and moderately up [Figure 6-9(b)]. These directions are nearly antipodal and suggest that the dike captured both normal and reversed polarity magnetizations. In addition, the two-polarity magnetization indicates that secular variation may be averaged within this single dike. The 585 °C unblocking temperature and two-polarity magnetization suggest that this magnetization is primary (i.e., Oligocene in age). Future work on the contact zone around this dike should further constrain the age of magnetization.

The mean direction for the Oligocene dike is $D=177^\circ$, $I=-56^\circ$ $n=9$, $k=15$, $\alpha_{95}=13.8^\circ$, after the north and down directions are inverted through the origin to their south and up antipodes. This mean direction [Figure 6-9(b)] overlaps with the expected Oligocene direction for southwestern Nevada of $D=172^\circ$, $I=-59^\circ$, $\alpha_{95}=5.0^\circ$ derived from the lower Tertiary reference pole for North America of Van der Voo (1990). Correction for the minor ($\sim 5^\circ$) tilting of Bare Mountain related to recent motion of the BMF moves the characteristic direction to $D=170^\circ$, $I=-57^\circ$, which is nearly coincident with the expected Oligocene direction [Figure 6-9(b)]. However, removal of the more significant northeast plunge of Bare Mountain moves the characteristic direction to $D=187^\circ$, $I=-31^\circ$, significantly away from the Oligocene reference direction [Figure 6-9(b)]. This shallower inclination is inconsistent with Oligocene or younger expected mean inclinations for North America, suggesting that the northeast plunge of Bare Mountain predates Oligocene dike emplacement. Continued work on these dikes is needed to establish clearly this timing relationship. Yet, if this timing relationship is correct, then the similarity of dike and expected directions [Figure 6-9(b)] indicates that Bare Mountain has not rotated since the Oligocene, in contrast to the 85° of Miocene or younger clockwise rotation proposed by Snow and Prave (1994).

Samples from the Antelope Valley carbonates exhibit moderate to weak NRM intensities between 1 and 10 mA/m. Similar to the Oligocene dikes, demagnetization reveals two components of magnetization: (i) a secondary magnetization parallel to the earth's present field with unblocking temperatures up to 300 °C and (ii) a characteristic magnetization with unblocking temperatures between 300 and 500 °C [Figure 6-10(a)]. In *in situ* coordinates, characteristic directions are either northwest and moderately down or southeast and moderately up on both limbs of the fold [Figure 6-10(b)]. Correction for bedding tilt associated with folding disperses the directions, suggesting that the rocks were remagnetized after folding [Figure 6-10(b)].

The weak NRM intensities, well delineated demagnetization trajectories, and maximum 450 °C unblocking temperature, well below the 580 °C Curie temperature for pure magnetite, are similar to intensity and unblocking temperature spectra of remagnetized carbonates around the world (e.g., Channell and McCabe, 1994). These remagnetizations are often associated with tectonic events (Stamatatos et al., 1995), especially compressional deformation. Interestingly, the nearly antipodal directions suggest the remagnetization episode at Bare Mountain spanned across at least one reversal of the earth's magnetic

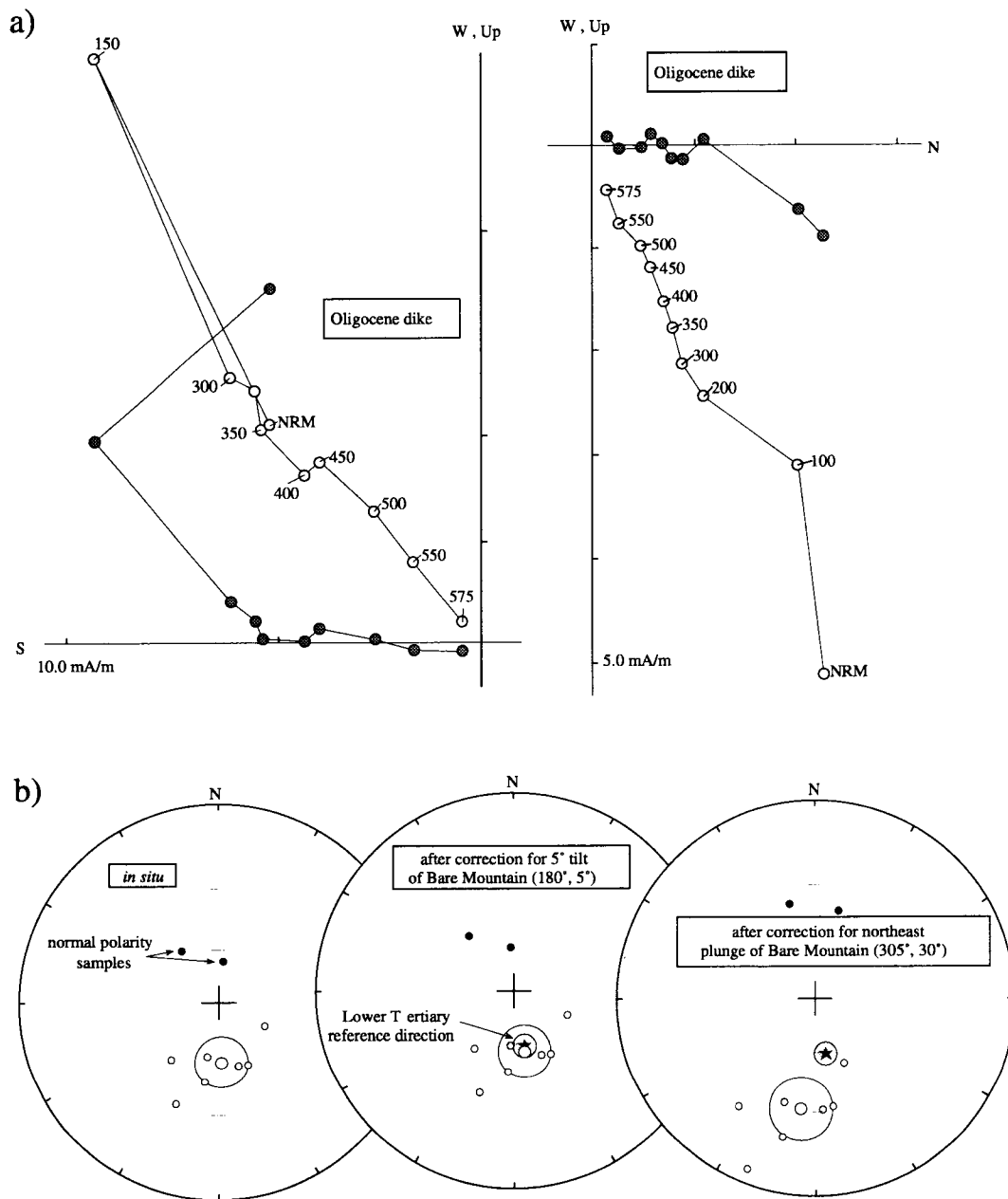


Figure 6-9. Paleomagnetic results from the Oligocene dike in the northwest corner of Bare Mountain. (a) Orthographic projections (*in situ* coordinates) of vector endpoints during progressive thermal demagnetization for normal and reversed characteristic magnetizations. Open (solid) symbols represent projections of the vector onto the horizontal (vertical) plane. Demagnetization steps are in degrees Celsius. (b) Equal-angle projections (stereonet) showing the sample (small circles) and site-mean direction (larger circle) and associated α_{95} (largest circle). Closed (open) circles represent projections onto the lower (upper) hemisphere. Structural corrections for each stereonet are shown as strike and dip of the rotation axis. The star shows the reference Lower Tertiary direction and associated α_{95} derived from the reference APW path of North America (Van der Voo, 1990).

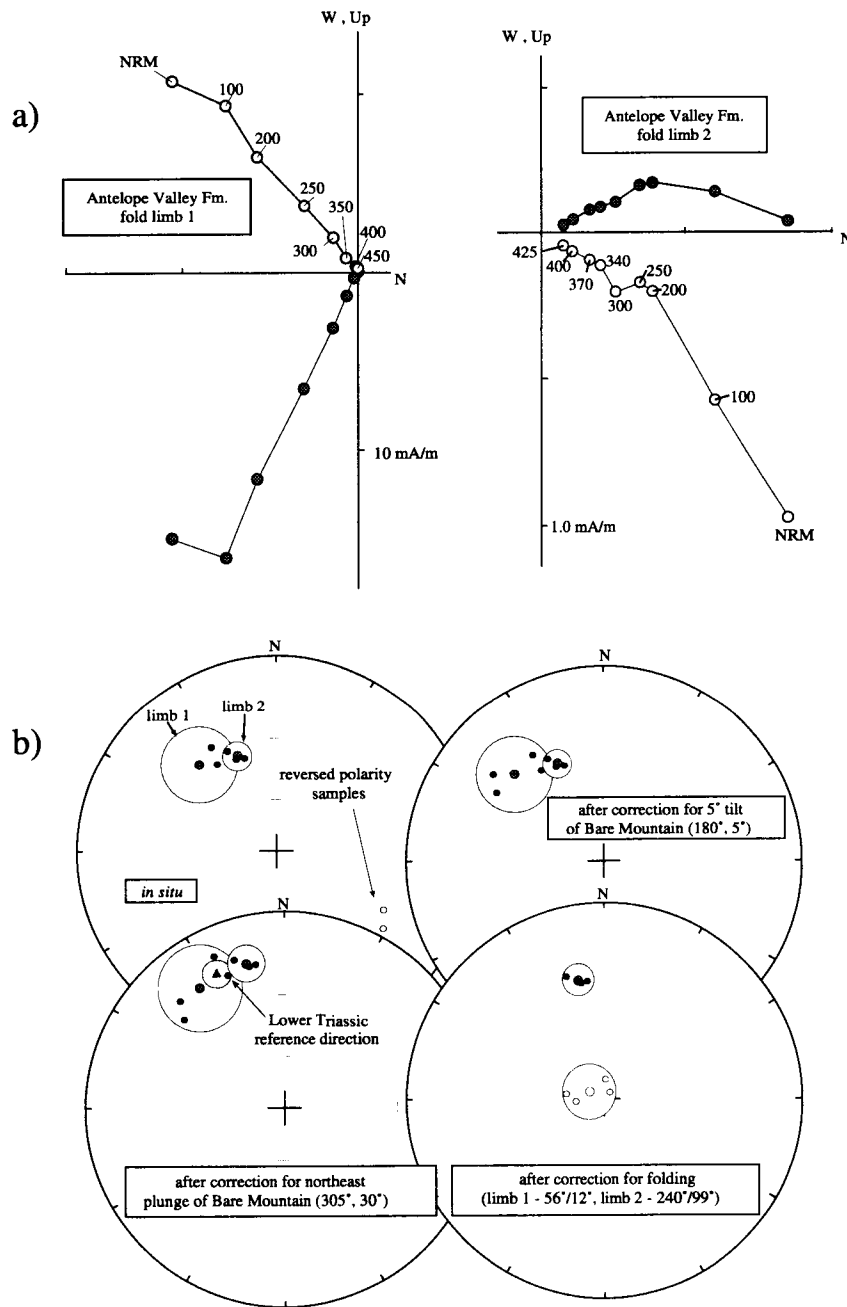


Figure 6-10. Paleomagnetic results from the Antelope Valley Formation in the Meiklejohn Peak fold on northeastern Bare Mountain. (a) Orthographic projections in *in situ* coordinates of vector endpoints during progressive thermal demagnetization for normal and reversed characteristic magnetizations. Symbols are the same as in Figure 6-9. (b) Equal-angle projections (stereonet) showing the hand-sample (small circles) and site-mean directions (larger circles) and associated α_{95} (largest circle). Symbols are the same as in Figure 6-9. Structural corrections for each stereonet are shown as the strike and dip of the rotation axis. The triangle shows the reference Lower Triassic direction and associated α_{95} derived from the reference APW path of North America (Van der Voo, 1990).

field. Based upon the directional data discussed below, it appears that the Antelope Valley rocks were remagnetized in late Permian or early Triassic, consistent with previously published remagnetization ages for Paleozoic carbonates of southern Nevada (Gillett and Van Alstine, 1982).

Mean direction for the characteristic direction from the carbonates is $D=324^\circ$, $I=31^\circ$ $n=22$ cores from 7 hand samples, $k=29.7$, $\alpha_{95}=11.2^\circ$ in *in situ* coordinates. Correction for the minor ($\sim 5^\circ$) tilting of Bare Mountain related to recent motion of the BMF moves the characteristic direction to $D=322^\circ$, $I=28^\circ$ [Figure 6-10(b)]. Correction for the northeast plunge of Bare Mountain moves the characteristic direction to $D=333^\circ$, $I=16^\circ$ [Figure 6-10(b)]. This mean direction overlaps with the expected Early Triassic direction for southwestern Nevada of $D=333^\circ$, $I=15^\circ$, $\alpha_{95}=4.0^\circ$ derived from the Early Triassic reference pole for North America of Van der Voo (1990).

Similar to the Oligocene dike results, the characteristic magnetization for the Antelope Valley does not deviate from the expected directions for southwestern Nevada. If this preliminary result is confirmed by future results, then Bare Mountain apparently has not rotated since at least the Early Triassic and perhaps not at all. More importantly, these results indicate that the Paleozoic carbonates and especially the Antelope Valley Formation, as well as the Cenozoic igneous rocks, are worthwhile candidates for more extensive paleomagnetic research.

6.3 ASSESSMENT OF PROGRESS TOWARD MEETING PROJECT OBJECTIVES

Compilation of data on tectonics, faulting, and seismicity into the tectonics Geographic Information System (GIS), and critical review of the compiled tectonic data are proceeding on schedule. Regional data sets that have been compiled into the GIS to date include: digital terrain elevation, Quaternary faults, *in situ* stress, historic earthquakes, conodont color alteration indices, and volcanic fields. Compilation of data on fault activity (e.g., fault orientation, total displacement, slip direction, slip rate, recurrence interval, date of last major earthquake, associated earthquake magnitudes, length of surface rupture, etc.) into the GIS is in progress and will be reported in an upcoming major milestone report. The tectonics GIS will provide the basis for assessing adequacy of existing and anticipated data for evaluating compliance with quantitative waste isolation performance objectives.

Slip- and dilation-tendency analysis techniques have been developed (Ferrill et al., 1994b; Morris et al., 1994) and provide interactive means for evaluating the relative risk of slip on existing faults, relative risk of magma injection along faults or extension fractures, and the potential effect of existing fractures on groundwater flow patterns (Wittmeyer and Ferrill, 1994). The slip-tendency technique also provides an independent means for critically evaluating fault-plane orientations inferred from earthquake focal-mechanism solutions and nodal plane selections made on the basis of existing stress inversion techniques. The slip- and dilation-tendency analysis techniques provide new tools for assessing compliance with performance objectives and for reducing KTUs that address aspects of tectonic modeling, earthquake hazard assessment, fault-plane solution interpretation, relationships between tectonic processes and groundwater, and effects of tectonics on igneous activity.

Tectonic field analyses are well under way and include fission track, paleomagnetic, and microstructural analyses of ranges in the vicinity of YM. Analyses of alluvial fans around Bare Mountain are providing an independent constraint on the movement history of the BMF. These studies are providing

significant new constraints on tectonic models and rates of deformation in the YM area. Examples of fault and dike interaction have been identified and are in various stages of investigation.

Regional tectonic modeling of the greater Death Valley Region, including YM, was initiated during the present reporting period. These models consist of 13 map-view reconstructions of the region spanning the past 36 Ma. Field reconnaissance was performed to evaluate key elements of the regional reconstructions. A structural analog modeling laboratory is near completion and will be instrumental in developing models of strike-slip releasing bends and extensional structures analogous to those in the YM area.

Data and references compiled by the Tectonics Research Project staff have been used to develop Compliance Determination Strategies on Structural Deformation (LARP 3.2.1.5), Evidence of Igneous Activity (LARP 3.2.1.9), and Structural Deformation and Groundwater (LARP 3.2.2.8). Digital terrain models, boundary data, Quaternary fault coverage, and *in situ* stress data compiled by Tectonics Research Project staff, along with visualization methods developed for tectonics research, are being used in a collaborative effort with the Regional Hydrology Research Project to study regional groundwater flow in the regional carbonate aquifer.

Seven major national conference presentations were made during the past year (Ferrill et al., 1994a,b; Morris et al., 1994; Wittmeyer and Ferrill, 1994; Young et al., 1994; Henderson and Ferrill, 1995; Ferrill et al., 1995). Two articles have been submitted to be considered for publication in refereed journals. Task 3 is planned to culminate in a NUREG report scheduled for completion on August 28, 1995.

6.4 PLANS FOR NEXT REPORTING PERIOD

Continued development and documentation of the slip- and dilation-tendency analysis techniques are planned for the next reporting period, including uncertainty analysis and stress inversion. The recently constructed structural analog modeling laboratory will be tested, and modeling activities will begin with sandbox modeling of strike-slip releasing bends similar to models for the central Death Valley pull apart and Crater Flat Valley. Compilation and analysis of the fault-slip database will continue during the next reporting period. Field work will be conducted at Bare Mountain, Nevada, to evaluate in further detail the pattern of faulting within Bare Mountain, and at the northern end of Bare Mountain where the Tertiary volcanic sequence is separated from the Paleozoic strata of Bare Mountain by a low-angle extensional detachment.

Efforts of the Regional Tectonics Research Project during the next reporting period will concentrate on Task 4—Field Investigations and Task 6—Regional Tectonic Modeling. Regional tectonic modeling activity will be increased during the next reporting period with planned emphasis on the 3D structural geometry and tectonic history of the Death Valley and YMR, including the possible subsurface linkage of the Bare Mountain and YM Faults (Scott, 1990; Young et al., 1993). Specific activities that are planned to address these issues include (i) use of geometric modeling techniques to interpret deep structural geometry; (ii) use of structural analog modeling to produce 3D fault geometries that can be compared with structures in the Bare Mountain/Crater Flat/YM and greater Death Valley Regions; and (iii) continued fission track, microstructural, and paleomagnetic analyses of Bare Mountain in an attempt to constrain the 3D displacement paths of Bare Mountain.

Collaborations between Tectonics Research and Volcanism Research are expected to continue during the next reporting period, with an emphasis on field examples of fault and dike interaction and volcanic hazard assessment.

Integrated work between the Regional Tectonics Research and Regional Hydrology Research Projects will continue during the next reporting period with continued evolution of the potential effects of *in situ* stress on transmissivity and regional groundwater flow.

6.5 REFERENCES

- Burchfiel, B.C., D.S. Cowan, and G.A. Davis. 1992. Tectonic overview of the Cordilleran orogen in the western United States. *The Cordilleran Orogen: Conterminous U.S.* B.C. Burchfiel, P.W. Lipman, and M.L. Zoback, eds. The Geology of North America G-3: Boulder, CO: Geological Society of America: 407–479.
- Butler, R.F. 1992. *Paleomagnetism*. Boston, MA: Blackwell Scientific Publications.
- Carr, M.D., and S.A. Monsen. 1988. A field trip guide to the geology of Bare Mountain. *This extended land: Geological Society of America Cordilleran Section Meeting, Field Trip Guidebook*. D.L. Weide, and M.L. Faber, eds. Geoscience Department Special Publication. Las Vegas, NV: University of Nevada at Las Vegas: 2: 50–57.
- Carr, W.J., and L.D. Parrish. 1985. *Geology of Drill Hole USW-VH-2, and Structure of Crater Flat, Southwestern, Nevada*. U.S. Geological Survey Open-File Report 85-475. Denver, CO: U.S. Geological Survey.
- Caskey, S.J., and R.A. Schweickert. 1992. Mesozoic deformation in the Nevada Test Site and vicinity: Implications for the structural framework of the Cordilleran fold and thrust belt and Tertiary extension north of Las Vegas Valley. *Tectonics* 11(6): 1,314–1,331.
- Channell, J.E.T., and C. McCabe. 1994. Comparison of magnetic hysteresis parameters of unremagnetized and remagnetized limestones. *Journal of Geophysical Research* B3(99): 4,613–4,623.
- Faulds, J.E., J.W. Bell, D.L. Feuerbach, and A.R. Ramelli. 1994. *Geologic Map of the Crater Flat Area, Nevada*. Reno, NV: Nevada Bureau of Mines and Geology.
- Ferrill, D.A., and G.L. Stirewalt. 1995. *Project Plan for Research on Tectonic Processes in the Central Basin and Range Region*, Revision 0, Change 8. San Antonio, TX: Center for Nuclear Waste Regulatory Analyses.
- Ferrill, D.A., A.P. Morris, and D.B. Henderson. 1995. Kinematic models of fold-thrust belt curvature: Role of vertical-axis rotation. *EOS, Transactions of the American Geophysical Union* 76(17): S95.
- Ferrill, D.A., S.R. Young, and D.B. Henderson. 1994a. Geometry and kinematics of coseismic faulting along the Landers rupture zone using time and space patterns of seismicity. *EOS, Transactions of the American Geophysical Union* 75(44): 437.

- Ferrill, D.A., S.R. Young, A.P. Morris, D.B. Henderson, and R.H. Martin. 1994b. 3-Dimensional stress domains interpreted from fault slip patterns in southern California and Nevada. *Geological Society of America Abstracts with Programs—1994 Annual Meeting*. Boulder, CO: Geological Society of America: 26(7): A185.
- Fisher, R.A. 1953. Dispersion on a sphere. *Proceedings of the Royal Astronomical Society of London* A217: 295–305.
- Frizzel, V.A., Jr., and J. Shulters. 1990. *Geologic Map of the Nevada Test Site, Southern Nevada, 1:100,000*. U.S. Geologic Survey Miscellaneous Investigations Series Map I-2046. Reston, VA: U.S. Geologic Survey.
- Gillett S.L., and D.R. Van Alstine. 1982. Remagnetization and tectonic rotation of upper Precambrian and lower Paleozoic strata from the Desert Range, southern Nevada. *Journal of Geophysical Research* 87(B13): 10,929–10,953.
- Gilmore, T.D. 1992. *Geodetic Leveling Data Used to Define Historical Height Changes Between Tonopah Junction and Las Vegas, Nevada*. U.S. Geological Survey Open-File Report 92-450. Menlo Park, CA: U.S. Geological Survey.
- Hamilton, W.B. 1988. Detachment faulting in the Death Valley Region, California and Nevada. *Geologic and Hydrologic Investigations of a Potential Nuclear Waste Disposal Site at Yucca Mountain, Southern Nevada*. M.D. Carr and J.C. Yount, eds. U.S. Geological Survey Bulletin 1790. Reston, VA: U.S. Geological Survey.
- Henderson, D.B., and D.A. Ferrill. 1995. Digital elevation models applied to Basin and Range tectonics research. *Association of American Geographers 91st Annual Meeting Abstracts*. Washington, DC: Association of American Geographers: 127.
- Kirschvink, J.L. 1980. The least-squares line and plane and the analysis of paleomagnetic data. *Geophysical Journal of the Royal Astronomical Society* 62: 743–746.
- Klinger, R.E., and L.W. Anderson. 1994. Topographic profiles and their implications for late Quaternary activity on the Bare Mountain fault, Nye County, Nevada. *Geological Society of America Abstracts with Programs—1994 Annual Meeting*. Boulder, CO: Geological Society of America: 26(2): 63.
- Maldonado, F. 1990. Structural geology of the upper plate of the Bullfrog Hills detachment fault system, southern Nevada. *Geological Society of America Bulletin* 102: 992–1,006.
- Merrill, R.T., and M.W. McElhinny. 1983. *The Earth's Magnetic Field*. London, England: Academic Press, Inc.
- Miller, E.L., M.M. Miller, C.H. Stevens, J.E. Wright, and R. Madrid. 1992. Late Paleozoic paleogeographic and tectonic evolution of the western U.S. Cordillera: *The Cordilleran Orogen: Conterminous U.S.* B.C. Burchfiel, P.W. Lipman, and M.L. Zoback, eds. The Geology of North America G-3: Boulder, CO: Geological Society of America: 56–106.

- Monsen, S.A. 1983. *Structural Evolution and Metamorphic Petrology of the Precambrian-Cambrian Strata, Northwest Bare Mountain, Nevada*. MS Thesis. Davis, CA: University of California at Davis: 66 p.
- Monsen, S.A., M.D. Carr, M.C. Reheis, and P.A. Orkild. 1992. *Geologic Map of Bare Mountain, Nye County, Nevada*. U.S. Geological Survey Miscellaneous Investigations Series, Map I-2201. Reston, VA: U.S. Geological Survey.
- Morris, A.P., D.A. Ferrill, and D.B. Henderson. 1994. Slip tendency analysis and fault reactivation. *EOS, Transactions of the American Geophysical Union* 75(44): 591.
- Ofoegbu, G.I., and D.A. Ferrill. 1995. *Finite Element Modeling of Listric Normal Faulting*. CNWRA 95-008. San Antonio, TX: Center for Nuclear Waste Regulatory Analyses.
- Poole, F.G., J.H. Stewart, A.R. Palmer, C.A. Sandberg, R.J. Madrid, R.J. Ross, Jr., L.F. Hintze, M.M. Miller, and C.T. Wrucke. 1992. Latest Precambrian to latest Devonian time; Development of a continental margin. *The Cordilleran Orogen: Conterminous U.S.* B.C. Burchfiel, P.W. Lipman, and M.L. Zoback, eds. The Geology of North America G-3. Boulder, CO: Geological Society of America: 407–479.
- Ramsay, J.G. 1967. *Folding and Fracturing of Rocks*. London, England: McGraw-Hill.
- Reheis, M.C. 1986. Preliminary study of Quaternary faulting on the east side of Bare Mountain, Nye County, Nevada. *Geologic and Hydrologic Investigations of Yucca Mountain, Nevada*. U.S. Geological Survey Open File Report 86-576. Denver, CO: U.S. Geological Survey: 103–111.
- Sawyer, D.A., R.J. Fleck, M.A. Lanphere, R.G. Warren, D.E. Broxton, and M.R. Hudson. 1994. Episodic Caldera Volcanism in the Miocene Southern Nevada Volcanic Field: Revised stratigraphic framework, $^{40}\text{Ar}/^{39}\text{Ar}$ geochronology, and implications for magmatism and extension. *Geological Society of America Bulletin* 106(10): 1,304–1,318.
- Scott, R.B. 1990. Tectonic setting of Yucca Mountain, southwest Nevada. *Basin and Range Extensional Tectonics Near the Latitude of Las Vegas, Nevada*. Geological Society of America Memoir 176. B.P. Wernicke, ed. Boulder, CO: Geological Society of America: 251–282.
- Snow, J.K. 1992. Large-magnitude Permian shortening and continental-margin tectonics in the southern Cordillera. *Geological Society of America Bulletin*. 104: 80–105.
- Snow, J.K. 1994. Mass balance of Basin and Range extension as a tool for geothermal exploration. *Transactions of the Geothermal Resources Council*. Davis, CA: Geothermal Resources Council: 18: 23–30.
- Snow, J.K., and A.R. Prave. 1994. Covariance of structural and stratigraphic trends: Evidence for anticlockwise rotation within the Walker Lane Belt Death Valley region, California and Nevada. *Tectonics* (13): 712–724.

- Snow, J.K., and B. Wernicke. 1989. Uniqueness of geological correlations: An example from the Death Valley extended terrain. *Geological Society of America Bulletin* 101: 1,351–1,362.
- Snow, J.K., and B. Wernicke. 1993. Large-magnitude Permian shortening and continental-margin tectonics in the southern Cordillera: Reply. *Geological Society of America Bulletin* 104: 280–283.
- Snyder, D.B., and W.J. Carr. 1984. Interpretation of gravity data in a complex volcano-tectonic setting, south-western Nevada. *Journal of Geophysical Research*. 89: 10,193–10,206.
- Stamatakos, J., R. Van der Voo, and J. Pares. 1995. The temporal and spatial distribution of secondary magnetizations within fold-thrust belts: Implications for the nature of remagnetizations related to tectonism. *XXI General Assembly of the International Union of Geology and Geophysics*. Abstracts, Week B. Boulder, CO: American Geophysical Union: B119.
- Stone, P.S., and C.H. Stevens. 1993. Large-magnitude Permian shortening and continental-margin tectonics in the southern Cordillera: Discussion. *Geological Society of America Bulletin* 104: 279–280.
- Swadley, W.C., D.L. Hoover, and J.N. Rosholt. 1984. *Preliminary Report on Late Cenozoic Faulting and Stratigraphy in the Vicinity of Yucca Mountain, Nye County, Nevada*. U.S. Geological Survey Open File Report 84-788. Reston, VA: U.S. Geological Survey.
- Van der Voo, R. 1990. Phanerozoic paleomagnetic poles from Europe and North America with continental reconstructions. *Reviews of Geophysics* 28:167–206.
- Wittmeyer, G.W., and D.A. Ferrill. 1994. Effect of contemporary regional stress on the anisotropy of transmissivity in fractured rock aquifers. *EOS, Transactions of the American Geophysical Union* 75: 44: 258.
- Woodcock, N.H. 1977. Specification of fabric shape using an eigenvalue method. *Geological Society of America Bulletin* 88: 1,231–1,236.
- Young, S.R., A.P. Morris, and G. Stirewalt. 1993. Geometric analysis of alternative models of faulting at Yucca Mountain, Nevada. *Third Annual International High-Level Radioactive Waste Management Conference Proceedings*. La Grange Park, IL: American Nuclear Society: 1: 1,818–1,825.
- Young, S.R., D.A. Ferrill, R.H. Martin, D.B. Henderson, R. Klar, and K. Spivey. 1994. Tectonics GIS for the central Basin and Range and Yucca Mountain, Nevada, region. *Geological Society of America Abstracts with Programs–1994 Annual Meeting*. Boulder, CO: Geological Society of America: 26: 7 A-190.
- Zhang, Y., and R.A. Schweickert. 1991. Structural analysis of Bare Mountain, southern Nevada. *Geological Society of America Abstracts with Programs–1991 Annual Meeting*. Boulder, CO: Geological Society of America: 23: A185–A186.

Zijderveld, J.A.D. 1967. A.C. demagnetization of rocks: Analysis and results. *Methods of Paleomagnetism*.
D.W. Collinson, K.M. Creer, and S.K. Runcorn, eds. Amsterdam, Holland: Elsevier: 256–286.

7 FIELD VOLCANISM

by Brittain E. Hill, F. Michael Conway, Charles B. Connor, and Peter LaFemina

Investigators: Brittain E. Hill, Charles B. Connor, F. Michael Conway, and Peter LaFemina

NRC Project Officer: Linda A. Kovach

7.1 OVERALL TECHNICAL OBJECTIVES

The Yucca Mountain Region (YMR) has been the site of recurring basaltic eruptions during the last 8 million yr (Vaniman et al., 1982; Smith et al., 1990). This volcanic activity has led to the formation of numerous volcanoes, six of which are less than about 1 million yr old and located within 20 km of the candidate repository site. Because of this igneous activity, it is necessary to evaluate the potential for volcanic disruption of the candidate high-level radioactive waste repository at Yucca Mountain (i.e., 10 CFR 60.122, Nuclear Regulatory Commission, 1991).

The probabilities of igneous activity and potential consequences on repository performance are the subject of considerable debate. Current research shows, however, that the probability of igneous activity at the candidate repository site is greater than 1×10^{-4} in 10^4 yr (e.g., Connor and Hill, 1995; Crowe et al., 1995). The uncertainty associated with this probability is large and may be at least one order of magnitude higher than the calculated probabilities (Connor and Hill, 1995; Crowe et al., 1995). Ongoing research by the Center for Nuclear Waste Regulatory Analyses (CNWRA), Los Alamos National Laboratory, and the State of Nevada also shows that basaltic volcanoes in the YMR likely represent a range of eruptive energetics, which can produce vastly different effects on repository performance (e.g., Barr et al., 1993; Hill and Connor, 1994). Highly explosive eruptions can fragment and entrain significant amounts of wall rock and transport that material tens to hundreds of kilometers away from the vent (e.g., Amos, 1986; Fedotov, 1983). Conversely, relatively gentle effusions of magma from fissure-fed eruptions may produce very limited disruption and dispersal of subsurface material (e.g., Self et al., 1974). These probability and consequence models will need to be evaluated in detail as part of prelicensing and licensing activities.

The Field Volcanism Research Project is designed to better characterize the effects of basaltic igneous activity on repository performance. This characterization will be possible through investigations of the (i) mechanics of basaltic eruptions, (ii) extent and characteristics of shallow hydrothermal systems and diffuse degassing associated with basaltic volcanoes, and (iii) nature of basaltic intrusive geometries in the shallow subsurface. Successful completion of the Field Volcanism Research Project, which began in April 1993, will require study of Neogene to Quaternary basaltic volcanoes in the western Great Basin (WGB) and comparison with historically active basaltic volcanoes located elsewhere.

Volcanism research independent of U.S. Department of Energy (DOE) activities is necessary to support specific sections of the Nuclear Regulatory Commission (NRC) License Application Review Plan (LARP) (Nuclear Regulatory Commission, 1994). Insight into the frequency, distribution, and volume of basaltic magmatism in the YMR, volcanism effects at the repository and regional scales, and the relationship between volcanism and regional tectonic and structural settings forms an integral part of site characterization activities (Potentially adverse conditions: evidence of igneous activity, LARP Section 3.2.1.9) and the description of total system performance (Assessment of compliance with the requirement for cumulative releases of radioactive materials, LARP Section 6.1) (Nuclear Regulatory Commission,

1994). The CNWRA Field Volcanism Research Project also indirectly supports other site characterization activities that do not require directed research (Potentially adverse conditions: natural phenomena and groundwater, LARP Section 3.2.2.7). The Compliance Determination Strategy (CDS) associated with evidence of Quaternary volcanism concludes that independent research must be conducted to evaluate Key Technical Uncertainties (KTUs) associated with volcanism and that volcanism poses a high risk to the NRC of reaching unwarranted conclusions regarding compliance with 40 CFR Part 191 (U.S. Environmental Protection Agency, 1991) and 10 CFR 60.122(c)(15) (Nuclear Regulatory Commission, 1991).

Three KTUs related to igneous activity, identified as part of the CDS concerned with evidence of Quaternary igneous activity, are identified in the LARP (Nuclear Regulatory Commission, 1994):

- Determining the three-dimensional structure and tectonic setting of Yucca Mountain
- Determining the probability of igneous activity and resulting disruption of the candidate repository
- Prediction of future system states

The presence of these KTUs leads to the NRC strategy that the sections of the DOE license application dealing with volcanism will be subject to a detailed safety review supported by analyses. Most of these KTUs also require independent tests, analyses, or other investigations for evaluation, along with detailed safety reviews. In addition to the KTU evaluation, independent research in volcanism provides a basis to question how DOE research will address the probabilities and potential consequences of igneous activity on repository performance and to evaluate the DOE responses to these questions. This research also will facilitate technical interactions with DOE, and other affected parties.

7.2 SIGNIFICANT TECHNICAL ACCOMPLISHMENTS

Activities designed to address issues related to the probability and consequences of igneous activity in the YMR during the last 6 mo include:

- Field work at Cerro Negro volcano, Nicaragua, during the June 1995 eruption
- Detailed sampling and analysis of pyroclastic fall deposits from Lathrop Wells volcano, Nevada
- Compilation and preliminary analysis of soil-gas studies conducted between 1992 and 1994 at Cerro Negro, Tolbachik, and Parícutin volcanoes

A paper on the significance of amphibole crystals in Quaternary YMR basalts, which was reported in Connor and Hill (1994), also was presented at the 1995 International High-Level Radioactive Waste Management Conference (Hill et al., 1995). Other significant accomplishments include a detailed compilation of the chronology of the 1975–1976 Tolbachik eruption, development of new procedures for soil-gas and temperature measurements at historically active volcanoes, and preparation for extensive field work at Tolbachik volcano in August 1995.

7.2.1 The June 1995 Eruption of Cerro Negro Volcano, Nicaragua

The Field Volcanism Research Project utilizes a dual approach to evaluate the consequences of potential igneous activity in the YMR. This approach involves studies of both extinct WGB igneous features and of historically active volcanoes that are analogous to YMR volcanoes but located outside the WGB. Clearly, the eruptive styles of volcanic activity in the WGB, the duration of this activity, petrogenesis of magmas, and geology of near-surface structures must be evaluated using detailed field studies in the region. However, much about the dynamic nature of volcanism (e.g., eruption mechanics, extent and longevity of degassing and thermal anomalies, and perturbation of groundwater flow) also must be determined from the study of historically active cinder cones that have had well documented and monitored eruptions. No cinder cone eruptions have occurred in the western United States in the last 100 yr, requiring that these critical data be collected from historically active analog volcanoes elsewhere. In addition, many features necessary to evaluate dynamic volcanic processes are not present or preserved at WGB volcanoes. Active analog volcanoes provide critical information on these features, which are important to assessing the consequence of igneous activity on repository performance.

Cerro Negro volcano, Nicaragua (Figure 7-1), is the site of the most recent small-volume basaltic eruptions at a cinder cone in the western hemisphere, having erupted in April 1992 and May–June 1995 (Global Volcanism Network, 1992; Connor et al., 1993a). Many previous eruptions of Cerro Negro were well documented and provide important information on the dynamic nature of basaltic cinder cone volcanism (e.g., Connor et al., 1993a). Cerro Negro first erupted in 1850, with at least 20 documented eruptions occurring up through 1994. The longest lasting eruption occurred in 1960, when activity persisted for approximately 3 mo (Simkin and Siebert, 1994). Wadge (1984) suggested that magma output at Cerro Negro was relatively steady state ($0.2 \text{ m}^3/\text{s}$). However, the frequency and explosivity of Cerro Negro eruptions increased from 1947 to 1971. Following a 21-yr hiatus, explosive eruptions resumed in 1992.

Cerro Negro is characterized by unusually explosive eruptions, which may represent the upper end of basaltic eruption explosivities in the absence of meteoric water. Preliminary research suggests that this explosivity may be controlled by relatively high magmatic water contents (2–3 weight percent) associated with highly crystalline (i.e., viscous) magmas (McKnight et al., 1994; Roggensack et al., 1994). Three prior eruptions of Cerro Negro (1968, 1971, and 1992) have been studied in detail. Based on isopach maps of these three eruptions, the 1992 eruption was significantly more dispersive and energetic than either the 1971 or 1968 eruptions (Connor et al., 1993a). During the explosive phase of the 1968 eruption, convective ash-column heights rose between 150 and 1,200 m above the cinder cone, and total erupted volume was approximately $1.7 \times 10^7 \text{ m}^3$ of ash (Rose et al., 1973). This explosive activity took place over 46 d and consisted of numerous strombolian and vulcanian bursts (Taylor and Stoiber, 1973). This period of explosive activity was followed by the effusion of lavas from the south flank of the volcano. In contrast, 1992 activity took place over two eruptive phases of 17.75 and 19 hr duration. During these episodes, eruptive columns were maintained at much greater height (3.5–7.5 km) than occurred during 1968 activity, and the resulting ash deposit was more voluminous and widely dispersed than the 1968 deposit. In contrast to the 1968 eruption, no lavas were emitted during the 1992 eruption. Sampling the products of the most recent and previously documented eruptions is required to better understand the physical conditions that lead to highly explosive basaltic eruptions. This research will be used to determine if those conditions exist at volcanoes in the YMR.

CNWRA and Florida International University volcanologists conducted degassing studies at Cerro Negro between September 1993 and June 1995, some of which have been reported in Connor (1993b), Connor et al. (1993b), and Conway et al. (1994). A commonly held view is that

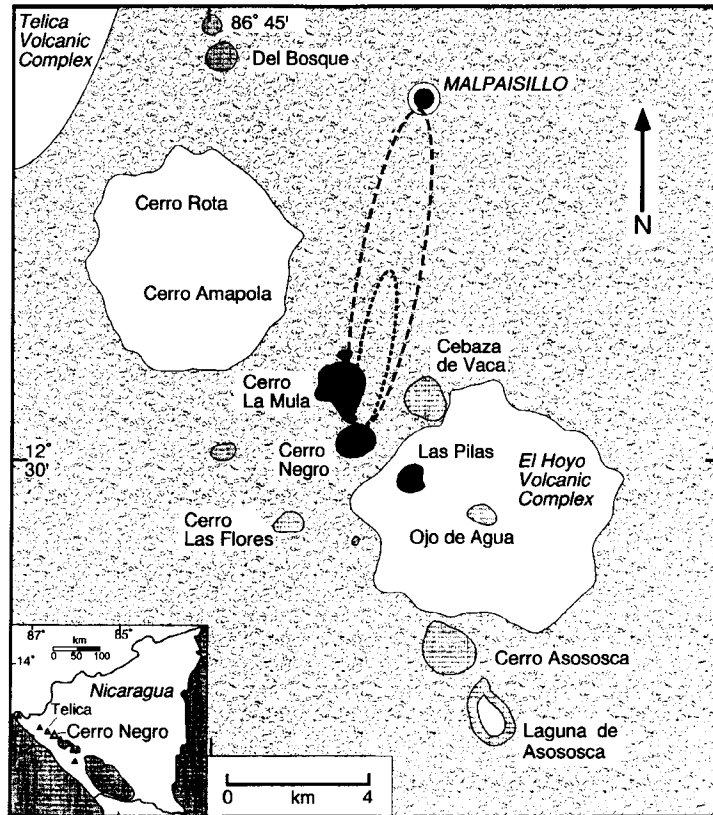


Figure 7-1. Location map of Cerro Negro and adjacent volcanoes, Nicaragua. Volcanoes named in this report are highlighted, and location of the town of Malpaisillo is shown by circles. Dashed ellipses show the interpreted extent of 0.5- and 1-mm-thick ash deposits for June 2-5, 1995, activity.

fumarolic and solfataric activity at cinder cones ended with cessation of the eruption (e.g., Williams and McBirney, 1979, p. 238). However, work at Parícutin and at Jorullo volcanoes, Mexico (e.g., Connor, 1989), has shown that 100-400 °C fumaroles and soil-mercury anomalies can persist for 35 to 220 yr after the eruption ceases. During an eruption, volcano degassing intuitively should be more areally extensive and intense than in the months after the eruption, although no studies to date have investigated the details of this process at basaltic cinder cones. Documenting this expected increase in volcano degassing provides important data for incorporating the effects of igneous activity in repository performance assessment models.

The current eruption of Cerro Negro began on May 24 with increased frequency and intensity of seismicity at and up to 15 km around the volcano, which continued through May 28. Ash plumes to about 100 m high were first observed on May 29, with periodic eruptions occurring once or twice per hour. The eruptions correlated with periods of increased seismic activity. On June 1, the seismicity again increased in frequency and intensity, with eruptions occurring about every 15 min. Ash from these eruptions is very fine grained and consists primarily of basaltic fragments with minor amounts of free crystals (plagioclase, olivine, subordinate amounts of clinopyroxene). CNWRA volcanologists arrived at Cerro Negro and began field studies on June 2, 1995.

Field work at Cerro Negro during June 1995 was conducted with the assistance of Marta Navarro and Oscar Canales of the Instituto Nicaraguense de Estudios Territoriales (INETER). This work consisted of:

- Conducting radon surveys at areas of previously defined soil-gas anomalies
- Performing soil-mercury sampling at radon station locations
- Characterizing the explosive activity during this eruption
- Measuring self-potential (i.e., changes in ground potentials due to electro-kinetic or electro-chemical effects) across thermal areas
- Monitoring temperature variations of high-temperature areas continuously over periods of several days
- Preparing detailed descriptions and sampling of proximal fall and flow deposits, including sampling for leachate analyses
- Sampling of numerous lava flows from previous periods of activity for petrographic and geochemical analyses

The soil-gas surveys constrain the areal extent and magnitude of elevated gas-flux from erupting basaltic volcanoes. Temperature surveys provide valuable information on the effects of cooling and degassing at cinder cones of comparable size to those in the YMR. In addition, these data can be used to test the accuracy of numerical models that simulate cinder cone cooling and degassing. Studies of the fall deposits will be used to develop models of eruption energetics and will serve as a basis for comparison with poorly preserved deposits at YMR and elsewhere in the WGB. Finally, geochemical analyses of the eruption products will document the amount of chemical zonation that can occur in a single basaltic eruption and provide critical data for developing and testing physical process models.

Small basaltic eruptions commonly are accompanied by increased seismic activity (e.g., Luhr and Simkin, 1993). Ash from basaltic volcanoes occurs in the fissures of many YMR Quaternary faults (e.g., Menges et al., 1994), indicating a possible relationship between basaltic eruptions and locally extensive faulting. Understanding the extent and magnitude of the seismic activity associated with the current eruption of Cerro Negro will provide critical data on interpreting this apparent relationship between faulting and volcanism in the YMR. These data currently are being compiled by geologists at INETER and will be provided at a later date.

7.2.1.1 Radon Studies

Radon (^{222}Rn) is a naturally occurring radioactive gas ($t_{1/2}=3.823$ d) that decays through alpha-particle emission. At active volcanoes, radon concentration in soils and fumarole gases is used to identify areas of active convective upwelling and to monitor changes in degassing through time (Crenshaw et al., 1982; Cox, 1983; Baubron et al., 1991; LeCloarec et al., 1994). Radon concentration is ideally suited for identifying and monitoring convective transport because of the limited ability of radon to diffuse through soils due to its short half-life. Several investigations have demonstrated that the mean depth of radon escape from soils is 1.75–2.25 m (Graustein and Turekian, 1990; Appleby and Oldfield, 1992) in areas where radon flux is diffusive, resulting from disintegration of radon-emanating ^{226}Ra . In water, the

diffusivity of radon is approximately six orders of magnitude less than in air, and mean diffusion length in water is approximately 1 mm. Near active volcanoes, radon concentration is commonly observed to be 100 to 1,000 times background values during degassing episodes (Baubron et al., 1991). Given the diffusivity of radon in water and pore gases, it is only possible to achieve these concentrations by convective transport. Correlation of radon anomalies with thermal areas and soil Hg anomalies (e.g., Varekamp and Buseck, 1984; Williams, 1985) is further indication of convective transport. LeCloarec et al. (1994) suggest radon gas originates from decay of ^{226}Ra in both magma and the surrounding wall rock.

At Cerro Negro volcano, radon concentration has been monitored at 57 stations dispersed on and around the volcano during field investigations in March and June 1994, during which time no eruptive activity was occurring, and in June 1995, during volcanic eruption. Radon concentration is measured in the field by burying an electrostatically charged detector about 50 cm deep in surficial deposits and leaving the detector in place for several days to weeks. Voltage changes are measured in the field and represent the time-integrated activity of radon in the sample detector, which is expressed in picoCuries per liter (pCi l^{-1}). Background gamma radiation was monitored using sealed chambers and found to be negligible. Previous radon studies (e.g., Connor and Hill, 1994) have documented that local (1–10 m) variations in radon concentration are common, due to differences in soil permeability. Precision of the radon detectors has been tested by placing two detectors in the same site. Both detectors record the same radon levels within 10 percent, which is used as a measure of analytical precision. Samples for mercury analysis are collected from the bottom of the hole that was dug for the radon detectors. These samples are sieved to 0.2 mm and analyzed by atomic fluorescence spectrometry.

The March 1994 study was conducted under dry field conditions for 12 d. Sample stations focused on the area within about 1 km of Cerro Negro and included the thermal areas of Cerro La Mula [Figure 7-2(A)]. Ambient ground temperatures were about 25 °C, with thermal anomalies on the southeastern flank of Cerro La Mula (50–65 °C) and at fumaroles on the northern rim of Cerro Negro (60–90 °C). Radon concentrations show two distinct populations above a background concentration of about 1.5 pCi l^{-1} [Figure 7-2(B)]. Radon anomalies on southeastern Cerro La Mula and on Cerro Negro correspond to zones of high temperature and elevated soil-mercury concentrations (Conway et al., 1994) [Figure 7-2(A)]. However, another radon anomaly is located about 0.5 km southeast of Cerro Negro. Although there are no thermal anomalies in this area, soil-mercury concentrations also are significantly above background concentrations of 20 ppb. This anomaly zone aligns with the trend of the 1952 and 1954 fissure eruptions on the southern flank of Las Pilas volcano (McBirney, 1955).

The June 1994 radon study occupied many of the same sites as the March 1994 study and extended to greater distances north and south of Cerro Negro [Figure 7-3(A)]. Field conditions were considerably wetter than in March 1994, with late afternoon and evening rainfall common. Ambient ground temperatures were 25 °C, with thermal anomalies on the southeastern flank of Cerro La Mula (40–71 °C) and at fumaroles on the northern rim of Cerro Negro (59–86 °C). Radon concentrations were significantly elevated relative to the March 1994 survey [Figure 7-2(B)], mean values about one order of magnitude greater than in March. Most of this increase occurs in background values. The highest radon values are in the 20- to 40- pCi l^{-1} range for both data sets, and anomalous areas in June 1994 are the same as those in March 1994.

Near-surface processes likely account for the change in radon distribution between March and June 1994. These near-surface processes include increased mixing of air in shallow soils during the dry season or atmospheric pumping, both of which may dilute radon concentration above the groundwater table (Schery and Gaeddert, 1982), which is lower during the dry season. Alternatively, increased vigor

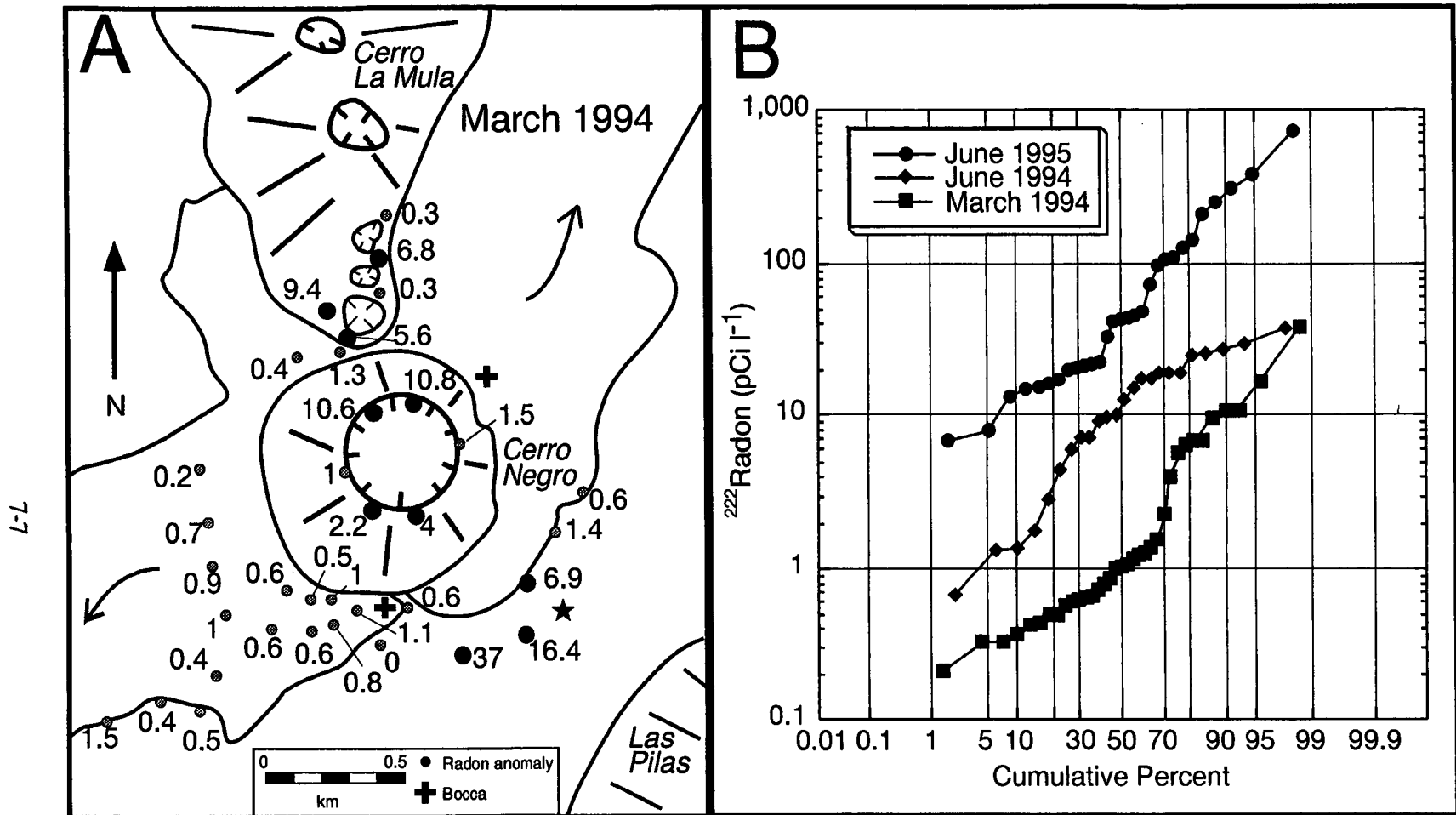


Figure 7-2. (A) Location and concentrations of soil-gas radon for March 1994 study. Radon values shown in pCi l⁻¹. Shaded inset shows stations on the northern crater wall of Cerro Negro, which also is shaded in the smaller scale map. Star is location of seismic station, arrows represent lava-flow directions. (B) Population distributions for March and June 1994 and June 1995 radon surveys. Background thresholds are represented by the first major inflection point on the cumulative percent curve.

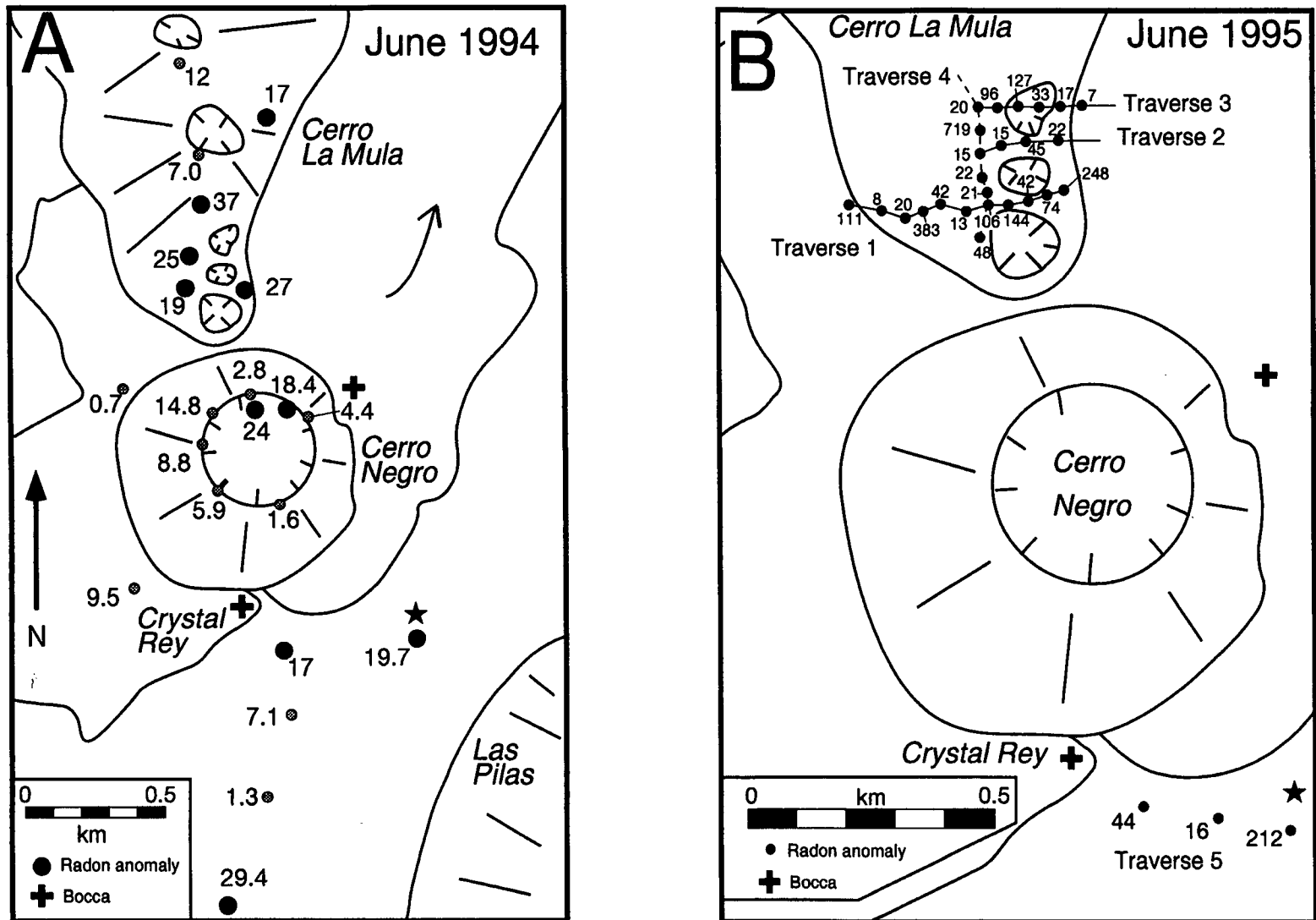


Figure 7-3. (A) Location and concentrations of soil-gas radon for June 1994 study. Radon values in pCi l⁻¹. Shaded inset shows stations on the northern crater wall of Cerro Negro, which also is shaded in the smaller scale map. Arrows represent lava-flow directions. (B) Location and concentrations of soil-gas radon for June 1995 study. Note scale change. Star is location of seismic station, arrows represent lava-flow directions.

of convection in the geothermal system may occur seasonally, in response to increased recharge. However, the lack of large changes in radon concentration in anomalous areas compared with background areas argues against change in flow in the geothermal system as a whole. Thus, data collected in March and June 1994 represent the natural background activity of radon on and near Cerro Negro volcano.

Radon measurements for the June 1995 study were made close to the Cerro Negro seismic station and on the Cerro La Mula Ridge immediately north of Cerro Negro [Figure 7-3(B)]. A total of 29 radon stations were established, most of which were located within 10 m of sites from 1994 radon surveys at Cerro Negro. Field conditions were drier than the June 1994 survey, with significant rainfall occurring only twice during the week-long survey. Thermal anomalies on the southeastern flank of Cerro La Mula ranged from 70–84 °C; temperatures could not be measured on Cerro Negro due to ongoing eruptions. Radon concentrations were significantly elevated relative to the March and June 1994 surveys [Figure 7-2(B)], with mean radon concentration of 40 pCi l⁻¹ and 10 stations with concentrations > 100 pCi l⁻¹.

Radon flux at these stations showed considerable change during this sampling period. For example, a radon sample at the seismic station had a total radon concentration of 396 pCi l⁻¹ from June 2–3, which dropped to 146 pCi l⁻¹ between June 4–5. Overall, this station had an average concentration of 212 pCi l⁻¹ during the sample interval [Figure 7-3(B)]. The same site had a radon concentration of 17 pCi l⁻¹ in June 1994. All other radon stations on the south side of the volcano showed a similar drop during June 1995 and order-of-magnitude increases in radon between June 1994 and June 1995. Radon flux also is highly variable on Cerro La Mula (Figure 7-4). For example, on traverse 1, relatively elevated radon concentrations were measured on June 2–3, with marked decreases in radon on June 3–6 (Figure 7-4). This overall pattern shows that a short-lived pulse of radon-enriched gas was associated with the earlier stage of the June 1995 eruption, which decayed to near ambient levels during the following days. Even on June 3–6, however, some stations have very high radon concentrations compared with observed concentrations in 1994, including one measured concentration of 1,922 pCi l⁻¹ on June 5–6 (Figure 7-4).

These data indicate that a period of increased soil degassing occurred during eruptive activity on June 2–3. The maximum radon concentrations recorded during these periods were more than an order of magnitude higher than recorded previously at Cerro Negro. Variations in the patterns of radon flux observed on Cerro La Mula suggest that gas flow is controlled by north-trending fractures. This pattern is consistent with the fracture-zone widths and orientations observed on Las Pilas volcano during the 1952 and 1954 eruptions (McBirney, 1955). These data also document that elevated degassing can occur up to at least a kilometer away from the volcano along structural trends during a relatively small eruption. The origin of anomalous radon may be magmatic or from the opening of new flow pathways during seismic activity, or both (LeCloarec et al., 1994). In either case, the high concentration and rapid fluctuation of radon indicate transport by convection.

7.2.1.2 Eruption Dynamics

Eruptive activity at Cerro Negro was observed May 28 through mid-June¹. CNWRA staff recorded activity from June 2 through June 5. During this time, eruptions consisted of small explosive bursts, which formed convective ash columns that remained coherent for several minutes before dissipating in an estimated 10–40 km/hr wind. Eruptive activity was characterized by discrete explosions

¹Wilfred Strauch, INETER, personal communication, 1995.

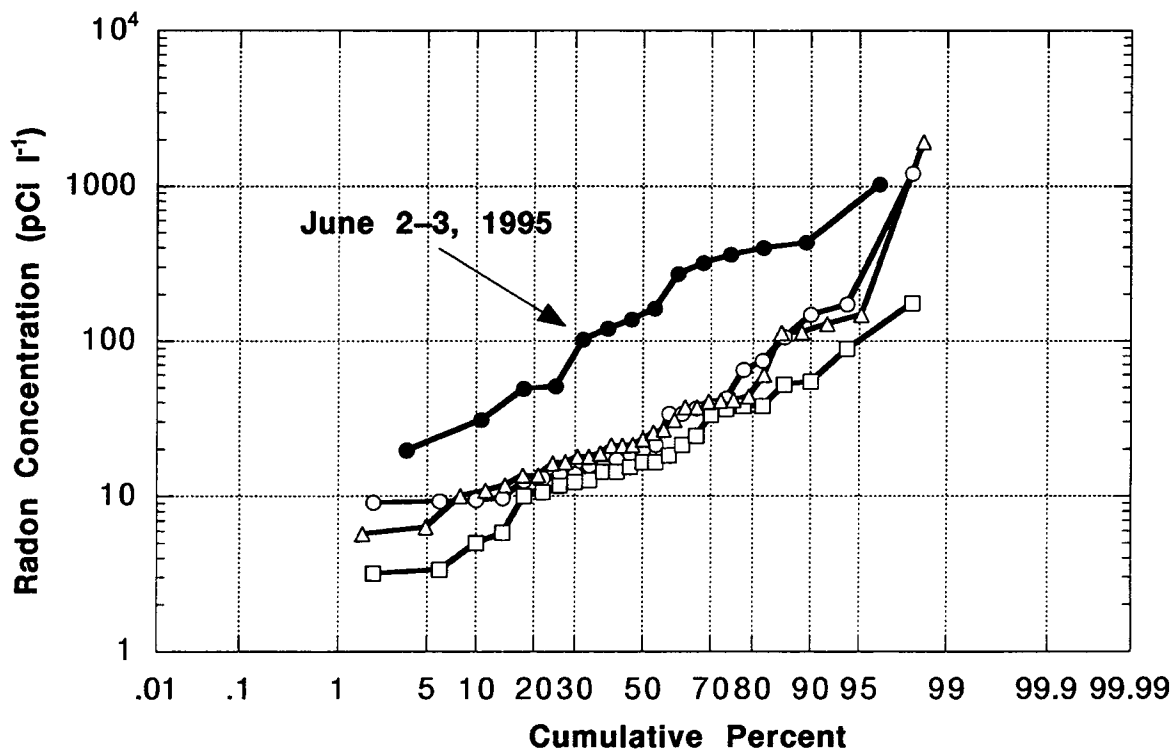


Figure 7-4. Cumulative percent radon concentration plotted by day during the June 1995 eruption. Radon concentrations were significantly higher on June 2-3 (solid circles) compared with concentrations on June 3-4 (open circles), June 4-5 (open triangles), and June 5-6 (open squares). Concentrations measured after June 3 are nonetheless greater than concentrations measured in 1994.

that occurred on average every 8 ± 5 min [Figure 7-5(A)]. There is no apparent periodicity to the timing of the observed eruptions, although patterns of overall increasing and decreasing repose times are apparent [Figure 7-5(A)]. Column heights were measured through triangulation with known elevations. The eruptions produced convective columns that reached up to 1,040 m above the cone rim and commonly reached at least 400 m [Figure 7-5(B)]. There is, however, no apparent correlation between column height and repose time [Figure 7-5(B)]. Although the intensity of the eruption will naturally affect column height, the relatively strong prevailing wind dissipated the eruption column before upward convection had ceased. Based on maximum column heights observed, in the absence of strong winds, the column heights likely would have been at least 1 km high for many periods of the eruption.

Wilson et al. (1978) determined a method to estimate thermal energy release Q in joules from the column heights H of instantaneous explosions:

$$Q = \left(\frac{H}{1.37} \right)^4 \quad (7-1)$$

Using the range of column heights for the June 1995 eruption, estimated thermal energy releases ranged from 3×10^7 to 3×10^{11} joules. These energy releases are minimum estimates, because additional thermal energy was likely consumed in vaporizing some amount of water to generate the explosions (Wilson et al., 1978). In comparison, the sustained columns from the April 1992 eruption of Cerro Negro represented energy releases of 4.3×10^{16} to 1.0×10^{17} joules (Connor, 1993b).

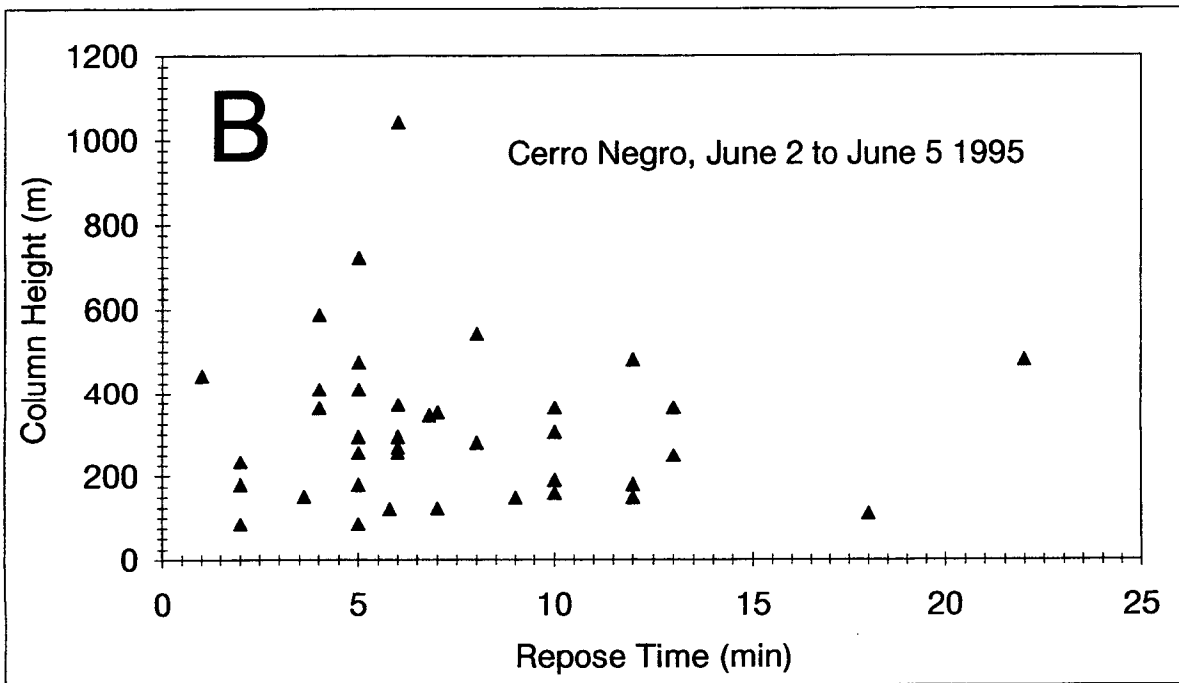
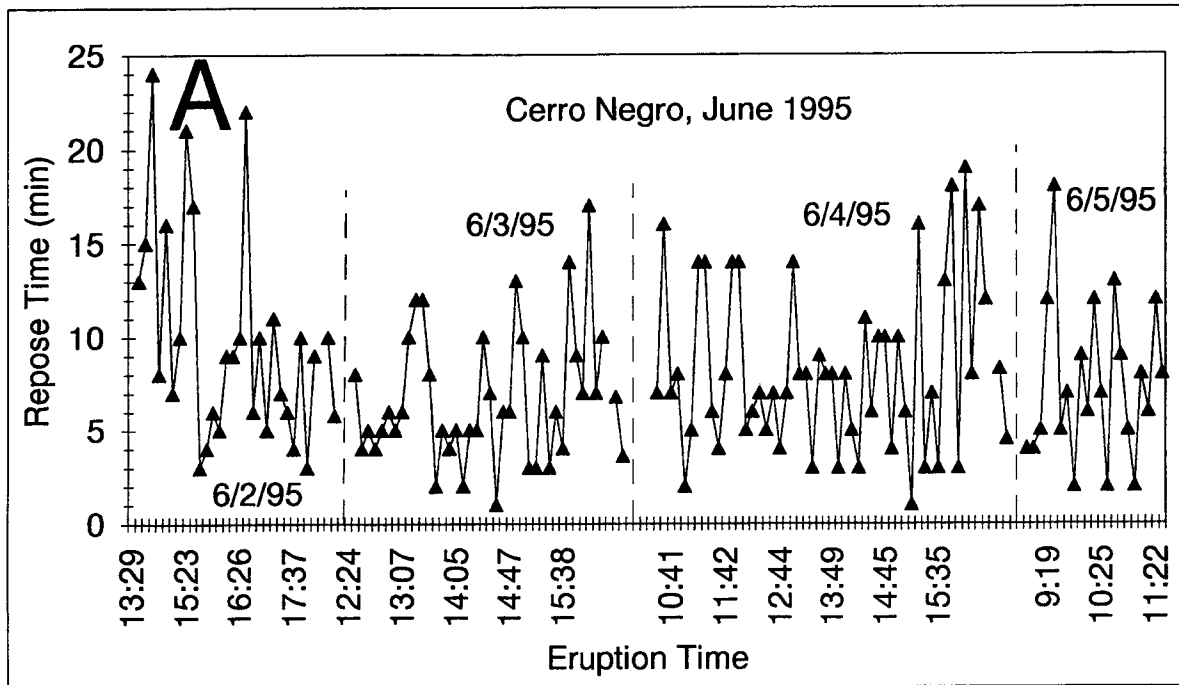


Figure 7-5. (A) Timing of Cerro Negro eruptions for June 2–5, 1995. Eruptions show no obvious pattern, although periods of waxing and waning activity occur. (B) Column height for the June 1995 eruption shows no correlation with repose time. Prevailing winds diluted many eruption columns before convective rise was complete, leading to anomalously low column heights.

The primary eruption product was fine ash, which consisted of angular fragments of olivine, clinopyroxene, and plagioclase, with subordinate amounts of finer-grained basalt. Maximum grain size by visual estimation is 0.25 mm, with an apparent average grain size of 0.1 mm. The very fine grain size, abundance of crystal fragments, and lack of obvious juvenile clasts are characteristics of a dominantly phreatic eruption (e.g., Cas and Wright, 1988). Bulk density of the ash deposits is $1.3 \pm 0.2 \text{ kg m}^{-3}$ and was measured through weighing multiple samples of loosely compacted ash of known volumes. In a period of 20.5 hr, ash accumulations reached a maximum thickness of 1 mm at 0.75 km north of the cone, resulting in an accumulation rate of 0.05 mm hr^{-1} . However, surface winds and rainfall caused large variations in ash accumulation, and ash beds rarely were preserved intact for more than a day. For the period June 2–5, ash transport was dominantly to the north, with trace amounts of ash reported 10 km north of Cerro Negro in the town of Malpaisillo (Figure 7-1). A roughly $2 \times 10 \text{ km}$ elliptical pattern of ash distribution likely occurred, with an average thickness of 0.5 mm. A second $1 \times 5 \text{ km}$ ellipse with a thickness of 0.5 mm represents a proximal ash accumulation of about 1 mm (Figure 7-1). Using these areas, $1.0 \times 10^4 \text{ m}^3$ of ash were erupted during this 96-hr period, giving an average eruption rate of $100 \text{ m}^3 \text{ hr}^{-1}$. In comparison, the 1992 eruption of dominantly magmatic material had an average eruption rate of $1.7 \times 10^6 \text{ m}^3 \text{ hr}^{-1}$ (Connor, 1993b). The low eruption rates for the June 1995 activity also are consistent with a phreatically driven eruption.

Many of these explosive eruptions produced ballistically transported blocks. From observation points 0.5 km north of the volcano, these blocks ranged in size from decimeters to about 1 m in diameter. During most explosions, these blocks were contained within the crater and occasionally were projected 50–100 m above the crater rim. However, ballistic projectiles occasionally were transported beyond the crater rim and impacted as far as half way down the outer cone slope, after reaching maximum heights of 100 m above the cone rim. Flight times for these blocks were 4 to 5 s, from hearing the initial explosion in the crater to observed impact on the crater flanks. The April 1992 eruption of Cerro Negro destroyed large areas of the cone and widened the crater significantly, making existing topographic maps inaccurate. However, cone heights of 150 m on the northern wall were measured in September 1993, with inner crater and outer cone slopes of 33° . The crater is 370 m in diameter, with the main vent located centrally in the crater 90 m below the northern crest of the cone. Cone and block trajectory parameters are shown schematically in Figure 7-6. Using these parameters, estimated ejection velocities were on the order of 100 to 120 m s^{-1} for the larger blocks that reached maximum heights.

The most intense activity was observed during June 2 at approximately 11:30 a.m. During an eruption at this time, a small dilute pyroclastic flow formed on the NW flank of the cone. The flow originated through upwelling of ash from the crater and not through collapse or spallation from the eruption column. Deposits of this pyroclastic flow were sampled on June 5. These deposits are found on the NW flank of the cone and extend a short distance (less than 100 m) from the base. The deposit is 1 cm thick on the NW cone flank 60 m above the base of the cone and overlies the very fine ash that characterizes the June 1995 activity. The flow deposit is massive and nonconsolidated, fine grained (median diameter = 0.2ϕ or 0.9 mm, where $\phi = \log_2 \text{ mm}$), and very well sorted (simple sorting = 0.25ϕ). Although this deposit has the high degree of sorting and grain-size characteristic of surges, sorting is better than commonly observed in basaltic surge deposits (e.g., Wohletz, 1983). One explanation for this high degree of sorting is that the deposit was produced from a dilute, very low energy surge, which lacks a hydromagmatic component common in most other basaltic surge deposits (e.g., Wohletz and Sheridan, 1979). This interpretation is consistent with the generally phreatic character of the June 1995 eruption.

Based on these preliminary observations, activity at Cerro Negro appears to be dominantly phreatic at this time. The regularity of the eruptions, the consistent fine grain-size of the deposits, and

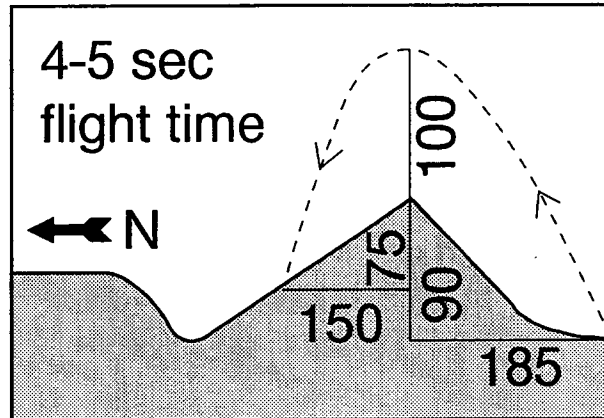


Figure 7-6. Schematic diagram of parameters used to calculate ejection velocities of large blocks during June 1995 activity at Cerro Negro

lack of obvious juvenile components support the interpretation of activity as phreatic. It is possible that this activity resulted from the intrusion of a small volume of magma to shallow depth, providing heat to drive explosive activity.

7.2.1.3 Self-Potential and Temperature

A self-potential anomaly was mapped across Cerro La Mula Ridge, 750 m north of the active crater at Cerro Negro. This anomaly has an amplitude of 100 mV and correlates highly with the location of low-temperature fumaroles (60 to 88 °C) and radon anomalies. O. Canales (INETER) measured temperature increases of around 30 °C in this area, associated with the 1995 eruptive activity. The self-potential anomaly was monitored continuously between June 4 and June 5 using a datalogger. The amplitude of the anomaly was observed to change by 40 mV during this period. These amplitude changes correspond with diurnal changes in air and ground temperatures and with periods of rainfall. These temporal changes in the anomaly can be explained in terms of a simple convection model.

7.2.1.4 Summary of Cerro Negro Studies

The soil-radon study conducted during the 1995 eruption of Cerro Negro is the first known example of soil-degassing data collected directly during the eruption of a basaltic cinder cone. This study documents that order of magnitude increases in soil degassing can occur up to 0.75 km from the erupting cinder cone, primarily along local zones of structural weakness. The increase in soil degassing is manifest by both an increase in the magnitude of radon anomalies and an increase in background radon concentrations. Related increases in the temperatures of thermal areas and variations in self-potential support the conclusion of significantly elevated convective gas transport associated away from an erupting basaltic cinder cone. In contrast to these extensive subsurface effects, the subaerial products of the 1995 eruption are highly ephemeral and likely would not be preserved in the local geological record. Observation and direct analysis of the eruption products support the interpretation that while new magma was likely emplaced at shallow depths to provide the heat necessary for the 1995 eruption, this new magma did not erupt. Models of the consequences of igneous activity on repository performance thus need to account for zones of increased thermal and degassing effects that can extend for at least 0.75 km

from the intruding magma. In addition, the 1995 Cerro Negro study shows that multiple influxes of magma may occur to shallow depths yet not erupt. The poor preservation potential of these eruption products requires that performance assessment models should consider that periods of elevated temperature and degassing occurred without leaving a discernible volcanic deposit.

7.2.2 Yucca Mountain Region Eruption Dynamics

The explosivity of a basaltic eruption is controlled by many magma properties, including volatile content, composition, ascent and eruption rate, and crystallinity (e.g., Wilson and Head, 1981; Williams and McBirney, 1979). In addition, basaltic eruptions can range from weak eruptions with local deposits of scoria and spatter, to highly explosive eruptions capable of substantial wall rock fragmentation and transport of material hundreds of kilometers from the vent (e.g., Budnikov et al., 1983; Williams, 1983). Characteristics of pyroclastic deposits, such as grain-size distributions or isopach maps, commonly are used to determine the energetics of basaltic eruptions (e.g., Walker, 1973; Pyle, 1989). Although these techniques are well developed for historical or well-preserved deposits, few techniques are available to determine eruption dynamics from sparsely preserved deposits. An ongoing task in the Field Volcanism Research Project is to develop methods to determine eruption dynamics from poorly preserved pyroclastic deposits.

One method commonly used to determine eruption energetics is the grain-size distribution of pyroclastic fall deposits. Walker and Croasdale (1972) described a field of relatively low-energy (i.e., strombolian) and higher energy (i.e., surtseyan) basaltic eruptions based on median diameter versus simple sorting plots for well-preserved deposits. Other higher energy eruptions, often called “violent strombolian” (e.g., Walker, 1973; 1993), are characterized by smaller median diameters than normal strombolian fall deposits.

The 1975 eruption of Tolbachik volcano in Kamchatka, Russia, has been summarized in previous reports (Connor, 1993a; Hill and Connor, 1994). Early stages of this eruption were characterized by a sustained convective column that reached altitudes of at least 10 km, with ash transport at least 300 km away from the volcano (Gusev et al., 1979; Budnikov et al., 1983). However, deposits from this eruption all plot within the field of strombolian eruptions defined by Walker and Croasdale (1972) (Hill and Connor, 1994). Relative to the data used by Walker and Croasdale (1972), the Tolbachik falls are slightly less sorted and are finer grained. These subtle differences may represent a distinction in eruption energetics, which is being investigated as part of ongoing CNWRA research.

Pyroclastic deposits for Quaternary YMR volcanoes are poorly preserved. Pyroclastic fall deposits are preserved in isolated localities up to 2.4 km from the youngest volcano in the YMR, Lathrop Wells (Swadley and Carr, 1987). Although Quaternary basaltic ash has been reported in numerous fault trenches up to about 30 km away from Lathrop Wells (Menges et al., 1994), these deposits have not yet been chronologically or chemically correlated with Lathrop Wells (Crowe et al., 1995). The upper parts of the Lathrop Wells fall sections are not preserved. Obvious features of alluvial reworking and eolian sediment infiltration characterize the tops of all examined fall deposits (Figure 7-7). In addition, a small geochemical discontinuity between the fall deposits and the outer deposits of the main Lathrop Wells cone (Crowe et al., 1995) is likely caused by the erosional removal of the uppermost fall deposits.

The most complete section sampled is located 1.1 km south of the main Lathrop Wells cone, on the north slope of a small bedrock high (Figure 7-7). This section is 170 cm thick and consists of at least 12 granulometrically distinct beds. Other sections are significantly thinner and have fewer internal

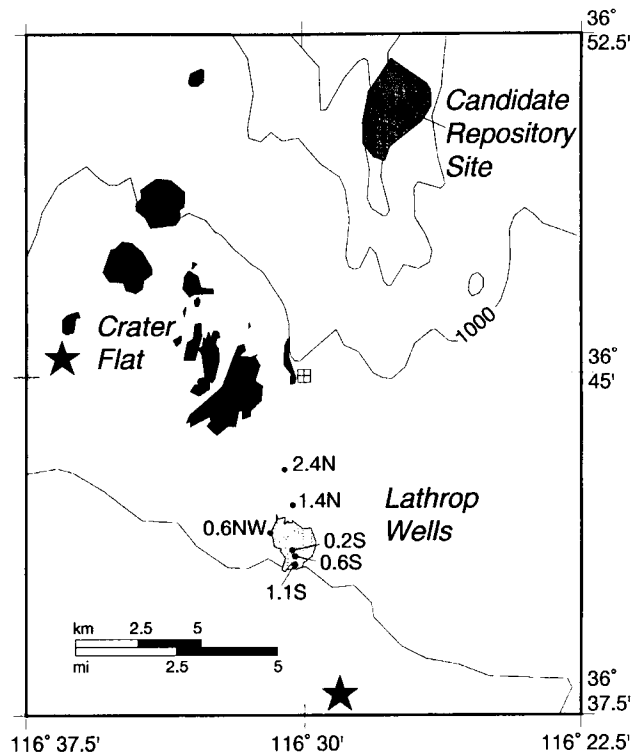


Figure 7-7. Location of pyroclastic fall samples from the Lathrop Wells volcano used in granulometry studies. Sample locations represent distance and direction from the main Lathrop Wells Cone. Basalt outcrops in black from Faulds et al. (1994) and Swadley and Carr (1987), stars mark the location of aeromagnetic anomalies (Kane and Bracken, 1983; Langenheim et al., 1993).

beds. From the Lathrop Wells fall deposits, 40 samples were sieved using standard methods. Samples that showed significant amounts of eolian sediment were not included in this analysis. Cumulative frequency plots were produced to determine the median diameter ($Md = \phi_{50}$, where $\phi = \log_2$ mm) and simple sorting ($1/2 [\phi_{84} - \phi_{16}]$) parameters for these deposits.

All the analyzed fall deposits for Lathrop Wells plot within the Walker and Croasdale (1972) field of strombolian fall deposits (Figure 7-8). As expected, there is a significant amount of variation in both median diameter and simple sorting within the fall sections, which is likely due to variations in the intensity of the eruption rather than atmospheric effects (e.g., Carey and Sparks, 1989). However, the Lathrop Wells samples also have the same median diameter-simple sorting characteristics as the 1975 Tolbachik fall deposits, which were produced from eruptions considerably more energetic than strombolian. Although there are currently no robust grain-size parameters to distinguish between normal strombolian and higher energy magmatic eruptions, the relative decrease in median diameter and sorting observed in both the Lathrop Wells and 1975 Tolbachik deposits may be controlled by eruption energetics (e.g., Walker, 1973). Clearly, additional research is needed to determine basaltic eruption energetics from poorly preserved pyroclastic deposits.

7.3 ASSESSMENT OF PROGRESS

Research in the Field Volcanism project during the last 6 mo continues to provide critical data for assessing the potential consequences of basaltic magmatic activity on repository performance. Most importantly, soil-gas and eruption dynamics studies were conducted during the June 1995 eruption of Cerro Negro volcano, Nicaragua. These studies demonstrate that areas of intense degassing can extend

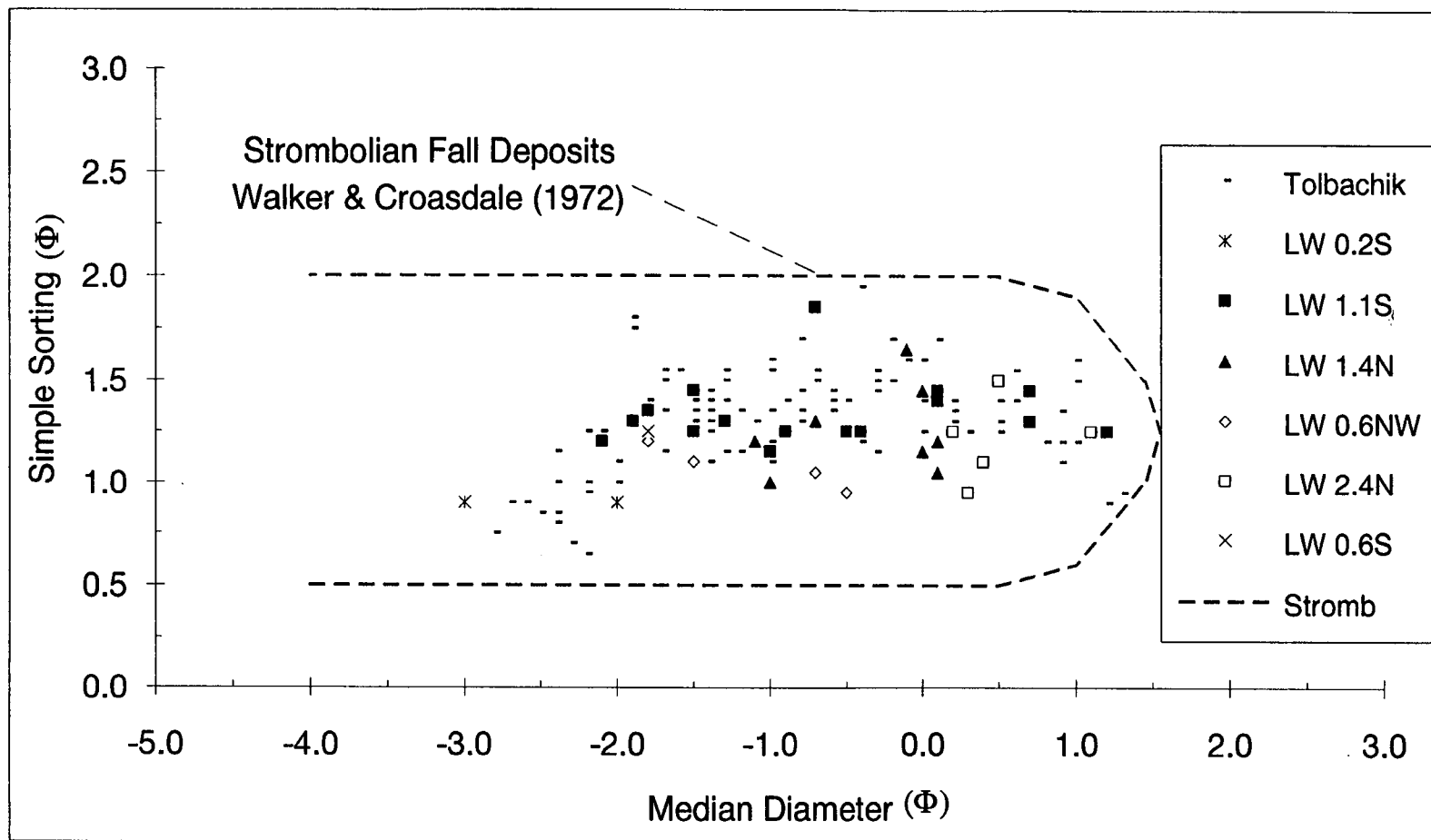


Figure 7-8. Median diameter and simple sorting parameters for Lathrop Wells (Figure 7-7) and the 1975 Tolbachik eruption pyroclastic fall deposits. Both deposits plot in the field of typical strombolian eruptions (Walker and Croasdale, 1972), although many of the Tolbachik deposits were produced by eruptions of significantly higher explosivity.

at least 1 km away from the volcano, likely along major structural zones. Degassing during the eruption can increase an order of magnitude over degassing rates observed in the months to years following a major eruption. Small eruptions, which have a very low preservation potential in the geologic record, can have periods of significantly elevated temperature and degassing associated with magma emplacement to shallow depths, even though the magma is not erupted directly. In addition, self-potential studies at a thermal area immediately north of Cerro Negro show that variations in temperature and self-potential can be explained by a simple convection model. All these processes will be used directly in performance assessment to bound the effects of igneous activity on repository performance.

The explosivity of an eruption directly controls the amount of wall rock that can be disrupted. Currently, wall rock is being used as an analog for the waste package, although there are important differences between undisturbed wall rock and the disturbed zone in the proposed repository. Determining the explosivity of the Quaternary YMR volcanoes is difficult due to the poor preservation of the pyroclastic deposits. Through examination of recent deposits from well-documented eruptions, previous work has shown that common granulometric parameters are not sensitive to basaltic eruption dynamics (Hill and Connor, 1994). Pyroclastic fall deposits from the Lathrop Wells volcano have the same characteristics of deposits as are exhibited by the explosive 1975 Tolbachik eruption. The explosivity of the Lathrop Wells eruption cannot be accurately characterized using available methods on the sparsely preserved deposits. Future studies in the Field Volcanism Research Project are directed toward utilizing a combination of quantitative petrographic analysis of vesicle-size distributions and determinations of magmatic volatile contents to derive eruption energetics from poorly preserved pyroclastic deposits.

Research conducted in the Field Volcanism Research Project directly supports evaluation of current KTUs on the inability to sample many features of igneous activity and the prediction of future system states. This research also is an integral part of the independent tests and analyses required for preparation of LARP Sections 3.2.1.9 and 6.1. There are relatively few volcanoes in the YMR, and many features of these volcanoes are poorly preserved. Research conducted as part of the Field Volcanism Research Project will provide scientifically defensible boundaries on the range of magmatic processes that may be possible during future basaltic eruptions. In addition, the study of historically active and WGB analog volcanoes and the application of that knowledge to YMR volcanoes provide a comprehensive and defensible basis for evaluation of compliance with 40 CFR Part 191, 10 CFR 60.112, and 10 CFR 60.122.

7.4 PLANS FOR NEXT REPORTING PERIOD

Field work will be conducted at the 1975 Tolbachik volcanoes in Kamchatka, Russia, during August 1995. This work will include ground magnetics and self-potential studies of shallow subsurface volcanic structures, continued soil-gas studies, examination of medial to distal pyroclastic fall deposits, and reconnaissance work on the local geologic setting of the Tolbachik volcanoes. Analysis and modeling of data collected from 1994 and 1995 field studies will continue, with an emphasis on developing petrographic tools to determine eruption explosivities and integration of soil-gas studies. In conjunction with the Volcanic Systems of the Basin and Range Research Project, field investigations on the physical characteristics of YMR and other WGB volcanoes will continue.

7.5 REFERENCES

Amos, R.C. 1986. *Sunset Crater, Arizona: Evidence for a Large Magnitude Strombolian Eruption*. M.S. Thesis. Tempe, AZ: Arizona State University.

- Appleby, P.G., and F. Oldfield. 1992. Application of lead-210 to sedimentation studies. *Uranium-series Disequilibrium: Applications to Earth, Marine, and Environmental Sciences*. M. Ivanovich and R.S. Harmon, eds. Oxford, England: Clarendon Press: 731-778.
- Barr, G.E., E. Dunn, H. Dockery, R. Barnard, G. Valentine, and B. Crowe. 1993. *Scenarios Constructed for Basaltic Igneous Activity at Yucca Mountain and Vicinity*. Sandia National Laboratories Report SAND91-1653. Albuquerque, NM: Sandia National Laboratories.
- Baubron, J.C., P. Allard, J.-C. Sabroux, and J.-P. Toutain. 1991. Soil gas emanations as precursory indicators of volcanic eruptions. *Journal of the Geological Society of London* 148: 571-576.
- Budinkov, V.A., Y.K. Markhinin, and A.A. Ovsyannikov. 1983. The quantity, distribution and petrochemical features of pyroclastics of the great Tolbachik fissure eruption. *The Great Tolbachik Fissure Eruption, Geological and Geophysical Data, 1975-1976*. S.A. Fedotov and Ye.K. Markhinin, eds. New York, NY: Cambridge University Press: 41-56.
- Carey, S., and R.S.J. Sparks. 1989. Quantitative models of the fallout and dispersal of tephra from volcanic eruption columns. *Bulletin of Volcanology* 48: 109-125
- Cas, R.A.F., and J.V. Wright. 1988. *Volcanic Successions*. Winchester, MA: Unwin Hyman Inc.
- Connor, C.B. 1989. Soil Hg anomalies at Parícutin volcano, Michoacan-Guanajuato Volcanic Field, Mexico. *Geofisica Internacional* 28(5): 1,029-1,042.
- Connor, C.B. 1993a. *Technical and Regulatory Basis for the Study of Recently Active Cinder Cones*. IM-20-5704-141-001. San Antonio, TX: Center for Nuclear Waste Regulatory Analyses.
- Connor, C.B. 1993b. Field volcanism research. *NRC High-Level Radioactive Waste Research at CNWRA January-June 1993*. W.C. Patrick, ed. CNWRA 93-01S. San Antonio, TX: Center for Nuclear Waste Regulatory Analyses: 12-1 to 12-18.
- Connor, C.B., and B.E. Hill. 1994. Field volcanism research. *NRC High-Level Radioactive Waste Research at CNWRA January-June 1994*. Budhi Sagar, ed. CNWRA 94-01S. San Antonio, TX: Center for Nuclear Waste Regulatory Analyses: 161-187.
- Connor, C.B., and B.E. Hill. 1995. Three nonhomogeneous Poisson models for the probability of basaltic volcanism: Application to the Yucca Mountain Region, Nevada, U.S.A. *Journal of Geophysical Research* 100(B6): 10,107-10,125.
- Connor, C.B., L. Powell, W. Strauch, M. Navarro, O. Urbina, and W.I. Rose. 1993a. The 1992 eruption of Cerro Negro, Nicaragua: An example of Plinian-style activity at a small basaltic cinder cone. *EOS, Transactions of the American Geophysical Union* 74(43): 640.
- Connor, C.B., S. McDuffie, and B.E. Hill. 1993b. Field volcanism research. *NRC High-Level Radioactive Waste Research at CNWRA July-December 1993*. W.C. Patrick, ed. CNWRA 93-02S. San Antonio, TX: Center for Nuclear Waste Regulatory Analyses: 10-1 to 10-26.

- Conway, F.M., A.W. Macfarlane, C.B. Connor, P.C. LaFemina, and M. Reimer. 1994. Degassing at a young cinder cone: Volcan Cerro Negro. *Geological Society of America Abstracts with Program—1994 Annual Meeting*. Boulder, CO: Geological Society of America: 26(7): 435.
- Cox, M.E. 1983. Summit outgassing as indicated by radon, mercury, and pH mapping, Kilauea Volcano, Hawaii. *Journal of Volcanology and Geothermal Research* 16: 131–151.
- Crenshaw, W.B., S.N. Williams, and R.E. Stoiber. 1982. Fault location by radon and mercury detection at an active volcano in Nicaragua. *Nature* 300: 345–346.
- Crowe, B.M., F.V. Perry, J. Geissman, L. McFadden, S. Wells, M. Murrell, J. Poths, G.A. Valentine, L. Bowker, and K. Finnegan. 1995. *Status of Volcanic Hazard Studies for the Yucca Mountain Site Characterization Project*. Los Alamos National Laboratory Report LA-12908-MS. Los Alamos, NM: Los Alamos National Laboratory.
- Faulds, J.E., J.W. Bell, D.L. Feuerbach, and A.R. Ramelli. 1994. *Geologic Map of the Crater Flat Area, Nevada*. Nevada Bureau of Mines and Geology Map 101. Reno, NV: Nevada Bureau of Mines and Geology.
- Fedotov, S.A., 1983. Chronology and features of the southern breakout of the Great Tolbachik fissure eruption, 1975–1976. *The Great Tolbachik Fissure Eruption, Geological and Geophysical Data, 1975–1976*. S.A. Fedotov and Ye.K. Markhinin, eds. New York, NY: Cambridge University Press: 11–26.
- Global Volcanism Network. 1992. Violent strombolian activity at Cerro Negro. *Bulletin of the Global Volcanism Network* 17(3): 2–4.
- Graustein, W.C., and K. Turekian. 1990. Radon fluxes from soils to the atmosphere measured by ^{210}Pb - ^{226}Ra disequilibrium in soils. *Geophysical Research Letters* 17: 841–844.
- Gusev, N.A., V.I. Dvigalo, and A.A. Razina. 1979. Remote sensing in studies of the Tolbachik eruption. *Academy of Sciences of the USSR: Volcanology and Seismology* 2: 27–42.
- Hill, B.E., and C.B. Connor. 1994. Field volcanism research. *NRC High-Level Radioactive Waste Research at CNWRA July–December 1994*. Budhi Sagar, ed. CNWRA 94-02S. San Antonio, TX: Center for Nuclear Waste Regulatory Analyses: 141–154.
- Hill, B.E., S.J. Lynton, and J.F. Luhr. 1995. Amphibole in Quaternary basalts of the Yucca Mountain region: Significance to volcanism models. *Proceedings of Sixth the Annual International High-Level Radioactive Waste Management Conference*. La Grange Park, IL: American Nuclear Society: 132–134.
- Kane, M.F., and R.E. Bracken. 1983. *Aeromagnetic Map of Yucca Mountain and Surrounding Regions, Southwest Nevada*. U.S. Geological Survey Open-File Report 83-616. Reston, VA: U.S. Geological Survey.

- Langenheim, V.E., K.S. Kirchoff-Stein, and H.W. Oliver. 1993. Geophysical investigations of buried volcanic centers near Yucca Mountain, southwestern Nevada. *Proceedings of the Fourth Annual International High-Level Radioactive Waste Management Conference*. La Grange Park, IL: American Nuclear Society: 1,840–1,846.
- LeCloarec, M.F., M. Pennisi, E. Corazza, and G. Lambert. 1994. Origin of fumarolic fluids emitted from a nonerupting volcano: Radionuclide constraints at Vulcano (Aeolian Islands, Italy). *Geochimica et Cosmochimica Acta* 58: 4,401–4,410.
- Luhr, J.F., and T. Simkin. 1993. *Parícutin, the Volcano Born in a Mexican Cornfield*. Phoenix, AZ: Geoscience Press.
- McKnight, S.B., K. Roggensack, and S.N. Williams. 1994. Historical eruption dynamics, volumes, and geochemistry of a young volcano, Cerro Negro Nicaragua. *EOS, Transactions of the American Geophysical Union* 75(44): 731.
- McBirney, A.R. 1955. Thoughts on the eruptions of the Nicaraguan volcano Las Pilas. *Bulletin of Volcanology* 17: 113–117.
- Menges, C.M., J.W. Whitney, J.A. Coe, J.A. Oswald, J.R. Wesling, F.H. Swan, A.P. Thomas, J.B. Paces, and S. Mahan. 1994. Preliminary results of paleoseismic investigations of Quaternary faults on eastern Yucca Mountain, Nye County, Nevada. *EOS, Transactions of the American Geophysical Union* 75(44): 452.
- Nuclear Regulatory Commission. 1991. *Disposal of High-Level Radioactive Wastes in Geologic Repositories*. Title 10, Energy, Part 60 (10 CFR Part 60). Washington, DC: U.S. Government Printing Office.
- Nuclear Regulatory Commission. 1994. *License Application Review Plan for a Geologic Repository for Spent Nuclear Fuel and High-Level Radioactive Waste*. NUREG-1323. Washington, DC: U.S. Government Printing Office.
- Pyle, D.M. 1989. The thickness, volume and grainsize of tephra fall deposits. *Bulletin of Volcanology* 51: 1–15.
- Rose, W.I., Jr., S. Bonis, R.E. Stoiber, M. Keller, and T. Bickford. 1973. Studies of volcanic ash from two recent Central American eruptions. *Bulletin Volcanologique* 37: 338–364
- Roggensack, K., S.N. Williams, R.L. Hervig, S.B. McKight, C.B. Connor, and M. Navarro. 1994. Evidence of polybaric fractionation: Melt inclusions in 1992 eruption of Cerro Negro volcano, Nicaragua. *EOS, Transactions of the American Geophysical Union* 75(44): 747.
- Schery, S.D., and D.H. Gaeddert. 1982. Measurements of the effect of cyclic atmospheric pressure variation on the flux of ²²²Rn from soil. *Geophysical Research Letters* 9: 835–838.
- Self, S., R.S.J. Sparks, B. Booth, and G.P.L. Walker. 1974. The 1973 Heimaey strombolian scoria deposit, Iceland. *Geological Magazine* 111: 539–548.

- Simkin, T., and L. Siebert. 1994. *Volcanoes of the World*. Tucson, AZ: Geoscience Press.
- Smith, E.I., T.R. Feuerbach, and J.E. Faulds. 1990. The area of most recent volcanism near Yucca Mountain, Nevada: Implications for volcanic risk assessment. *Proceedings of the First International High-Level Radioactive Waste Management Conference*. La Grange Park, IL: American Nuclear Society: 81-90.
- Swadley, W.C, and W.J. Carr. 1987. *Geologic Map of the Quaternary and Tertiary Deposits of the Big Dune Quadrangle, Nye County, Nevada, and Inyo County, California*. U.S. Geological Survey Miscellaneous Investigations Series Map I-1767. Reston, VA: U.S. Geological Survey.
- Taylor, P.S., and R.E. Stoiber. 1973. Soluble material on ash from active Central America volcanoes. *Geological Society of America Bulletin* 84: 1,031-1,042.
- U.S. Environmental Protection Agency. 1991. *Environmental Radiation Protection Standards for Management and Disposal of Spent Nuclear Fuel, High-Level and Transuranic Radioactive Wastes*. Title 40, Protection of Environment, Part 191 (40 CFR Part 191). Washington, DC: U.S. Government Printing Office.
- Vaniman, D.T., B.M. Crowe, and E.S. Gladney. 1982. Petrology and geochemistry of Hawaiite lavas from Crater Flat, Nevada. *Contributions to Mineralogy and Petrology* 80: 341-357.
- Varekamp, J.C., and P.R. Buseck. 1984. Changing mercury anomalies in Long Valley, California. *Geology* 12: 283-286.
- Wadge, G. 1984. Comparison of volcanic production rates and subduction rates in the Lesser Antilles and Central America. *Geology* 12: 555-558.
- Walker, G.P.L. 1973. Explosive volcanic eruptions: a new classification scheme. *Geologische Rundschau* 62: 431-446.
- Walker, G.P.L. 1993. The pyroclastic deposits of El Parícutin. *50 Años Del Volcán Parícutin, Reunión Internacional Conmemorative, Programa y Resúmenes, Urapan, Michoacán*. Mexico City: Instituto de Geofísica.
- Walker, G.P.L., and R. Croasdale. 1972. Characteristics of some basaltic pyroclastics. *Bulletin of Volcanology* 35: 303-317.
- Williams, H., and A.R. McBirney. 1979. *Volcanology*. San Francisco, CA: Freeman, Copper and Company.
- Williams, S.N. 1983. Plinian air-fall deposits of basaltic composition. *Geology* 11: 211-214.
- Williams, S.N. 1985. Soil radon and elemental mercury distribution in relation to magmatic resurgence at Long Valley caldera. *Science* 229: 551-553.

- Wilson, L., and J.W. Head, III. 1981. Ascent and eruption of basaltic magma on the Earth and Moon. *Journal of Geophysical Research* 86(B4): 2,971-3,001.
- Wilson, L., R.S.J. Sparks, T.C. Huang, and N.D. Watkins. 1978. The control of volcanic column heights by eruption energetics and dynamics. *Journal of Geophysical Research* 83(B4): 1,829-1,836.
- Wohletz, K.H. 1983. Mechanisms of hydrovolcanic pyroclast formation: Grain-size, scanning electron microscopy, and experimental studies. *Journal of Volcanology and Geothermal Research* 17: 31-63.
- Wohletz, K.H., and M.F. Sheridan. 1979. A model of pyroclastic surge. *Geological Society of America Special Paper 180*. Boulder, CO: Geological Society of America: 177-194.

8 REGIONAL HYDROGEOLOGIC PROCESSES OF THE DEATH VALLEY REGION

by Gordon W. Wittmeyer, Donna Balin, and Richard V. Klar

Investigators: David A. Ferrill, Sidney Jones, Richard V. Klar, William M. Murphy, David A. Pickett, Stuart A. Stothoff, and Gordon W. Wittmeyer (CNWRA); Donna Balin (Consultant)

NRC Project Officer: Thomas J. Nicholson

8.1 TECHNICAL OBJECTIVES

Yucca Mountain (YM) has been proposed as a potential site for a high-level nuclear waste repository, in part because of the favorable geochemical and hydrologic environment provided by its 700-m thick unsaturated zone. Siting the repository in the unsaturated zone may significantly reduce the potential for waste canister corrosion and subsequent dissolution of the waste form. Moreover, the low water flux rates that are presumed to exist in the unsaturated zone reduce the likelihood that dissolved radionuclides would be rapidly transported to the accessible environment. Mechanisms that may saturate the repository horizon, and thus compromise favorable conditions provided by the YM site, include rapid infiltration of water from the surface through highly conductive fracture networks and an increase in the elevation of the regional water table. The first mechanism is a site-scale or subregional issue and is not addressed by this research project. Elevation of the water table may occur due to increased recharge to the regional carbonate system along stream channels and mountain fronts in topographically closed basins 100 km to the north and northeast of YM or by neotectonic disruption of structural or stratigraphic features that control the steep hydraulic gradient north of the proposed repository block at YM. Even if elevation of the regional water table does not saturate the repository block, the reduced thickness of the unsaturated zone has the potential to diminish travel times within the vadose zone. In addition, travel times in the saturated zone and the location of potential discharge areas for dissolved radionuclides down gradient from YM are performance-related issues addressed by this research project. The primary objectives of this research project are to: (i) analyze existing conceptual models and develop new conceptual models of the regional hydrogeologic flow regime in the Death Valley region that contains YM, and (ii) construct numerical models of regional flow that may be used to assess the potential for the water table beneath YM to rise in response to wetter climatic conditions.

Predictions made with numerical models will be used by the U.S. Department of Energy (DOE) in its license application to demonstrate that the YM site meets the overall performance standards outlined in 10 CFR 60.112 and the geologic subsystem performance standard defined in 10 CFR 60.113(a)(2). In addition, the DOE may choose to use numerical models to demonstrate the absence or influence of potentially adverse conditions including: the effects of future pumping on the regional flow system [10 CFR 60.122(c)(2)]; structural deformation and groundwater [10 CFR 60.122(c)(4)]; the potential for deleterious changes to the hydrologic system [10 CFR 60.122(c)(5)]; the potential for changes to the hydrologic conditions resulting from climate change [10 CFR 60.122(c)(6)]; the potential for water table rise [10 CFR 60.122(c)(22)]; and the presence and influence of favorable conditions, including the clear absence of fully saturated pathways connecting the repository to the water table [10 CFR 60.122(b)(8)(ii)]. Understanding of the regional hydrogeologic system developed in this project will be used to guide review of the DOE license application and associated precicensing submittals and to assess the adequacy of the models used by the DOE to demonstrate compliance with the regulatory requirements and environmental standards.

Understanding of the regional hydrogeologic system gained from this research project will also be used to construct specific Compliance Determination Methods outlined in the License Application Review Plan (LARP) (Nuclear Regulatory Commission, 1994). Literature reviews and hydrogeologic data gathered in Task 1 of the project will provide information that may be directly used to assess the description of individual systems and characteristics of the site (LARP Section 3.1) and, in particular, the description of the hydrologic and geochemical systems (LARP Sections 3.1.2 and 3.1.3, respectively). Evidence gleaned from literature reviews and data analyses in conjunction with conceptual and numerical models of the regional flow regime developed in this research project will be directly used to determine if the applicant has provided convincing evidence of the presence or absence of favorable hydrogeologic conditions and potentially adverse hydrogeologic conditions (LARP Sections 3.2.1.1, 3.2.2.1, 3.2.2.3, 3.2.2.6, 3.2.2.8, 3.2.2.9, 3.2.2.11, and 3.2.4.2). Flow models developed in this project will also be used to confirm whether velocity fields and travel times within the saturated zone estimated by the DOE are accurate enough to demonstrate compliance with the Ground Water Travel Time performance objective (LARP Section 3.3).

Compliance Determination Strategies (CDSs) for the LARP sections listed previously have been developed but will not be finalized until a thorough review and integration of the various LARP sections have been conducted. However, the Regional Hydrogeology Research Project will be instrumental in resolving specific technical uncertainties identified during the CDS development process. Key Technical Uncertainties (KTUs) that pose a high risk of noncompliance with the total-system or subsystem performance requirements may require that the Nuclear Regulatory Commission conduct independent research to resolve the issue. Uncertainty in developing a conceptual and mathematical model for transport of liquid and vapor phase water that is representative of the YM site flow system has been identified as a KTU that must be addressed in LARP Sections 3.2.2.1, 3.2.2.9, 3.2.2.12, 3.2.3.7 and 3.3.

The Regional Hydrogeology Research Project has been divided into five tasks: Task 1—Collect and analyze data and existing models; Task 2—Construct alternative conceptual models of key hydrogeologic processes in the Death Valley region of the western Great Basin; Task 3—Construct and calibrate mathematical and numerical models of subsurface flow at local, basin, and regional scales; Task 4—Use geochemical data to evaluate and refine regional flow models; and Task 5—Apply models to analyze problems critical to repository performance. Current plans call for completion of Tasks 1 and 2 during the first 2 yr of the project, with the remaining tasks to be initiated in the third year and completed by the fifth and final year of the project. Efforts during the past 6 mo have primarily focused on Tasks 2 and 3. The primary technical objectives of Task 2 are to: (i) critically evaluate geologic, hydrogeologic, and geochemical data from the Death Valley region; and (ii) use data compiled in the computerized Geographic Information System (GIS) to construct alternative conceptual models of flow in the Death Valley region. The primary technical objectives of Task 3 are to: (i) develop numerical models of regional flow in the Death Valley region and (ii) develop or acquire parameter estimation methods for automatically calibrating these flow models.

8.2 SIGNIFICANT TECHNICAL ACCOMPLISHMENTS

During the past 6 mo, research has primarily been focused on assembling hydraulic, hydrogeologic, hydrostratigraphic, meteorological, geochemical, and geologic structure data into the Center for Nuclear Waste Regulatory Analyses ARC/INFO GIS database. These efforts were summarized in Wittmeyer et al. (1995), which was submitted to the Nuclear Regulatory Commission on April 27, 1995. This report was divided into separate chapters describing the data, maps, and ARC/INFO coverages

compiled for the Death Valley region physiography, surface water hydrology, precipitation and climatology, recharge and discharge, wells and water levels, pre-Cenozoic surface hydrogeology, and hydrochemistry. During the 2 mo following the completion of this intermediate milestone, efforts have been redirected toward development of hydrostratigraphic cross sections to be used in the construction of a three-dimensional (3D) regional hydrogeologic model. Because the time and effort needed to construct each cross section is considerable, the locations of the first three cross sections have been selected so that they transect geologic structures and hydrogeologic features that may control the saturated zone flow regime near YM. By preparing these cross sections first, work can proceed on the development of alternative conceptual models of saturated flow in those areas most likely to impact the YM site-scale flow regime.

The saturated zone feature that may have the greatest potential to compromise repository performance is a relatively steep (300 m in 2 km) (Fridrich et al., 1994) hydraulic gradient located at the northern extreme of the perimeter of the proposed YM repository. If this steep hydraulic gradient is formed by the juxtaposition of high- and low-permeability units across a fault zone, there is concern that future tectonism may alter the throw across the fault and permit water levels to rise beneath YM. Numerical modeling studies performed by Ahola and Sagar (1992) suggest that disruption of the hydraulic barrier that forms the steep hydraulic gradient may cause a water table rise of 275 m beneath YM. Inasmuch as current construction plans call for the repository to be located approximately 300 m above the water table, a 275-m water table rise would dramatically decrease unsaturated zone travel times and may cause the repository to fail the overall system performance standards (10 CFR 60.112). It has been noted by Winograd and Thordarson (1975) and Fridrich et al. (1994) that the steep hydraulic gradient at YM appears to be part of a regional hydraulic feature that extends from just northeast of Bare Mountain, westward to Shoshone Mountain, northward along the Eleana Range, and then eastward across Oak Spring Butte, at the north of Yucca Flat, and into the Groom Lake area. According to Winograd and Thordarson (1975), the steep eastward hydraulic gradient between the Eleana Range and Yucca Flat is due to thrust faulting that has placed portions of the highly permeable Paleozoic carbonate unit over the low-permeability argillite units of the Eleana Formation and thus effectively compartmentalized the Paleozoic carbonate unit. Whether a similar geologic structure is responsible for the steep hydraulic gradient north of YM is an open question.

8.2.1 Conceptual Models of the Steep Hydraulic Gradient

The presence of the steep hydraulic gradient at YM is inferred from measured water levels from boreholes UE25-WT#6 and USW G-2, which are located approximately 300 and 1,600 m to the south of Yucca Wash, respectively. Borehole UE25-WT#6 was drilled to a depth of 372 m, while borehole USW G-2 was drilled to a depth of 1,831 m. Water surface elevations in UE25-WT#6 and USW G-2 are 1,034 m and 1,029 m above mean sea level, respectively (Ciesnik, 1995). The low hydraulic head portion of the steep gradient is derived using data from wells UE25-WT#16, UE25-WT#18, and USW H-1, which have water levels of 738.2 m, 730 m, and 730.9 m, respectively (Fridrich et al., 1994). Approximately 2,000 m to the southeast, water surface elevations decline to around 730 m, which yields a gradient of 0.15 (300 m in 2 km). Except for a north-trending region with a moderate hydraulic gradient of 0.024 (40 m in 1.7 km) paralleling Solitario Canyon, the gradient within the immediate vicinity of the repository is 0.0001. Perched water bodies are fairly prevalent in the immediate vicinity of the repository horizon (Section 9.2.3). However, the 531-m saturated thickness penetrated by USW G-2 suggests that the high water surface elevations measured in the two wells do not indicate the presence of a perched zone.

Czarnecki (1989) noted that the “cause and nature of the large hydraulic gradient are unknown.” However, he did propose three possible explanations including: (i) faults that juxtapose high-permeability units against low-permeability units or fault zones filled with low-permeability gouge, (ii) the presence of units that are resistant to fracturing such as argillite, or the presence of a volcanic dike or other intrusive rocks, and (iii) a change in the local stress regime that effects a spatial change in fracture frequency, aperture, or orientation across the steep gradient region. In his two-dimensional (2D) vertically integrated, subregional-scale numerical model of the YM flow system, Czarnecki (1989) effects the steep gradient by implementing a low-permeability barrier that diverts water around the western flank of the barrier, and then back to the southeast through the repository area. He notes that his model yields flow directions that are not perpendicular to the observed potentiometric contours. This observation is hardly surprising given his decision not to extend the barrier along the entire length of the steep hydraulic gradient. Moreover, if the structural or stratigraphic feature causing the steep gradient forces water to flow vertically downward, a 2D areal model, such as used by Czarnecki (1989), cannot correctly reproduce the observed potentiometric contours.

Fridrich et al. (1994) present a very detailed description and analysis of possible structural and stratigraphic features that could give rise to what they refer to as the “large hydraulic gradient.” This paper is prefaced by the authors’ recognition that existing data are insufficient to prove that the inferred steep hydraulic gradient does indeed drive flow from the north to the south, rather than representing the relative potentiometric levels in two separate flow systems. However, after assuming that the steep gradient is a feature of a single flow system, Fridrich et al. (1994) undertake an in-depth analysis of the hydrogeology of the Tertiary volcanics, which form the upper 1 to 2 km of the YM section. Within the volcanic units at YM, the degrees of hydrothermal alteration and lithostatic loading increase with depth. In addition, Fridrich et al. (1994) point out that alteration increases strongly to the north, and the ratio of the horizontal to vertical *in situ* stresses decreases to the south, which suggests a southward decrease in shear stress. Taken together, the spatial trends in the degree of alteration and the stress regime suggest that the bulk permeability in the tuff units decreases with depth, and increases from the north to the south, which is consistent with the presence of the steep gradient. The hydrostratigraphic units at YM consist from bottom to top of: (i) an aquitard formed by the nonwelded Lithic Ridge and older tuffs, (ii) a moderately productive aquifer formed by the variably welded Crater Flat Tuff, (iii) an aquitard formed by the bedded tuffs of the Calico Hills, and (iv) a very productive aquifer formed by the highly fractured, densely-welded Topopah Spring member of the Paintbrush Tuff.

These hydrostratigraphic units are cut by a series of north-trending, steeply dipping normal faults such as the Solitario Canyon Fault, the Ghost Dance Fault, the Bow Ridge Fault, and the Midway Valley Fault. Fridrich et al. (1994) contend that these faults may form the most permeable features within the tuffs, although their permeability is probably controlled by the lithology of the dissected unit. Across this series of normal faults, the throw is great enough in some areas to have juxtaposed the highly permeable Topopah Spring member against the bedded tuffs of the Calico Hills. Fridrich et al. (1994) prepared a detailed map of the geology at the water table under YM, which suggests very abrupt changes in bulk permeability along both west-east and north-south transects within the region in which the hydraulic gradient is small (0.0001). The extreme flatness of the gradient within this region indicates that the overall hydraulic regime is not controlled by the shallow tuff units, suggesting the presence of an extremely permeable unit, such as the lower carbonate aquifer (LCA), at depth.

Since the hydrogeology and structure of the upper tuff units do not appear to be the cause of the steep gradient, Fridrich et al. (1994) examined the influence of deeper units and structures, such as those formed by the buried contact between the Eleana Formation and the Paleozoic carbonate unit. They

speculate that the geometry of the large-scale Mesozoic folds and thrusts in the Paleozoic rocks, as truncated by the Tertiary unconformity, control the large-scale Mesozoic clastic-carbonate contact. Fridrich et al. (1994) note that an aeromagnetic high that parallels the regional steep gradient and extends into the YM steep gradient zone is probably caused by the magnetite-bearing Eleana Formation. There are additional lines of evidence that indicate a hydraulic connection between the shallow tuff units and the LCA. A heat flow low measured in the unsaturated zone above the steep gradient area may be caused by local downwelling of water from the tuffs to the LCA. Linear thermal highs measured to the south of the steep gradient may be caused by water upwelling from the LCA. Carbon isotope data appear to support the theory that water flows upward from the LCA into the tuff units in the low-gradient area. As additional evidence to support this upwelling theory, the authors point out that when borehole UE25 P#1 penetrated the tuff-carbonate contact, an upward gradient was detected. These data taken together suggest that the clastic-carbonate contact is at least coincident with the steep hydraulic gradient, and may, in fact, be its cause.

The evidence for the coincidence of the steep hydraulic gradient and the clastic-carbonate contact cannot be used to determine the exact structure and stratigraphy in this area. However, by using gravity measurements and detailed information on north-south stratigraphic changes in the deep volcanics, Fridrich et al. (1994) are able to construct two alternative flow models. The presence of a gravity low immediately to the south of the steep hydraulic gradient suggests a downward deflection (0.5 km) of the denser clastic and carbonate strata. Fridrich et al. (1994) speculate that this downward deflection of the clastic and carbonate strata formed a graben, which was subsequently buried by less dense volcanic material. Lithologic data from six boreholes drilled to the south of the steep gradient indicate an abrupt stratigraphic thickening (50 to 100 %) in the area of the steep gradient. This stratigraphic thickening clearly supports the authors' model of a graben that has been covered with less dense tuffaceous rock.

Fridrich et al. (1994) argue that because the LCA at YM is buried by approximately 2 km of tuff units, the Paleozoic rocks have a different effect on the hydraulic regime at YM than they do elsewhere along the regional steep gradient. They assert that even if the Paleozoic rocks are critical to the hydraulic system, they can only be so if the structure of the Tertiary tuff units effects a hydraulic connection to the LCA. Accordingly, their first conceptual model of the steep gradient provides a vertical path along the fault on the northern boundary of the graben that drains water from the brecciated lavas to the LCA. The downwelling of water along this fault is consistent with the local heat flow low. In their second conceptual model, a spillway is formed on the upthrown side of the fault by the juxtaposition of highly altered tuffs against the northern extent of the welded tuff aquifer. The abrupt transition from relatively impermeable units to very permeable units across the fault zone gives rise to the steep gradient.

8.2.2 Development of Hydrostratigraphic Cross Sections

A major goal of the Regional Hydrogeology Research Project is the acquisition or development of a detailed 3D hydrostratigraphic model of the Death Valley flow system. However, construction of this hydrostratigraphic model may prove difficult due to the large size of the region, the spatial variability of the stratigraphy, and the paucity of boreholes that penetrate the Paleozoic section. The boundaries of existing conceptual models of this system extend from Ivanpah Valley, California, in the south (Bedinger et al., 1989) to Big Smokey Valley in the north (Burbey and Prudic, 1991), and from the Silver Peak Range in the west [Rice (1984); Bedinger et al. (1989); Burbey and Prudic (1991)] to the Pahrangat Range in the east [Rice (1984); Rush (1971); Waddell et al. (1984); Bedinger et al. (1989)]. The area

covered by these conceptual flow models ranges from approximately 27,000 km² (Rush, 1971), to over 67,000 km² (Burbey and Prudic, 1991).

Existing hydrogeologic studies indicate three predominant regional-scale hydrostratigraphic units: (i) a series of valley-fill aquifers composed of Holocene to Pliocene alluvial and lacustrine deposits; (ii) the LCA composed of Devonian to middle Cambrian limestone and dolomite; and (iii) the lower clastic confining unit (LCCU) composed of lower Cambrian to Precambrian quartzite, shale, and siltstone (Winograd and Thordarson, 1975). On the Nevada Test Site (NTS), there are two additional Paleozoic hydrostratigraphic units: (i) the upper carbonate aquifer (UCA) composed of Permian to Pennsylvanian limestone; and (ii) the upper clastic confining unit (UCCU) consisting of Mississippian to Devonian shale, argillite, and quartzite (Winograd and Thordarson, 1975). These two hydrostratigraphic units, as well as the overlying Tertiary volcanic units, do not appear to extend throughout the entire Death Valley region. Other Tertiary volcanic units occur in other areas of the Death Valley region; however, their hydrogeologic properties are largely unknown.

The spatial density of boreholes from which the deep lithology can be inferred varies greatly over this large region. The density is greatest at Yucca Flat, Pahute Mesa, Rainier Mesa, and YM on the NTS, and at farming, ranching and mining operations near Beatty, Nevada, and the southern Amargosa Desert. Moreover, except for one wildcat oil well in Tickaboo Valley and two exploratory boreholes near the southern end of the Desert Range, most of the boreholes that penetrate the Paleozoic units are on the NTS. The accuracy of the 3D hydrostratigraphic model will be greatest within the NTS due to the large number of deep (>500 m) boreholes drilled for the weapons testing program and for the YM site characterization project.

The first three cross sections that are to be developed for the 3D hydrostratigraphic model will transect the regional steep gradient, which, except for the east-west trending reach in northern Crater Flat near Bare Mountain, is entirely contained within the NTS. The control provided by the relatively large number of boreholes penetrating the Paleozoic units as well as the surface exposure of Paleozoic units appears to be sufficient to construct cross sections perpendicular to the reach of the regional steep gradient parallel to the eastern slope of the Eleana Range and western edge of northern Yucca Flat. Unlike the model of the steep hydraulic gradient at YM presented by Fridrich et al. (1994), it is postulated herein that all reaches of the regional steep gradient are controlled by the Belted Range Thrust. Therefore, the deep stratigraphy of the Eleana Range-Yucca Flat cross section will be used to construct the initial hydrostratigraphic cross section through the YM steep gradient.

8.2.3 Eleana Range-Las Vegas Range Cross Section

The hydrostratigraphic cross section shown in Figure 8-1 extends from an area west of the Eleana Range on the NTS, southeastward through the Las Vegas Range. The section was modified from Caskey and Schweickert (1992); stratigraphic information concerning the lower clastic aquitard and LCA was obtained from unpublished information by James C. Cole of the U.S. Geological Survey, Denver, Colorado (Characteristics of the pre-Tertiary rock units at the Nevada Test Site and vicinity: Revision of May 3, 1995). Information regarding the Spotted Range thrust was derived from Barnes et al. (1982), and other details regarding surface geology were derived from Frizzell and Shulters (1990). The location of this cross section is shown in Figure 8-2. The patterned polygons shown in Figure 8-2 depict the pre-Cenozoic surface hydrostratigraphy (Wittmeyer et al., 1995), while the location of the cross section is designated

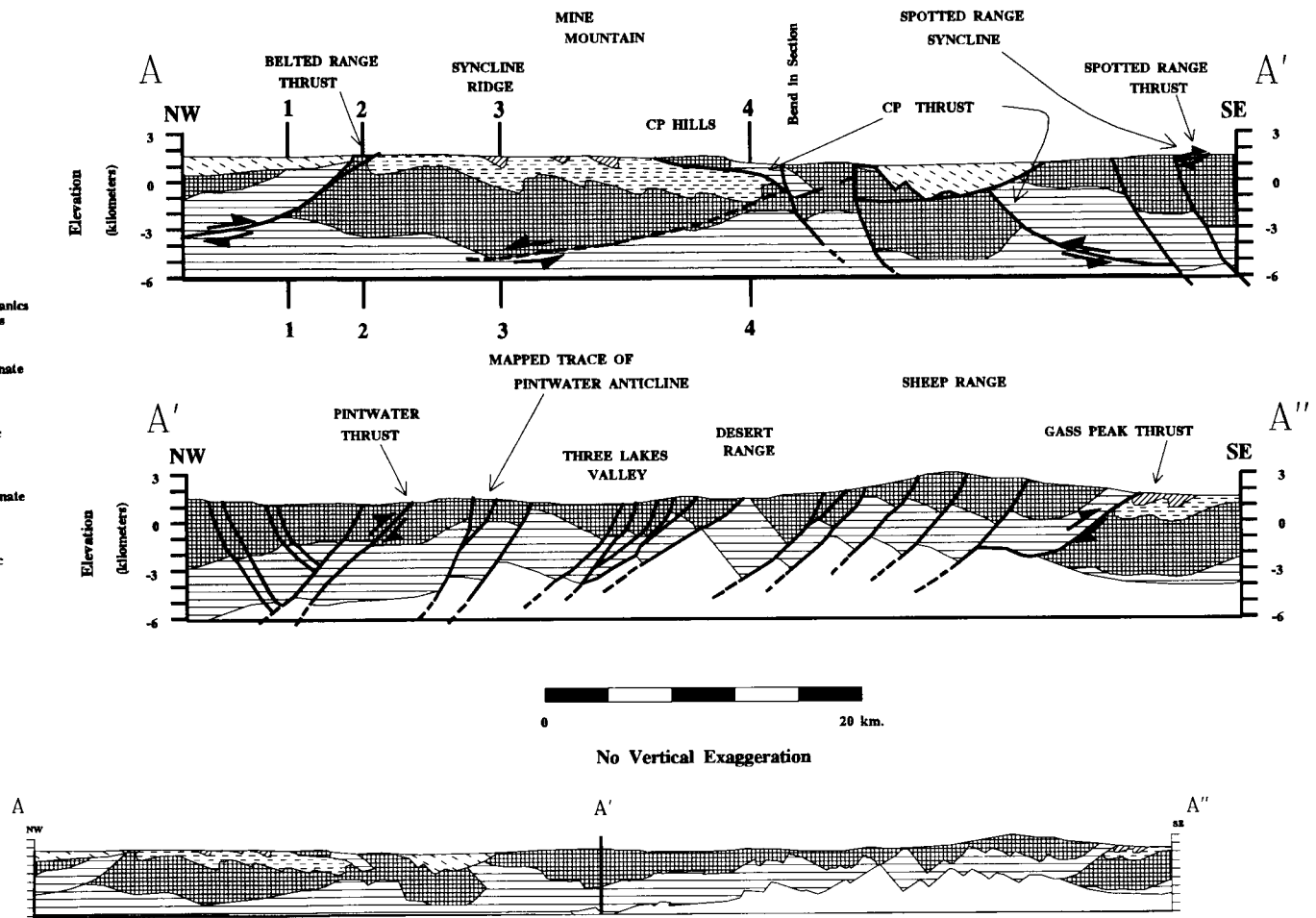


Figure 8-1. Eleana Range-Las Vegas Range hydrostratigraphic cross section

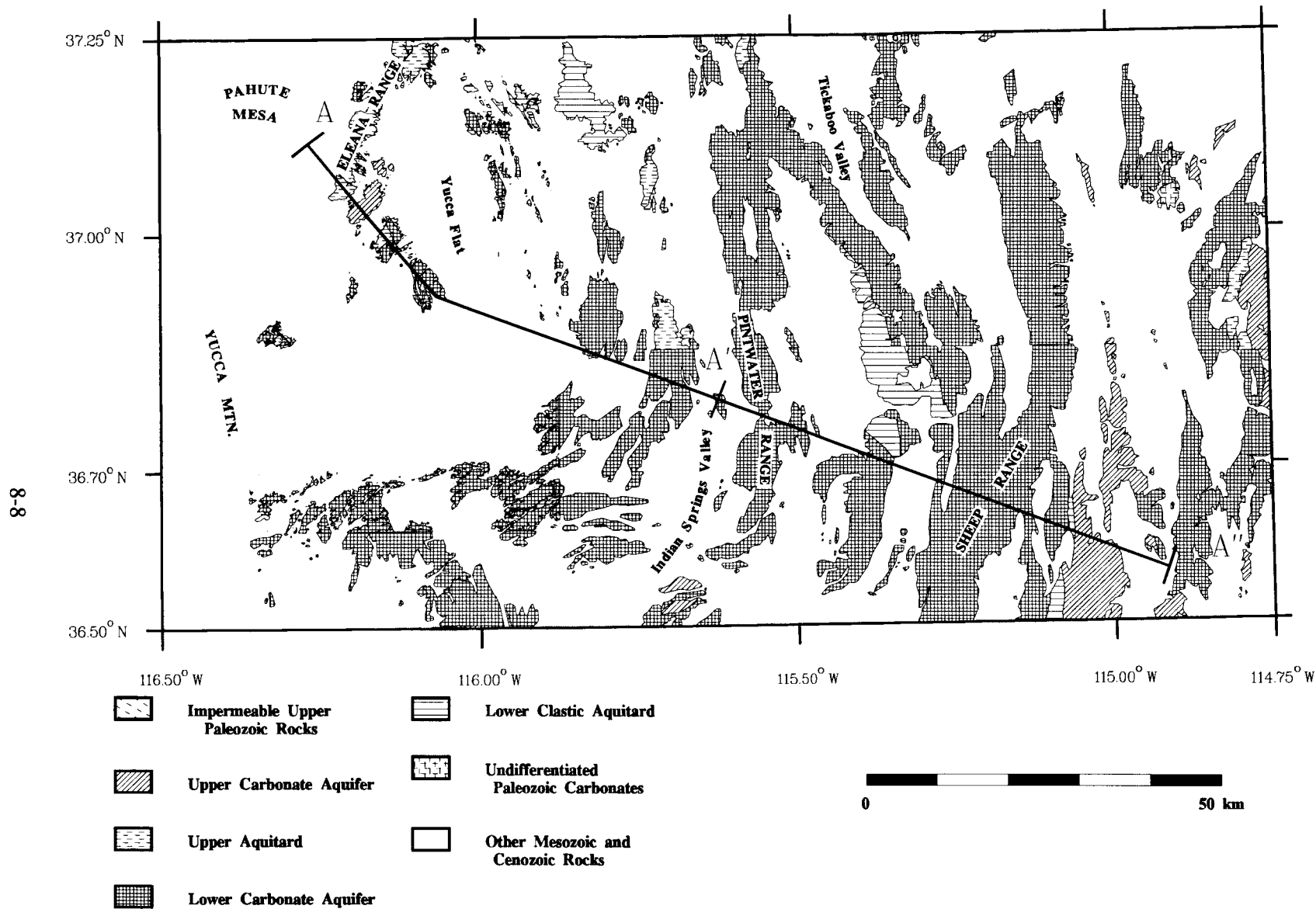


Figure 8-2. Location of Eleana Range-Las Vegas Range cross section overlain on pre-Cenozoic surface hydrostratigraphy

by A-A'-A". The base geologic maps that were used to construct Figure 8-2 were less detailed than those used to develop the cross section. Therefore, the surface hydrogeology along the trend in Figure 8-2 differs from Figure 8-1.

Caskey and Schweickert (1992) proposed a formal revision to the nomenclature for thrust faults lying in the area of the NTS. They recognized two separate, oppositely vergent thrust systems that had previously been called simply the "CP Thrust," a name originally assigned by Barnes and Poole (1968). This name had been used to refer to any structure in the area that thrust Proterozoic or Cambrian strata above younger Devonian or Mississippian rocks¹. Caskey and Schweickert (1992) proposed a clarification based on the recognition of these distinct opposing relationships. They gave the name "Belted Range Thrust" to the east-vergent thrust located northwest of Yucca Flat, and chose to restrict usage of "CP Thrust" for the west-vergent backthrust exposed in the CP Hills and at Mine Mountain.

Robinson (1985) recognized earlier the opposing vergence of the thrust systems. He informally referred to the west-vergent backthrust as the "Tippipah fault zone" prior to its designation as the Belted Range Thrust by Caskey and Schweickert (1992). Use of the latter term has since been incorporated into other literature [e.g., Cole et al. (1994)].

Evidence for the Belted Range Thrust comes from only a few pieces of geological information. At the NTS, isolated small outcrops of the Proterozoic/Lower Cambrian Wood Canyon Formation are present immediately north of Rainier Mesa at Gold Meadows (Frizzell and Shulters, 1990). The Paleozoic sequence is obscured by a cover of Tertiary volcanics southeast of this outcrop; however, Devonian carbonates outcrop farther southeast in the Eleana Range near Tongue Wash east of Rainier Mesa. Like the Wood Canyon strata, these carbonate rocks dip westward, and an undeformed sequence of beds would show progressively younger rocks toward the west (toward the Wood Canyon outcrops). However, the clastic Wood Canyon Formation represents a significantly older part of the geological sequence and is inferred to be thrust on top of the carbonate section. The actual contact lies under the intervening Tertiary volcanic cover with an estimated 6,100–7,600 m (20,000–25,000 ft) of stratigraphic throw¹. Other east-vergent thrust faults in the Eleana Range juxtapose the older on top of younger Eleana Formation rocks with significantly less stratigraphic displacement. These smaller thrust faults are considered to be splices of the footwall (referred to as "duplexing" in the footwall).

Further evidence of the Belted Range Thrust comes from subsurface data derived from well ER12-1, which is located near Tongue Wash immediately east of Rainier Mesa. The normal stratigraphic sequence has been extensively faulted to produce an almost random sampling of units. The complexly shuffled sequence includes rocks ranging in age from Ordovician to Mississippian (Cole et al., 1994), and Devonian carbonates overlie Mississippian clastic rocks at two separate elevations in the well (Drellack et al., 1991). It should be noted that Drellack et al. (1991) state that the oldest rocks recorded from well ER12-1 are Silurian (?) in age, although their report was issued before the completion of paleontological analyses. In addition, it has not yet been determined if the Mississippian rocks in ER12-1 represent the Eleana Formation or Chainman Shale. Drellack et al. (1991) state that the Mississippian rocks represent the Eleana Formation; however, their report was completed prior to the paper by Cashman and Trexler (1994), in which the Chainman Shale is distinguished from the Eleana Formation. The complex faulting observed in ER12-1 represents the subsurface expression of the Belted Range Thrust inferred from the surface geology described previously, along with subsequent extensional overprinting.

¹J. Cole, personal communication, 1995.

To the southwest at Bare Mountain, a similar relationship juxtaposes rocks as old as the Zabriskie Quartzite (Lower Cambrian) with the Eleana Formation [Mississippian and Upper Devonian? (Monsen et al., 1992)]. This fault has been called the Meiklejohn Peak thrust (Zhang and Schweickert, 1991) or the duplex zone of the Meiklejohn thrust (Snow, 1992), but is correlated with the Belted Range Thrust in the NTS (Figure 8-3). A number of structures on the NTS area make a sharp westward bend as they are followed toward the south. This same trend would make the position of the Meiklejohn thrust compatible with the Belted Range Thrust. They are also compatible in terms of their vergence and stratigraphic throw [maximum estimated displacement of 7,220 m (23,700 ft)]²; therefore, they are envisaged to be linked into a single fault system.

If the Belted Range Thrust is continuous with the Meiklejohn thrust at Bare Mountain, the fault would have a significant impact on groundwater flow patterns. As shown in Figure 8-1, the fault juxtaposes units of the LCCU with formations of the LCA and creates a structural high within the LCCU along the western side of the fault. This feature, therefore, would form a significant hydrologic barrier to flow from the Eleana Range to the west side of Yucca Flat.

8.2.4 Flow Regime Within the Eleana Range-Las Vegas Range Cross Section

As shown in Figure 8-4, the first leg of the projected trace of the Belted Range Thrust intersects the sinuous, regional steep hydraulic gradient at roughly a right angle. The contours in this figure show estimated steady-state water levels from Wittmeyer et al. (1995). Note that where intersected by the cross section, the hydraulic gradient is considerably smaller (0.034) than at YM (0.15) or across the Eleana Range-Yucca Flat area (approximately 0.12); however, the contour spacing is probably exaggerated by the inclusion of a water level measurement that causes a local high to the east-southeast of the bend in the cross section shown in Figure 8-2. Nevertheless, because the water-level contours and the first leg of the cross section are nearly orthogonal, one can assume that there is little flow in or out of the plane of the section. Since there is little flow in or out of the cross section, the hydraulic effects of the complex stratigraphy shown in Figure 8-1 can be determined by constructing a 2D vertical flow model.

The original 2D spatial domain extended horizontally from the northwestern end of A-A', southeast to the bend in section (Figure 8-1). Boreholes on the NTS are rarely deeper than 1,800 m (6,000 ft); however, the vertical extent of the original spatial domain was extended to a depth of more than 7,900 m (26,000 ft) to examine the influence of deeper hydrogeologic units on the shape and location of the hydraulic gradient. Five hydrostratigraphic units were defined: (i) the LCCU, (ii) the LCA, (iii) the UCCU, (iv) the UCA, and (v) the Tertiary tuff units (TTA). Because the flow regime was assumed to be steady state and because there were no non-zero prescribed flux boundary conditions or internal sinks or sources, absolute values of hydraulic conductivity were not required. The values of relative hydraulic conductivity ranged over two orders of magnitude with LCCU and UCCU being assigned a value of 1, TTA was one order of magnitude greater at 10, LCA was two orders of magnitude greater at 100, and UCA was assigned the value 200. The bulk hydraulic conductivity of both the LCA and the UCA is believed to be the result of extensive fracturing (Winograd and Thordarson, 1975). However, the UCA is assumed to be twice as permeable as the LCA because it lies closer to the surface at which the

²This figure was obtained using the geologic map of Bare Mountain (Monsen et al., 1992) and unpublished 1995 stratigraphic data of Cole et al. (1994); maximum displacement actually 23,690 ft, minimum displacement 14,040 ft.

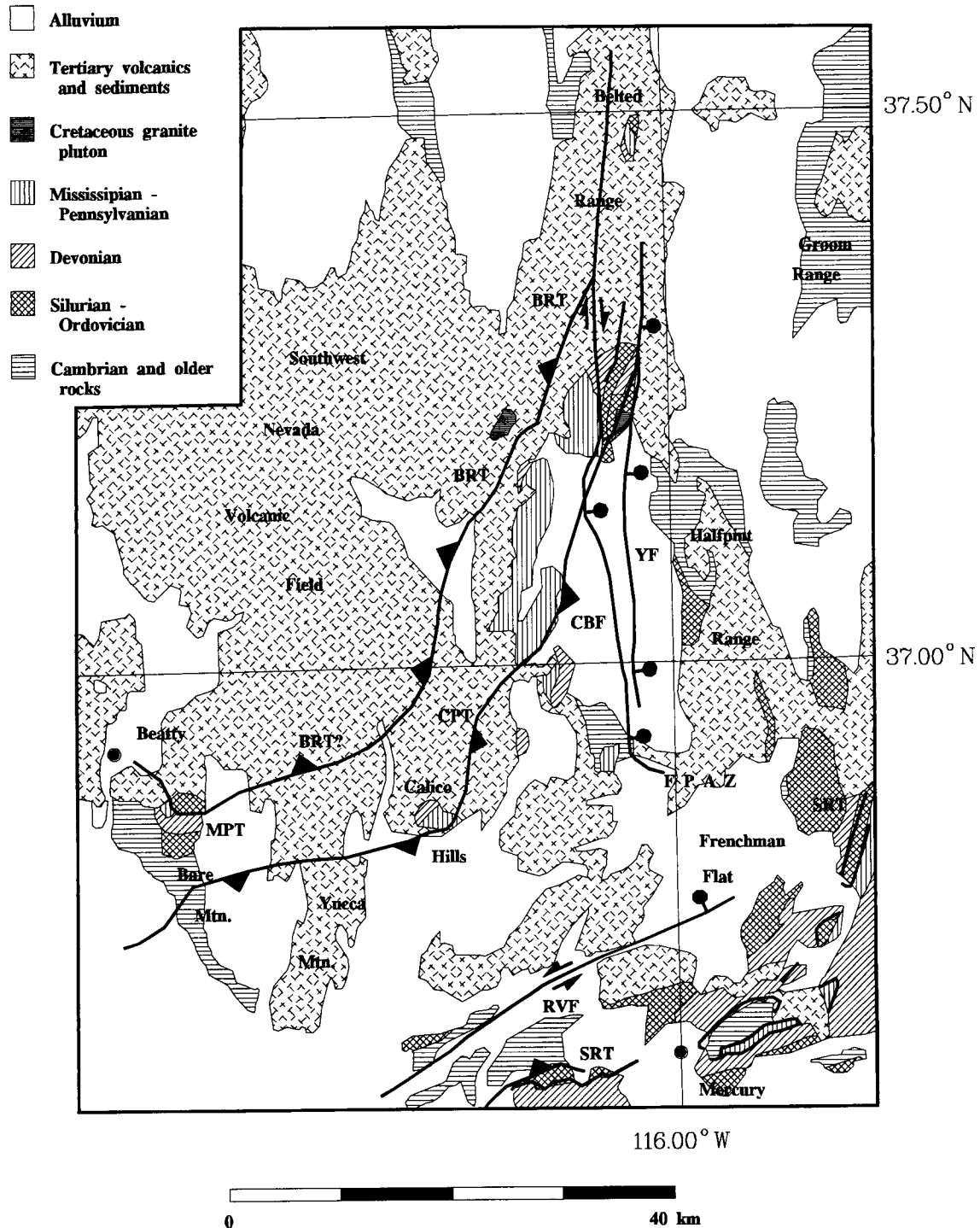


Figure 8-3. Simplified geologic map of the NTS region showing mapped and inferred locations of Mesozoic thrusts and other major tectonic features. BRT=Belted Range Thrust (Caskey and Schweickert, 1992); FPAZ=French Peak accommodation zone; RVT=Rock Valley Fault; SRT=Spotted Range Thrust; YF=Yucca Fault; CPT=CP Thrust; CBF=Carpet Bag Fault; MPT=Meiklejohn Peak Thrust (from Cole et al., 1994).

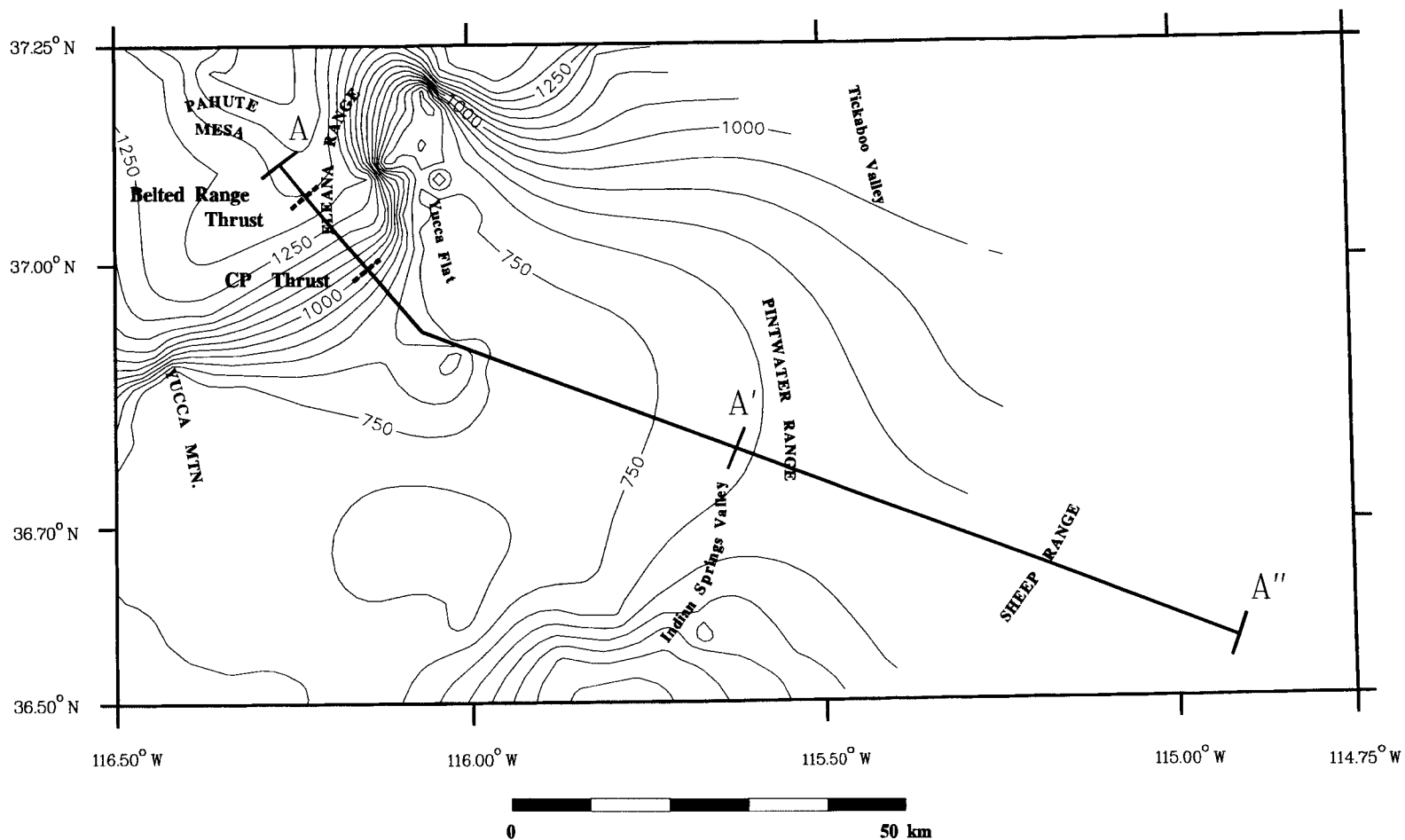


Figure 8-4. Location of Eleana Range-Las Vegas Range cross section overlain on water level contour map from Wittmeyer et al. (1995). Positions of CP and Belted Range thrusts conform to Figure 8-1.

lithostatic stress is less and the subhorizontal fractures are less likely to be closed. At the left and right vertical boundaries, hydraulic heads were set to 1,400 and 750 m, respectively. These prescribed head values were extracted from the water level contour map in Figure 8-4. The positions of the CP and Belted Range thrusts shown in Figure 8-4 are based on Figure 8-1 and do not conform to the interpretation of Cole (Figure 8-3).

Initially, the computer code PORFLOW-2.50 (Analytical & Computational Research, Inc., 1993) was used to model saturated flow in the 2D vertical cross section to make use of the code's ability to incorporate a free-surface boundary condition. However, the extreme contrast in hydraulic conductivity between adjacent computational cells transected by the free-surface appeared to cause convergence problems for the free-surface location algorithm. Consequently, a very simple method was adopted to model the hydraulic regime imposed by the hydrostratigraphic cross section shown in Figure 8-1. The flow regime was approximated by a steady-state, horizontally aligned, one-dimensional (1D) confined aquifer, in which the hydraulic conductivity along the horizontal was defined to be the depth-averaged hydraulic conductivity. Further simplification was attained by converting this 1D, two-point boundary value problem into an initial value problem. The flux through the 1D domain (0.4515 m/d) was computed by multiplying the harmonic mean of the vertically averaged hydraulic conductivity (26.682 m/d) by the mean hydraulic gradient $[(1,400-750) \text{ m}/38,412 \text{ m}=0.016922]$. Integration of the differential equation proceeded from left to right with the initial value given by the left-side prescribed head of 1,400 m.

The hydraulic head profile and the negative of the hydraulic gradient are shown in Figure 8-5. As shown by the head profile, the gradient is relatively steep at the extreme left and right of the section, with a relatively mild gradient in the center. At the points marked 1 and 4 in Figure 8-5, the hydraulic gradients are 0.058 and 0.050, respectively. The hydrostratigraphy at points 1 through 4 is shown in Figure 8-1. From Figure 8-1, it is apparent that the steepness of the gradient at point 1 is the result of juxtaposing the great thickness of low-permeability LCCU, a result of the Belted Range Thrust, against the much more permeable LCA. The steep gradient at point 4 appears to be caused by the thinning of the LCA, the thickening of the LCCU, and the placement of a portion of the LCCU over the UCCU and against the upper UCA by the west-vergent CP Thrust. At points 2 and 3 in Figure 8-5, the hydraulic gradients are 0.0066 and 0.0060, respectively. As seen from Figure 8-1, the relatively moderate gradient at point 2 occurs where the thickness of the LCA appears to be greatest and where the LCA has been pushed to the surface along the Belted Range Thrust. The mild gradient at point 3 appears to be the result of both the relatively thick section of the LCA and the thickest section of the more permeable UCA.

This cross section and its associated hydraulic head profile differ from the steep gradient at YM in that the model predicts two regions with steep hydraulic gradients, rather than one. In addition, the steep portions (0.058) of the head profile in this model have maximum gradients that are less than half the magnitude of that observed at YM (0.15). Nowhere does the slope of the flattest portion of the computed head profile approach that at YM (0.006 and 0.0001, respectively). However, this model does suggest that the presence of either the Belted Range Thrust or the CP Thrust beneath the thick volcanic units may explain the steep gradient at YM. Note in Figure 8-3 that the inferred traces of the two thrusts transect YM from the east to the west. However, based on the location of the steep gradient at YM and Figure 8-3, it appears that the CP Thrust is more likely to explain the steep gradient at YM than the Belted Range Thrust.

In a 2D flow regime, the complex hydrogeology of the cross section would induce significant vertical flow. However, the simple model used here assumes that the head contours are parallel to each other and perpendicular to the direction of flow. For this reason, the hydraulic head profile computed using this model may not accurately reflect the shape and location of the true water table.

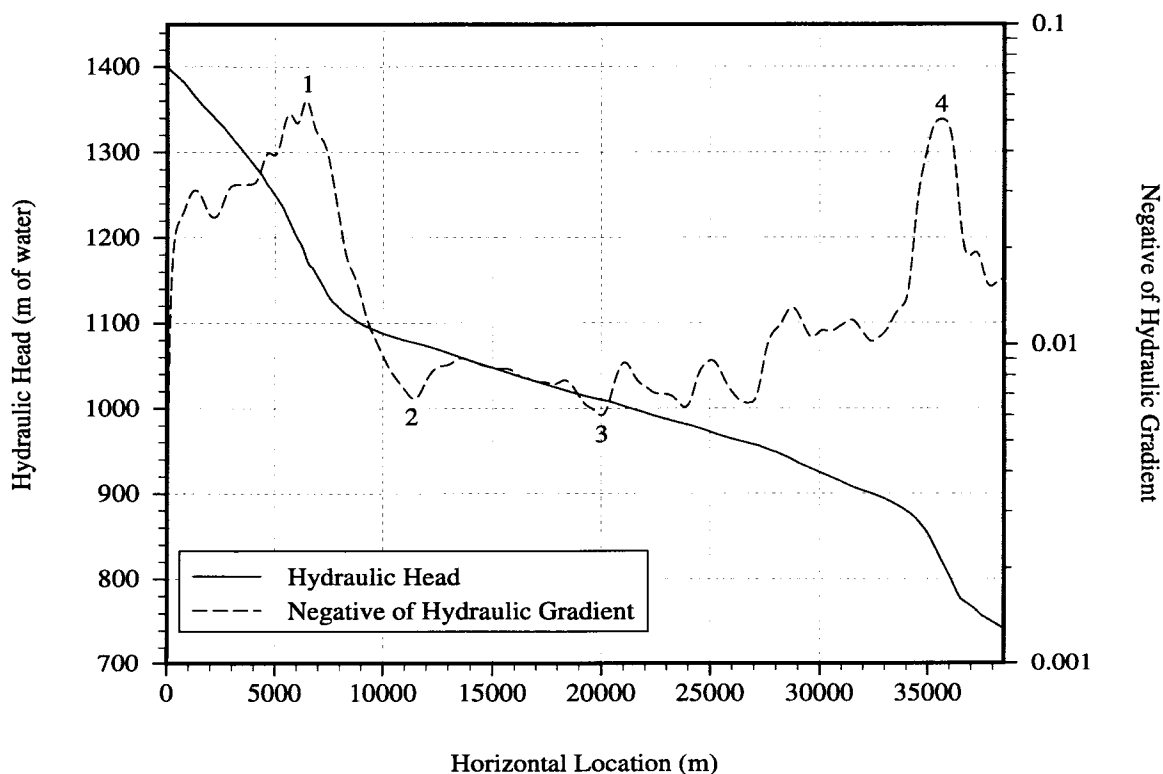


Figure 8-5. Predicted steady-state hydraulic head and hydraulic head gradient between the northwest terminus and the bend in the Eleana Range-Las Vegas Range hydrostratigraphic section

8.3 ASSESSMENT OF PROGRESS TOWARD MEETING PROJECT OBJECTIVES

During the past 6 mo, significant progress has been made in constructing new data sets, acquiring existing data sets, and developing new map coverages for the ARC/INFO GIS database for the Death Valley regional flow system. These efforts are summarized in Wittmeyer et al. (1995). In addition, some progress has been made in the last 2 mo toward the development of alternative conceptual models of the steep hydraulic gradient at YM and the regional steep hydraulic gradient extending along a sinuous path from YM, northeast to Groom Lake. A hydrostratigraphic cross section was constructed that extends from the Eleana Range, east-southeast to the Las Vegas Range. Major structural features included in this cross section are the Belted Range Thrust to the northwest and the CP Thrust to the east-southeast. Where the Belted Range Thrust has led to a thick section of the LCCU being placed above the LCA, a relatively steep hydraulic gradient is predicted using a simplified flow model. Where the west-vergent CP Thrust has placed a small portion of the LCCU over the LCA and UCA, a second relatively steep hydraulic gradient is predicted by the flow model. In the region between the Belted Range and CP Thrusts, the LCA attains its maximum thickness, which results in a comparatively mild hydraulic gradient. While the assumptions made in the construction of the flow model preclude determining the actual location of the free surface, the computed hydraulic head profile does provide an estimate of the horizontal variation of

the vertically averaged head. The model therefore suggests that one plausible explanation for the cause of the regional steep gradient is the presence of the Belted Range or CP Thrusts. By extrapolation, one may also infer that the same structural features, buried beneath a thick sequence of Tertiary volcanics, may cause the steep gradient at YM.

8.4 PLANS FOR NEXT REPORTING PERIOD

During the next reporting period, efforts will focus on construction of additional cross sections for use in the development of the 3D hydrostratigraphic model of the Death Valley region. Efforts will also continue on the preparation of a report describing existing conceptual models of the Death Valley flow system. To complete work on the hydrostratigraphic cross section presented in Section 8.2, a 2D or 3D flow code capable of accurately modeling the shape and location of the free-surface will be acquired or developed. After this code is obtained, a 2D vertical cross-sectional model will be constructed, and the predicted position of the free surface will be compared to that obtained from the simplified model described in Section 8.2.

8.5 REFERENCES

- Ahola, M.P., and B. Sagar. 1992. *Regional Groundwater Modeling of the Saturated Zone in the Vicinity of Yucca Mountain, Nevada: Iterative Performance Assessment—Phase 2*. NUREG/CR-5890. Washington, DC: Nuclear Regulatory Commission.
- Analytical & Computational Research, Inc. 1993. *PORFLOW User's Manual Version 2.50*. Bel Air, CA: Analytical & Computational Research, Inc.
- Barnes, H., and F.G. Poole. 1968. *Regional Thrust-Fault System in Nevada Test Site and Vicinity*. E.B. Eckel, ed. Boulder, CO: U.S. Geological Society of America: 233–238.
- Barnes, H., E.B. Ekren, C.L. Rodgers, and D.C. Hedland. 1982. *Geologic and Tectonic Maps of the Mercury Quadrangle, Nye and Clark Counties, Nevada*. U.S. Geological Survey Miscellaneous Investigations Series, Map I-1197, 1:24,000. Washington, DC: U.S. Geological Survey.
- Bedinger, M.S., K.A. Sargent, and W.H. Langer. 1989. *Studies of Geology and Hydrology in the Basin and Range Province, Southwestern United States, For Isolation of High-Level Radioactive Waste—Characterization of the Death Valley Region*. United States Geological Survey Professional Paper 1370-F. Washington, DC: U.S. Geological Survey.
- Burbey, T.J., and D.E. Prudic. 1991. *Conceptual Evaluation of Regional Ground-Water Flow in the Carbonate-Rock Province of the Great Basin, Nevada, Utah, and Adjacent States*. United States Geological Survey Professional Paper 1490-D. Washington, DC: U.S. Geological Survey.
- Cashman, P.H., and J.H. Trexler, Jr. 1994. The case for two, coeval, Mississippian sections at the Nevada Test Site. *Geological Investigations of an Active Margin*. S.F. McGill and T.M. Ross, eds. Geological Society of America Cordilleran Section Guidebook. Boulder, CO: Geological Society of America.

- Caskey, S.J., and R.A. Schweickert. 1992. Mesozoic deformation on the Nevada Test Site and vicinity: Implications for the structural framework of the Cordilleran fold and thrust belt and Tertiary extension north of Las Vegas. *Tectonics* 11(6): 1,314–1,331.
- Ciesnik, M.S. 1995. *Ground-Water Altitudes and Well Data, Nye County, Nevada, and Inyo County, California*. U.S. Geological Survey Open-File Report 93-89. Denver, CO: U.S. Geological Survey.
- Cole, J.C., J.H. Trexler, P.H. Cashman, and M.R. Hudson. 1994. Structural and stratigraphic relations of Mississippian rocks at the Nevada Test Site. *Geological Investigations of an Active Margin*. S.F. McGill and T.M. Ross, eds. Geological Society of America Cordilleran Section Guidebook. Boulder, CO: Geological Society of America: 66–75.
- Czarnecki, J.B. 1989. Characterization of the subregional ground-water flow system at Yucca Mountain and vicinity, Nevada-California. *Radioactive Waste Management and the Nuclear Fuel Cycle* 13(1-4): 51–61.
- Drellack, S.L., Jr., L.B. Prothro., P.H. Thompson, and R.L. McCall. 1991. *Preliminary Geology and Drill Hole Data Report for Groundwater Characterization Well ER12-1 Nevada Test Site, Nye County, Nevada*. Prepared for U.S. Department of Energy/Field Office, NV. Springfield, VA: National Technical Information Service: 77 p.
- Fridrich, C.J., W.W. Dudley, and J.S. Stuckless. 1994. Hydrogeologic analysis of the saturated-zone ground-water system, under Yucca Mountain, Nevada. *Journal of Hydrology* 154: 133–168.
- Frizzell, V.A., Jr., and J. Shulters. 1990. *Geologic Map of the Nevada Test Site, Southern Nevada*. U.S. Geological Survey Miscellaneous Investigations Series, Map I-2046, 1:24,000. Washington, DC: U.S. Geological Survey.
- Monsen, S.A., M.D. Carr, M.C. Reheis, and P.P. Orkild. 1992. *Geologic Map of Bare Mountain, Nye County, Nevada*. U.S. Geological Survey Miscellaneous Investigations Series, Map I-2201, 1:24,000. Washington, DC: U.S. Geological Survey.
- Nuclear Regulatory Commission. 1994. *License Application Review Plan for the Review of a License Application for a Geologic Repository for Spent Nuclear Fuel and High-Level Radioactive Waste*. NUREG-1323. Washington, DC: Nuclear Regulatory Commission.
- Rice, W.A. 1984. *Preliminary Two-Dimensional Regional Hydrologic Model of the Nevada Test Site and Vicinity*. SAND83-7466. Albuquerque, NM: Sandia National Laboratories.
- Robinson, G.D. 1985. *Structure of Pre-Cenozoic Rocks in the Vicinity of Yucca Mountain, Nye County, Nevada—A Potential Nuclear-Waste Disposal Site*. U.S. Geological Survey Bulletin 1647. Washington, DC: U.S. Geological Survey.
- Rush, F.E. 1971. *Regional Ground-Water Systems in the Nevada Test Site Area, Nye, Lincoln, and Clark Counties, Nevada*. United States Geological Survey Water Resources-Reconnaissance Series Report 54. Washington, DC: U.S. Geological Survey.

- Snow, J.K. 1992. Large-magnitude Permian shortening and continental-margin tectonics in the southern Cordillera. *Geological Society of America Bulletin* 104: 80–105.
- Waddell, R.K., J.H. Robinson, and R.K. Blankenagel. 1984. *Hydrology of Yucca Mountain and Vicinity, Nevada-California, Investigative Results through Mid-1983*. Water Resources Investigations Report 84-4267. Denver, CO: U.S. Geological Survey.
- Winograd, I.J., and W. Thordarson. 1975. *Hydrogeologic and Hydrochemical Framework, South-Central Great Basin, Nevada-California, with Special Reference to the Nevada Test Site*. U.S. Geological Survey Professional Paper 712-2. Washington, DC: U.S. Geological Survey.
- Wittmeyer, G., R. Klar, G. Rice, and W. Murphy. 1995. *The CNWRA Regional Hydrogeology Geographic Information System Database*. CNWRA-009. San Antonio, TX: Center for Nuclear Waste Regulatory Analyses.
- Zhang, Y., and R.A. Schweickert. 1991. Structural analysis of Bare Mountain, southern Nevada. *Geological Society of America Abstracts with Programs–1991 Annual Meeting*. Boulder, CO: Geological Society of America: A185–A186.

9 SUBREGIONAL HYDROGEOLOGIC FLOW AND TRANSPORT PROCESSES

by *Amvrossios C. Bagtzoglou, Peter C. Lichtner, Stuart A. Stothoff, and David R. Turner*

Investigators: Amvrossios C. Bagtzoglou, Hannah M. Castellaw, David A. Ferrill, Joyce Foegelle, D. Brent Henderson, Peter C. Lichtner, Kathy Spivey, Gerry L. Stirewalt, Stuart A. Stothoff, Timothy L. Tolley, and David R. Turner (CNWRA), Michael Muller, Sandy Nguyen, and Steven B. Seida (SwRI), and Mohan S. Seth (Consultant)

NRC Project Officer: Thomas J. Nicholson

9.1 TECHNICAL OBJECTIVES

Yucca Mountain (YM) was originally selected as a candidate high-level waste (HLW) repository site because: (i) it is situated in a remote location, (ii) the general area has a low population density, and (iii) it is characterized by an unsaturated zone, which, at places, is 700 m thick (U.S. Department of Energy, 1986). The favorable geochemical and hydrologic environment provided by this last condition led scientists to presume that high fluxes of water would not readily reach the repository, thus rendering unlikely the occurrence of corrosion and spent fuel dissolution. The complex hydrologic regimes associated with highly heterogeneous rocks, nonisothermal flow, and conductive structural features, such as fracture and fault zones have defined the need for further research regarding the suitability of the site for HLW disposal.

Research requirements dealing with such site characteristics as groundwater travel time (GWTT), favorable conditions (FACs), and potentially adverse conditions (PACs) relate to support of the Nuclear Regulatory Commission (NRC) staff's License Application Review Plan (LARP) (Nuclear Regulatory Commission, 1994). For example, understanding the subregional (site) and regional hydrogeology is required in order to determine the GWTT in the unsaturated and saturated zones. Other processes and phenomena of importance include, but are not limited to, the potential for flooding of the repository as a consequence of water table rise from meteorological or climatic changes, volcanism, or faulting. Furthermore, it will be necessary to assess the inherent variability and distribution of hydrogeologic and transport properties, initial and boundary conditions, hydro-geostratigraphic unit interfaces, and coupled effects modeling strategies used by the U.S. Department of Energy (DOE) to support estimation of GWTT and moisture fluxes.

In the NRC LARP, these research requirements are expressed in the context of several Key Technical Uncertainties (KTUs) that are influenced by, or pertain to, various subregional hydrogeologic flow and transport processes. These KTUs are: (i) Uncertainty in Determining Effects of Structural Deformation and Tectonic Processes on the Flow and Transport of Groundwater, (ii) Uncertainty in Identifying Geochemical Processes and Conditions That Affect Radionuclide Retardation and Determining and Predicting the Magnitude of the Effects at Yucca Mountain, (iii) Uncertainty in Developing a Conceptual and Mathematical Model for Transport of Vapor and Liquid Phase That is Representative of the Yucca Mountain Site Flow System, (iv) Uncertainty in Prediction on Future Changes to the Hydrologic System Resulting from a Combination of Climatic and Tectonic Changes and Human Activities (Including Heat Effects from Waste Emplacement and Future Groundwater Withdrawals), (v) Uncertainty in Determining the Fastest Path of Likely Radionuclide Travel From the Disturbed Zone to the Accessible Environment, (vi) Predicting Precipitation and Temperature (Climate) at the Yucca Mountain Site for

10,000 yrs into the Future, (vii) Uncertainties Associated with Variability of Model Parameter Values, and (viii) Uncertainties Associated with Development and Validation of Conceptual and Mathematical Models. It is useful to describe briefly some aspects of the hydrogeologic conditions prevailing at the site before formulating the specific objectives of this research.

First, the proposed repository is intended to be situated deep in unsaturated tuffs, about 300 m below land surface and 250 m above the water table (U.S. Department of Energy, 1988). Second, in addition to the presence of markedly distinct geologic units and faults, the geologic units are variably fractured. For example, the Topopah Spring welded unit, in which the proposed repository is to be located, is a low-porosity welded tuff believed to be densely fractured, while the underlying Calico Hills, a nonwelded-vitric or zeolitized unit, is a higher porosity, nonwelded tuff with seemingly much lower fracture density (U.S. Department of Energy, 1988). Finally, the net annual infiltration from rainfall and surface water over YM may vary from -1.0 to 5.0 mm/yr, from a mean annual rainfall of about 150 mm/yr. These mean values do not take into account the more extreme rainfall rates that may occur due to inter-annual fluctuations, inter-seasonal fluctuations, and individual storms. In addition, these values reflect only contemporary rainfall and infiltration conditions. Typically, groundwater flow assessments are made using simplistic, average infiltration rate models. This methodology may not be satisfactory for compliance demonstrations. The NRC needs to be cognizant of alternative infiltration models that could be applicable to the YM site. Under ambient conditions, it is likely that radionuclides released from the repository zone will be transported predominantly in the unsaturated flow regime. However, locally saturated flow conditions may also occur in the vadose zone, possibly due to short and intense rainfalls, due to extremes in climatic fluctuations on larger time scales, or due to repository-induced elevated temperatures.

The research conducted under the Subregional Hydrogeologic Flow and Transport Processes Research Project, hereafter called the Subregional Hydrogeology Research Project, is in direct response to NRC staff-identified research needs, supporting portions of the NRC LARP (Nuclear Regulatory Commission, 1994) related to the evaluations of DOE compliance with site-scale groundwater flow and transport requirements. The anticipated products of this research project will have a direct application to the LARP in the areas of: (i) evaluating overall system performance; (ii) appraising performance of the geologic setting (GS); and (iii) determining compliance with various siting criteria (i.e., PACs and FACs). In particular, the Subregional Hydrogeology Research Project will deal with issues identified in the LARP sections on assessment of compliance with FACs and PACs for the hydrologic system (including 3.2.2.1—Nature and Rate of Hydrogeologic Processes; 3.2.2.4—Unsaturated Zone Hydrogeologic Conditions; 3.2.2.3—GWTT Substantially Exceeding 1,000 yr; 3.2.2.9—Changes to Hydrologic Conditions; 3.2.2.12—Perched-Water Bodies; and 3.3—Assessment of Compliance with the GWTT Performance Objective). This research project will also contribute significantly to the execution of the Vertical Slice Implementation Plans, and in particular to resolution of the technical issue on “Location and Characterization of Structural Features which Significantly Affect Water and Vapor Movement.”

The activities of this Research Project address groundwater flow and transport assessment for selected technical issues associated with the following: (i) infiltration and recharge (both focused and distributed) processes, (ii) conditions and properties that contribute to perched-water zone development, (iii) thermally driven vapor-phase transport processes including coupled effects, and (iv) temporal and spatial distributions of initial and boundary conditions for site and repository-scale modeling. The Subregional Hydrogeology Research Project has been divided into seven tasks: Task 1—Peer Review; Task 2—Contribution to the Center for Nuclear Waste Regulatory Analyses (CNWRA) Semi-Annual Research Reports; Task 3—Development of Three-Dimensional (3D) Site-Scale Model; Task

4—Evaluation of Approaches for Estimating Infiltration and Recharge; Task 5—Characterization of the Potential for Present or Future Perched-Water Development; Task 6—Site-Scale Flow and Transport Modeling; and Task 7—Coordination of Apache Leap Tuff Site (ALTS) Studies.

9.2 SIGNIFICANT TECHNICAL ACCOMPLISHMENTS

During this period, the Subregional Hydrogeology Research Project has focused on: (i) developing approaches for evaluating uncertainties inherent in Geological Framework Models (GFM) of the YM site; (ii) updating the CNWRA databases, and associated models, with geological and hydrogeological information; (iii) developing an infiltration evaluation methodology, based on Geographic Information System (GIS) technology; (iv) compiling, evaluating, and combining available isotopic and geochemical data with the existing 3D GFM for the YM site; (v) combining surface complexation models with mass transport; (vi) enhancing the numerical code CTOUGH so that it can handle atmospheric interactions in a computationally efficient manner; (vii) conducting a peer-review of the project plan; and (viii) interacting with the University of Arizona NRC contractors and coordinating the field studies at the ALTS. In the following, progress made to date on four key areas of research is reported: (i) development of GFM at YM, (ii) estimation of spatial distribution of recharge factors at YM, (iii) evaluation of the potential for perched water development at YM, and (iv) surface complexation models and mass transport.

9.2.1 Development of Geological Framework Models at Yucca Mountain

by A.C. Bagtzoglou, D.B. Henderson, and G.L. Stirewalt

Because of the natural heterogeneity, stratification, alteration, fracturing, and other characteristics of the porous rock, significant variability of flow and radionuclide transport pathways and travel times is expected to occur at YM. Therefore, the development of detailed geostatigraphic models is an important first step in any flow and transport modeling activity. Geostatigraphic models used in early simulations of the YM site were developed using inadequate geologic information. The DOE, recognizing that simplistic approaches to modeling the YM geological framework lead to serious limitations in the generality of the flow and transport simulations, has launched an effort to produce a geostatistically-based hydrogeologic stratigraphy for YM (Wilson et al., 1994). However, before any of these geostatistical approaches can be applied, effort needs to be invested to make certain the GFM is realistic and consistent with available data. Moreover, an evaluation of conceptual uncertainties in the model developed often reveals areas in which differences between the model and available data are significant.

For example, consider the preliminary EarthVision 3D GFM described in the work of Stirewalt and Henderson (1995). This model, developed using the EarthVision software, comprises a stack of seven lithostratigraphic units. The model also includes three major structural features, namely the Bow Ridge, Ghost Dance, and Solitario Canyon Faults. Figure 9-1 depicts a plan view of the 3D model in the area south of Yucca Wash. The various shades of grey correspond to variations in the shaded topographic relief as determined from U.S. Geological Survey digital elevation data in Digital Elevation Model format at a 30-m pixel resolution under an illumination source at an azimuth of 105° and an elevation of 30°. This figure presents an approximation of the outcrop of the combined Topopah Spring subunits. The outcrop is located at the west side of Solitario Canyon and is presented in two distinct ways. The dark outline corresponds to the distributions of these subunits as projected by two successive versions, hereafter called iterations, of the CNWRA 3D geological framework model (GFM-1 and GFM-2). The white area corresponds to the distributions from the geologic map of Frizzell and Shulters (1990). A great degree of

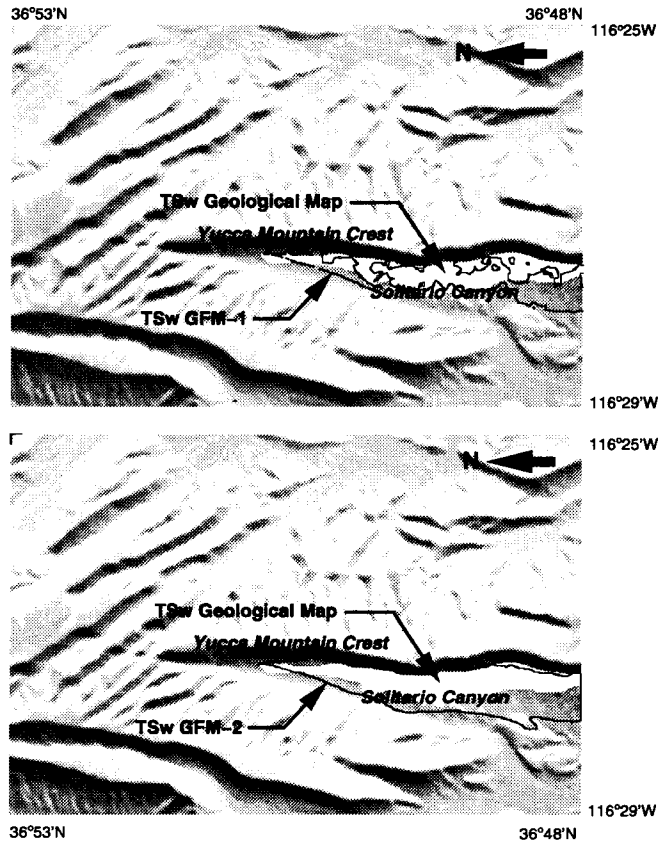


Figure 9-1. Topopah Spring welded unit outcrop as predicted by the CNWRA GFM, and comparison with geologic map of Frizzell and Shulters (1990)

similarity is evident between the two approximations and the geologic map. Both the total length and outcrop area are approximately the same. GFM-1 appears to be producing more tortuous and discontinuous patterns, whereas GFM-2 is substantially closer in appearance to the geologic map than GFM-1. The tortuous patterns in GFM-1 are a manifestation of higher degree polynomial surfaces being fitted to local data at overlapping stratigraphic horizons. GFM-2 was developed from GFM-1 by removing data points from such overlapping horizons, thus producing smoother surfaces. However, near the south part of the area under investigation, both approximations disagree substantially with the geologic map. Since geologic maps are also prone to highly subjective interpretations and uncertain data, rather than classifying the areas where differences exist as areas of low accuracy, it is more appropriate to classify them as areas of high uncertainty, deserving to be identified as candidates for further model refinement, more detailed field mapping, or both. In this work, all iterative enhancements in the realism of the geological model(s) are being evaluated using image-processing techniques (i.e., *normalized cross correlation*) of unit outcrops. The normalized cross correlation approach displaces one image over another by a certain distance, within some predetermined search window, and evaluates the cross correlation of one image with respect to the other. It also provides an estimate of the translational component (in terms of numbers of pixels) required so that the two images are more closely correlated. A normalized cross correlation of unity indicates that the two images are exactly the same. As an example, for the two CNWRA GFM iterations, the results of the image-processing analyses are summarized in Table 9-1.

Table 9-1. Normalized cross correlation between the modeled and mapped Topopah Spring unit outcrop as a function of search window size (in pixels)

Comparison Between	Window Size				
	2	10	20	30	40
Geologic Map/(GFM-1)	0.259	0.303	0.309	0.309	0.309
Geologic Map/(GFM-2)	0.490	0.514	0.515	0.516	0.516

The moderate increase in the cross correlation, between GFM-2 and the geologic map, from 0.490 to 0.516 indicates the existence of a minor translational component. There exists an offset difference between the model and the geologic map equal to 5 and 1 pixels in the east-west and north-south directions, respectively. Also, GFM-2 is exhibiting a stronger cross correlation with the geologic map than GFM-1 for all search window sizes. The method developed, and reported herein, will be applied to: (i) constraining the geologic units comprising the framework model of YM; (ii) providing the framework over which geostatistical variability can be incorporated into the CNWRA GFM; and (iii) evaluating the unit outcrop spatial distributions and their associated uncertainty, which feed directly into the GIS-based infiltration evaluation methodology, presented in Section 9.2.2.

9.2.2 Estimation of Spatial Distribution of Recharge Factors at Yucca Mountain

by S.A. Stothoff, A.C. Bagtzoglou, and H.M. Castellaw

Determining compliance with the performance objectives for both the repository system and the GS requires prediction of groundwater flow. Since infiltration is one of the possible sources of water in the subsurface, the amounts and locations of infiltration are controlling factors in the movement of groundwater throughout the GS. In fractured, unsaturated rock, such as that found at the YM site, occurrence of infrequent, high-intensity rainfall events may modify, perhaps drastically, the subsurface flow regime from the one predicted by assuming that all rainfall events have averaged intensities. Indeed, the DOE has concluded that the spatial and temporal distribution of infiltration may be the most important factors influencing groundwater flow path development (U.S. Department of Energy, 1992). Deep percolation fluxes are affected by processes active in the near-surface zone, including evaporation, transpiration, liquid water flow, and vapor flow. Each of these processes is governed by several factors. For example, precipitation has been found to vary substantially over the YM region, both spatially and temporally, and winter storms are, in general, more uniform and of longer duration than summer storms (Hevesi et al., 1992a, b; 1994a). These observations indicate that, especially for summer storms, a spatially uniform precipitation pattern is clearly not applicable, even at the subregional scale. Similarly, evaporation from the ground surface is affected by air temperature, atmospheric vapor pressure, wind speed profile, incident solar radiation, surface soil and rock texture, plant activity, surficial temperature, and surficial moisture content. Many of these factors, such as surficial slope and orientation (which control incident solar radiation), surficial composition, and plant distributions, are or can be mapped at the YM site.

9.2.2.1 Technical Approach

Earlier studies of the YM GS assumed highly idealized material properties and forcing functions. As field studies progress, the models are becoming more sophisticated. To date, most numerical studies

of the long-term flow of moisture in the GS have assumed that the infiltration of water past the root zone, herein called recharge, is constant in both space and time, while recognizing that this assumption is questionable. This assumption has the consequence that flux rates at the repository horizon may be relatively uniform in space and time under certain conditions (e.g., horizontally uniform stratigraphy). If there are strong focusing mechanisms for moisture flow, there may be considerable impact on repository performance. A first step toward characterizing the spatial variability of potential recharge was presented by Flint and Flint (1994), in which the unsaturated hydraulic conductivity was estimated for the top layer in each grid block in the Wittwer et al. (1993) 3D site model. Using the depth at which seasonal variations of moisture content in the porous media diminish as a reference depth, the present-day moisture content at the reference depth is used to assess the unsaturated hydraulic conductivity. Applying a unit-gradient assumption to this hydraulic conductivity and neglecting fracture flow, yields an areally averaged flux of 1.4 mm/yr, with a high value of 13.4 mm/yr and a low value of 0.02 mm/yr.

In the work presented herein, the idea of using an index to examine the spatial variability of potential recharge is being extended to account for additional characteristics of the near-surface environment at YM. Each characteristic, or potential recharge index, forms a grid-layer in an ARC/INFO GIS database. The ARC/INFO, a GIS toolset, is available from Environmental Systems Research Institute Incorporated. GIS systems consist of software applications closely coupled to a geographic database. Major GIS functions include spatial operations, data linkage, and database manipulations. Spatial operations enable spatial relationships in data to be explored. GIS systems store data in relational databases, enabling associations of data sets from a variety of sources to be accessible through a common interface. When the appropriate factors affecting infiltration are associated using ARC/INFO, potential recharge may be estimated through the implementation of simple phenomenological conceptual models. Using the database manipulation capability of ARC/INFO, sets of grid-layers can be superimposed to find zones with concatenating potential recharge indices, which presumably would be high recharge areas. The surface elevation data have the finest resolution used in the study, at a 30x30-m pixel size; all other indices are interpolated to the same resolution. For example, consider three grid-layers describing the evapotranspiration potential, topographic relief, and soil type. Consider further, that at a particular location the grid indicates that the evapotranspiration potential is very low, the ground is almost flat, and the soil is sandy. Then, using the ARC/INFO database manipulation capability, one could easily determine that at this particular location the recharge potential is very high.

Potential recharge indices can be categorized, depending on whether the index affects precipitation, evaporation, transpiration, rate of flow underground, or runoff. Indices based on various properties relevant to fractured porous media have fundamental effects on potential recharge. Examples include the matrix hydraulic conductivity, fracture density, fracture aperture distribution, and depth of alluvial cover. Such data are relatively sparse. By assuming that the measured data are indicative of the layer as a whole, and using available layer outcrop information, estimates of the spatial distribution of surficial media properties are obtained. Several representative values of each recharge index can be derived from the frequency distribution associated with each grid-layer. The values for all recharge indices are associated in selected, finite combinations. Each combination of values corresponds to one computational run in a one-dimensional (1D) numerical flow model. The results of each computational run provide estimates for the downward flux rate for each unique combination and, thus, a response surface can be developed for the flux rate. The values of all recharge indices will be evaluated, for each grid cell, through interpolation from the flux response surface, with the end result being a grid-layer depicting a contour map of recharge rates for the YM site. Figure 9-2 illustrates the concept of the GIS-based infiltration evaluation methodology in schematic form.

Simple recharge indices can also be derived purely from topological considerations, such as elevation, ground slope and orientation, and ground concavity. For example, potential insolation is affected by the ground slope, ground orientation, and ridge shadowing, all of which are highly variable in the YM washes above the proposed repository. Figure 9-3 depicts a color density map of the mean daily solar radiation, in dimensionless form, at YM on a typical winter day, chosen here to be February 1. Ground topography also affects wind profiles, which have an effect on potential evaporation and transpiration rates. Finally, temperature and atmospheric vapor density are also dependent on elevation.

9.2.2.2 Sensitivity Model

A 1D simulator is used herein to evaluate the effects of recharge indices on potential recharge. The simulator, BREATH (Stothoff, 1995), accounts for the transport of liquid, vapor, and energy in a porous medium under the influence of atmospheric forcings including longwave and shortwave radiation, atmospheric vapor density and temperature, precipitation, and wind speed. The model considers evaporation, but does not consider transpiration. The assumption that vegetation is not present is considered a conservative assumption as desert vegetation is quite effective in reducing net infiltration. The BREATH model further assumes that all precipitation takes place as rainfall (snow and ice are not considered). This assumption may not be conservative, as snow cover cuts evaporation losses and provides extended recharge periods when melting. Snow cover is known to occur at YM for periods of days to weeks. Also, any rainfall in excess of the soil capacity is assumed to run off, thus runoff and runoff water balances are not explicitly considered.

In all the simulations reported here, the BREATH simulator is presented with atmospheric boundary conditions based on data measured hourly or daily over a 10-yr period at a National Weather Service meteorological station (National Climatic Data Center, 1994). The station is located at the Desert Rock airport, approximately 30 miles from YM and several hundred meters lower in elevation. Radiation is not measured at this meteorological station, so simple models are used to estimate longwave radiation based on the reported values of cloud cover and air temperature. Shortwave radiation is estimated based on the theoretical insolation at the top of the atmosphere and the cloud cover. Also, precipitation is only reported on a daily basis; thus, daily precipitation is disaggregated based on hourly values for precipitation rate classes.

In arid and semiarid regions, distinct evaporation phases can be readily identified. Immediately following rainfall events, the soil is moist enough that the atmospheric conditions determine evaporation rates. After the top of the soil column dries out, evaporation is controlled by the rate with which the soil

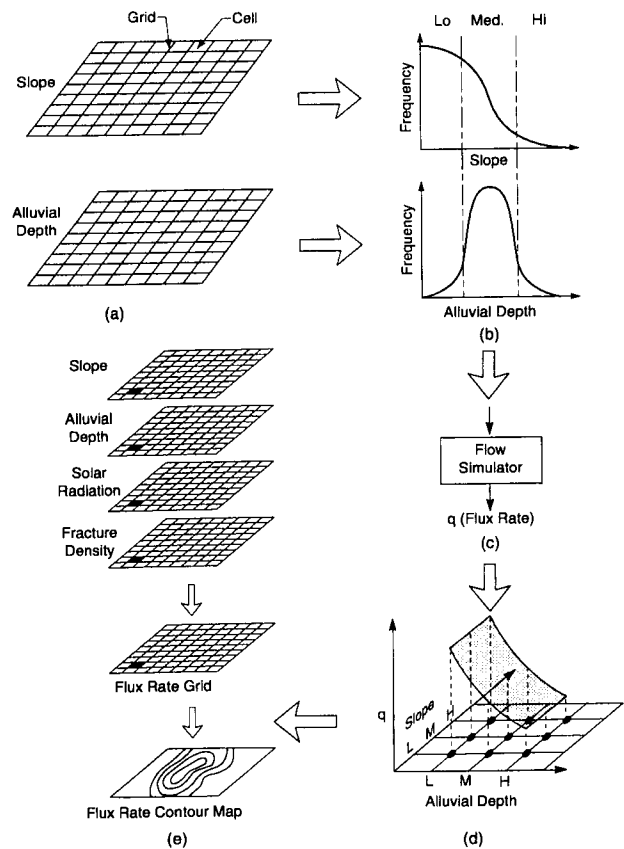


Figure 9-2. Schematic for GIS-based infiltration evaluation methodology

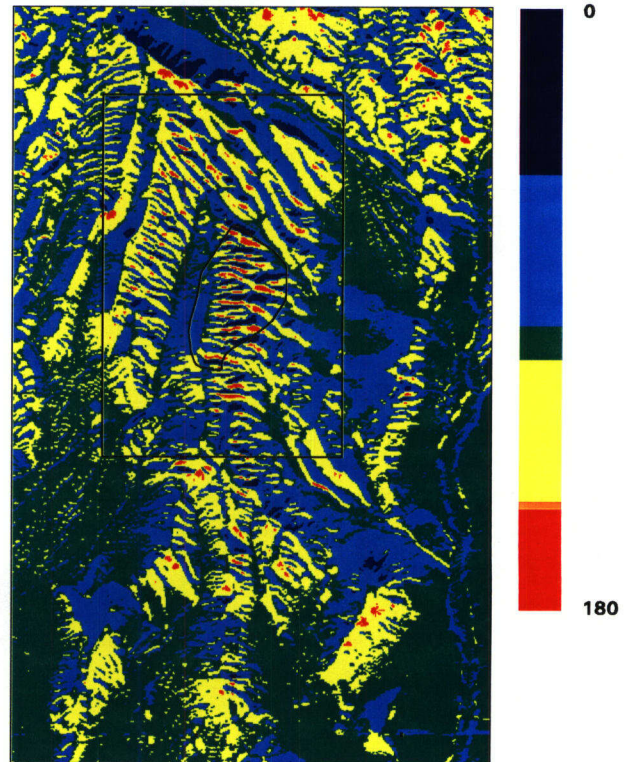
can deliver water vapor to the top of the column. Extensive testing of various averaging periods for atmospheric data has revealed that once the surface dries after a precipitation event, long-term average conditions are sufficient to capture the atmospheric boundary conditions, but hourly information is often necessary in the periods of time immediately surrounding precipitation events. Accordingly, one-month averaged atmospheric conditions are used, except in the 1 day immediately prior to and following each precipitation event. Simulations using this strategy run several times faster than simulations using the raw hourly data, and, depending on the porous medium, the difference in predictions of long-term average infiltration ranges from negligible to a maximum of about 10 percent. The deviation tends to become larger for situations with larger net infiltration rates.

9.2.2.3 Sensitivity Analyses

In order to identify processes that would be expected to have a strong impact on predicted values of long-term net infiltration, the sensitivity of the BREATH model predictions to weather and climatic boundary conditions is investigated using a hypothetical 30-m-deep vertical column of alluvium with homogeneous hydraulic properties representative of YM. At the bottom boundary, a unit-gradient condition is imposed, which is equivalent to a zero gradient in moisture content.

Thus, the only flux crossing the lower boundary is liquid flux due to gravity drainage. The lower boundary is placed sufficiently deep that gravity drainage occurs for a significant distance above the bottom boundary. As a result, the boundary condition has minimal impact on predictions. However, it must be noted that the unit-gradient assumption implicitly precludes net upward evaporative flux through the column, such as might occur with an underlying water table or perched water body.

In order to evaluate the sensitivity of model predictions to atmospheric boundary conditions, some performance measure is needed. Perhaps the most relevant performance measure is the long-term-average moisture flux crossing the bottom of the simulated column. The long-term average moisture flux is estimated by cycling the 10-yr sequence of boundary conditions until a cyclic steady state is achieved. When cyclic steady state is reached, the 10-yr-average moisture content profile is the same from decade to decade and the 10-yr-average moisture flux is identical throughout the column. For the columns considered herein, cyclic steady state is achieved in as little as a few decades for cases that have high net recharge rates. However, cyclic steady state may take centuries to millenia for cases with the lowest net recharge rates. For such slow-converging cases, simulations were often restarted with new initial conditions closer to an estimated steady state and trends in the decadal results were used to estimate average fluxes



Mean Daily Solar Radiation on February 1

Figure 9-3. Yucca Mountain mean daily solar radiation on February 1, of a typical year, as inferred from ARC/INFO calculations. Mean daily solar radiation is given in dimensionless units.

and average moisture contents. It is anticipated that the reported results are within 5 percent of the ultimate steady-state values, with moisture contents less accurately calculated than the corresponding fluxes.

Two porous medium columns are considered. For each medium, a base case simulation is run using the Desert Rock weather cycle. The sensitivity of the performance measure to each atmospheric boundary condition is evaluated by varying the mean of one boundary condition and maintaining all remaining conditions at their base case values. For the air-temperature boundary condition, a constant value is added to each hourly reading. For all other boundary conditions except for shortwave radiation, each hourly reading is multiplied by a constant value. As the shortwave radiation loading is strongly dependent on the slope of the ground surface, four additional cases are examined: a north-, south-, east-, and west-facing 30° slope. Only a small percentage of the ground surface in the YM area has a greater slope, so this represents a somewhat extreme case. Note that runoff and runoff are handled identically regardless of the assumed slope, so that the slope only affects the energy balance. The two porous media considered correspond to hypothetical alluvium properties that result in relatively large and relatively small amounts of long-term net infiltration. Alluvial properties for both cases are shown in Table 9-2.

The alluvial properties for the high-infiltration case, Case 1, are within ranges of properties reported in the works of Guertal et al. (1994), Hudson et al. (1994), Hevesi and Flint (1993), and Hevesi et al. (1994b). A somewhat counterintuitive decrease in net infiltration with increasing intrinsic permeability for soils at less than 50 percent saturation has been observed in the simulations reported here. Accordingly, the low-infiltration case (Case 2) is obtained by increasing the permeability somewhat beyond the reported values but maintaining all other properties identical.

For a given porous medium, an increase in long-term net infiltration is coincident with an increase in long-term-average moisture content. In Figure 9-4, the long-term net infiltration for each simulation is plotted versus the long-term-average moisture content in the gravity-drainage portion of the column. There is clearly a log-linear relationship between the long-term averages that is independent of which meteorological input is varied. The slope of the relationship is dependent on material properties. Of course, the log-linear relationship must break down once the medium approaches saturation.

In Figure 9-5, the cyclic steady-state fluxes are plotted for each perturbation. In general, all weather perturbations result in a larger absolute change in net infiltration but smaller relative change for the high-infiltration case. Average values and increments for each atmospheric and surface condition are

Table 9-2. Porous medium parameters used in sensitivity analyses

Properties	Value Used
Porosity	0.3
Air Entry Pressure (Pa)	2×10^5
van Genuchten $m=1-1/n$ Shape Parameter	0.1
Specific Storage Coefficient (1/cm)	10^{-5}
Depth (m)	30
Intrinsic Permeability for Case 1 (cm^2)	10^{-5}
Intrinsic Permeability for Case 2 (cm^2)	10^{-2}

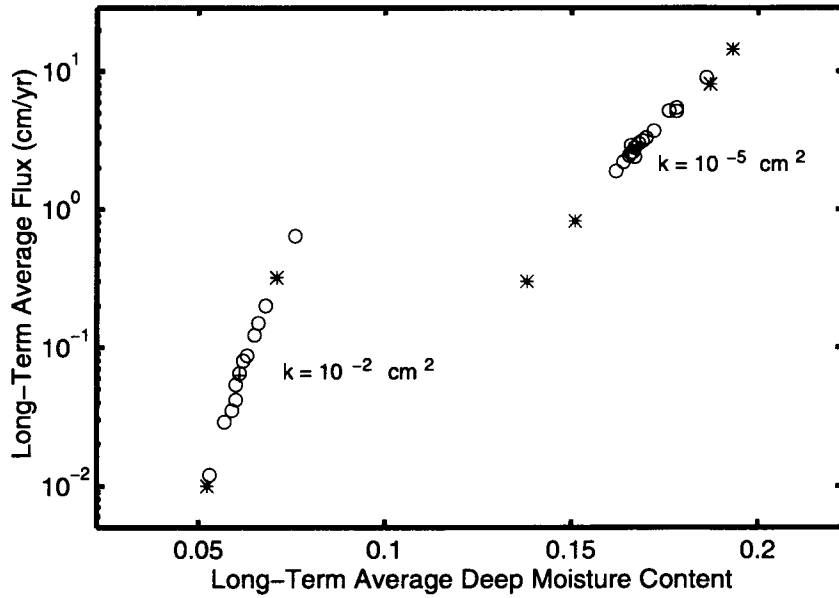


Figure 9-4. Relationship between average moisture content at 30 m depth and average flux through the column

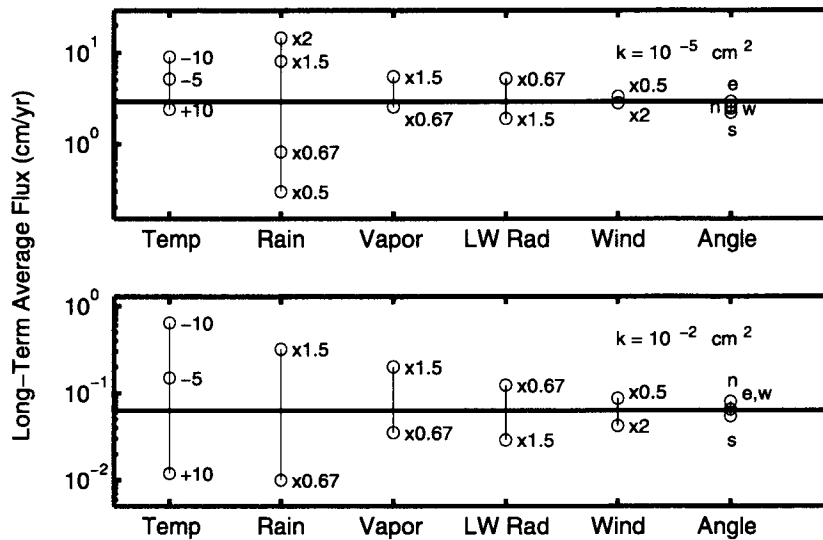


Figure 9-5. Sensitivities of average flux to various meteorologic forcings. The horizontal line is the base case flux.

labeled in Figure 9-5. The leftmost three perturbations—air temperature, rainfall rate, and atmospheric vapor density—are examined in ranges that are representative of climatic change or large elevation change. Mean air temperatures at YM may be expected to be cooler than the base case by a few °C over the range of YM elevations, so variation in net infiltration rates should be limited to a factor of two to three due to air temperature effects. Orographic effects should lower the average atmospheric water vapor density with elevation by some fraction of the range investigated, somewhat counteracting the effects of dropping atmospheric temperature with elevation. The variation in average rainfall over YM due to orographic effects is not expected to be large. Interestingly, the effects of temperature and vapor density are not symmetric; decreasing temperature or increasing vapor density has a larger effect than increasing temperature or decreasing vapor density.

The remaining sets of perturbations examine the effects of longwave radiation, windspeed, and solar insolation due to ground sloping 30° to the north, south, east, and west. The examined range in mean longwave radiation represents uncertainty due to the lack of measured data at Desert Rock and is intentionally large. As longwave radiation should be fairly uniform over YM, errors in incorporating longwave radiation should yield a bias of no more than a factor of two. Similarly, the windspeed range was selected to get a rough estimate of bias; windspeed has little effect on estimated long-term net infiltration.

The effects of the surface slope are particularly interesting. For the high-infiltration, rapid-redistribution medium, net recharge is almost insensitive to the solar loading, with the lowest recharge about three fourths of the highest recharge. The timing of rainstorms has a noticeable impact. For example, west-facing slopes have appreciably less recharge than east-facing slopes, despite getting somewhat less solar radiation, as high-intensity rainstorms usually occur during afternoons and evenings in the summer months. On the other hand, for the low-infiltration case, net infiltration is ranked strictly by total solar load, with the greatest net infiltration occurring where the solar load is least. The lowest recharge is about two thirds of the highest recharge. These simulations do not indicate that variation in solar loading has a large impact on net infiltration.

As net infiltration varies with average solar loading of the high-permeability medium but is impacted by short-term solar load variation for the low permeability medium, it may be inferred that evaporation from the high-permeability medium is under significant climate control for longer periods than from the low-permeability media. The implication follows that high-permeability media are able to support higher evaporation rates than low-permeability media, thereby leaving less water for net infiltration. Enhanced evaporation from high-permeability media would explain the counterintuitive finding that low-permeability media can exhibit higher infiltration rates than corresponding high-permeability media.

Two sets of observations place the current study in perspective. Meteorological data are available from a basin in central Nevada (McKinley and Oliver, 1994) at an elevation of over 2,100 m, which exhibits a mean air temperature 10 °C cooler, a mean vapor density about two thirds of the Desert Rock data, and about twice the precipitation. The elevation of Yucca Crest is roughly halfway between the central Nevada basin elevation and the Desert Rock elevation so the meteorological data represent an extreme well outside YM ranges and thereby provide a convenient range for sensitivities. The second set of observations arises from extrapolating the current results over periods of climatic change. Expert elicitation of future climate changes at YM over the next 10,000 yr from five experts (DeWispelare et al., 1993) yields predictions of temperature changes of 4 to -2 °C, precipitation changes of -20 to 90 percent, and cloud cover changes of -5 to 30 percent. The maximal increased cloud cover would increase calculated average longwave radiation by several percent and decrease calculated average shortwave

radiation by somewhat more than 10 percent, so that little impact on infiltration would be anticipated. The expert opinions of precipitation and temperature variation generally would yield little or no change in infiltration estimates over the next 5,000 yr, with infiltration dropping to, at most, half of current values. During periods of decreased temperature and increased precipitation, which may occur near the end of the 10,000-yr period considered, applying the calculated sensitivities to temperature and precipitation yields predictions of at least an order of magnitude more infiltration than presently might be observed. The increase in infiltration is primarily due to increased precipitation; however, the sensitivity to temperature would also yield significant increases in infiltration if the temperature were to drop several degrees more than anticipated.

9.2.3 Evaluation of the Potential for Perched Water Development at Yucca Mountain

by D.R. Turner and A.C. Bagtzoglou

The potential for existing or future perched-water bodies is identified in 10 CFR 60.122(c)(23) as a PAC for the disposal of HLW in a geologic repository. Current research at the CNWRA is developing geographic and geologic databases that can be used to identify and evaluate the potential for perched-water zones at YM, Nevada. Perched water is common in arid environments. For example, perched water flows from seeps in the zeolitized Indian Trail Tuff in the U12n tunnel at Rainier Mesa, 50 km northwest of YM (Thordarson, 1965; Russell et al., 1987; Wang et al., 1993). Isotopic signatures (δD and $\delta^{18}O$) indicate that the perched waters at Rainier Mesa are similar to modern meteoric waters and recharge relatively quickly from local winter precipitation (Russell et al., 1987). Evidence also suggests that waters from seeps in zeolitized tuffs are chemically similar to water from the unsaturated zone below the perched-water body, but are distinct from shallower waters (Wang et al., 1993). Preliminary field evidence from seeps and geophysical analyses suggests that perched water exists at the Peña Blanca natural analog site in Chihuahua, Mexico (Pearcy et al., 1993). A perched-water zone at the ALTS in Arizona (Bassett et al., 1994) can be distinguished from other water bodies on the basis of $\delta^{34}S$ analysis. Perched water at the ALTS occurs within a tuff unit, and initial ^{14}C age dates suggest that the water may be as much as 3,000 yr old. Finally, perched water has been encountered at YM in five air-drilled boreholes at depths of about 400 to 500 m (Burger and Scofield, 1994).

Perched-water bodies tend to be transient features that are formed where there is a contrast in hydrologic properties (Freeze and Cherry, 1979). These contrasts may result from differences between stratigraphic units. For example, permeability at YM tends to decrease with increased welding of the tuff units. Contrasts may also occur due to the juxtaposition of low-conductivity strata adjacent to more permeable strata along a structural feature such as a fault, or any other form of identifiable (e.g., through geophysical testing) geological persistent discontinuity. YM is crisscrossed by numerous faults, as can be seen in Figure 9-6, thus increasing substantially the possibility of this type of structural relationship and resultant perched-water bodies to exist. The rotation of these blocks may create a structural trap to permit accumulation of infiltrating water, allowing a perched-water body to form. The formation of a perched-water body also depends on whether the fault/fracture acts as a barrier to fluid flow or a conduit. Preliminary numerical analyses of the role of fault, presented by Bagtzoglou and Muller (1994), indicate that, depending on the properties of the surrounding material, fault zones can interchangeably act as both barriers and conduits to flow. Mineralogical changes within or between strata may also cause perched water due to a change in permeability. Such mineralogical changes within or between strata may also cause a change in permeability due to changes in volume or plugging of pore spaces during secondary

mineral formation. One example is the formation of relatively impermeable layers in response to alteration of primary phases such as feldspar to secondary clays such as kaolinite and smectite.

9.2.3.1 Methods for Constraining the Occurrence of Perched Water

Several lines of evidence may help to refine computer flow models used to evaluate the potential for formation of future perched-water zones at YM. To the extent possible, most of these methods should be applied in the context of a geographic and geologic framework to preserve the spatial aspect of the data that is site-specific to YM.

The first step toward enhancing modeling efforts is to construct a 3D geologic framework that embodies the current level of understanding of YM. As discussed in Section 9.2.1, current efforts under way at the CNWRA have produced a computerized geologic framework that includes lithostratigraphy, hydrostratigraphy, and geologic structure (Stirewalt et al., 1994; Stirewalt and Henderson, 1995) of the subregion. Lithostratigraphy and geologic structure are based on surface geologic maps of the site (Scott and Bonk, 1984). Subsurface geology is constrained by both well control and through the construction of balanced cross sections (Young et al., 1992). Hydrologic properties include porosity, saturated hydraulic conductivity, and water content. Original data are from DOE site characterization activities (e.g., Craig and Reed, 1991; Flint and Flint, 1990; Loscot and Hammermeister, 1992; Whitfield et al., 1993). It is important to note, however, that the currently available hydrologic properties are based on a relatively small data set, consisting of only 17 boreholes.

Faulting may create traps by placing low-permeability units in contact with high-permeability units across the fault plane. With a geologic and hydrostratigraphic framework of the YM subregion in place, it is possible to use first-level screening to identify regions within the model at which faulting might lead to conditions favorable to the formation of localized perched-water zones. These areas can then be examined in more detail to determine if the available hydrologic and geochemical data support the formation of perched water in the geologic past. One method for evaluating fault-controlled traps has been developed for the petroleum industry (Allan, 1989). This approach focuses on constructing cross sections in the plane of one of two intersecting faults. Calculating the volume of the trap geometry at the intersection (Figure 9-7) then gives some estimate of the maximum size of a potential perched-water body formed by faulting. It is

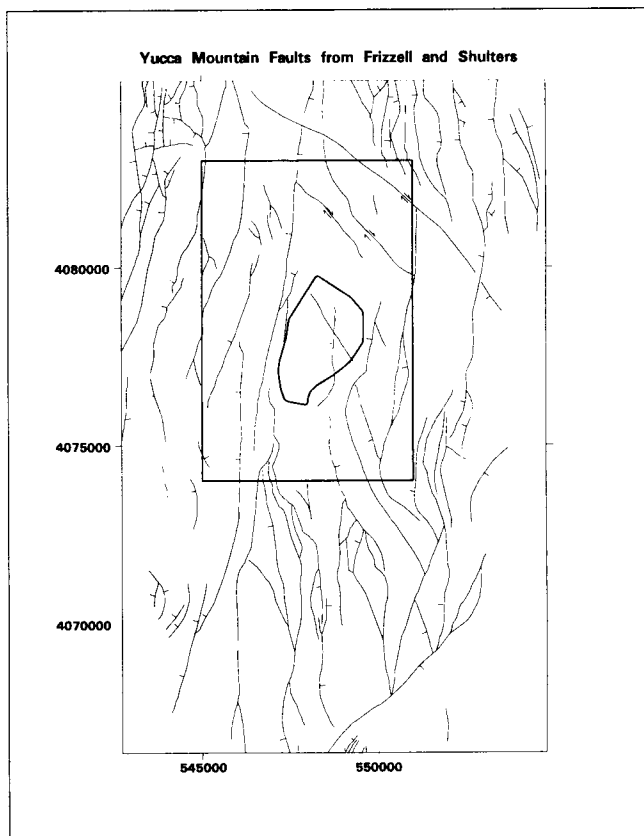


Figure 9-6. Major faults present in the YM site, as identified in the geologic map by Frizzell and Shulters (1990). Map coordinates are in Universal Transverse Mercator (UTM) units.

important to note that the use of Allan diagrams is simply an estimate of the volume of a geometry favorable to forming perched water. Depending on infiltration, a perched zone may or may not form. Its sustainability and transient characteristics are also dependent on the infiltration rates. In unsaturated rock, there is an additional complication with the dependence of hydraulic conductivity on the degree of saturation. As saturation varies, the relative hydraulic conductivities of juxtaposed units will also vary, and because of differences in porosity and pore size, this variation is likely to occur at different rates. At some saturation, the hydraulic conductivities will be equal, and as saturation decreases (or increases) past this point, the relationship between the relative hydraulic conductivities of the units in the trap may be reversed. In this fashion, the size and occurrence of potential localized perched-water bodies in unsaturated tuffs at YM can be determined as a function of saturation level.

Another means of refining computer models of flow at YM is to use available water and mineral chemistry to identify where perched water might have occurred in the geologic past. Hydrochemical facies and environmental tracers such as the stable isotopes have long been used to distinguish water bodies and to identify potential flow paths (National Academy of Sciences, 1992). Radiometric age dates can be determined for both mineral deposits and groundwaters and used to estimate rates of fluid flow and timing of changes in paleohydrological conditions. Because this information has a geographic and geologic context, it is best used in association with a GIS framework.

Chemical data are being gathered at YM as part of the DOE site characterization efforts. These data include groundwater chemistry of the unsaturated zone (Yang et al., 1988; Yang, 1992) and chemical and isotopic analyses of minerals deposited from past and present groundwaters (e.g., Bish and Chipera, 1989; Whelan and Stuckless, 1992). Trends in these data have been used to interpret paleohydrology and fluctuations in the static water table (National Academy of Sciences, 1992). For example, a decrease in $\delta^{18}\text{O}$ with depth for calcite (Figure 9-8) may be due in part to the geothermal gradient and partly to climatic changes (Whelan and Stuckless, 1992).

The current effort at CNWRA is focused on compiling, evaluating, and combining available isotopic and geochemical data with the existing 3D geological framework for the YM subregion (Stirewalt et al., 1994) to create coverages that provide a basis from which to evaluate the potential for perched water at YM. At present, geochemical data are available for over 20 wells in the subregion. Initial focus has been on mineralogy and mineral isotopes. In addition to characterizing the current conditions at the site, these types of data will also be used to define boundary and initial conditions for flow and transport at YM and to check model results. One example of combining mineralogical data with the geological framework is the cross section shown in Figure 9-9. Smectite as weight percent (Bish and Chipera, 1989) is superimposed on the lithostratigraphy of the 3D framework model. Plotting data in this fashion shows spatial trends in mineralogy related to stratigraphy. For example, smectite content increases toward the north, with the highest concentrations observed in well USW G-2. This trend is likely due to hydrothermal alteration that was associated with the Timber Mountain Caldera (Bish and Aronson, 1993) north of YM. Smectite content also varies with depth, with higher smectite concentrations occurring in fractured, welded tuff (high permeability) above bedded, nonwelded tuff (low permeability). Trends in mineralogy of this type point to areas of focused flow and help to delineate paleohydrology. High concentrations of clays such as smectite may also serve to create low-permeability zones that are favorable to the formation of perched-water zones. This situation may be enhanced at YM where both higher smectite content and higher infiltration rates (Flint and Flint, 1994) are found in the northern part of the subregion.

It is worth noting the scarcity of available water chemistry data that can be included in a 3D model. Data on unsaturated zone water chemistry are difficult to obtain, and the amount of data is limited

P = Permeable
I = Impermeable

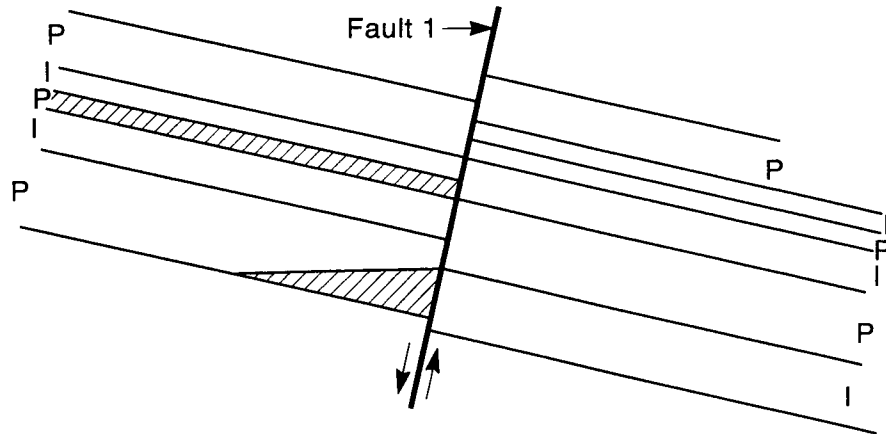


Figure 9-7. Cross section of a hypothetical fault-induced trap. Cross-hatched areas represent potential perched-water zones.

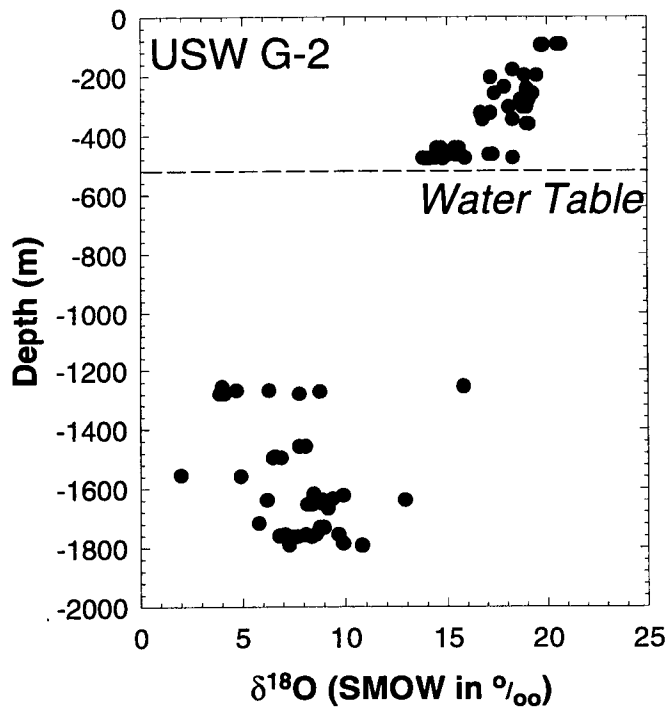


Figure 9-8. Depth versus $\delta^{18}\text{O}$ for secondary calcite (Data modified from Whelan and Stuckless, 1992)

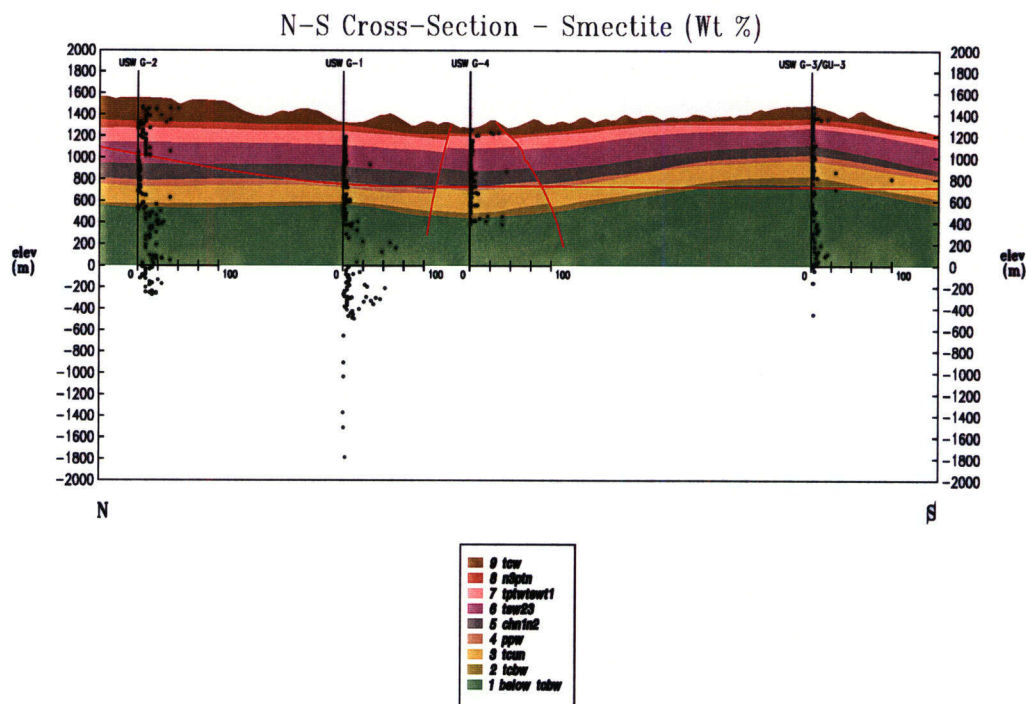


Figure 9-9. Smectite content (as weight percent) shown as a function of depth (Data modified from Bish and Chipera, 1989)

(Yang et al., 1988; Yang, 1992). More water chemistry data are available from the saturated zone (e.g., McKinley et al., 1991), but these data are typically for integrated samples collected over the entire screened thickness of the aquifer(s) penetrated by a well. For this reason, it is difficult to assign a depth or stratigraphic level to these samples.

9.2.4 Surface Complexation Models and Mass Transport

by P.C. Lichtner and D.R. Turner

The possibility of release of radionuclides from the waste package and their migration to the accessible environment as dissolved constituents in groundwater is of fundamental concern to evaluating the suitability of YM, Nevada, as a potential HLW repository. One important mechanism for retarding radionuclide migration is sorption on mineral surfaces. This section discusses some of the complications that result from combining sorption reactions with a time-space description of solute transport by advection, diffusion, and dispersion coupled to homogeneous aqueous reactions and heterogeneous mineral precipitation and dissolution reactions.

Several sorption models, including ion-exchange and surface complexation, are currently in use. Surface complexation models have been used to model sorption of metal ions and ligands over a wide range of chemical conditions. The more sophisticated formulations of surface complexation models provide for incorporation of the electric double layer. These models are based on the hypothesized formation of

surface complexes at the mineral-solution interface analogous to the formation of aqueous complexes. Because of the difficulty in identifying species complexes on mineral surfaces, surface complexes generally serve more as fit parameters than as actual representations of physical species.

A fundamental difficulty that arises when combining surface complexation models with mass transport is maintaining electric neutrality in the aqueous solution. Although electroneutrality is maintained in a closed static system, an open system involving diffusive and advective transport of an aqueous solution that is initially electrically neutral may not remain so as the system evolves in time. This effect of charge imbalance does not occur with ion-exchange models because for each ion sorbed, an equal amount of charge is desorbed and released into solution. Hence the aqueous solution always remains electrically neutral. This electroneutrality need not be the case, however, with surface complexation models. The cause of charge imbalance in these models results from the variable number of occupied surface sites that, in general, changes with time and distance.

9.2.4.1 Application of Surface Complexation Models to Sorption of Np^{5+} and U^{6+}

The geochemical speciation code MINTEQA2 (Allison et al., 1991) has been developed to implement several different types of surface complexation models. Based on the assumed analogy between reactions at the mineral-water interface and aqueous complexation reactions in the bulk solution, MINTEQA2 uses mass action and mass balance constraints to calculate the distribution of a given species between the sorbed and aqueous phases. For the purposes of evaluating problems relating to HLW disposal, the MINTEQA2 thermodynamic database has been modified at CNWRA to include equilibrium constants for actinides and other radionuclides (Turner, 1993). Surface complexation model parameters, determined based on batch sorption experimental data, are also available for a number of radionuclide-mineral systems (Turner, 1995). Output format from MINTEQA2 was modified slightly to directly compute the distribution coefficient (K_d in mL/g) that is commonly used in performance assessment transport calculations.

MINTEQA2 was used to calculate sorption of U^{6+} and Np^{5+} on goethite in a batch system over a range in pH. The Diffuse-Layer surface complexation model was used (Allison et al., 1991), and the assumed surface reactions and their binding constants are given in Table 9-3. Other model conditions are given in Table 9-4. In this preliminary analysis, the complete groundwater chemistry at YM is not considered, but a relatively dilute system has been assumed, similar to the ionic strength of water from well J-13. The results for the batch distribution coefficients for U and Np are shown in Figure 9-10 plotted

Table 9-3. Surface complexation reactions for sorption of uranium and neptunium on goethite

Reaction	Log K
$>\text{FeOH}^0 + \text{H}^+ \rightleftharpoons >\text{FeOH}_2^+$	9.17
$>\text{FeOH}^0 - \text{H}^+ \rightleftharpoons >\text{FeO}^-$	-7.35
$>\text{FeOH}^0 + \text{UO}_2^{2+} + 2 \text{H}_2\text{O} - 3\text{H}^+ \rightleftharpoons >\text{FeOUO}_2(\text{OH})_2^-$	-10.19
$>\text{FeOH}^0 + \text{NpO}_2^+ \rightleftharpoons >\text{FeOHNpO}_2^+$	5.21

Table 9-4. Diffuse-layer (MINTEQA2) model parameters used

Parameter	Value
Solid Concentration	1 g/L
Site Density	2.3 sites/mm ²
Surface Area	50 m ² /g
Total Site Concentration	1.9×10 ⁻⁴ moles sites/L
Ionic Strength	0.001 M NaCl
Total U ⁶⁺ , Np ⁶⁺	10 ⁻⁷ M
pH	2–12

as a function of pH ranging from 2 to 12. For both actinide-goethite systems, sorption is strongly affected by pH, increasing with increasing pH to a maximum, and then declining slightly at higher pH. For the U⁶⁺-goethite system, the sorption maximum is reached at pH 6 to 7, while the calculated sorption maximum for Np⁵⁺-goethite is at a higher pH (9 to 10). Over most of the pH range considered, sorption on goethite is typically several orders of magnitude greater for U⁶⁺ as compared to Np⁵⁺. Calculated U⁶⁺-goethite sorption is also more strongly affected by pH, with K_d increasing by about nine orders of magnitude from pH 2 to 7, as compared to a five order of magnitude increase in the K_d for Np⁵⁺-goethite.

The introduction of carbon into a batch system has been shown by experiment to reduce actinide sorption at higher pH (e.g., Hsi and Langmuir, 1985). The current modeling also predicts reduced actinide sorption in the presence of carbonate. The conceptual model used here does not invoke the formation of any actinide-carbonate surface complexes (Table 9-3), and relies on the formation of aqueous actinide complexes with carbonate over much of the pH range considered to effectively compete with the mineral surface. For the U⁶⁺-goethite system, the formation of strong uranyl-carbonate complexes [Figure 9-11(a)] reduces the predicted K_d by about an order of magnitude over much of the pH range (about 4 to 10). As the uranyl-carbonate species decrease at higher pH (>10.5) relative to the more hydrolyzed uranyl species UO₂(OH)₃ and UO₂(OH)₄²⁻, the predicted sorption for carbon-free and carbonate systems converge. Calculated sorption for Np⁵⁺-goethite is also reduced in the presence of carbon, but by much less than for the U⁶⁺-goethite system. This reduced sorption is due to the lack of a strong Np⁵⁺-carbonate complex [Figure 9-11(b)]. For example, NpO₂CO₃ does not become significant until at a relatively high pH, and only becomes a dominant aqueous species over a relatively narrow pH range (9 to 10). As can be seen from Figure 9-10, the K_d predicted from the surface complexation model is highly dependent on the solution composition.

9.2.4.2 Combining Sorption Reactions with Mass Transport

Incorporating sorption reactions with mass transport leads to the spatial separation of different solute species resulting from their relative affinity to the sorbate. Sorption fronts may be self-sharpening or self-broadening depending on the shape of the sorption isotherm. An added complication is caused by the changing number and types of surface sites as minerals dissolve and precipitate. Surface site concentrations are inextricably tied to mineral abundances. The site concentration can be computed from

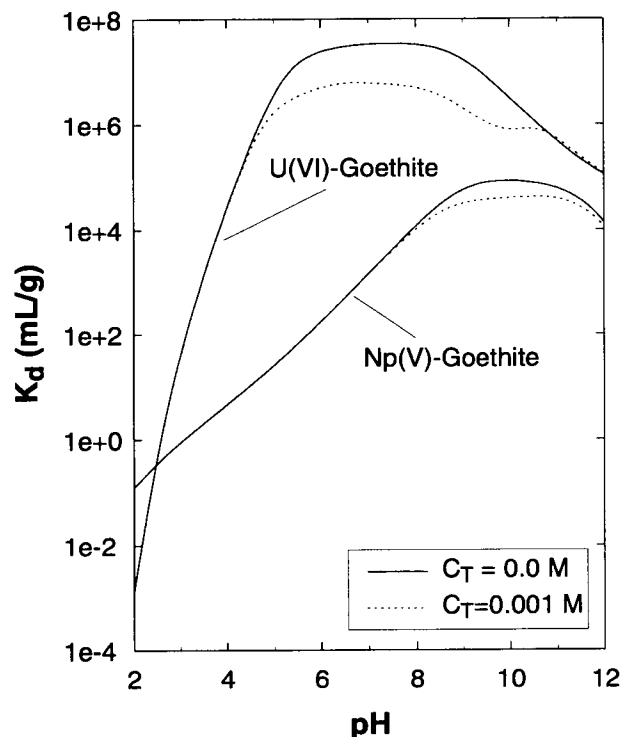
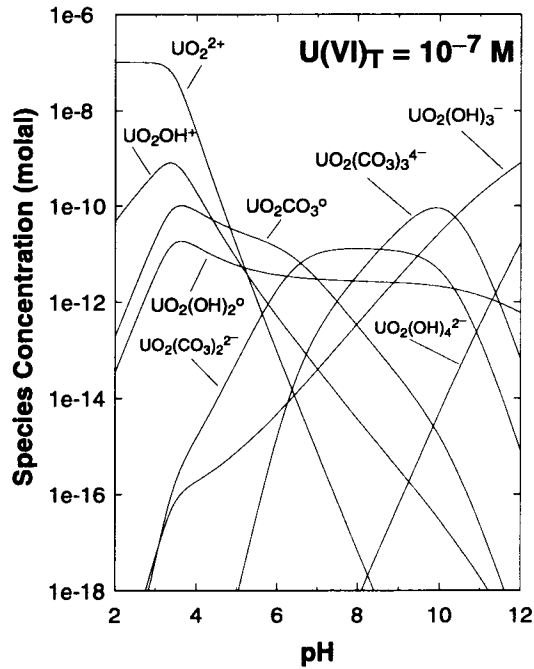


Figure 9-10. Logarithm of the distribution coefficient for sorption of uranium and neptunium on goethite plotted as a function of pH with (dashed curve) and without (solid curve) CO_2 present. Total carbon (C_T) in moles/L H_2O

the concentration of each mineral. Multisite surface complexation reactions may be formulated in terms of a set of independent primary species. Examples of such reactions have been presented in Table 9-3 for sorption of uranium and neptunium on goethite. Complications may arise, however, as a precipitation layer covers already occupied sites. In addition, as a mineral dissolves, surface sites are replaced by new ones. If it is assumed that the dissolution process is slow compared to the rate of adsorption, the new sites are instantaneously occupied by sorbing ions.

Electroneutrality of the aqueous solution is not automatically guaranteed when sorption reactions are combined with mass transport equations. For sorption models with a variable number of unoccupied sites, charge is not, in general, conserved using the standard sorption models when combined with mass transport. The nonconservation of charge in surface complexation models is directly related to the rate of change with time of the unoccupied site density. However, surface charge alone is not conserved in surface complexation models as it is in ion-exchange models. For example, in the electric double layer model, surface charge plus the charge contained within the diffuse layer is conserved. Therefore, one way to correct for nonconservation of charge is to include in the mass transport equations the contribution from nonspecific adsorbed ions contained in the diffuse layer. This property can be attained by introducing the surface excess concentration (Borkovec and Westall, 1983). The surface excess concentration in the diffuse layer may be positive or negative. Conservation of charge in the aqueous phase follows from conservation of charge of adsorbed and nonspecifically adsorbed species in the diffuse layer. This condition is simply the statement that surface charge is balanced by the total charge contained within the diffuse layer. For

(a) U(VI) Speciation



(b) Np(V) Speciation

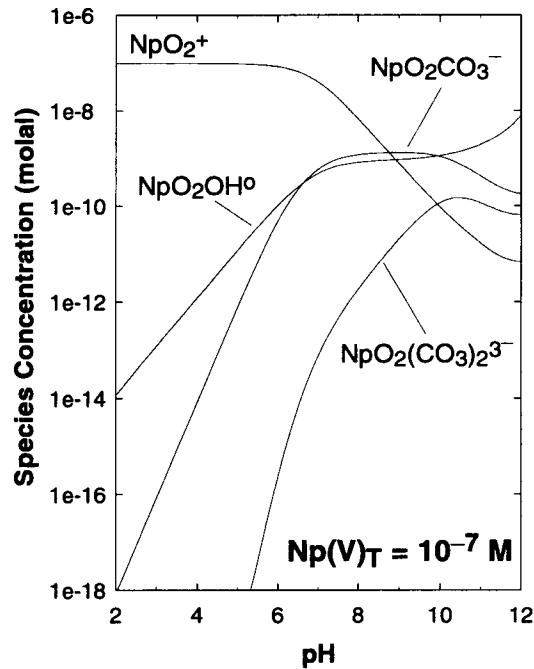


Figure 9-11. Logarithm of the concentration of selected (a) uranium- and (b) neptunium-bearing species plotted as a function of pH

the simpler surface complexation models that do not explicitly include the double layer, there does not appear to be any way to rigorously conserve charge when these models are combined with solute transport.

Retardation, important to transport of radionuclides in a radioactive waste repository, is influenced by nonspecific sorption of solute species in the electric diffuse layer as well as specific adsorption on the charged surface. Due to the fact that species in the diffuse layer are not transported in the bulk solution, they give rise to an additional retardation effect beyond that given by the specifically adsorbed species. The local distribution coefficient gives the ratio of total concentration of adsorbed species including contributions from both the specific and nonspecific adsorbed species to the aqueous concentration. The ratio of the distribution coefficients with and without the contribution from nonspecific adsorbed ions is close to unity if the contribution from nonspecific adsorbed ions is small compared to the specifically adsorbed ions. However, in general, because the excess double layer concentration may be positive or negative, the distribution coefficient may become negative or even vanish. The importance of the effect of incorporating charge conservation for sorption reactions into transport models still needs to be quantitatively addressed. The effect would be expected to be more important at low ionic strengths and for radionuclides that are not strongly retarded.

9.3 SUMMARY AND ASSESSMENT OF PROGRESS

NRC regulations in 10 CFR Part 60 for siting and performance require the DOE to provide sufficient site-specific data and analyses—including simulation models—to show compliance. The NRC licensing staff needs to assess the DOE submittals, including the Site Characterization Plan, Study Plans, Topical Reports, and, ultimately, the License Application, with respect to the characterization and modeling of subsurface water flow and radionuclide transport over large space-time scales at the YM site. The Subregional Hydrogeology Research Project is developing the technical knowledge base that will give the CNWRA the technical capabilities to independently support the NRC provision of appropriate, timely prelicensing guidance to the DOE. The methods, numerical tools, and concepts being developed and tested under this research project support the NRC in evaluation of studies or predictions of large-scale flow and radionuclide transport through the heterogeneous unsaturated fractured rock of YM. These capabilities will enable the NRC to regulate and make licensing decisions from an informed technical position concerning the disposal of HLW, as directed by the Nuclear Waste Policy Act.

Specifically, under Task 3, image-processing techniques have been implemented for the evaluation of the realism and inherent uncertainty in iterative enhancements of geological framework models at YM. Under Task 4, a GIS-based infiltration evaluation methodology has been presented, and a series of infiltration sensitivity analyses have identified processes that are expected to have a significant impact on predicted values of long-term net infiltration at the YM site. Efforts under Task 5 concentrated on isotopic and geochemical data compilation, evaluation, and combination with the existing 3D geological framework for the YM site in order to create coverages that provide a basis from which to evaluate the potential for perched water formation. This effort, together with the application of the Allan diagram approach, provides the means to identify regions within the study area where faulting, or other mechanisms, might lead to conditions favorable to the formation of localized perched-water zones. Under Task 6, some of the complications that stem from the combination of sorption reactions with mass transport models have been identified, and theoretical work has been initiated so that more sophisticated formulations of surface complexation models provide for the incorporation of the electric double layer. Under the same task, the geochemical speciation code MINTQA2 was used to calculate sorption of U^{6+} and Np^{5+} on goethite in a batch system with pH ranging from 2 to 12. Finally, under Task 7, CNWRA

staff interacted with the University of Arizona research group and provided a letter report describing the CNWRA data needs and a field testing plan for the ALTS.

9.4 PLANS FOR NEXT REPORTING PERIOD

The infiltration sensitivity work reported here provides guidance for the application of GIS techniques to the estimation of the spatial distribution of net infiltration over the YM area. As indicated here, the hydraulic properties of the subsurface medium have a large role in determining net infiltration, but the climatic inputs also have a role. Over a 10,000-yr period, the sensitivity analysis indicates that infiltration at YM may increase by as much as an order of magnitude or may decrease by a factor of two. The hypothesized variation in net infiltration is primarily due to variation in precipitation, with a lesser influence due to variation in surface temperature. Under current climatic conditions, micrometeorologic variability at the subregional scale would not be expected to yield a variation in net infiltration more than a factor of two due to any micrometeorologic input considered. Micrometeorologic variability is easily accommodated through a GIS database that includes elevation and solar loading. In future work, the sensitivity analyses will be continued using hydraulic properties representative of nonwelded tuffs and welded-tuff fractures in the YM area. These sensitivity results will be combined with a GIS description of the spatial distribution of geology, elevation, and solar loading to arrive at an estimated spatial distribution of recharge at the subregional scale. First-level screening using Allan diagrams determines areas where hydrology and geometry are favorable to the formation of localized perched water. Subsequent analyses will focus on the geochemical data available for these areas in an effort to further define where perched water may have occurred in the past. The availability of geochemical data is likely to be one of the limiting factors in selecting those areas for more detailed examination. As additional data become available, particularly for water chemistry in the unsaturated zone, and as data on the perched-water bodies encountered to date in the YM subregion (Burger and Scofield, 1994) are released, they will be incorporated in the 3D geological framework. These data will be used to constrain conceptual models and provide a means of establishing boundary and initial conditions for numerical models and evaluation of model results. Future work will also investigate the quantitative effects of charge conservation on retardation of radionuclides under conditions appropriate to the proposed repository at YM, Nevada. During the next period, further refinements and enhancements of the YM GFM will be incorporated. In particular, structural features that are considered as significantly affecting water and vapor movement will be incorporated into the CNWRA model. Geostatistical variability will also be incorporated to address issues dealing with model prediction uncertainty and data sufficiency. Finally, as part of independent model development efforts, a collaborative research effort will be pursued at the ALTS with the University of Arizona.

9.5 REFERENCES

- Allan, U.S. 1989. Model for hydrocarbon migration and entrapment within faulted structures. *American Association of Petroleum Geologists Bulletin* 73: 803-811.
- Allison, J.D., D.S. Brown, and K.J. Novo-Gradac. 1991. *MINTEQA2/PRODEFA2, A Geochemical Assessment Model for Environmental Systems: Version 3.0 User's Manual*. EPA/600/3-91/021. Athens, GA: Environmental Protection Agency.

- Bagtzoglou, A., and M. Muller. 1994. *Stochastic Analysis of Large-Scale Unsaturated Flow and Transport in Layered, Heterogeneous Media*. CNWRA 94-012. San Antonio, TX: Center for Nuclear Waste Regulatory Analyses.
- Bassett, R., S. Neuman, T. Rasmussen, A. Guzman, G. Davidson, and C. Lohrstorfer. 1994. *Validation Studies for Assessing Unsaturated Flow and Transport through Unsaturated Fractured Rock*. NUREG/CR-6203. Washington, DC: Nuclear Regulatory Commission.
- Bish, D.L., and J.L. Aronson. 1993. Paleogeothermal and paleohydrologic conditions in silicic tuff from Yucca Mountain, Nevada. *Clays and Clay Minerals* 41: 148-161.
- Bish, D.L., and S.J. Chipera. 1989. *Revised Mineralogic Summary of Yucca Mountain, Nevada*. LA-11497-MS. Los Alamos, NM: Los Alamos National Laboratory.
- Borkovec, M., and J. Westall. 1983. Solution of the Poisson-Boltzmann equation for surface excesses of ions in the diffuse layer at the oxide-electrolyte interface. *Journal Electroanalytical Chemistry* 150: 325-337.
- Burger, P., and K. Scofield. 1994. Perched water at Yucca Mountain and their implications on the Exploratory Studies Facility (abstract). *EOS, Transactions of the American Geophysical Union* 75(44): 250.
- Craig, R.W., and R.L. Reed. 1991. *Geohydrology of Rocks Penetrated by Test Well USW H-6, Yucca Mountain, Nye County, Nevada*. U.S. Geological Survey Water-Resources Investigations Report 89-4025. Denver, CO: U.S. Geological Survey.
- DeWispelare, A.R., L.T. Herren, M.P. Miklas, and R.T. Clemen. 1993. *Expert Elicitation of Future Climate in the Yucca Mountain Vicinity*. CNWRA 93-016. San Antonio, TX: Center for Nuclear Waste Regulatory Analyses.
- Flint, L.E., and A.L. Flint. 1990. *Preliminary Permeability and Water-Retention Data for Nonwelded and Bedded Tuff Samples, Yucca Mountain Area, Nye County, Nevada*. U.S. Geological Survey Open File Report 90-569. Denver, CO: U.S. Geological Survey.
- Flint, A.L., and L.E. Flint. 1994. Spatial distribution of potential near surface moisture flux at Yucca Mountain. *Fifth Annual International High-Level Radioactive Waste Management Conference Proceedings*. La Grange Park, IL: American Nuclear Society: 2,352-2,358.
- Freeze, R.A., and J.A. Cherry. 1979. *Groundwater*. Englewood Cliffs, NJ: Prentice-Hall, Inc.
- Frizzell, V.A., Jr., and J. Shulters. 1990. *Geologic Map of the Nevada Test Site, Southern Nevada. 1:100,000*. U.S. Geological Survey Miscellaneous Investigations Series Map I-2046. Reston, VA: U.S. Geological Survey.

- Guertal, W.R., A.L. Flint, L.L. Hofmann, and D.B. Hudson. 1994. Characterization of a desert soil sequence at Yucca Mountain, Nevada. *Fifth Annual International High-Level Radioactive Waste Management Conference Proceedings*. La Grange Park, IL: American Nuclear Society: 2,755–2,763.
- Hevesi, J.A., J.D. Istok, and A.L. Flint. 1992a. Precipitation estimation in mountainous terrain using multivariate geostatistics: Part I: Structural analysis. *Journal of Applied Meteorology* 31(7): 661–676.
- Hevesi, J.A., A.L. Flint, and J.D. Istok. 1992b. Precipitation estimation in mountainous terrain using multivariate geostatistics: Part II: Isohyetal Maps. *Journal of Applied Meteorology* 31(7): 677–688.
- Hevesi, J.A., and A.L. Flint. 1993. The influence of seasonal climatic variability on shallow infiltration at Yucca Mountain. *Fourth Annual International High-Level Radioactive Waste Management Conference Proceedings*. La Grange Park, IL: American Nuclear Society: 122–131.
- Hevesi, J.A., D.S. Ambos, and A.L. Flint. 1994a. A preliminary characterization of the spatial variability of precipitation at Yucca Mountain, Nevada. *Fifth Annual International High-Level Radioactive Waste Management Conference Proceedings*. La Grange Park, IL: American Nuclear Society: 2,520–2,529.
- Hevesi, J.A., A.L. Flint, and L.E. Flint. 1994b. Verification of a one-dimensional model for predicting shallow infiltration at Yucca Mountain. *Fifth Annual International High-Level Radioactive Waste Management Conference Proceedings*. La Grange Park, IL: American Nuclear Society: 2,323–2,332.
- Hsi, C-K.D., and D. Langmuir. 1985. Adsorption of uranyl onto ferric oxyhydroxides: Application of the surface complexation site-binding model. *Geochimica et Cosmochimica Acta* 49: 1,931–1,941.
- Hudson, D.B., A.L. Flint, and W.R. Guertal. 1994. Modeling a ponded infiltration experiment at Yucca Mountain, Nevada. *Fifth Annual International High-Level Radioactive Waste Management Conference Proceedings*. La Grange Park, IL: American Nuclear Society: 2,168–2,174.
- Loscot, C.L., and D.P. Hammermeister. 1992. *Geohydrologic Data from Test Holes UE-25 UZ#4 and UE-25 UZ#5, Yucca Mountain Area, Nye County, Nevada*. U.S. Geological Survey Open File Report 90-369. Denver, CO: U.S. Geological Survey.
- McKinley, P., and T. Oliver. 1994. *Meteorological, Stream-Discharge, and Water-Quality Data for 1986 Through 1991 from Two Small Basins in Central Nevada*. U.S. Geological Survey Open File Report 93-651. Denver, CO: U.S. Geological Survey.
- McKinley, P.W., M.P. Long, and L.V. Benson. 1991. *Chemical Analyses of Water for Selected Wells and Springs in the Yucca Mountain Area, Nevada and Southeastern California*. U.S. Geological Survey Open File Report 90-355. Denver, CO: U.S. Geological Survey.

- National Academy of Sciences. 1992. *Groundwater at Yucca Mountain: How High Can It Rise?* Report by the Panel on Coupled Hydrologic/Tectonic/Hydrothermal Systems at Yucca Mountain, Board on Radioactive Waste Management. Washington, DC: National Academy Press.
- National Climatic Data Center. March 1984 through February 1994. *WBAN Hourly Surface Observations*. Asheville, NC: National Oceanic and Atmospheric Administration.
- Nuclear Regulatory Commission. 1994. *Draft License Application Review Plan for the Review of a License Application for a Geologic Repository for Spent Nuclear Fuel and High-Level Radioactive Waste, Yucca Mountain Site, Nevada*. NUREG-1323. Washington, DC: Nuclear Regulatory Commission.
- Pearcy, E., W. Murphy, R. Green, B. Leslie, and J. Prikryl. 1993. Geochemical natural analogs. *NRC High-Level Radioactive Waste Research at CNWRA—Calendar Year 1991*. W. Patrick, ed. NUREG/CR-5817. Washington, DC: Nuclear Regulatory Commission: 7-1 to 7-32.
- Russell, C., J. Hess, and S. Tyler. 1987. Hydrogeologic investigations of flow in fractured tuffs, Rainier Mesa, Nevada Test Site. *Flow and Transport Through Unsaturated Fractured Rock*. D.D. Evans and T.J. Nicholson, eds. Geophysical Monograph 42. Washington, DC: American Geophysical Union: 43–50.
- Scott, R.B., and J. Bonk. 1984. *Preliminary Geologic Map (1:12,000 scale) of Yucca Mountain, Nye County, Nevada, with Geologic Cross Sections*. U.S. Geological Survey Open File Report 84-494. Denver, CO: U.S. Geological Survey.
- Stirewalt, G.L., and D.B. Henderson. 1995. A preliminary three-dimensional geological framework model for Yucca Mountain. *Sixth Annual International High-Level Radioactive Waste Management Conference Proceedings*. La Grange Park, IL: American Nuclear Society: 116–118.
- Stirewalt, G.L., D.B. Henderson, and S. Young. 1994. *A Preliminary Three-Dimensional Geological Framework Model for Yucca Mountain, Nevada: Report to Accompany Model Transfer to the Nuclear Regulatory Commission*. CNWRA 94-023. San Antonio, TX: Center for Nuclear Waste Regulatory Analyses.
- Stothoff, S. 1995. *BREATH Version 1.1—Coupled Flow and Energy Transport in Porous Media: Simulator Description and User Guide*. NUREG-CR 6333. Washington, DC: Nuclear Regulatory Commission. In press.
- Thordarson, W. 1965. *Perched Ground Water in Zeolitized-Bedded Tuff, Rainier Mesa and Vicinity, Nevada Test Site, Nevada*. U.S. Geological Survey Open File Report TEI-862. Denver, CO: U.S. Geological Survey.
- Turner, D.R. 1993. *Mechanistic Approaches to Radionuclide Sorption Modeling*. CNWRA 93-019. San Antonio, TX: Center for Nuclear Waste Regulatory Analyses.
- Turner, D.R. 1995. *A Uniform Approach to Surface Complexation Modeling of Radionuclide Sorption*. CNWRA 95-001. San Antonio, TX: Center for Nuclear Waste Regulatory Analyses.

- U.S. Department of Energy. 1986. *Final Environmental Assessment: Yucca Mountain Site, Nevada Research and Development Area, Nevada*. DOE/RW-0073. Washington, DC: U.S. Department of Energy.
- U.S. Department of Energy. 1988. *Site Characterization Plan, Yucca Mountain Site, Nevada Research and Development Area, Nevada*. DOE/RW-0199. Washington, DC: U.S. Department of Energy.
- U.S. Department of Energy. 1992. *Report of Early Site Suitability Evaluation of the Potential Repository Site at Yucca Mountain, Nevada*. Washington, DC: U.S. Department of Energy.
- Wang, J.S.Y., N.G.W. Cook, H.A. Wollenberg, C.L. Carnahan, I. Javandel, and C.F. Tsang. 1993. Geohydrologic data and models of Rainier Mesa and their implications to Yucca Mountain. *Fourth Annual International High-Level Radioactive Waste Management Conference Proceedings*. La Grange Park, IL: American Nuclear Society: 675–680.
- Whelan, J.F., and J.S. Stuckless. 1992. Paleohydrologic implications of the stable isotopic composition of secondary calcite within the Tertiary volcanic rocks of Yucca Mountain, Nevada. *Third Annual International High-Level Radioactive Waste Management Conference Proceedings*. La Grange Park, IL: American Nuclear Society: 1,572–1,581.
- Whitfield, M.S., C.M. Cope, and C.L. Loscot. 1993. *Borehole and Geohydrologic Data for Test Hole USW UZ-6, Yucca Mountain Area, Nye County, Nevada*. U.S. Geological Survey Open File Report 92-28. Denver, CO: U.S. Geological Survey.
- Wilson, M.L., J.H. Gauthier, R.W. Barnard, G.E. Barr, H.A. Dockery, E. Dunn, R.R. Eaton, D.C. Guerin, N. Lu, M.J. Martinez, R. Nilson, C.A. Rautman, T.H. Robey, B. Ross, E.E. Ryder, A.R. Schenker, S.A. Shannon, L.H. Skinner, W.G. Halsey, J.D. Gansemer, L.C. Lewis, A.D. Lamont, I.R. Triay, A. Meijer, and D.E. Morris. 1994. *Total-System Performance Assessment for Yucca Mountain—SNL Second Iteration (TSPA-1993)*. SAND93-2675. Albuquerque, NM: Sandia National Laboratories.
- Wittwer, C.S., G. Chen, and G.S. Bodvarsson. 1993. Studies of the role of fault zones in fluid flow using the site-scale numerical model of Yucca Mountain. *Fourth Annual International High-Level Radioactive Waste Management Conference Proceedings*. La Grange Park, IL: American Nuclear Society: 667–674.
- Yang, I. 1992. Flow and transport through unsaturated rock—Data from two test holes, Yucca Mountain, Nevada. *Third Annual International High-Level Radioactive Waste Management Conference Proceedings*. La Grange Park, IL: American Nuclear Society: 732–737.
- Yang, I.C., A.K. Turner, T.M. Sayre, and P. Montazer. 1988. *Triaxial-Compression Extraction of Pore Water from Unsaturated Tuff, Yucca Mountain, Nevada*. USGS-WRI-88-4189. Denver, CO: U.S. Geological Survey.
- Young, S.R., G.L. Stirewalt, and A.P. Morris. 1992. *Geometric Models of Faulting at Yucca Mountain*. CNWRA 92-008. San Antonio, TX: Center for Nuclear Waste Regulatory Analyses.

10 HIGH-LEVEL WASTE NEAR-FIELD PROCESSES AND VARIATIONS

by William M. Murphy, Roberto T. Pabalan, and Christopher J. Goulet

Investigators: William M. Murphy, Roberto T. Pabalan, James D. Prikryl, and Christopher J. Goulet

NRC Project Officer: Ralph E. Cady

10.1 TECHNICAL OBJECTIVES

The near field of the proposed repository for high-level radioactive waste (HLW) at Yucca Mountain (YM), Nevada, is the portion of the repository that would be altered to an extent that affects repository performance. Modifications may result from construction, emplacement of waste and engineered barrier materials, thermal loading, fluid circulation, and chemical reactions. Many uncertainties are associated with these processes and their complex couplings. Numerous Key Technical Uncertainties (KTUs) with regard to repository licensing have been identified that derive from near-field processes and variations. The general technical objectives of the HLW Near-Field Processes and Variations Research Project (Near-Field Project) are to generate hypotheses for the behavior of the near field of the proposed repository at YM, to identify processes and variations that are significant with regard to repository performance and that engender KTUs, and to perform research to attempt to address selected uncertainties.

Research in the Near-Field Project has focused initially on testing the hypothesis that releases of much of the radionuclide inventory from the engineered barrier system (EBS) will be controlled by the properties of secondary minerals composed of oxidized U (uranyl) and other components of the geologic environment. Experimental studies designed to mimic conditions in a repository at YM (e.g., Wronkiewicz et al., 1992) and studies of U deposits that are natural analogs of the proposed repository (e.g., Murphy and Percy, 1992; Percy et al. 1994) indicate that a calcium uranyl silicate hydrate, uranophane {nominally $\text{Ca}(\text{UO}_2)_2[\text{SiO}_3(\text{OH})_2 \cdot \text{H}_2\text{O}]$ }, is a probable end product of the alteration of spent nuclear fuel at YM. Natural uranophane has been noted to incorporate Th in its structure (Fron del, 1958). Similarly, uranophane that is secondary after spent fuel could incorporate much of the nuclear waste inventory and control its release from the EBS. Despite this reasonable scenario, the role of secondary uranyl minerals is generally disregarded in evaluations of repository performance (e.g., Nuclear Regulatory Commission, 1995). This omission is due in part to the dearth of thermodynamic data for uranyl silicate minerals, which could be used in predictive modeling of repository behavior. In a recent review, Murphy and Pabalan (1995) concluded that no reliable thermodynamic data exist for uranophane. A specific technical objective of the Near-Field Project is to evaluate thermodynamic data for uranyl minerals and to generate critical data through original experimentation. This report outlines the behavior of uranyl minerals as a function of temperature using available data and thermodynamic theory. It also presents data on the experimental synthesis of uranophane for use in solubility and coprecipitation studies designed to generate additional data that may be used in predictions of the performance of the proposed repository.

KTUs that are directly addressed by this work involve demonstration of repository performance with regard to cumulative release, particular subsystem performance objectives, and specific siting criteria. KTUs regarding development and validation of conceptual and mathematical models and variability (temporal, spatial, etc.) of model parametric values are addressed directly in research on uranyl minerals. Accurate determination of the properties of uranyl minerals will assist in testing the validity of their

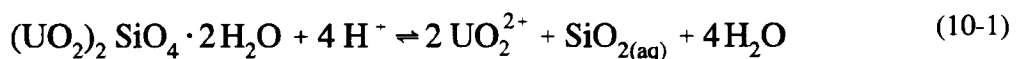
incorporation in conceptual models for the repository system. Parametric values for uranyl mineral solubilities and coprecipitation of other waste species can be used to constrain the source term for radionuclide releases and to address the subsystem performance objective KTU on prediction of effects of environmental conditions on the waste package during the containment period and of the effects of environmental conditions on the EBS during the post-containment period. Determination of fundamental thermodynamic properties provides a theoretical basis for extrapolation, also addresses these KTUs. Additionally, the KTU on characterizing the chemistry of the groundwater in the partially saturated hydrologic zone of YM, Nevada, which is founded on siting criteria, is addressed by developing an understanding of the constraints on water chemistry provided by interactions with uranyl phases.

10.2 SIGNIFICANT TECHNICAL ACCOMPLISHMENTS

10.2.1 Review of Literature on Thermodynamic Data for Uranyl Minerals

Empirical thermodynamic data for uranyl minerals are limited. Properties for the uranyl hydrate, schoepite ($\text{UO}_3 \cdot 2\text{H}_2\text{O}$), are recommended in the recently published, comprehensive review of chemical thermodynamics of U edited by Wanner and Forest (1992). These data, which are derived from calorimetric studies, are examined in detail in Section 10.2.2. Attempts have been made to determine equilibrium solubilities of uranyl minerals by Nguyen et al. (1992) and Casas et al. (1994) using synthetic and natural samples, respectively. These studies were critically reviewed by Murphy and Pabalan (1995) who judged the data to be mostly unreliable. Principal problems in the experimental studies and data interpretations are: Reaction stoichiometries were not firmly ascertained; chemical formulas used in thermodynamic interpretations were inconsistent with analytical data; phases other than those of primary interest were contaminants or precipitates and demonstrably affected some results; and solubility reversals were not attempted.

Dissolution studies for soddyite from Nguyen et al. (1992) provide the most likely basis for retrieval of reliable thermodynamic data. However, Nguyen et al. (1992) assumed that the soddyite conformed to its nominal ideal stoichiometry. Excess Si detected in the reactant material and in solution was assumed to be a consequence of the presence and dissolution of amorphous silica. For the reaction



the corresponding equilibrium constant is defined by

$$K = [\text{UO}_2^{2+}]^2 [\text{SiO}_{2(\text{aq})}] / [\text{H}^+]^4 \quad (10-2)$$

where square brackets represent thermodynamic activities corresponding to a standard state of a one molal solution referenced to infinite dilution. Nguyen et al. (1992) report $\log K = 5.74 \pm 0.21$ at 30 °C and the corresponding standard free energy of formation of soddyite from the elements, $\Delta G_f^\circ = -3,685 \pm 20 \text{ kJ mole}^{-1}$. (Uncertainties are based on uncertainties in standard state properties for the aqueous species and H_2O and propagated standard deviations of analytical results.) However, equilibrium was approached only from undersaturation (i.e., the reaction was not reversed), so the solubility must be regarded as a lower limit.

10.2.2 Temperature Dependence of Uranyl Mineral Solubility

Data recommended by Wanner and Forest (1992) permit evaluation of the solubility of schoepite as a function of temperature. Dissolution of schoepite may be expressed as



The equilibrium solubility of schoepite may be expressed by the mass action relation for reaction (10-3) as

$$K = \frac{[\text{UO}_2^{2+}][\text{H}_2\text{O}]^3}{[\text{UO}_3 \cdot 2\text{H}_2\text{O}][\text{H}^+]^2} \quad (10-4)$$

where K stands for the equilibrium constant and square brackets denote thermodynamic activities. The temperature dependence of K is given by the Van't Hoff relation

$$\frac{d \ln K}{dT} = \frac{\Delta H_r^0}{RT^2} \quad (10-5)$$

where T denotes temperature in kelvins, ΔH_r^0 stands for the standard state enthalpy of reaction, and R represents the ideal gas constant. The standard enthalpy of reaction is given as a function of temperature as the integral of the standard heat capacity of reaction (ΔC_p^0)

$$\Delta H_{(T)}^0 - \Delta H_{(T^0)}^0 = \int_{T^0}^T \Delta C_p^0 dT \quad (10-6)$$

where $\Delta H_{(T^0)}^0$ stands for the enthalpy of reaction at the reference temperature (T^0). $\Delta H_{298.15\text{K}}^0 = -50.30 \text{ kJ}\cdot\text{mole}^{-1}$ from Wanner and Forest (1992). The heat capacity of reaction (10-3) is given by

$$\Delta C_p^0 = 3C_{p,\text{H}_2\text{O}}^0 + C_{p,\text{UO}_2^{2+}}^0 - C_{p,\text{schoepite}}^0 \quad (10-7)$$

where $C_{p,i}^0$ represents the standard heat capacity of species i . Using heat capacity functions and values from Wanner and Forest (1992) for UO_2^{2+} (extrapolated above 328K) and schoepite, and a constant heat capacity for H_2O of $75.48 \text{ J}\cdot\text{K}^{-1}\cdot\text{mole}^{-1}$, which is accurate within less than 1 percent between 25 and 100 °C (Weast, 1988), the heat capacity of reaction (10-3) calculated using Eq. (10-7) is given by

$$\begin{aligned} \Delta C_p^0 &= 492.71 (\text{J}\cdot\text{K}^{-1}\cdot\text{mole}^{-1}) - 1.1668 (\text{J}\cdot\text{K}^{-2}\cdot\text{mole}^{-1})T - \frac{5308 (\text{J}\cdot\text{mole}^{-1})}{T - 190 (\text{K})} \\ &= A - B T - \frac{C}{T - D} \end{aligned} \quad (10-8)$$

Using Eqs. (10-6) and (10-8), the integral of Eq. (10-5) yields the equilibrium solubility of schoepite as Nuclear Waste Regulatory Analyses a function of temperature, which can be expressed as

$$\begin{aligned} \ln K - \ln K^0 &= \int_{T^0}^T \frac{\Delta H^0(T)}{RT^2} dT \\ &= \int_{T^0}^T \frac{A(T-T^0)}{RT^2} - \frac{B(T^2-T^0{}^2)}{2RT^2} - \frac{C}{RT^2} \ln \left[\frac{T-D}{T^0-D} \right] + \frac{\Delta H^0(T^0)}{RT^2} dT \end{aligned} \quad (10-9)$$

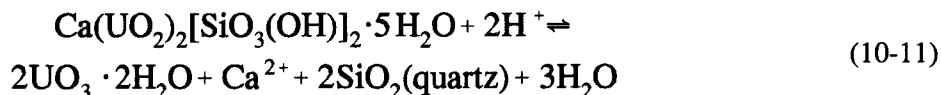
where K^0 denotes the equilibrium constant at T^0 . $K_{298.15K} = 6.50 \times 10^4$ derived from standard state free energies of formation of reactants and products in reaction (10-3) taken from Wanner and Forest (1992). Solving the definite integral in Eq. (10-9) yields

$$\begin{aligned} \ln K - \ln K^0 &= \frac{A}{R} \ln \frac{T}{T^0} + \left(\frac{-AT^0}{R} + \frac{(BT^0)^2}{2R} + \frac{\Delta H^0(T^0)}{R} \right) \left(\frac{1}{T^0} - \frac{1}{T} \right) \\ &\quad - \frac{B(T-T^0)}{2R} + \frac{C}{R} \left[\frac{T-D}{DT} \ln \left(\frac{T-D}{T^0-D} \right) + \frac{\ln T^0}{D} - \frac{\ln T}{D} \right] \end{aligned} \quad (10-10)$$

The dependence of equilibrium solubility on temperature can be seen in Figure 10-1, which shows the natural logarithm of the equilibrium constant calculated using Eq. (10-10) plotted as a function of inverse temperature. Although the inclusion of temperature-dependent heat capacity factors in the integral alters the predicted solubility curve, the difference is small between 25 and 100 °C. The solid line in Figure 10-1 represents calculations that include the heat capacity and its temperature dependence. The dashed line represents an assumed constant standard enthalpy of reaction (i.e., $\Delta C_p^0=0$).

According to Figure 10-1, the equilibrium solubility of schoepite increases with decreasing temperature. This retrograde solubility is further illustrated by comparing the aqueous activity of UO_2^{2+} at different temperatures. At pH 8, $[UO_2^{2+}]$ at equilibrium with schoepite equals 6.48×10^{-12} at 25 °C and 0.17×10^{-12} at 100 °C. In a progressively cooling repository near field, the solubility of schoepite would progressively increase. This process could provide a mechanism for subsequent release of U and other waste species sequestered in secondary schoepite.

Equilibrium between uranophane and schoepite can be expressed as



Enthalpy and Gibbs free energy data are presently unavailable to perform a solubility analysis for uranophane. However, if the standard enthalpy of formation of uranophane is assumed to be close to that of schoepite plus quartz and water, the enthalpy of reaction (10-11) would be dominated by the enthalpy of the Ca^{2+} ion, and its value would be large and negative. For these conditions, with decreasing temperature in the near field, schoepite plus quartz will be thermodynamically favored to form at the

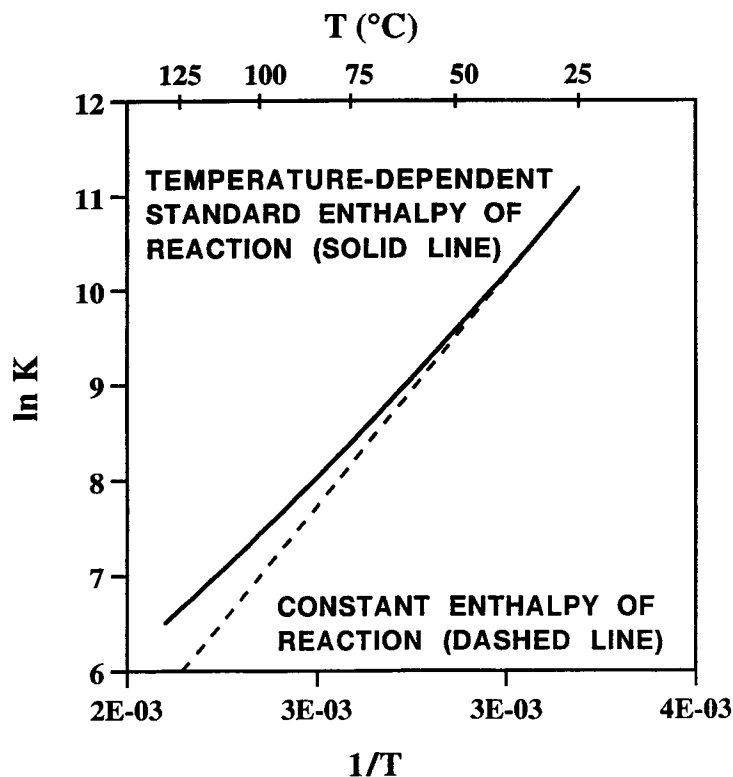


Figure 10-1. Natural logarithm of the equilibrium constant for the dissolution of schoepite (reaction 10-3) as a function of inverse temperature in kelvins. Temperature in °C is given at the top of the figure. The dashed line was calculated assuming a constant value of the standard enthalpy of reaction equal to its value at 25 °C. The solid line was calculated using Eq. (10-10).

expense of uranophane despite the retrograde solubility of schoepite, which follows from the Van't Hoff relation applied to reaction (10-11). This result suggests that the solubility of uranophane is also retrograde with temperature, even more strongly than schoepite solubility.

In nature secondary uranyl minerals tend to form in a sequence, such as schoepite, soddyite, uranophane, characterized by increasing incorporation of cations from the environment (e.g., Pearcy et al., 1994). Equilibrium solubility with decreasing temperature in a closed system, as described in relation to reaction (10-11), would probably lead to the reverse sequence. Open system behavior is typical of alteration of rocks in the unsaturated zone at YM, where zeolitized rocks are commonly enriched in Ca and Mg relative to the primary bulk rock composition (e.g., Murphy, 1993). It is likely that environmental conditions will have a strong effect on formation of secondary uranyl minerals. Spent nuclear fuel oxidizes to U_4O_9 in moist air. At temperatures below 200 °C this phase is apparently metastable, and complete oxidation to a U(6+) phase does not occur over periods of time in excess of 4 yr under laboratory conditions (Einzigler et al., 1992). However, in the presence of synthetic groundwater at 95 °C, unirradiated UO_2 alters to secondary uranyl minerals including uranophane (Wronkiewicz et al., 1992). Liquid water is clearly necessary for formation of secondary phases that incorporate components such as Si or Ca from the geologic setting. Liquid water is also required for transport of waste species out of the EBS (except for potential gas phase species such as ^{14}C). It is logical that spent nuclear fuel in the proposed repository at YM will react with liquid water to form secondary uranyl minerals prior

to releases from the EBS by groundwater flow or aqueous diffusion. As the activity of aqueous Ca increases uranophane will tend to form rather than schoepite or soddyite despite diminishing temperature. Also, Fe derived from corrosion of waste container materials could affect the composition of secondary uranyl minerals in the repository near field. Solubility experiments are being designed to maximize the potential to acquire reliable thermodynamic data for reactions between likely secondary uranyl minerals and aqueous solutions. These data can then be used to predict near-field behavior for variable environmental conditions.

10.2.3 Synthesis of Uranophane

Although natural uranyl mineral samples are available, they are typically of insufficient quantity or purity for use in solubility experiments. In addition, crystal defects in natural samples, which may be present due to radiation damage, could adversely affect the results of the experiments. Furthermore, radioactive decay daughter products (e.g., Th) in natural samples may complicate determination of U concentrations if techniques that measure radio activities (e.g., liquid scintillation) are used. Consequently, efforts have been devoted to synthesis of uranyl minerals for experimental study. Although a radiation field and radiation damage will exist in the near field, their effects are beyond the present scope of study. However, experimental studies are anticipated on coprecipitation of radionuclide species (e.g., Pu and Np) in secondary uranyl minerals.

Uranophane for potential use in solubility and coprecipitation studies has been synthesized based on the method of Cesbron et al. (1993) using reagent grade uranyl acetate dihydrate $[\text{UO}_2(\text{CH}_3\text{COO})_2 \cdot 2\text{H}_2\text{O}]$, sodium metasilicate nonahydrate $[\text{Na}_2\text{SiO}_3 \cdot 9\text{H}_2\text{O}]$, and calcium acetate monohydrate $[\text{Ca}(\text{CH}_3\text{COO})_2 \cdot \text{H}_2\text{O}]$. About 105 g of the reagents in the stoichiometric ratio Ca:U:Si = 2:1:1 were placed in a teflon-lined stainless steel reaction vessel which was subsequently capped and evacuated to remove $\text{CO}_2(\text{g})$. Then 1,300 g of deionized, degassed water (with pH lowered to about 1 by addition of HCl) was introduced into the vessel. The temperature was raised to 150 °C, and the reaction allowed to occur for about ten days. After cooling, the supernatant liquid was decanted; its pH at room temperature was measured to be 4.62. The solid product was washed several times with deionized water and dried overnight in an oven at about 60 °C.

An x-ray powder diffraction (XRD) pattern of the synthetic uranophane is shown in Figure 10-2, together with a reference pattern for uranophane taken from the International Centre for Diffraction Data (1993) database. The synthetic uranophane XRD pattern was determined with a Siemens D-500 x-ray diffractometer and Kristalloflex 800 x-ray generator using $\text{CuK}\alpha$ radiation, a scan step of $0.02^\circ 2\theta$, and a time constant of 2 seconds. For comparison, the XRD pattern is illustrated for hand-picked uranophane from a sample collected at the Nopal I U deposit, and peaks are indicated in the XRD pattern reported by Nguyen et al. (1992) for synthetic uranophane. Correspondence between these patterns is good. Only one small peak appears in the pattern for the synthetic sample that is absent in the PDF pattern. This peak does not correspond to potential contaminant minerals, and it does appear in the patterns for the Nopal sample and the pattern for synthetic uranophane from Nguyen et al. (1992). The magnitude and sharpness of the peaks in the XRD pattern indicate that the synthesized material is well crystallized. Figure 10-3 is a scanning electron photomicrograph showing the fine grained character and acicular morphology of uranophane synthesized in this study.

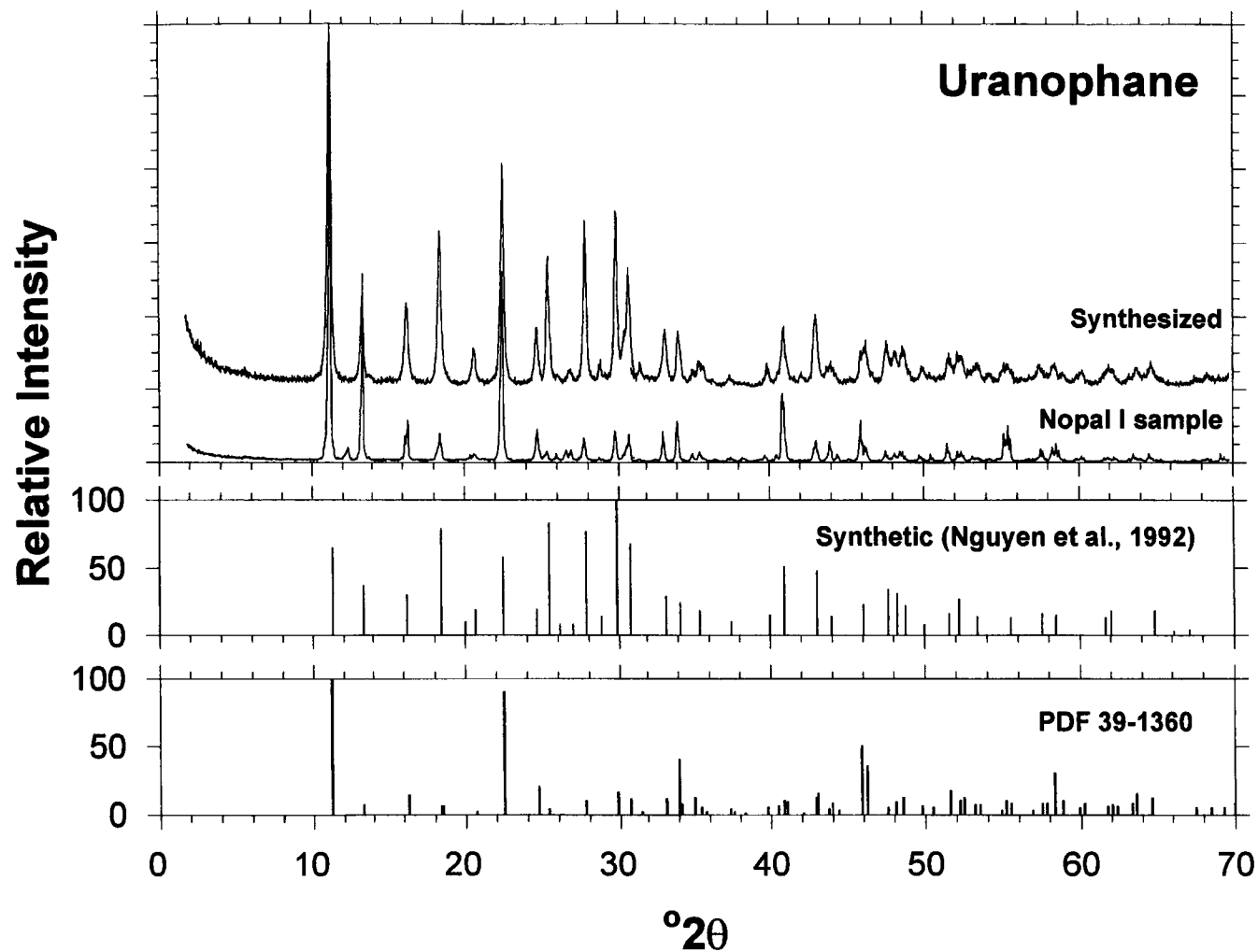


Figure 10-2. XRD pattern of uranophane synthesized in this study compared with the XRD pattern (PDF 39-1360) taken from the International Centre for Diffraction Data (1993) database, and diffraction data for synthetic uranophane reported by Nguyen et al. (1992) and uranophane collected at the Nopal I U deposit

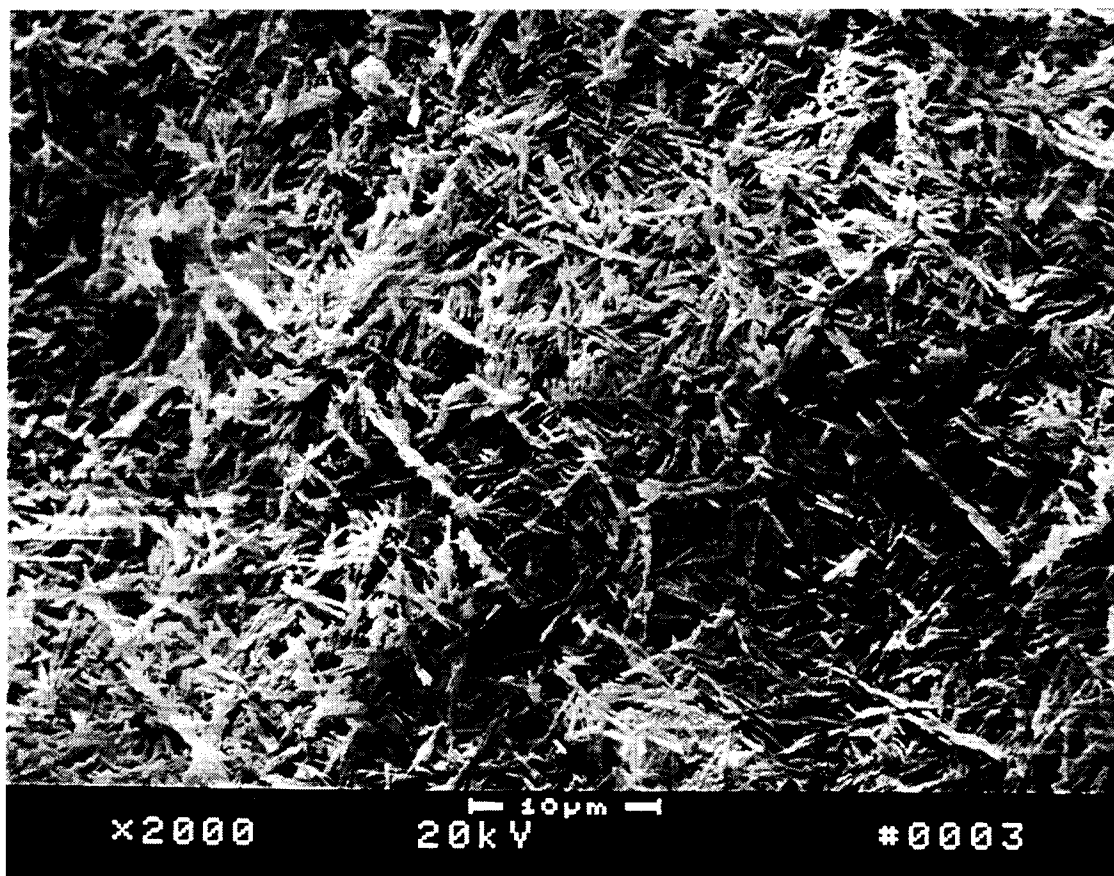


Figure 10-3. Scanning electron photomicrograph of uranophane synthesized in this study

10.3 ASSESSMENT OF PROGRESS TOWARD MEETING PROJECT OBJECTIVES

Although the Near-Field Project was only initiated mid way through this reporting period, considerable progress has been made on two fronts identified for detailed analyses. A literature review and critical analysis were performed on the thermodynamic properties of uranyl silicate minerals, and a plan was developed for original experimentation (Murphy and Pabalan, 1995). Based on relevant experimental and natural analog data, uranophane was identified as a primary phase of interest. It was successfully synthesized and partially characterized in preparation for solubility and coprecipitation studies.

On another front, conceptual and numerical modeling was conducted to examine coupled thermohydrochemical effects in the near field. A theoretical basis was developed for coarse iterative coupling of two-phase thermohydrologic modeling with the code CTOUGH and detailed gas-water-rock kinetic and equilibrium mass transfer relations with the code EQ6.

In these two areas of detailed study, progress was made in generation of hypotheses for the behavior of the near field, identification of processes and variations that are significant with regard to repository performance, and conduct of original research to attempt to address these uncertainties. When

completed the research is anticipated to bear directly on numerous KTUs associated with near-field processes and variations.

10.4 PLANS FOR NEXT REPORTING PERIOD

Detailed research will continue in the fields of uranyl mineral thermodynamics and coupled thermohydrochemistry. Synthetic uranophane will be characterized further to establish its stoichiometry, and experiments to study the solubility of uranophane at 25 °C will be initiated. A set of thermodynamic data, initial geochemical conditions, and model phase assemblage will be established for thermohydrochemical modeling. Thermohydrology models will be refined and portions of the near field identified for detailed chemical modeling. In addition, a major effort will be devoted to development of a topical report comprising a comprehensive survey of hypotheses for near-field processes and variations. The objective of this study is to identify additional processes and variations that are likely to be significant with regard to repository performance and for which original research is warranted to address KTUs.

10.5 REFERENCES

- Casas, I., J. Bruno, E. Cera, R.J. Finch, and R.C. Ewing. 1994. *Kinetic and Thermodynamic Studies of Uranium Minerals Assessment of the Long-Term Evolution of Spent Nuclear Fuel*. SKB Technical Report 94-16. Stockholm, Sweden: Swedish Nuclear Fuel and Waste Management Company.
- Cesbron, F., P. Ildefonse, and M.C. Sichere. 1993. New mineralogical data on uranophane and beta-uranophane; synthesis of uranophane. *Mineralogical Magazine* 57: 301–308.
- Einzig, R.E., L.E. Thomas, H.C. Buchanan, and R.B. Stout. 1992. Oxidation of spent fuel in air at 175 to 195 °C. *Journal of Nuclear Materials* 190: 53–60.
- Fron del, C. 1958. Systematic mineralogy of uranium and thorium. *U.S. Geological Survey Bulletin 1064*. Washington, DC: U.S. Government Printing Office.
- International Centre for Diffraction Data. 1993. *Powder Diffraction File PDF-2 Database Sets*. Swarthmore, PA: International Centre for Diffraction Data: 1–43.
- Murphy, W.M., and R.T. Pabalan. 1995. *Review of Empirical Thermodynamic Data for Uranyl Silicate Minerals and Experimental Plan*. CNWRA 95-014. San Antonio, TX: Center for Nuclear Waste Regulatory Analyses.
- Murphy, W.M., and E.C. Pearcy. 1992. Source-term constraints for the proposed repository at Yucca Mountain, Nevada derived from the natural analog at Peña Blanca, Mexico. *Proceedings of the Scientific Basis for Nuclear Waste Management XV*. C.G. Sombret, ed. Pittsburgh, PA: Materials Research Society: 521–527.
- Murphy, W.M. 1993. Geochemical models for gas-water-rock interactions in a proposed nuclear waste repository at Yucca Mountain, Nevada. *Conference Proceedings FOCUS '93: Site Characterization and Model Validation*. La Grange Park, IL: American Nuclear Society: 115–126.

- Nguyen, S.N., R.J. Silva, H.C. Weed, and J.E. Andrews, Jr. 1992. Standard Gibbs free energies of formation at the temperature 303.15 K of four uranyl silicates: soddyite, uranophane, sodium boltwoodite, and sodium weeksite. *Journal of Chemical Thermodynamics* 24: 259–276.
- Nuclear Regulatory Commission. 1995. *Phase 2 Demonstration of the NRC's Capability to Conduct a Performance Assessment for a High-Level Waste Repository*. NUREG-1464. Washington, DC: Nuclear Regulatory Commission.
- Pearcy, E.C., J.D. Prikryl, W.M. Murphy, and B.W. Leslie. 1994. Alteration of uraninite from the Nopal I deposit, Peña Blanca District, Chihuahua, Mexico, compared to degradation of spent fuel in the proposed U.S. high-level nuclear waste repository at Yucca Mountain, Nevada. *Journal of Applied Geochemistry* 9: 713–732.
- Wanner, H., and I. Forest, eds. 1992. *Chemical Thermodynamics of Uranium*. Amsterdam, North Holland: Elsevier Science Publishers B.V.
- Weast, R.C. 1988. *CRC Handbook of Chemistry and Physics*, 69th Edition. R.C. Weast, ed. Boca Raton, FL: CRC Press.
- Wronkiewicz, D.J., J.K. Bates, T.J. Gerding, E. Veleckis, and B.S. Tani. 1992. Uranium release and secondary phase formation during unsaturated testing of UO₂ at 90 °C. *Journal of Nuclear Materials* 190: 107–127.